The Dissertation Committee for Bharath Bangalore Rajeeva Certifies that this is the approved version of the following Dissertation:

Plasmon-Mediated Patterning of Nanoparticles and Biomolecules for Functional Nano-Devices

Committee:

_____
Yuebing Zheng, Supervisor

_____
Andrew K. Dunn

_____
Brian A. Korgel

_____
C. Grant Willson

Plasmon-Mediated Patterning of Nanoparticles and Biomolecules for Functional Nano-Devices

by

Bharath Bangalore Rajeeva

Dissertation

Presented to the Faculty of the Graduate School of

The University of Texas at Austin

in Partial Fulfillment

of the Requirements

for the Degree of

Doctor of Philosophy

The University of Texas at Austin

December 2018

Dedication

I dedicate this dissertation to my parents and sister.

Acknowledgements

I would like to thank my advisor Dr. Yuebing Zheng for his invaluable guidance and advice throughout my graduate study. He always engaged in an open discussion about research ideas, no matter how unlikely or far-fetched the idea. In addition, I was provided the independence to forge my own path and take risks with ambitious projects. Without his advising and motivation, I would not have been able to carry through with any of the major accomplishments and publications of this study. I would like to thank the other members of my committee, Prof. Andrew Dunn, Prof. Grant Willson, and Prof. Brian Korgel, for their helpful comments and advice during my study that improved the quality of this work.

I have had the privilege to work with some amazing collaborators over the years. I would like to thank Dr. Derek Hernandez, Dr. Leonardo Scarabelli, Dr. Evan Perillo, Palash Acharya, Andrew Briggs, Dr. Pranaw Kunal, Dr. Jeremy Jarrett, Ahmed Hassan, Dr. Brett Walker, Prof. Andrew Dunn, Prof. Seth Bank, Prof. Vaibhav Bahadur, Prof. Luis Liz-Marzan, Prof. William Yu, and Prof. Jason Shear for collaborating with me in my projects. The FLIM measurement sessions and conversations with Evan helped my work significantly. I would like to thank all my lab members for their help throughout my graduate studies. I am grateful to Dr. Linhan Lin, Dr. Mingsong Wang, Dr. Zilong Wu, Xiaolei Peng, Yaoran Liu, Jingang Li and Pavana Kollipara for all their help and collaboration. Their motivation and positive thinking pushed me to work hard and overcome obstacles in research.

I would like to thank all the undergraduate researchers over the years; Bharadwaj Pingali for his work on surface functionalization, Daniel Penley for editing the manuscripts, and Majd Alabandi for his work on the app development. I also had a great time working

as a teaching assistant (TA) for the Materials Engineering Lab. I would like to thank Steve, Federico, and Abhimanyu Bhat for assisting me during my TA days. I am thankful to Dr. Richard Piner for his help with AFM and Raman measurements.

I would like to express my gratitude to Dr. Matt Colburn for giving me an opportunity to work in his team at Facebook Reality labs. The exposure to the world of augmented reality broadened my thought process and made me a better problem solver.

I have been extremely fortunate to have wonderful family and friends who have supported me throughout my journey. I am indebted to my parents, Dr. Kala R Swamy, and Dr. B. N. Rajeeva, my sister Bhoomika, and my Ajji (grandma) for their love, sacrifice and constant encouragement to aim high. Thanks to my uncle Keerthi, aunt Mala, cousin Mukul and Paati (grandma) for their encouragement. I would also like to thank my aunt Sridevi and uncle Srinath who helped me immensely during my stay in Austin. I am grateful to all my friends in Austin, especially Vatsal, Esha, Ankith, Nitin, Pranav, Priyanka, Venky, Sravan, and Vikas for their support and numerous memorable moments. The journey wouldn't have been so enjoyable without all the people mentioned above.

Abstract

Plasmon-Mediated Patterning of Nanoparticles and Biomolecules for Functional Nano-Devices

Bharath Bangalore Rajeeva, Ph.D.

The University of Texas at Austin, 2018

Supervisor: Yuebing Zheng

Nanoscale components are taking over the current generation devices in the semiconductor, biomedical, energy, and display industries. The translation of novel nanoparticles and biomolecules into practical applications depends on their precise patterning on a substrate. However, it has remained challenging to manufacture complex structures at sub-micrometer resolution due to inherent technological barriers, such as ink-spreading, and long post-processing time. This dissertation presents the progress made towards plasmon-mediated immobilization at scales ranging from single-nanoparticle regime up to large-area patterning. We exploit the photothermal and photochemical effects arising from hot spots of plasmonic nanoparticles for immobilization. We explore multi-photon plasmonic photolithography (MPPL) for patterning at single NP resolution and introduce laser-induced bubble printing to achieve large-area patterning. In addition, we also demonstrate simultaneous synthesis and structuring of nanoparticles and nanoalloys using a laser-mediated micro-bubble reactor. We demonstrate immobilization of multiple materials including bovine-serum albumin (BSA) hydrogels, quantum dots, silver nanorings, and immiscible bimetallic alloys. The fabricated structures are used in

applications such as emission-rate modification, surface enhanced spectroscopy, ultra-fast nucleation, and catalysis. The systems and methods developed in this work will aid in the realization of multi-functional substrates with tailored catalytic, optical, electronic, and magnetic functions.

Table of Contents

List of Figures xiii

Chapter 1: Introduction 1

1.1 Background 1

1.1.1 Colloidal Nanoparticles 1

1.1.2 Printing of Colloidal Nanoparticles 2

1.2 Plasmonics 5

1.2.1 Enhanced Light Scattering and Absorption 7

1.2.2 Plasmon-Mediated Spontaneous Emission Enhancement 8

1.3 Goal and Organization 10

1.4 References 11

Chapter 2: Multi-Photon Plasmonic Lithography 15

2.1 Introduction 15

2.2 Hot Spot Confined Multi-Photon Lithography 16

2.3 Protein Hydrogel Immobilization 17

2.4 Single Nanoparticle Dark-Field Scattering Spectroscopy 21

2.4.1 Characterization of the Protein Immobilization 24

2.4.2 Control Experiments 25

2.5 Fluorescence Lifetime Imaging Microscopy 27

2.8 Summary 28

2.9 References 29

Chapter 3: Large-Area Bubble Printing of Quantum Dots 34

3.1 Introduction 34

3.2 Bubble-Mediated Immobilization 36
3.2.1 Gold Nanoisland Substrate 37
3.2.2 Particle-Immobilization Mechanism 38
3.2.3 Large-Area Printing 41
3.3 Quantum Dot Printing 42
3.4 Multi-Color Quantum Dot Printing 47
3.5 Printing on Flexible Substrate 49
3.6 Summary 51
3.7 References 52
Chapter 4: Haptic-Interfaced Printing and Fluorescence Tuning 56
4.1 Introduction 56
4.2 Haptic-Integration and Printing 58
4.2.1 Coordinates Registration 58
4.2.2 Haptic-Interfaced Printing 59
4.3 Coordinate Scaling 61
4.4 Quantum Dot Fluorescence Tuning 62
4.5 Plasmon-Quantum Dot Interactions 65
4.6 Haptic-Interfaced Tuning of Plasmon-QD Interaction 68
4.7 Summary 70
4.8 References 71
Chapter 5: “Point-and-Shoot” Synthesis and Applications of Metallic Ring Arrays 74
5.1 Introduction 74
5.2 Printing Setup 76

5.3 Silver Ring Printing 77
5.3.1 Silver Ink Reduction 78
5.3.2 Mechanism for Ring Morphology 79
5.3.3 Structural Characterization 81
5.3.4 Optical Characterization 83
5.4 Dual-Mode Optical Spectroscopy 85
5.5 Microfluidic Device Integration 88
5.6 Summary 90
5.7 References 91
Chapter 6: Unified Synthesis and Structuring of Immiscible Metallic Nanoalloys 95
6.1 Introduction 95
6.2 Printing Setup 97
6.3 Nanoalloy Structuring 98
6.3.1 Structural Characterizations 99
6.3.2 High-Resolution Transmission Electron Microscopy 100
6.3.2 Chemical Characterizations 103
6.4 US^3 Mechanism 104
6.4.1 Computational Fluid Dynamics and Random Walk Simulations 105
6.4.2 Thermodynamic Analysis 109
6.5 Catalysis 112
6.6 Summary 113
6.7 References 114

Chapter 7: Conclusion 118

7.1 Summary 118

7.1.1 Immobilization at Single Nanoparticle Resolution 119

7.1.2 Large-area Immobilization via Bubble Printing 120

7.1.3 One-step synthesis and patterning of metal nanoparticles and nanoalloys 120

7.2 Future Work 121

7.3 References 122

Bibliography 125

List of Figures

Figure 1.1: Schematic demonstrating the wide applicability of colloidal nanoparticles prepared with varied materials. Reproduced from Lohse *et al.* with permission. Copyright 2012, American Chemical Society. 2

Figure 1.2: Comparison of the various nanoparticle patterning techniques. The patterning capability with sub-micron resolution, high throughput, and minimal post-processing is challenging to achieve. 4

Figure 1.3: Schematic showing the movement of electrons upon electromagnetic field incidence in the case of (a) SPPs, and (b) LSPs. Reproduced from Juan *et al.* with permission. Copyright 2011, Nature Publishing Group. 6

Figure 1.4: Normalized time-resolved fluorescence of QDs on a glass slide (red) compared with QDs on an Au film (blue) and coupled to a single NPA (green). The instrument response function (IRF) is also shown. Reproduced from Akselrod *et al.* with permission. Copyright 2015, Nature Publishing Group. 9

Figure 1.5: Summary of the goals of the goals of the dissertation study. In this study, we exploit the plasmon-enhanced photothermal and photochemical effects to achieve the immobilization of nanoparticles of various sizes and compositions. 10

Figure 2.1: Schematic of the multi-photon absorption in conjunction with the simulated electric field and hot spot distribution of a single 60 nm AuNT in response to the in response to a linearly polarized electromagnetic wave. Reproduced with permission from ref 28. Copyright 2008 John Wiley & Sons, Inc. 17

Figure 2.2: Schematic representation of the selective localization of BSA hydrogel molecules at the tip of a single AuNT. The protein is cross-linked close to the tip via MPPL, and not elsewhere. 18

Figure 2.3: SEM images showing the regioselective localization of BSA hydrogel on single AuNTs under various incident light polarization and intensity at (a,b) incident laser power of 1mW and (c) incident laser power of 2mW. Inset in (a-c) shows the BSA hydrogel positions isolated via image processing. The direction of the electric field vector of the incident laser is denoted at the top-right of each figure. (d,e) Simulated field intensity distributions over the surface of AuNT. The intensity enhancement (|E|/|E0|) is depicted on the color scale, indicating higher intensity at one or two tips, depending on the polarization. 20

Figure 2.4: Correlated single-particle dark-field spectroscopy and SEM. (a) Typical markers of BSA hydrogel prepared by direct laser writing to locate the individual AuNTs. (b) Dark-field image of multiple nanoparticles in the vicinity of the marker before fabrication. The extremely bright spot is the strong scattering from the marker (c) Dark-field image of the same region after fabrication. (d) SEM imaging of the region indicating the presence of well-separated single nanoparticles. 22

Figure 2.5: Representative dark-field scattering spectra of (a) pristine AuNT, single AuNT before and after fabrication with an incident laser power of (b) 1mW (c) 2mW indicating a red-shift post fabrication (d) FDTD simulated spectra of pristine AuNT and AuNT coated with BSA hydrogel on one, two and three tips, respectively. Simulations were performed for AuNT of 60nm edge length and 25nm thickness. The BSA hydrogel with a refractive index of 1.5 was added at one, two and three tips to mimic the experimental structures as seen in Figure 2 (a-c).... 25

Figure 2.6: Dark-field scattering spectra of two independent controls: (a) Before and after 2mW laser irradiation without the presence of BSA and RB (b) Before and after exposure of AuNT to BSA and RB fabrication solution without any laser irradiation. The “after” plot was offset along the y-axis for clarity. The inset shows the corresponding high magnification SEM image, with a scale bar of 100nm. 26

Figure 2.7: FLIM of the AuNT-BSA hydrogel nanoparticles fabricated using a 2mW incident laser. (a) FLIM image showing the control BSA hydrogel and AuNT-BSA hydrogel in the same FOV. (b) Histogram of lifetimes obtained from the same FOV indicating two separate lifetimes of ~70ps and ~240ps for AuNT-BSA hydrogel and control BSA hydrogel respectively. 27

Figure 3.1. Working principle of BP of QDs on plasmonic substrates. (a) Schematic of the optical setup for BP. (b) Schematic showing the QDs being trapped towards the bubble generated on the substrate, and the eventual immobilization of QDs on the substrate. (c) Illustration of the QDs immobilized along the path traversed by the laser beam to create patterns of QDs on the substrate. 37

Figure 3.2: (a) SEM image of the plasmonic substrate for bubble printing. Spots of 940 nm in diameter were randomly chosen on the image, and the %area coverage of the AuNPs was calculated as shown in the table. (b) All spots show uniform AuNP coverage with a standard deviation of 0.54%... 38

Figure 3.3: Overlay of SEM image and the simulated “hot spots” distributions on the semi-continuous AuNIs substrate. **d,** Simulated and experimental absorption spectra of the AuNIs substrate. 39

Figure 3.4: Particle trapping at a microbubble that is generated through the plasmon-enhanced photothermal effects. (a) Schematic illustration (in a cross-sectional view) of the particle-trapping mechanism by a single microbubble. The blue spheres indicate the suspended particles in the DI water. The particles follow the convective flow due to the frictional force. The inset shows the force distribution when a particle is trapped by the microbubble (indicated as the red dash line). PB and PL indicate the pressure in the bubble and liquid, respectively, which introduce a net force of FP pushing the particle outward. The surface tension FS introduce a drag force FD. (b) Simulated temperature distribution around a 1 μm bubble in a cross-sectional view. (c) Simulated flow velocity distribution around a 1 μm bubble with logarithmic scale in a cross-sectional view. The black lines indicate streamlines of the convective flow. (d) Time-resolved trapping process of a single 5.31 μm PS bead by a 1 μm bubble. Scale bar: 5 μm..... 40

Figure 3.5: (a) Merged fluorescence image of the patterned lines of QDs demonstrating the line-width variation in response to change in the incident laser power. The inset shows the SEM of the patterned line of QDs with a line-width of 680 nm. (b) Large area patterning of QDs rectangles created using BP with various line spacing. The line spacing is 1 μm, 1.5 μm, and 2 μm (bottom to top). (c) (a) High-resolution two-photon fluorescence image which resembles individual pixels. (d) The width of each pixel is obtained by calculation of the FWHM of the spots based on the intensity. 44

Figure 3.6: Versatile bubble printing capabilities: (a) Plot of pattern line-width vs. incident laser intensity. The linear fitting shows the on-demand capability of tuning the patterning dimensions by the laser power. (b) Bubble printing of red QDs into a contour of a butterfly as shown by fluorescence image. The line-width is 1μm. (c) Bright-field image of a Charlie Chaplin pattern of QDs via raster scanning in BP. The overall size is 120 μm×90 μm with 1μm line-space. (d, e) Bright-field and fluorescence images [tetramethylrhodamine isothiocyanate (TRITC) filter set] of Mona Lisa printed with red QDs using a raster scanning approach. The size of the complete image is 150 μm×90 μm. (f) Magnified fluorescence image depicting the high-resolution patterning capability of BP. (g) Fluorescence lifetime imaging of the QDs showing high-density uniform patterning capability of BP. (h) Fabrication of a microscale (80 μm×80 μm) QR code with blue QDs printed via raster scanning. The scale bar is 25 μm. 45

Figure 3.7: (a, b) Optical profilometry images of a 40 μm × 80 μm region around the right eye of the Monalisa pattern (Figure 3.6d). The average and rms roughness of the printed QDs are 12.6 nm and 16.5 nm, respectively. (c) The emission spectrum of control QDs on drop-casted on glass and AuNI (FWHM=30.2 nm), along with printed QDs (FWHM=34.1 nm). The printed QDs showed a blue-shift of ~1 nm and FWHM increase of 3.9 nm. 47

Figure 3.8: Towards multi-color QD printing: (a) (Left) Fluorescence images of bubble-printed red, yellow and blue QDs into three patterns. (Right) Corresponding fluorescence spectra of the three patterns depicting emission peaks from blue to red. (b) Integration of multiple QDs on a single substrate using multi-step bubble printing. The example is a USA map with the states of Texas, California, and Pennsylvania printed with different QDs. The size of the map is 120 μm×200 μm and each state is fabricated via raster scanning with 1 μm line space. 48

Figure 3.9: Bubble printing of QDs on a flexible substrate: (a) Fluorescence image of the longhorn pattern printed with red QDs over a PET film obtained using TRITC filter set. (b) Bright-field image of the printed QDs with the PET film in the bent state. The strong adhesion of QDs to the substrate ensures that the high integrity of the pattern is maintained after the mechanical bending. (c, d) Optical images of the PET film under the original and bent states, respectively. (e) Optical profilometer image (Wyco 9100) of the PET film showing an RMS roughness of 35 nm. 50

Figure 3.10: (a) Printing of QDs with sub-micron resolution on a PET film. (b) Corresponding fluorescence image. (c) Optical profilometer image of the patterned longhorn, along with zoomed-in portion (d) of the image. 51

Figure 4.1: (a) A schematic of the draw-view of the app showing the various buttons such as save, undo, and the new file. (b) A flow chart of the algorithm for registering and populating the coordinate and shutter matrix. 59

Figure 4.2: Haptic-interfaced bubble printing: (a) Illustration of haptic-interfaced bubble printing (HIBP). QDs in a single aqueous suspension can be immobilized on the substrate to exhibit variable emission wavelengths based on the hand movement over the smartphone screen, which in turn is replicated in the printing process. The bottom inset shows a magnified view of the CdSe/CdS QD along with an amphiphilic coating of PMAO-PEG. (b) Schematic of the experimental setup for the haptic-interfaced bubble printing. 60

Figure 4.3: Haptic printing and pattern scalability: (a) A hand-drawn spiral pattern over the smartphone is printed using red QDs on a plasmonic substrate. The fluorescence image of the spiral under the Tetramethylrhodamine (TRITC) channel is shown. (b) A snapshot of the basic shapes drawn on the smartphone screen. (c) HIBP of the pattern in (b) using red QDs at the different downscaling factors. (d-e) Bright-field optical images of the patterns of QDs on plasmonic substrates by HIBP. 61

Figure 4.4: Modification of fluorescence wavelengths and dynamics of patterned QDs: (a) Merged fluorescence image of yellow QDs patterned in four squares by variable BP parameters. The optical power, stage-translation speed, waiting time between the neighbouring lines, and line-spacing for the squares 1-4: (i) 0.52 mW/μm^2, 1000 µm/s, 500 ms, and 1 µm, (ii) 0.54 mW/μm^2, 500 µm/s, 600 ms, and 1 µm, (iii) 0.56 mW/μm^2, 100 µm/s, 800 ms, and 1 µm (iv) 0.58 mW/μm^2, 100 µm/s, 1 s, and 0.5 µm. Scale bar: 10 µm. (b) Fluorescence spectra from the four squares in a. (c) The relative intensity plots of the patterns fabricated in (a). 63

Figure 4.5: (a) Merged fluorescence images of patterns of yellow QDs printed with the various stage speeds and line spacing. For each pattern, the line spacing decreases from 4 μm to 0.5 μm (from bottom to top). The blue shifts occur at the lower stage speeds and the smaller line spacing. (b) Atomic force micrograph of the QDs printed at 10,000 μm/s. The image depicts a line-width of ~510 nm. (c) A contour plot of the ratio of the peak intensities for the blue (450-495 nm) and yellow (560-595 nm) light as a function of stage speed and line spacing. 65

Figure 4.6: Schematic of the optical setup for fluorescence-lifetime imaging microscopy (FLIM). PBS: Polarizing beam splitter, BD: Beam dump, SM: Scanning mirrors, DM: Dichroic mirror, PMT: Photomultiplier tube, and TCPSC: Time-correlated single-photon counting. 66

Figure 4.7: (a) Time-correlated fluorescence of red QDs (i) drop-casted on the glass, (ii) drop-casted on the plasmonic substrate, and (iii) bubble-printed on the plasmonic substrate. The lifetime decreases from 7.46 ns (QDs on glass) to 2.69 ns (QDs printed on the plasmonic substrate). (b) FLIM image of the patterned QDs with increasing power. (c) Fluorescence-lifetime modification by tuning the optical power in BP. (d) The plot of the mean lifetime vs optical power in BP. The mean lifetime increases from 2.26 ns to 2.84 ns with an increase of optical power in BP. 67

Figure 4.8. (a) The registered coordinates from the smartphone based on hand-drawn lines with the decreased hand movement speed (from left to right). (b) Fluorescence image of the corresponding patterns of yellow QDs by HIBP based on the hand-drawn lines in (a). Blue emission occurs to the printed QDs at the slower hand movement. (c) Fluorescence spectra of the corresponding marked regions on the lines of QDs in (b). (d) The registered coordinates from the smartphone based on hand-drawn patterns combining the variations of hand movement speed and line spacing. (e) Fluorescence image of the corresponding patterns of yellow QDs by HIBP based on the hand-drawn lines in (d). (f) Fluorescence spectra recorded from the marked regions in (e). The rectangles in (b) and (e) indicate the regions from which the fluorescence spectra are recorded. The numbers in (b) and (e) correspond to those in (c) and (f), respectively. 70

Figure 5.1: (a) Illustration of the bubble-mediated fabrication of Ag rings over the AuNI substrate. (b) Schematic of the optical setup comprising of the synchronized automated stage and optical shutter. 76

Figure 5.2: (a) Fabrication of Ag lines by a laser beam below the bubble-generation threshold power. The line-width increases when the laser power is increased from 0.2 mW/μm^2 to 0.5 mW/μm^2. The bubble is observable when the laser beam is at the end of the line. (b) Arrays of Ag inverted-U structures fabricated by a laser beam below the bubble-generation threshold power. (c) Dark-field optical image of an Ag ring array fabricated at a laser power of 0.75 mW/μm^2. The inset shows the bright-field optical image. (d-e) Dark-field optical images of arrays of Ag rings of variable sizes. The incident laser power is (d) 0.55 mW/μm^2, (e) 0.81 mW/μm^2, and (f) 0.95 mW/μm^2. The scale bar is 10 μm for all the panels. 78

Figure 5.3: Calculated temporal evolution of the bubble radius and the growth rate in the nondimensionalized form. 80

Figure 5.4: (a) Measured Ag ring diameter as a function of the incident laser power (b-c) SEM images of different Ag ring arrays fabricated with varied incident laser power. Scale bar in (b): 4 μm. (d-f) SEM image, EDS Ag mapping, and EDS Au mapping of an Ag ring on the AuNI substrate, which shows that the ring is composed of Ag while the Au nanoparticles are spread out everywhere. (g-i) AFM images and sectional analysis of a typical Ag ring. 82

Figure 5.5: (a) The relative transmittance spectra of the arrays of Ag rings fabricated at the variable laser power. The spectra were normalized with respect to that of the AuNI substrate as background. The inset show representative SEM images of four individual rings that increase their diameters (1.08 μm, 1.35 μm, 1,67 μm, and 2.02 μm) when the incident laser power changes from 0.53 mW/μm^2 to 0.89 mW/μm^2. (b) The FDTD-simulated relative transmittance spectra for the Ag rings in (a). (c) Simulated electric-field distribution at a 2 μm Ag ring upon the excitation of dipolar surface plasmon resonance mode. (d) The transmission spectra in the visible region. 83

Figure 5.6: (a) SEIRS of TNT on the three types of the Ag ring-AuNI substrates, which exhibit the different detuning between the plasmonic and molecular excitations. The spectra correspond to ring sizes of 1.08 μm, 1.67 μm and 2.02 μm from top to bottom, respectively. The lower panel shows the baseline-corrected spectra, which clearly reveal the molecular resonances. The baseline was obtained via a second-derivative method. (b) SERS spectra of R6G of variable concentrations on the Ag ring-AuNI substrate. (c) SERS signal counts of the different R6G modes based on multiple spectra taken at various random locations on the sample. The inset shows the simulated field distributions at the Ag ring-AuNI substrate. 86

Figure 5.7: (a) SERS spectra for 1μM R6G on the hybrid Ag ring-AuNI substrate *vs.* the bare AuNI substrate. (b) High-resolution Raman mapping of R6G over the Ag ring/AuNI hybrid substrate. (c) Raman counts of 1 μM R6G at 610 cm^{-1} and 1360 cm^{-1} as a function of the Ag ring size. The ring size decreases from 2.02 ± 0.08 μm to 1.08 ± 0.07 μm as the power reduces. (d) Concentration-dependent SERS spectra of crystal violet (CV) molecules on the 2.02 μm Ag ring substrate. 87

Figure 5.8: (a) A photo of a microfluidic chip consisted of a network of AuNIs confined within a microfluidic channel. (b) A bright-field optical image showing the fluid flow over the Ag ring array. 88

Figure 5.9: (a) Schematic of the one-inlet, one-outlet microfluidic setup wherein the silver precursor ink and R6G are introduced sequentially. The microfluidic channel width and height are 500 μm and 80 μm, respectively. (b) The plot of the mean pixel change of the optical images taken at various flow rates to demonstrate the stability of the fabricated Ag rings. The inset shows a typical difference image. (c) SERS signal counts of the different R6G modes based on many spectra taken at various random locations on the sample with 1.8 μm Ag ring. (d) SERS signal counts in the microfluidic chamber as a function of R6G concentration on the sample with 1.8 μm Ag ring. 89

Figure 6.1: Schematic demonstrating the optical setup and ion accumulation aspect of the US^3 strategy. The laser-induced MBT can lead to highly localized supersaturation of precursor ions near the substrate, enabling the synthesis and structuring of immiscible alloys. 98

Figure 6.2: (a) Bright-field optical image of the RGNs fabricated using US^3 strategy. The inset shows a completed sample of 2.25 mm^2 area. The bright reflection observed is due to the diffraction effect from the closely printed RGN lines. (b-d) Scanning electron microscopy (SEM) images of the printed RGNs with (b) 2 µm, (c) 4 µm, and (d) 8 µm line-widths. ... 98

Figure 6.3: (a) Optical profilometry data of printing rhodium gold (RhAu) nanoalloys (RGNs) with 4 µm line-spacing. (b,c) The height profile of the printed RGNs (along the red line). (d) High-resolution AFM imaging which corroborates the immobilization morphology, and the height profile of the printed RGNs. (e) Tunable sub-micron line-width of the structured RGNs as a function of the stage translation speed. 100

Figure 6.4: (a-b) HRTEM images of the transferred RGNs showing the crystallinity and the d lattice spacing of RGN. (c) HAADF-STEM image of the transferred RGNs, along with the inset of a two-dimensional (2D) overlapped energy-dispersive X-ray spectroscopy (EDS) mapping of Rh and Au. (d) Segregated Rh and Au 2D EDS mapping results showing the distribution of both the elements. (e) High-resolution transmission electron microscopy (HRTEM) image and 2D EDS mapping of a single RGN. Scale bar is 25 nm. 101

Figure 6.5: (a-b) Additional HRTEM images of the RGNs showing the increased d spacing of the particles in comparison with the pure Rh particles ($d_{<111>}$=0.219 nm). (a) Low-resolution TEM images of the RGNs transferred onto a TEM grid. (b) The particle size distribution of the RGNs showing a quasi-Gaussian distribution. 102

Figure 6.6: (a) EDS Spectra and 2D EDS mapping of the structured RGNs. (b) XPS of the RhAu sample with 2 μm line-spacing showing the surface characteristics of the sample. The molar ratio of Rh:Au obtained using XPS was 31:69 and 67% of the total detected Au was in the form of Au(0). Since maximum penetration depth of X-ray photoelectrons during analyses is only 8 nm, the entire structure of the resulting ≈25 nm RGNs cannot be probed using XPS and hence values obtained here are distinct from EDS analyses discussed above. (c) Transmission spectra of the sample at random locations spaced 200 μm away from each other. 104

Figure 6.7: (a) A side view bright field image of the microbubble showing a contact angle of 15. (b) The angle-dependent comparative analysis of the three major flow velocity components evaluated at angles of (c) 10°, (d) 20°, (e) 30°, (f) 40°, (g) 45°, (g) 60°. The thermophoretic flow velocity is observed to be two-orders lower than convection velocities, and thus neglected in the random walk simulations. 105

Figure 6.8: (a) Simulated temperature distribution in the vicinity of an MBT. The radius of the bubble is 1 μm. (b) Simulated flow velocity distribution around MBT with logarithmic scale in a cross-sectional view. (c) The trajectory of 200 ions simulated using the random walk simulations for a total time duration of 300 ms, showing the concentration of ions at the MBT/substrate interface. (d) The calculated incident ion flux, showing an exponential increase in the close vicinity of the MBT required to supplement the reduced ions. 107

Figure 6.9: (a) Ultra-fast camera image revealing the ultra-fast generation of the MBT. (b) Contour plot showing the average time required for an ion to reach from a specific location to the MBT. A majority of the ions within 10 μm vicinity reach the MBT in less than 1 ms. (c) A typical trajectory of an ion which can perform multiple loops in millisecond timeframe. 109

Figure 6.10: (a) The normalized critical nuclear radius as a function of supersaturation S, demonstrating a 3 order reduction in the radius. (b) The heat of formation E_f for RGNs at different Rh atomic concentration *x* and a total number of atoms of the NPs. 110

Figure 6.11: (a) UV-Visible absorption spectra showing the reduction of p-nitrophenol (pNP) catalyzed by the structured RGNs, Rh and Au substrates as well as control pNP solution. The inset shows the measurement configuration. (b) Conversation percentage of the reactants catalyzed by control samples (SiO_2, Rh and Au) and the RGNs. (c) EDS spectra of RGNs fabricated via US^3 with 2 μm, 4 μm and 8 μm line-spacing. The spectra are normalized with respect to Au peak. (d) Catalytic dependence of the RGNs on the line-spacing as characterized using the 400 nm reactant peak. 113

Figure 7.1: (a) Our work “"Point-and-Shoot" Synthesis of Metallic Ring Arrays and Surface-Enhanced Optical Spectroscopy” featured as Cover Picture by Advanced Optical Materials;[18] (b) Our work “Patterning and fluorescence tuning of quantum dots with haptic-interfaced bubble printing” featured as Back Cover by Journal of Materials Chemistry C;[11] (c) Our work “Regioselective Localization and Tracking of Biomolecules on Single Gold Nanoparticles” featured as Frontispiece by Advanced Science;[4] (d) Our work “Design and Applications of Lattice Plasmon Resonances” featured as Front Cover by Nano Research.[17] 119

Chapter 1: Introduction

1.1 BACKGROUND

The quest for achieving superior performance devices has motivated researchers to explore and exploit phenomena at the nanoscale. In the nanoscale, which is normally seen as going from 100 nm and down to just a few nanometers, the materials exhibit properties (e.g., electric conductivity, strength, melting point, color, etc.) different from those of their macroscopic equivalents. These unconventional properties have seen their widespread application in many commercial products, with current generation devices in the semiconductor, biomedical, energy and display industries are actively incorporating components fabricated at the nanoscale.

1.1.1 Colloidal Nanoparticles

The synthesis of well-designed nanocrystals in colloidal solution has evolved gradually since the 1950s, and has currently reached the situation wherein applications in both the research and industrial domain can be realized. With their unique physical and chemical properties that arise from spatial confinement and high surface volume ratio, colloidal nanoparticles (CNPs) are emerging as building blocks for new materials and devices.[1-4] An exponential rise in the popularity of CNPs was observed after the initial demonstration of ligand-stabilized quantum dots (QDs) and organic-solution gold nanoparticles.[5-6]

In the past two decades, CNP's applications have been actively explored, with tailor-made metal/semiconductor/dielectric materials being explored for each application niche (Figure 1.1). For instance, silver ions released from Ag CNPs under physiological conditions have enabled their use as antimicrobial agents.[7] Colloidal Pt, Ir, Pd NPs have

been utilized as catalysts in organic synthesis.[8]. Toward the biological domain, Au NPs integrated with appropriate biomolecules have opened up novel opportunities for the development of theranostic agents in biomedicine which provide both diagnostic and therapeutic capabilities.[9] CNPs also enable multiple optical phenomena and have been utilized for applications in energy, photonics, biomedical and semiconductor industries. For instance, CNPs such as QDs, dye-doped silica, Au CNPs, etc. are used for real-time optical imaging of cells and cellular processes.[10-13] In the case of energy applications, metal oxide CNPs have been used in the realization of next-generation solar cells.[14]

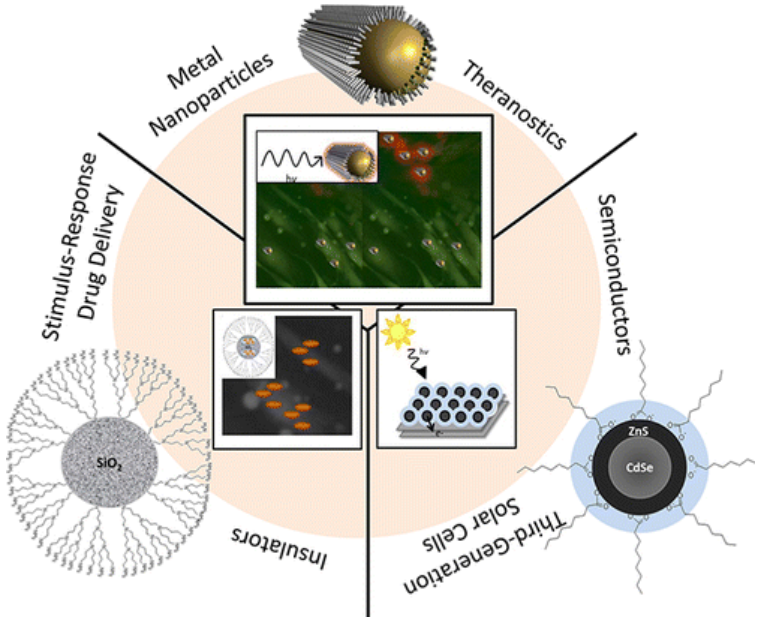

Figure 1.1: Schematic demonstrating the wide applicability of colloidal nanoparticles prepared with varied materials. Reproduced from Lohse *et al.* with permission. Copyright 2012, American Chemical Society.

1.1.2 Printing of Colloidal Nanoparticles

Tremendous progress in chemical synthesis has led to large-quantity CNPs with precisely controlled shapes, sizes, and compositions down to the atomic level.[15-16] The

CNPs have their sizes ranging from about one nanometer to several micrometers and are often dispersed in a host liquid medium. However, many applications in electronics, photonics, catalysis, and biomedicine require the assembly of CNPs onto the solid-state substrates with specific placement and patterns.[17-19] For example, metal plasmonic CNPs in well-designed patterns can work as metasurfaces and metamaterials due to the cooperative interactions, which exhibit exotic optical properties beyond natural materials such as a negative refractive index.[20] The optical responses of such metasurfaces and metamaterials depend on CNP sizes, shapes, compositions, spatial arrangements, and CNP surface chemistry, which need be precisely controlled for targeted applications such as photonic integrated circuits, electromagnetic cloaking, and ultrahigh resolution optical lithography.[21-22] Therefore, to achieve the full potential of CNPs for the large-scale functional materials and devices will require scalable nanomanufacturing techniques that can assemble CNPs into desired patterns on substrates at high throughput, resolution, and complexity while retaining their originally designed properties.

The patterning strategies can be primarily divided into top-down techniques and bottom-up techniques. Conventional top-down techniques such as photo-lithography rely on expensive mask-based approaches and are constrained in terms of their versatility.[23] Compared with the top-down fabrication of micro/nanoscale devices, the bottom-up approach based on the assembly of CNPs have advantages in the precise control of building blocks and the low-cost manufacturing.

Over the past decades, various non-conventional methods have been developed to pattern CNPs on substrates. Of promise are printing technologies such as Langmuir-Blodgett (LB) printing,[24] micro-transfer printing,[25] gravure printing,[26] inkjet printing,[27] and electrohydrodynamic jet (E-Jet) printing,[28] which have been successfully applied to create complex patterns of CNPs at a large scale. Despite their promise of achieving high

patterning resolution down to the single-particle level, the uses of LB and micro-transfer printing require masks for the patterning. Ink/nozzle-based printing techniques (i.e., Inkjet and E-Jet) are direct-writing approaches, which circumvent the reliance on a mask.

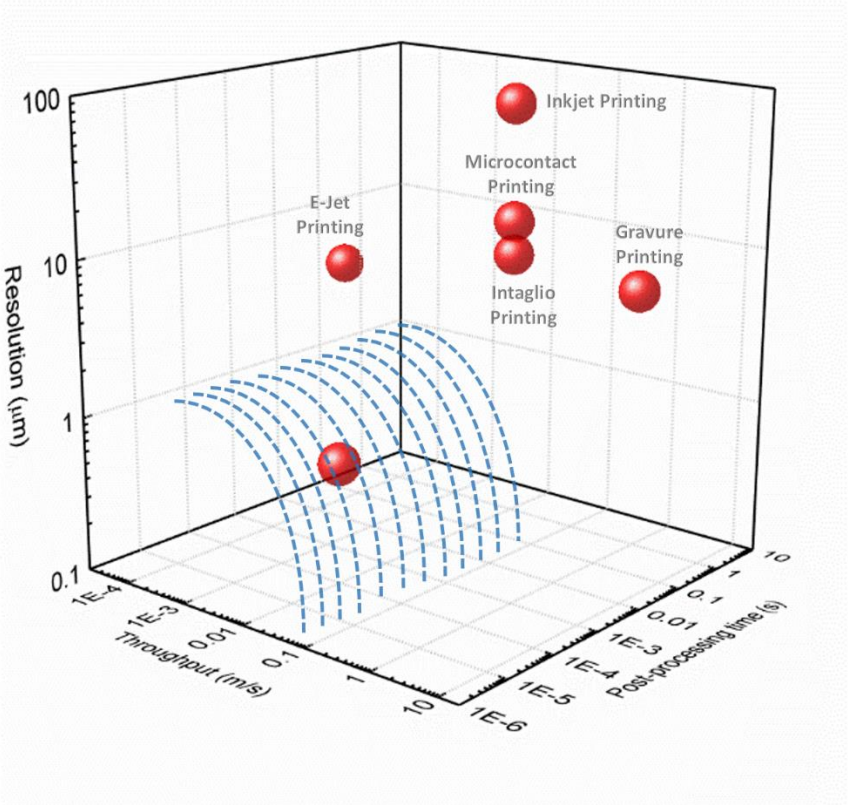

Figure 1.2: Comparison of the various nanoparticle patterning techniques. The patterning capability with sub-micron resolution, high throughput, and minimal post-processing is challenging to achieve.

Inkjet printing is currently a mature technology used to directly write patterned structures due to its low cost, efficient material use and waste elimination. It starts with the ejection of a finite quantity of colloidal solutions as inks from a nozzle onto the substrates. The ink dries via solvent evaporation. Numerous companies such as Kateeva, Fujifilm Dimatix, Samsung, and Seiko Epson have invested resources in the creation of inkjet heads that offer high precision and throughput. As a non-contact, additive and maskless technique, inkjet printing is versatile in writing a variety of CNP materials on both rigid

and flexible substrates. However, current direct-write technologies have several limitations, including (1) spatial resolution for manufacturing complex structures has been limited to the micrometer regime due to the spreading of the inks upon being delivered to the substrates; (2) considerable efforts required to prepare the CNP solutions as inks, which require special physiochemical properties such as viscosity and particle concentration. In most cases, as-synthesized CNP solutions cannot be used directly, and in some cases lead to clogging; and (3) long post-processing time is necessary for the inks to dry, which decreases the throughput. Thus with numerous limitations, an unconventional approach needs to be employed to simultaneously achieve multiple advantages such as high resolution, high throughput and minimal post processing steps. In this thesis, we explore the incorporation of plasmonics towards nanoparticle patterning.

1.2 PLASMONICS

The shrinking of optical devices such as lasers, sensors can enable numerous applications in photonic circuitry, displays, medical diagnosis, photo-thermal therapy, solar energy harvesting, etc. However, the convention optical devices are bulky and miniaturization is restricted by the diffraction limit and high costs. In recent decades, plasmonic which relates to the fundamental and applied study of surface plasmons (SPs) has emerged as a promising approach to address the above challenge. SPs, which correspond to strong light-coupled coherent oscillations of free electrons at the metal-dielectric interfaces have enabled the manipulating light at the nanoscale.[29-35] The surface SPs can be typically divided into two types: surface plasmon polariton (SPP) and localized surface plasmon resonances (LSPRs). As shown in Figure 1.1a, SPPs refer to the collective oscillation of the free electrons excited at the flat interface between a metal and a dielectric.[32]

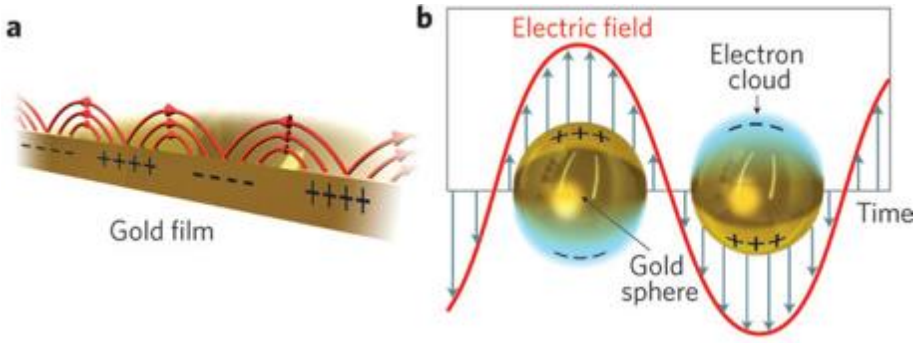

Figure 1.3: Schematic showing the movement of electrons upon electromagnetic field incidence in the case of (a) SPPs, and (b) LSPs. Reproduced from Juan *et al.* with permission. Copyright 2011, Nature Publishing Group.

The excitation of SPPs is achieved using glass prism which compensates the momentum mismatch between evanescent modes at the metal-dielectric interface and the incident wave via the total internal reflection phenomenon. Post SPP generation, light can be concentrated at the metal surfaces with significantly higher intensity than the incident intensity. Unlike the propagating nature of SPPs, LSPRs are a collective oscillation of bound electrons in individual metallic voids or particles with sub-wavelength dimensions, as shown in Figure 1.3b. At resonant frequencies, the LSPRs can efficiently couple with incident light without the requirement of momentum compensation. The incident light is concentrated near the sub-wavelength metallic structures, generating substantially enhanced local fields. Hence, plasmonic nanoparticles work as nanoantennas and exhibit highly concentrated electromagnetic field at sub-wavelength spots, known as “hot spots”. The LSPR frequency can be easily modulated by altering the size, shape, and material of the nanoparticles. The enhanced optical fields also manifest as efficient nanosources of heat, which can in-turn be harnessed for applications in cancer therapy, nanosurgery, phase transition, nanochemistry, and particle immobilization.[36]

1.2.1 Enhanced Light Scattering and Absorption

Plasmonic nanoparticles can exhibit significantly stronger scattering and absorption of light owing to the excitation of LSPRs. The basic theoretical approaches to understanding the light scattering and absorption for ultra-small nanoparticles is enabled using the quasi-static approximation.

With the pre-requisite that the size of a spherical nanoparticle is much smaller than the incident wavelength (<100 nm), a quasi-static approximation can be employed to describe its light scattering properties by solving the Laplace equation for the scalar electric potential: $\nabla^2\Phi = 0$ and $E = -\nabla\Phi$. Upon applying continuous boundary condition, the effective dipole moment of the metal nanoparticles can be expressed as:[37]

$$P = 4\pi\varepsilon_m a^3 \frac{\varepsilon_p - \varepsilon_m}{\varepsilon_p + \varepsilon_m} E_0 \qquad (1.1)$$

where ε_p is the complex dielectric constant of metal nanoparticles and ε_m is the dielectric constant of the surrounding medium. Further, the frequency-dependent ε_p can be expressed by the Drude model:[38]

$$\varepsilon_p = \varepsilon' + i\varepsilon'' = \varepsilon_\infty - \frac{\omega_p^2}{\omega^2 + i\omega} \qquad (1.2)$$

where ε' and ε'' are the real and imaginary part of the dielectric constant; ε_∞ is the contribution from the bound electrons; ω_p is the bulk plasma frequency of the metal and equates $Ne^2/\varepsilon_0 m^*$, where N is the free electron density, e is the charge of an electron, ε_0 is the vacuum permittivity, and m^* is the effective mass of an electron. With the dipole moment, the cross-sections of scattering (C_{sc}) and absorption (C_{abs}) of this dipole can be written as:

$$C_{sc} = \frac{8\pi}{3} a^2 q^4 \left| \frac{\varepsilon_p - \varepsilon_m}{\varepsilon_p + 2\varepsilon_m} \right|^2 \qquad (1.3)$$

$$C_{abs} = 4q\mathrm{Im}\left(\frac{\varepsilon_p - \varepsilon_m}{\varepsilon_p + 2\varepsilon_m} \right) \qquad (1.4)$$

where q is dimensionless size parameter and equates k_a, and k is the wave vector in the medium. By comparing Equations 1.3 and 1.4, it is seen that scattering cross-section increases faster than absorption cross-section as the nanoparticle radius increases. This implies that for efficient absorption and photothermal effect, smaller metal nanoparticles are more suitable. In addition, these two equations also unravel that the resonant enhancement of scattering and absorption is achieved when $\varepsilon_p = -2\varepsilon_m$, known as Fröhich condition. The resonance phenomenon integrated with various nanoparticles, like metallic, dielectric and semiconductor nanoparticles, or biomolecules can improve the properties of the immobilized moieties and lead to biosensing at sub-pico molar concentration, enhanced spectroscopy such as surface enhanced Raman spectroscopy, plasmon-enhanced fluorescence, developments in quantum optics, and potential applications in theranostics as well.[39-40]

1.2.2 Plasmon-Mediated Spontaneous Emission Enhancement

The realization of ultra-fast spontaneous emission rate of fluorophores and QDs is crucial for the development of single-photon sources, nanolasers, and various biosensing applications.[41] The placement of an emitter in an optical cavity can strongly enhance the spontaneous emission rate. This phenomenon is termed as the Purcell effect.[42] The strongly confined optical field resulting from the coherent oscillation of electrons on plasmonic cavities results in smaller cavities compared to conventional systems. This enables plasmonic nanostructures to have ultra-small mode volume, which in turn significantly enhances the Purcell factor given by: $F_p = \frac{3}{4\pi^2}\left(\frac{\lambda_c}{n}\right)^3\left(\frac{Q}{V}\right)$. Here Q is the quality factor, λ_c is the wavelength of light and n is the refractive index of the medium.

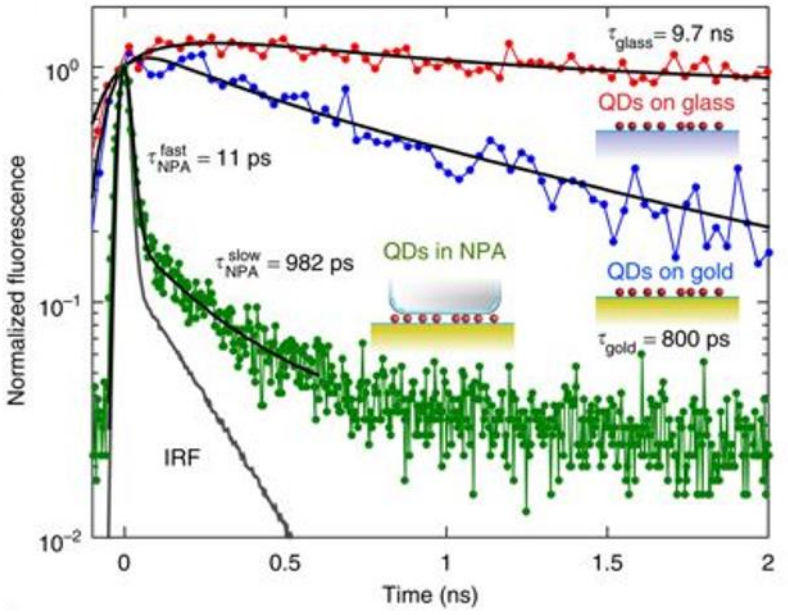

Figure 1.4: Normalized time-resolved fluorescence of QDs on a glass slide (red) compared with QDs on an Au film (blue) and coupled to a single NPA (green). The instrument response function (IRF) is also shown. Reproduced from Akselrod *et al.* with permission. Copyright 2015, Nature Publishing Group.

The dramatically enhanced emission rate can lead to a reduced lasing threshold and a fast radiative rate. These characteristics are critical to the development of single photon sources. By optimizing the fabrication conditions, Akselrod et. al. have demonstrated a spontaneous emission rate increase by a factor of 880 and simultaneously 2,300-fold enhancement in the total fluorescence intensity.[43] In case of dyes, Kinkhabwala et al demonstrated a maximum fluorescence enhancement rate of 1690 and a lifetime of SM *N*,*N*´-bis(2,6-diisopropyl-phenyl)-1,6,11,16-tetra-[4-(1,1,3,3-etramethylbutyl)phenoxy] quater-rylene-3,4:13,14-bis(dicarboximide) (TPQDI) shorter than 10 ps.[44]

1.3 GOAL AND ORGANIZATION

The goals of my doctoral research are to rationally design, fabricate and investigate the immobilization of functional nanoparticles (NPs) and biomolecules by exploiting the plasmonic effect of metal nanoparticles. The study also explores the influence of the plasmonic substrate over the patterned NPs and biomolecules. Plasmonic NPs with strong optical responses and high tunability can enhance the properties of moieties in their vicinity, thereby enabling the development of next-generation devices. In particular, my research will mainly focus on the fabrication and investigation of plasmon-NP/biomolecule hybrids and their interactions. The thesis is divided into three broad research aims: (1) immobilization of biomolecules on single NPs with ultra-high precision, (2) large-area, high-throughput and cost-effective fabrication of NPs on the plasmonic substrate, and (3) simultaneous reduction and immobilization of NPs from precursors on a plasmonic substrate.

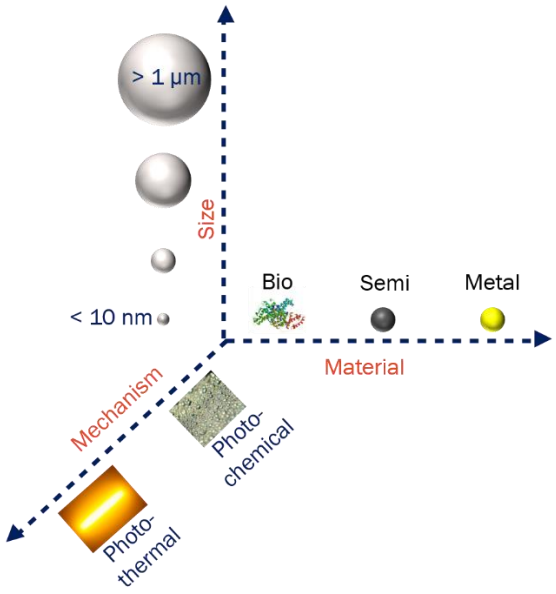

Figure 1.5: Summary of the goals of the goals of the dissertation study. In this study, we exploit the plasmon-enhanced photothermal and photochemical effects to achieve the immobilization of nanoparticles of various sizes and compositions.

The initial part of the study focuses on a single nanoparticle regime. Chapter 2 covers the utilization of the highly focused optical fields of NPs to achieve regioselective immobilization of bovine serum albumin (BSA) hydrogels on single Au nanoparticles using multi-photon plasmonic lithography. We further transition from single nanoparticle regime toward large-area immobilization. Chapters 3 demonstrates the fabrication and immobilization of quantum dots (QDs) using the photothermal effects of the plasmonic substrate. A plasmonic microbubble-mediated approach is developed and implemented to achieve the patterning. In chapter 4, we show the haptic-interfaced bubble printing along with the study of the influence of printing conditions over the plasmon-QD coupling. Chapter 5 details the combination of the photothermal and photochemical effects of a plasmonic substrate to induce single-step chemical reduction and immobilization of Ag nanoparticles from its precursor. The application of the patterned particles toward surface-enhanced optical spectroscopy is also shown. Chapter 6 shows the unified synthesis and structuring of immiscible nanoalloys and their catalytic properties. Finally, in chapter 7 we summarize the results and detail future work using plasmon-mediated immobilization strategy.

1.4 REFERENCES

1. Lohse, S. E.; Murphy, C. J., Applications of Colloidal Inorganic Nanoparticles: From Medicine to Energy. *J Am Chem Soc* **2012,** *134* (38), 15607-15620.
2. Howes, P. D.; Chandrawati, R.; Stevens, M. M., Colloidal nanoparticles as advanced biological sensors. *Science* **2014,** *346* (6205), 53.
3. Pellegrino, T.; Kudera, S.; Liedl, T.; Javier, A. M.; Manna, L.; Parak, W. J., On the development of colloidal nanoparticles towards multifunctional structures and their possible use for biological applications. *Small* **2005,** *1* (1), 48-63.
4. De Jong, W. H.; Borm, P. J. A., Drug delivery and nanoparticles: Applications and hazards. *Int. J. Nanomed.* **2008,** *3* (2), 133-149.
5. Murray, C. B.; Norris, D. J.; Bawendi, M. G., Synthesis and Characterization of Nearly Monodisperse Cde (E = S, Se, Te) Semiconductor Nanocrystallites. *J. Am. Chem. Soc.* **1993,** *115* (19), 8706-8715.

6. Brust, M.; Walker, M.; Bethell, D.; Schiffrin, D. J.; Whyman, R., Synthesis of thiol-derivatised gold nanoparticles in a two-phase liquid–liquid system. *Chem. Commun.* **1994,** (7), 801-802.

7. Xiu, Z. M.; Zhang, Q. B.; Puppala, H. L.; Colvin, V. L.; Alvarez, P. J. J., Negligible Particle-Specific Antibacterial Activity of Silver Nanoparticles. *Nano Lett.* **2012,** *12* (8), 4271-4275.

8. Goesmann, H.; Feldmann, C., Nanoparticulate Functional Materials. *Angew. Chem. Int. Edit.* **2010,** *49* (8), 1362-1395.

9. Rajeeva, B. B.; Menz, R.; Zheng, Y. B., Towards rational design of multifunctional theranostic nanoparticles: what barriers do we need to overcome? *Nanomedicine* **2014,** *9* (12), 1767-1770.

10. Wolfbeis, O. S., An overview of nanoparticles commonly used in fluorescent bioimaging. *Chem. Soc. Rev.* **2015,** *44* (14), 4743-4768.

11. Michalet, X.; Pinaud, F. F.; Bentolila, L. A.; Tsay, J. M.; Doose, S.; Li, J. J.; Sundaresan, G.; Wu, A. M.; Gambhir, S. S.; Weiss, S., Quantum dots for live cells, in vivo imaging, and diagnostics. *Science* **2005,** *307* (5709), 538-544.

12. Winnik, F. M.; Maysinger, D., Quantum Dot Cytotoxicity and Ways To Reduce It. *Acc. Chem. Res.* **2013,** *46* (3), 672-680.

13. Dreaden, E. C.; Alkilany, A. M.; Huang, X. H.; Murphy, C. J.; El-Sayed, M. A., The golden age: gold nanoparticles for biomedicine. *Chem. Soc. Rev.* **2012,** *41* (7), 2740-2779.

14. You, J. B.; Meng, L.; Song, T. B.; Guo, T. F.; Yang, Y.; Chang, W. H.; Hong, Z. R.; Chen, H. J.; Zhou, H. P.; Chen, Q.; Liu, Y. S.; De Marco, N.; Yang, Y., Improved air stability of perovskite solar cells via solution-processed metal oxide transport layers. *Nat. Nanotechnol.* **2016,** *11* (1), 75-81.

15. Chakraborty, I.; Pradeep, T., Atomically Precise Clusters of Noble Metals: Emerging Link between Atoms and Nanoparticles. *Chem. Rev.* **2017,** *117* (12), 8208-8271.

16. Saldanha, P. L.; Lesnyak, V.; Manna, L., Large scale syntheses of colloidal nanomaterials. *Nano Today* **2017,** *12*, 46-63.

17. Shen, C. Q.; Lan, X.; Zhu, C. G.; Zhang, W.; Wang, L. Y.; Wang, Q. B., Spiral Patterning of Au Nanoparticles on Au Nanorod Surface to Form Chiral AuNR@AuNP Helical Superstructures Templated by DNA Origami. *Adv. Mat.* **2017,** *29* (16), 1606533.

18. Kagan, C. R.; Lifshitz, E.; Sargent, E. H.; Talapin, D. V., Building devices from colloidal quantum dots. *Science* **2016,** *353* (6302), 885.

19. Zhu, J.; Hersam, M. C., Assembly and Electronic Applications of Colloidal Nanomaterials. *Adv. Mat.* **2017,** *29* (4), 1603895.

20. Kershaw, S. V.; Jing, L. H.; Huang, X. D.; Gao, M. Y.; Rogach, A. L., Materials aspects of semiconductor nanocrystals for optoelectronic applications. *Mater. Horiz.* **2017,** *4* (2), 155-205.

21. Wang, Y. Y.; Fedin, I.; Zhang, H.; Talapin, D. V., Direct optical lithography of functional inorganic nanomaterials. *Science* **2017,** *357* (6349), 385-388.

22. Hou, J.; Li, M. Z.; Song, Y. L., Patterned Colloidal Photonic Crystals. *Angew. Chem. Int. Edit.* **2018,** *57* (10), 2544-2553.

23. Zhang, N.; Sun, W. Z.; Rodrigues, S. P.; Wang, K. Y.; Gu, Z. Y.; Wang, S.; Cai, W. S.; Xiao, S. M.; Song, Q. H., Highly Reproducible Organometallic Halide Perovskite Microdevices based on Top-Down Lithography. *Adv. Mat.* **2017,** *29* (15), 1606205.

24. Rajoua, K.; Baklouti, L.; Favier, F., Electronic and Mechanical Antagonist Effects in Resistive Hydrogen Sensors Based on Pd@Au Core-Shell Nanoparticle Assemblies Prepared by Langmuir-Blodgett. *J. Phys. Chem. C* **2015,** *119* (18), 10130-10139.

25. Kim, B. H.; Nam, S.; Oh, N.; Cho, S. Y.; Yu, K. J.; Lee, C. H.; Zhang, J. Q.; Deshpande, K.; Trefonas, P.; Kim, J. H.; Lee, J.; Shin, J. H.; Yu, Y.; Lim, J. B.; Won, S. M.; Cho, Y. K.; Kim, N. H.; Seo, K. J.; Lee, H.; Kim, T. I.; Shim, M.; Rogers, J. A., Multilayer Transfer Printing for Pixelated, Multicolor Quantum Dot Light-Emitting Diodes. *ACS Nano* **2016,** *10* (5), 4920-4925.

26. Homenick, C. M.; James, R.; Lopinski, G. P.; Dunford, J.; Sun, J.; Park, H.; Jung, Y.; Cho, G.; Malenfant, P. R. L., Fully Printed and Encapsulated SWCNT-Based Thin Film Transistors via a Combination of R2R Gravure and Inkjet Printing. *ACS Appl. Mater. Interfaces* **2016,** *8* (41), 27900-27910.

27. You, M. L.; Zhong, J. J.; Hong, Y.; Duan, Z. F.; Lin, M.; Xu, F., Inkjet printing of upconversion nanoparticles for anti-counterfeit applications. *Nanoscale* **2015,** *7* (10), 4423-4431.

28. Kim, B. H.; Onses, M. S.; Lim, J. B.; Nam, S.; Oh, N.; Kim, H.; Yu, K. J.; Lee, J. W.; Kim, J. H.; Kang, S. K.; Lee, C. H.; Lee, J.; Shin, J. H.; Kim, N. H.; Leal, C.; Shim, M.; Rogers, J. A., High-Resolution Patterns of Quantum Dots Formed by Electrohydrodynamic Jet Printing for Light-Emitting Diodes. *Nano Lett.* **2015,** *15* (2), 969-973.

29. Homola, J., Surface plasmon resonance sensors for detection of chemical and biological species. *Chem. Rev.* **2008,** *108* (2), 462-493.

30. Homola, J., Present and future of surface plasmon resonance biosensors. *Anal. Bioanal. Chem.* **2003,** *377* (3), 528-539.

31. Wang, M. S.; Li, W.; Scarabelli, L.; Rajeeva, B. B.; Terrones, M.; Liz-Marzan, L. M.; Akinwande, D.; Zheng, Y. B., Plasmon-trion and plasmon-exciton resonance

energy transfer from a single plasmonic nanoparticle to monolayer MoS2. *Nanoscale* **2017,** *9* (37), 13947-13955.

32. Zayats, A. V.; Smolyaninov, I. I.; Maradudin, A. A., Nano-optics of surface plasmon polaritons. *Phys. Rep.* **2005,** *408* (3-4), 131-314.

33. Zhang, Z. L.; Fang, Y. R.; Wang, W. H.; Chen, L.; Sun, M. T., Propagating Surface Plasmon Polaritons: Towards Applications for Remote-Excitation Surface Catalytic Reactions. *Adv. Sci.* **2016,** *3* (1), 1500215.

34. Echtermeyer, T. J.; Milana, S.; Sassi, U.; Eiden, A.; Wu, M.; Lidorikis, E.; Ferrari, A. C., Surface Plasmon Polariton Graphene Photodetectors. *Nano Lett.* **2016,** *16* (1), 8-20.

35. Ee, H. S.; No, Y. S.; Kim, J.; Park, H. G.; Seo, M. K., Long-range surface plasmon polariton detection with a graphene photodetector. *Opt. Lett.* **2018,** *43* (12), 2889-2892.

36. Baffou, G.; Quidant, R., Thermo-plasmonics: using metallic nanostructures as nano-sources of heat. *Laser Photonics Rev.* **2013,** *7* (2), 171-187.

37. Fan, X.; Zheng, W.; Singh, D. J., Light scattering and surface plasmons on small spherical particles. *Light Sci. Appl.* **2014,** *3*, e179.

38. Luther, J. M.; Jain, P. K.; Ewers, T.; Alivisatos, A. P., Localized surface plasmon resonances arising from free carriers in doped quantum dots. *Nat. Mater.* **2011,** *10*, 361.

39. Schuller, J. A.; Barnard, E. S.; Cai, W. S.; Jun, Y. C.; White, J. S.; Brongersma, M. L., Plasmonics for extreme light concentration and manipulation. *Nat. Mater.* **2010,** *9* (3), 193-204.

40. Lakowicz, J. R., Plasmonics in biology and plasmon-controlled fluorescence. *Plasmonics* **2006,** *1* (1), 5-33.

41. Eggleston, M. S.; Messer, K.; Zhang, L. M.; Yablonovitch, E.; Wu, M. C., Optical antenna enhanced spontaneous emission. *Proc. Natl. Acad. Sci. USA.* **2015,** *112* (6), 1704-1709.

42. Cai, Y. Y.; Liu, J. G.; Tauzin, L. J.; Huang, D.; Sung, E.; Zhang, H.; Joplin, A.; Chang, W. S.; Nordlander, P.; Link, S., Photoluminescence of Gold Nanorods: Purcell Effect Enhanced Emission from Hot Carriers. *ACS Nano* **2018,** *12* (2), 976-985.

43. Hoang, T. B.; Akselrod, G. M.; Argyropoulos, C.; Huang, J. N.; Smith, D. R.; Mikkelsen, M. H., Ultrafast spontaneous emission source using plasmonic nanoantennas. *Nat. Commun.* **2015,** *6*, 7788.

44. Kinkhabwala, A.; Yu, Z.; Fan, S.; Avlasevich, Y.; Müllen, K.; Moerner, W. E., Large single-molecule fluorescence enhancements produced by a bowtie nanoantenna. *Nat. Photon.* **2009,** *3*, 654.

Chapter 2: Multi-Photon Plasmonic Lithography*

2.1 INTRODUCTION

The interaction of incident electromagnetic radiation with metallic nanoparticles results in collective electron oscillations, known as localized surface plasmon resonances (LSPRs). A consequence of the interaction is the ability to concentrate light fields with orders of magnitude enhancement at visible and near-infrared (NIR) wavelengths to the sub-wavelength scale. Such enhancements find profound applications in improving the efficiencies of several phenomena such as fluorescence,[1-3] surface-enhanced Raman scattering (SERS),[4-8] surface-enhanced infrared absorption,[9-11] single-molecule detection,[12-13] non-linear optical effects[14-16] ,and multiphoton polymerization.[17-18] Exploiting this highly confined optical field is crucial, but simultaneously it is also challenging to position the desired molecules or particles accurately at these locations on individual nanoparticles (NPs). Thus, strategies to achieve precise and accurate immobilization on a single NP regime are crucial.

Different approaches have been employed to achieve selective positioning of the molecules over defined hot spots of individual NPs, such as (i) incorporation of a two-step electron beam exposure and squeegee process,[19] where the first exposure step creates the plasmonic nanostructure and the second step selectively generates openings at hot spots,[20] (ii) integrating a microfluidic channel with appropriate flow control,[21] (iii) use of atomic force microscopy to manipulate the position of nanoparticles,[22] (iv) exploiting material selective surface chemistry for attachment,[23-24] and (v) using multi-photon plasmonic lithography (MPPL) to induce selective polymerization at hot spots due to the enhanced

* Rajeeva, B. B., Hernandez, D. S., Wang, M. S., Perillo, E.P., Lin, L. H., Scarabelli, L., Pingali, B., Liz-Marzan, L. M., Dunn, A. K., Shear, J. B., Zheng, Y. B. Regioselective Localization and Tracking of Biomolecules on Single Gold Nanoparticles. Advanced Science, 2015, 2, 1500232. Rajeeva, B. B. carried out the experimental work and participated in the preparation of manuscript.

electromagnetic field of the nanostructures.[17, 25-27] Among the above strategies, techniques (i)-(iv) are time-intensive, prone to inaccuracies and require prior knowledge of the precise hot spot location. In contrast, MPPL utilizes the inherent field enhancement of nanostructures to localize the desired molecules into the hot spots, making this approach fast and reliable.

In this chapter, we utilized MPPL using a focused Titanium:Sapphire femtosecond laser to selectively and rapidly (~20s to completely expose an area of 40×40 μm^2) localize cross-linked BSA hydrogels at the tips of a gold nanotriangle (AuNT). The tips of the AuNTs are the sites of maximum electromagnetic field intensity enhancement, a necessary element to induce crosslinking. The AuNTs are immobilized on silanized glass coverslips with ample inter-spacing to ensure that the single particles can be distinguished in dark-field scattering microscopy. The shape of the examined AuNTs was confirmed via correlated scanning electron microscopy (SEM). We demonstrate site selectivity and control over the extent of hydrogel fabrication on AuNT tips, processes that depend on the polarization and intensity of the incident laser, respectively. In addition, strong intensity dependency, short fabrication times and extensive rinsing greatly reduced non-specific protein adsorption on the substrate. Protein immobilization was tracked with single-particle dark-field scattering microscopy by recording the scattering spectra of an AuNT before and after the fabrication. The magnitude of the peak shift was found to be in positive correlation with the volume of protein present at the hot spots. Correlated fluorescence lifetime imaging microscopy (FLIM) was also performed to confirm protein immobilization.

2.2 HOT SPOT CONFINED MULTI-PHOTON LITHOGRAPHY

Conventional multi-photon lithography relies on a non-linear multi-photon absorption process, wherein the absorption of two photons of near-identical frequencies

excites a molecule from one state (usually the ground state) to a higher energy electronic state.[28] Since a non-linear process is several orders of magnitude weaker than linear absorption, very high optical flux is required to increase the number of such rare events. In most cases, a tightly-focused laser beam provides the necessary intensities and limits the process within the focal spot. In conjunction with a metal nanoparticle, the optical flux is selectively enhanced at the NP hot spots and confines the multi-photon excitation process to sub-100 nm regime on a single NP (Figure 2.1). Metal-enhanced multiphoton absorption has been primarily used in conjunction with commercial photoresists such as SU-8 and TSMR V-90 due to their potential applications in achieving highly resolved features.[17, 25, 29-31] MPPL has also been studied to visualize plasmon modes in nanostructures.[32-33]

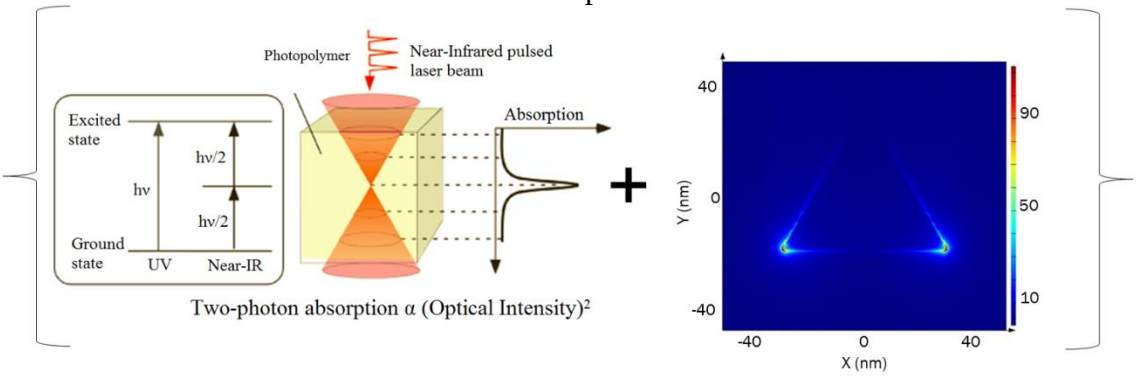

Figure 2.1: Schematic of the multi-photon absorption in conjunction with the simulated electric field and hot spot distribution of a single 60 nm AuNT in response to the in response to a linearly polarized electromagnetic wave. Reproduced with permission from ref 28. Copyright 2008 John Wiley & Sons, Inc.

2.3 Protein Hydrogel Immobilization

In recent years, understanding molecule-plasmon interactions have gathered attention for applications such as plasmonic switches[34-36] and nanoplasmonic rulers.[37-38] Advancing this application toward immobilizing biomaterials such as proteins would enable the exploration of biological phenomena at the nanoscale, where numerous cell-

matrix interactions occur. Numerous proteins have been cross-linked using multiphoton lithography, and many of these proteins were shown to retain their bioactivity; however, the resolution of current systems ~500 nm, is much larger than individual cell surface receptor interactions.[39-42] One particular protein/photosensitizer platform that has been regularly employed to fabricate densely cross-linked, 3D protein hydrogels is bovine serum albumin (BSA) in combination with Rose Bengal (RB).[43] Recently, Galloway and co-workers used light-assisted molecular immobilization (LAMI) to immobilize BSA within gold dimers to selectively direct the attachment of single Au nanoparticles.[44] While LAMI requires longer fabrication times to dehydrate proteins, BSA hydrogels can be deposited in a single step without considerable waiting time, using MPPL. Also, other techniques such as STED lithography do not have control over the position and are limited to ~100 nm resolution.[45]

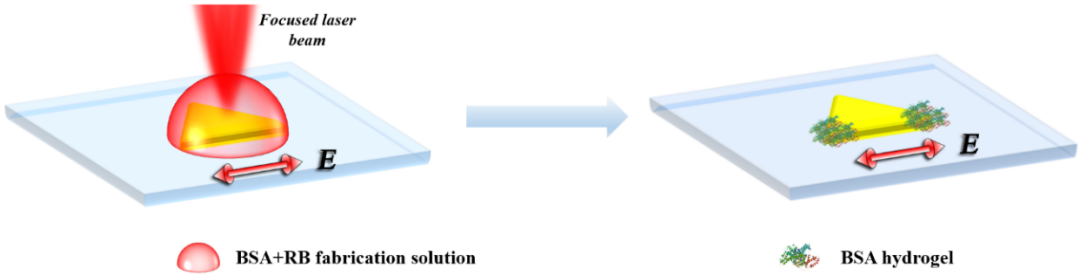

Figure 2.2: Schematic representation of the selective localization of BSA hydrogel molecules at the tip of a single AuNT. The protein is cross-linked close to the tip via MPPL, and not elsewhere.

The immobilization of BSA hydrogel was performed over well-dispersed AuNTs on a silanized glass coverslip. Colloidal solutions of AuNTs with a uniform edge length distribution of 59 ± 4 nm were prepared using a previously reported procedure[46] and cast on the coverslip. The AuNT solution was centrifuged and re-dispersed in water twice to minimize the concentration of surfactant, hexadecyltrimethylammonium chloride (CTAC).

BSA hydrogels were fabricated using multiphoton lithography (MPL) in an aqueous environment. The defining aspect of MPL is that photochemical crosslinking only occurs near the focal point of the incident laser, where laser intensity is high enough for photoreactants to absorb two or more photons near simultaneously, a phenomena known as nonlinear absorption. RB, the photosensitizer used in these studies, is a type II photosensitizer, which involves excitation to a long-lived reactive triplet state molecule. This reactive molecule results in intermolecular protein crosslinking, either through a singlet-oxygen or direct hydrogen-transfer mechanism.[47] Hydrogel fabrication performance is mainly dependent on the concentration of components in the fabrication solution and the intensity of the incident laser, with a higher concentration of RB leading to the formation of higher protein crosslinks. The intensity dependence is crucial in the present work since the two-photon process requires a sufficient high photon flux for nonlinear excitation to occur. This intensity dependence is exploited in case of MPPL wherein the field enhancement of the AuNT amplifies the energy at the tips, resulting in an enhanced energy density within these regions that exceed the threshold exposure (Figure 2.2).[17]

Figure 2.3 shows high-magnification SEM images of the successful fabrication of AuNT-BSA hydrogel hybrids using MPPL, and the corresponding field intensity distributions obtained by finite-difference time domain (FDTD) simulations using a commercial package by Lumerical Inc. In Figure 2.3a and b, fabrication was performed with an average laser power of 1mW, whereas in Figure 2.3c, the laser power was 2mW. All powers were measured at the back aperture of the objective. The low milliwatt powers at the objective back aperture yield peak laser intensities within the high numerical aperture focal volumes of ~10^{10} to 10^{12} Wcm^{-2}. Such powers are considerably lower than the requirements for direct laser fabrication, which require a minimum of ~14mW with our

scan parameters. Incident laser powers above 2mW resulted in complete coverage of the AuNT with the BSA hydrogel. In order to clearly isolate the locations of BSA hydrogels, the high magnification image was processed by a processing the image based on the gray level threshold. The spots on top of the AuNT in the inset of Figure 2.3a might be due to the diffusion of RB photoinitiator or because of imaging variations. We observe a positive correlation between the incident laser power and the apparent quantity of BSA hydrogel immobilized over the AuNTs.

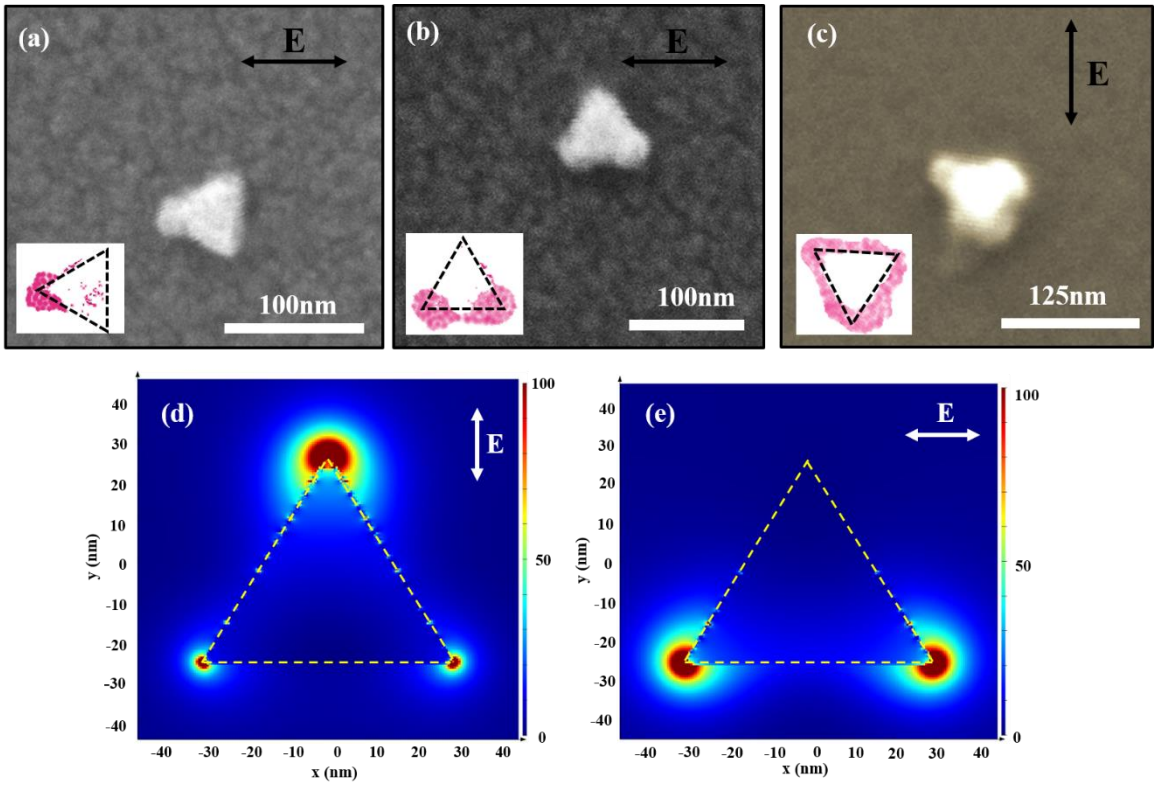

Figure 2.3: SEM images showing the regioselective localization of BSA hydrogel on single AuNTs under various incident light polarization and intensity at (a,b) incident laser power of 1mW and (c) incident laser power of 2mW. Inset in (a-c) shows the BSA hydrogel positions isolated via image processing. The direction of the electric field vector of the incident laser is denoted at the top-right of each figure. (d,e) Simulated field intensity distributions over the surface of AuNT. The intensity enhancement (|E|/|E0|) is depicted on the color scale, indicating higher intensity at one or two tips, depending on the polarization.

Regioselective immobilization is observed for lower laser fabrication depending on the polarization of the incident laser. Figure 2.3a shows localization experiments where the constant incident laser electric field vector was aligned along the triangle height during the fabrication process. This results in a dipole mode with a hot spot present at the triangle tip overlapping with the polarization direction, as shown by the FDTD simulation in Figure 2.3d. Similarly, when the electric field vector was directed along the edge of the triangle, a dipole mode originated with hot spots present along the two tips of the triangle positioned along the field vector (Figure 2.3e). This association of hot spot and polarization was reflected on the regioselective positioning of BSA hydrogel at only one and two tips, respectively (Figures 2.3a and b). The BSA hydrogel can be observed in the SEM images as clouding over the AuNTs.[44] The grain-like morphology on the substrate is the result of a thin layer of Au-Pt sputtered on the nonconductive glass substrate for SEM imaging. In addition, as expected, the volumes appear similar in both cases. The regioselectivity confirms that the mechanism for BSA hydrogel immobilization is dependent on the LSPR of the nanoparticle. On doubling the incident power, we observe the coverage of all three tips of the AuNT since the minute enhancements at the non-aligned tips (Figure 2.3e) can also result in intensities that are high enough for polymerization to occur.

2.4 Single Nanoparticle Dark-Field Scattering Spectroscopy

It is challenging to characterize changes occurring on single nanoparticles at the nanoscale. Conventional spectroscopic techniques provide limited information due to particle size heterogeneity and the relatively low concentration of molecules immobilized over the hot spots.[31] In contrast, single-nanoparticle dark-field scattering spectroscopy records the spectrum of single nanoparticles originating from LSPRs.[48-49] Thus, it is extremely sensitive to morphology and the refractive index variations at the particle

surfaces, aiding in tracking changes over single nanoparticles.[50-51] In our study, dark-field scattering microscopy provides valuable information regarding the immobilization of proteins on single nanoparticles.

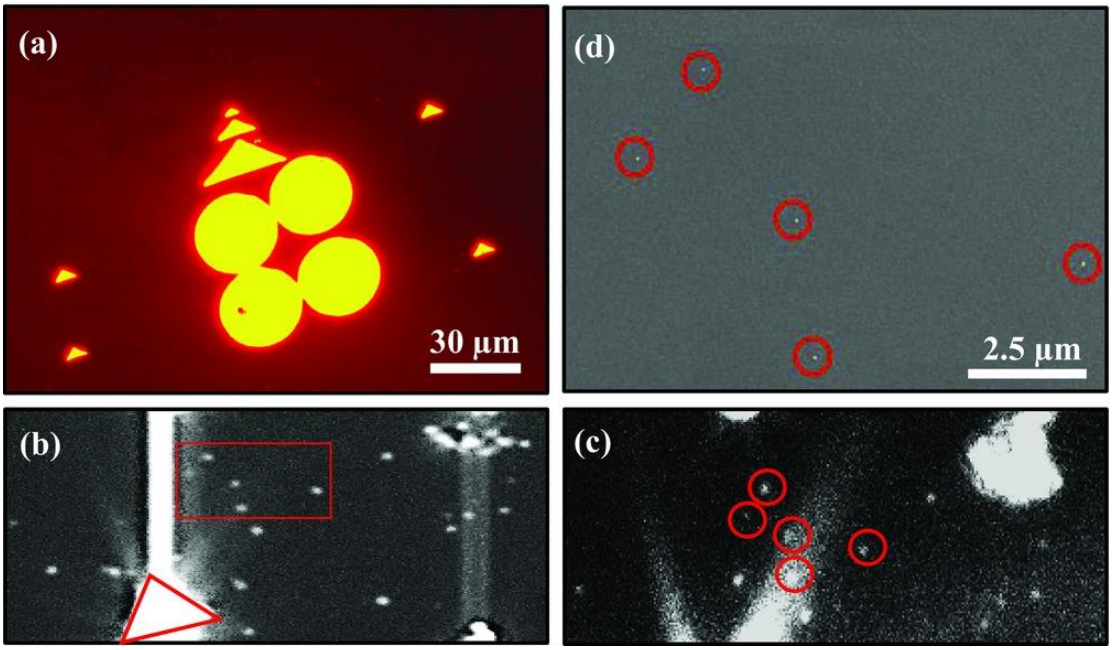

Figure 2.4: Correlated single-particle dark-field spectroscopy and SEM. (a) Typical markers of BSA hydrogel prepared by direct laser writing to locate the individual AuNTs. (b) Dark-field image of multiple nanoparticles in the vicinity of the marker before fabrication. The extremely bright spot is the strong scattering from the marker (c) Dark-field image of the same region after fabrication. (d) SEM imaging of the region indicating the presence of well-separated single nanoparticles.

Since the BSA hydrogel immobilized over the AuNTs is confined to a hot spot with dimensions well below 100 nm, direct ensemble spectroscopic measurements do not provide any inferable data. Previous reports related to ensemble measurements showed multiple broad peaks resulting from size heterogeneity and morphology changes.[31] Also, due to the large separation between AuNTs, the signal is not high enough to be deciphered

via conventional spectroscopic techniques. Hence, single particle analysis was selected as a strong tool for probing minute changes occurring over the nanoparticles.

Figure 2.4 shows the strategy employed for monitoring changes on a single particle. A Nikon TiE inverted microscope coupled to a Newton EMCCD spectroscopy detector (Andor Technology) is employed for dark-field scattering imaging and analysis. Direct-laser writing of the BSA hydrogel was performed using mask-direct MPL to create unique markers for monitoring the particles during fabrication, optical characterization, and SEM. A higher incident laser power of 14mW at the back aperture was used for direct-laser writing of the marker. Figure 2.4a shows the fluorescence image (using TRITC filter) of typical BSA markers, with the desired shapes drawn and replicated on the substrate using a digital micromirror device as a dynamic mask to guide fabrication. After immobilization of AuNT on the silanized coverslip, the dark-field image as well as spectra of 5-6 pristine AuNT particles at a region in the vicinity of the marker were obtained (Figure 2.4b). MPPL was performed by scanning the laser beam over predetermined regions on the substrates where the dark-field spectra were obtained. The fabrication process is rapid, as a 40×40 μm^2 area was scanned in 5s. Numerous layers were scanned at 0.5 micron increments to ensure the focal volume of the laser transected the AuNTs. To characterize the changes, the predetermined nanoparticles were located using the markers and the corresponding scattering spectra were obtained. Figure 2.4c shows the post-fabrication dark-field scattering image of the same region as in Figure 2.4b. The incident laser power, in this case, was 2mW at the back aperture. The variation between these images is due to loosely bound particles being washed away during the fabrication and rinsing process. In order to ensure analysis of a single particle in dark-field microscopy, the inter-particle distance was tuned to be at least 1µm, which was confirmed via correlated SEM imaging (Figure 2.4d).

2.4.1 Characterization of the Protein Immobilization

LSPRs are extremely sensitive to the refractive index (RI) changes occurring over the nanoparticle surroundings.[52] Figure 2.5a shows a representative dark-field scattering spectrum of a pristine AuNT immobilized on a glass coverslip. The spectra of 4 pure AuNTs were taken as a reference. The peak wavelength (λ_{max}) and full width at half maximum (FWHM) of pristine AuNTs calculated using Lorentzian peak fitting were 649±2 nm and 63±3 nm, respectively. The standard deviation observed in the peak wavelength is attributed to the variation in the size and orientation of individual particles resulting in slightly different spectra. The fabrication process was characterized using the approach described in Figure 2.4.

Figure 2.5b denotes the representative spectra of a single AuNT before and after fabrication of AuNT-BSA hydrogel with an incident laser power of 1mW, with spectra of 4 particles obtained and analyzed. A redshift of 19±5 nm in λ_{max} was observed after immobilization of BSA hydrogel. The redshift is a consequence of the increase in the refractive index around the AuNT. The standard deviation of the peak position is significant since, at such low powers, the immobilization is sensitive to the orientation of the AuNT with respect to the incident laser polarization, as seen in Figures 2.3 a and b. Figure 2.5c shows representative spectra for an incident laser power of 2mW, which results in coverage of all three tips of the AuNT with protein and a λ_{max} shift of 34±3 nm. Since the plasmon-induced field is localized at the tip, RI changes at distances above 15 nm do not have a strong influence on the LSPR. Thus, the effect of AuNT orientation is weaker due to the higher amount of immobilized protein. This minimizes the standard deviation observed in the case of higher laser power incidence. Our FDTD simulations support the experimentally observed resonance peak red-shift upon increasing the incident light power. The simulation depicts the changes occurring in the spectra when BSA hydrogel is

immobilized on one, two and three tips, respectively (Figure 2.5d). The λ_{max} of pristine AuNT is observed at 626 nm, and a maximum shift of 30nm is seen for BSA immobilized at all three tips. The deviation of λ_{max} can be due to the differences in the morphology (surface roughness, triangle shape, etc.) and medium refractive index in actual experiments and of those in the simulation.

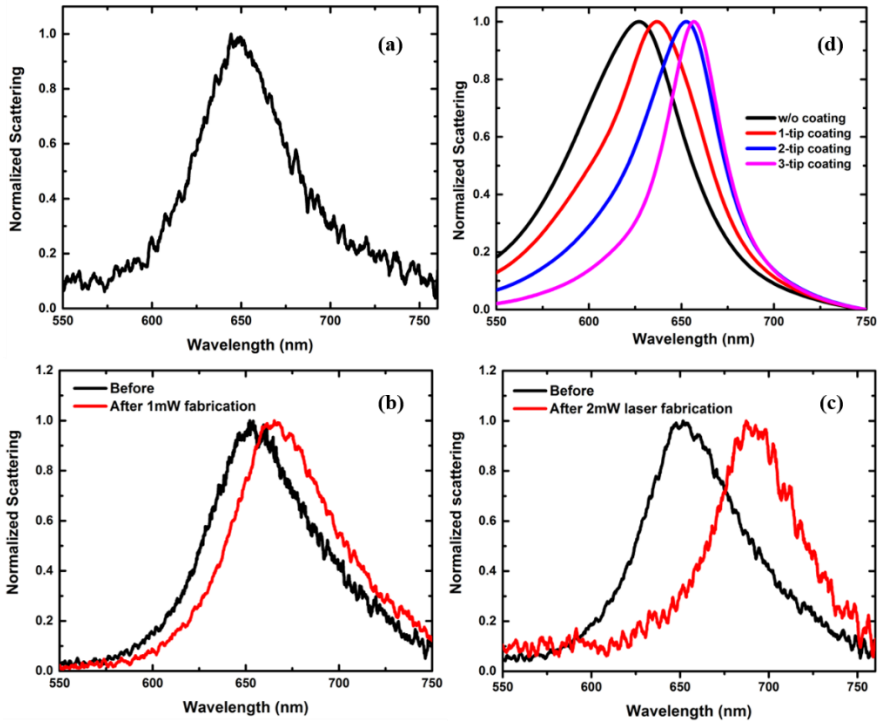

Figure 2.5: Representative dark-field scattering spectra of (a) pristine AuNT, single AuNT before and after fabrication with an incident laser power of (b) 1mW (c) 2mW indicating a red-shift post fabrication (d) FDTD simulated spectra of pristine AuNT and AuNT coated with BSA hydrogel on one, two and three tips, respectively. Simulations were performed for AuNT of 60nm edge length and 25nm thickness. The BSA hydrogel with a refractive index of 1.5 was added at one, two and three tips to mimic the experimental structures as seen in Figure 2 (a-c).

2.4.2 Control Experiments

Two independent sets of control experiments were investigated, and the results are summarized in Figure 2.6. The first control comprises elimination of the morphology

changes occurring due to laser irradiation. Figure 2.6a represents the spectra obtained for a single AuNT before and after irradiation using an average laser power of 2mW, the highest power used for MPPL. The post-fabrication spectra have been offset along the y-axis for better clarity. No significant shift in the spectrum peak wavelength or particle morphology was observed as a result of laser irradiation. In addition, to rule out the possibility of direct adsorption of BSA or RB molecules on AuNTs, the spectral response of AuNT was tracked before and after immersion in BSA fabrication medium. Techniques such as laser-assisted molecular immobilization (LAMI) are less effective since it relies on effective coverage of proteins prior to fabrication.[44] In contrast, due to the low fabrication times involved in MPPL, we observed no shift in the AuNT peak position and no morphology changes (Figure 2.6b).

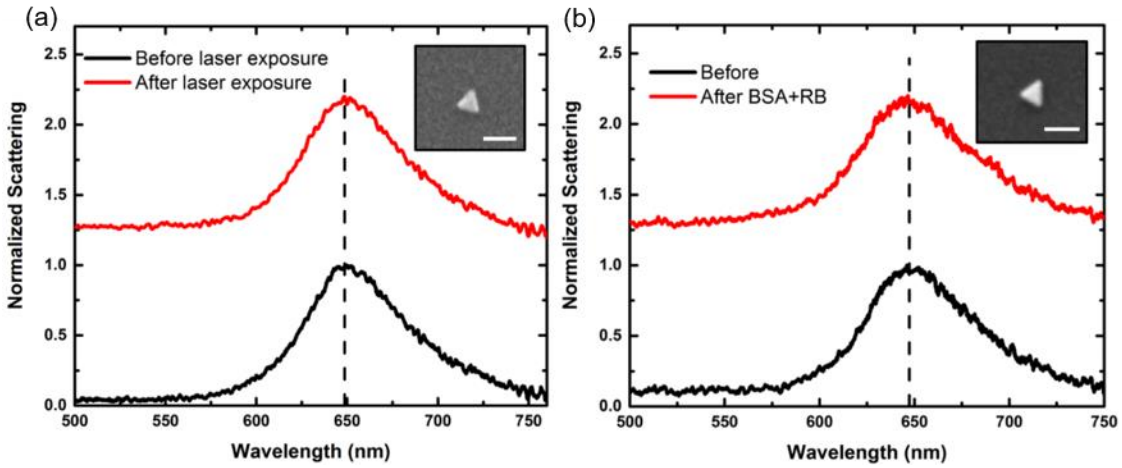

Figure 2.6: Dark-field scattering spectra of two independent controls: (a) Before and after 2mW laser irradiation without the presence of BSA and RB (b) Before and after exposure of AuNT to BSA and RB fabrication solution without any laser irradiation. The "after" plot was offset along the y-axis for clarity. The inset shows the corresponding high magnification SEM image, with a scale bar of 100nm.

2.5 FLUORESCENCE LIFETIME IMAGING MICROSCOPY

To further confirm AuNT-BSA hydrogel fabrication, multiphoton FLIM was employed. FLIM is built upon time-resolved detection and can provide a sensitive contrast mechanism to identify the local environment of a fluorophore.[53] Using FLIM, it was determined that two distinct lifetime populations are present for AuNT-BSA hydrogel and BSA hydrogel. With the aid of markers, the region of AuNT-BSA hydrogel fabricated with 2mW was analyzed using FLIM (refer to Figure 2.3c for the dark-field scattering image). The observed two-photon fluorescence signal is primarily due to the RB photosensitizer. Although there have been various reports of a strong influence of the surfactant molecules present over Au nanoparticles on the lifetime of RB,[54] this effect is negligible in the present case since in addition to regular rinsing of the substrate, the AuNT solution was centrifuged and re-dispersed in water twice to remove CTAC prior to immobilization on the glass coverslip.

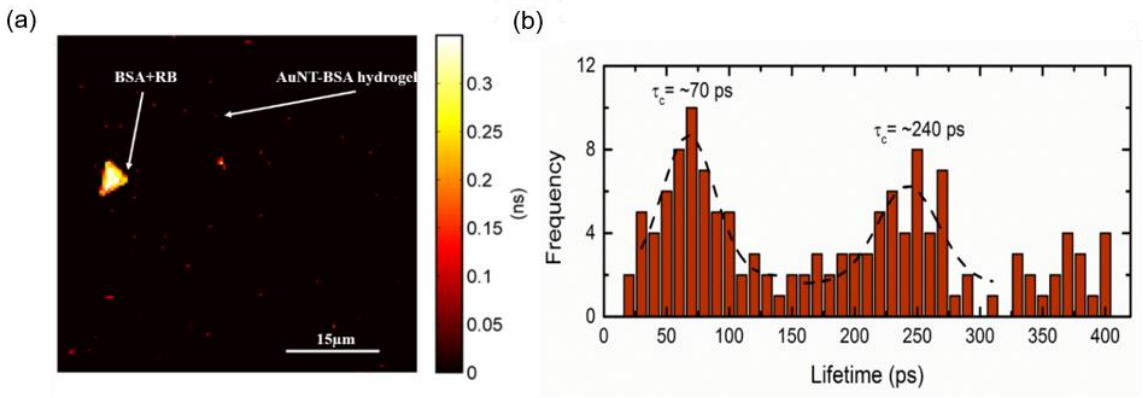

Figure 2.7: FLIM of the AuNT-BSA hydrogel nanoparticles fabricated using a 2mW incident laser. (a) FLIM image showing the control BSA hydrogel and AuNT-BSA hydrogel in the same FOV. (b) Histogram of lifetimes obtained from the same FOV indicating two separate lifetimes of ~70ps and ~240ps for AuNT-BSA hydrogel and control BSA hydrogel respectively.

Figure 2.7 shows the FLIM image along with a histogram of lifetime distribution within the field of view, which contains the BSA hydrogel fabricated using MPL and the

AuNT-BSA complexes fabricated by MPPL. A decrease in the fluorescence lifetime is observed over the particles, as compared to the control structure. The lifetime histogram reveals an average lifetime of ~70ps for AuNT-BSA hydrogel particles, whereas the control BSA hydrogel has an average lifetime of ~240ps. The presence of two lifetime populations at ~240ps and ~370ps for control BSA hydrogel may be due to self-quenching of RB molecules.[55] The reduction in lifetime may be attributed to the resonance energy transfer from the fluorophore to the AuNT, confirming the immobilization of BSA hydrogel on the AuNT.[54, 56]

2.8 SUMMARY

In conclusion, we employed MPPL to rapidly localize BSA hydrogel molecules at the tips of individual AuNTs. We further demonstrated regioselective positioning along with control over the amount of protein deposited on the AuNTs. A strong dependence on the LSPR is established resulting in polarization dependent positioning of the molecules over AuNTs, as is evident from SEM images. We also tracked the changes occurring on a single AuNT using dark-field scattering spectroscopy and compared the experimental results with FDTD simulations. A red-shift in the plasmon resonance peak wavelength, which is correlated with the incident laser power, confirms the immobilization of BSA hydrogel over AuNT. FLIM imaging was performed for additional confirmation of the immobilization. Our rapid and single-step protein immobilization technique along with single-nanoparticle dark-field monitoring can act as a framework to better understand light-molecule interactions at the sub-nanoparticle level. These precisely controllable nanoparticle-biomolecule complexes have potential applications in nanophotonics, nanomedicine and life sciences.

2.9 REFERENCES

1. Deng, W.; Xie, F.; Baltar, H. T.; Goldys, E. M., Metal-enhanced fluorescence in the life sciences: here, now and beyond. *Phys. Chem. Chem. Phys.* **2013,** *15* (38), 15695-15708.

2. Darvill, D.; Centeno, A.; Xie, F., Plasmonic fluorescence enhancement by metal nanostructures: shaping the future of bionanotechnology. *Phys. Chem. Chem. Phys.* **2013,** *15* (38), 15709-15726.

3. Tam, F.; Goodrich, G. P.; Johnson, B. R.; Halas, N. J., Plasmonic enhancement of molecular fluorescence. *Nano Lett.* **2007,** *7* (2), 496-501.

4. Shiohara, A.; Wang, Y.; Liz-Marzán, L. M., Recent approaches toward creation of hot spots for SERS detection. *J. Photochem. Photobiol. C: Photochem. Rev.* **2014,** *21*, 2-25.

5. Li, W.; Camargo, P. H.; Lu, X.; Xia, Y., Dimers of silver nanospheres: facile synthesis and their use as hot spots for surface-enhanced Raman scattering. *Nano Lett.* **2008,** *9* (1), 485-490.

6. Hsu, K. H.; Back, J. H.; Fung, K. H.; Ferreira, P. M.; Shim, M.; Fang, N. X., SERS EM field enhancement study through fast Raman mapping of Sierpinski carpet arrays. *J. Raman Spectrosc.* **2010,** *41* (10), 1124-1130.

7. Rodríguez-Fernández, J.; Funston, A. M.; Pérez-Juste, J.; Álvarez-Puebla, R. A.; Liz-Marzán, L. M.; Mulvaney, P., The effect of surface roughness on the plasmonic response of individual sub-micron gold spheres. *Phys. Chem. Chem. Phys.* **2009,** *11* (28), 5909-5914.

8. Tsoutsi, D.; Guerrini, L.; Hermida-Ramon, J. M.; Giannini, V.; Liz-Marzán, L. M.; Wei, A.; Alvarez-Puebla, R. A., Simultaneous SERS detection of copper and cobalt at ultratrace levels. *Nanoscale* **2013,** *5* (13), 5841-5846.

9. Lal, S.; Grady, N. K.; Kundu, J.; Levin, C. S.; Lassiter, J. B.; Halas, N. J., Tailoring plasmonic substrates for surface enhanced spectroscopies. *Chem. Soc. Rev.* **2008,** *37* (5), 898-911.

10. Le, F.; Brandl, D. W.; Urzhumov, Y. A.; Wang, H.; Kundu, J.; Halas, N. J.; Aizpurua, J.; Nordlander, P., Metallic nanoparticle arrays: a common substrate for both surface-enhanced Raman scattering and surface-enhanced infrared absorption. *ACS Nano* **2008,** *2* (4), 707-718.

11. Brown, L. V.; Zhao, K.; King, N.; Sobhani, H.; Nordlander, P.; Halas, N. J., Surface-Enhanced Infrared Absorption Using Individual Cross Antennas Tailored to Chemical Moieties. *J. Am. Chem. Soc.* **2013,** *135* (9), 3688-3695.

12. Camden, J. P.; Dieringer, J. A.; Wang, Y.; Masiello, D. J.; Marks, L. D.; Schatz, G. C.; Van Duyne, R. P., Probing the structure of single-molecule surface-enhanced Raman scattering hot spots. *J. Am. Chem. Soc.* **2008,** *130* (38), 12616-12617.

13. Cang, H.; Labno, A.; Lu, C.; Yin, X.; Liu, M.; Gladden, C.; Liu, Y.; Zhang, X., Probing the electromagnetic field of a 15-nanometre hotspot by single molecule imaging. *Nature* **2011,** *469* (7330), 385-388.

14. Guan, Z.; Polavarapu, L.; Xu, Q.-H., Enhanced two-photon emission in coupled metal nanoparticles induced by conjugated polymers. *Langmuir* **2010,** *26* (23), 18020-18023.

15. Ward, D. R.; Hüser, F.; Pauly, F.; Cuevas, J. C.; Natelson, D., Optical rectification and field enhancement in a plasmonic nanogap. *Nat. Nanotechnol.* **2010,** *5* (10), 732-736.

16. Ko, K. D.; Kumar, A.; Fung, K. H.; Ambekar, R.; Liu, G. L.; Fang, N. X.; Toussaint Jr, K. C., Nonlinear optical response from arrays of Au bowtie nanoantennas. *Nano Lett.* **2011,** *11* (1), 61-65.

17. Sundaramurthy, A.; Schuck, P. J.; Conley, N. R.; Fromm, D. P.; Kino, G. S.; Moerner, W., Toward nanometer-scale optical photolithography: utilizing the near-field of bowtie optical nanoantennas. *Nano Lett.* **2006,** *6* (3), 355-360.

18. Nah, S.; Li, L.; Fourkas, J. T., Field-Enhanced Phenomena of Gold Nanoparticles. *J. Phys. Chem. A* **2009,** *113* (16), 4416-4422.

19. Saboktakin, M.; Ye, X.; Chettiar, U. K.; Engheta, N.; Murray, C. B.; Kagan, C. R., Plasmonic enhancement of nanophosphor upconversion luminescence in Au nanohole arrays. *ACS Nano* **2013,** *7* (8), 7186-7192.

20. Metzger, B.; Hentschel, M.; Schumacher, T.; Lippitz, M.; Ye, X.; Murray, C. B.; Knabe, B.; Buse, K.; Giessen, H., Doubling the efficiency of third harmonic generation by positioning ITO nanocrystals into the hot-spot of plasmonic gap-antennas. *Nano Lett.* **2014,** *14* (5), 2867-2872.

21. Ropp, C.; Cummins, Z.; Nah, S.; Fourkas, J. T.; Shapiro, B.; Waks, E., Nanoscale imaging and spontaneous emission control with a single nano-positioned quantum dot. *Nat. Commun.* **2013,** *4*, 1447.

22. Bek, A.; Jansen, R.; Ringler, M.; Mayilo, S.; Klar, T. A.; Feldmann, J., Fluorescence enhancement in hot spots of AFM-designed gold nanoparticle sandwiches. *Nano Lett.* **2008,** *8* (2), 485-490.

23. Rodríguez-Lorenzo, L.; Alvarez-Puebla, R. A.; Pastoriza-Santos, I.; Mazzucco, S.; Stéphan, O.; Kociak, M.; Liz-Marzán, L. M.; García de Abajo, F. J., Zeptomol detection through controlled ultrasensitive surface-enhanced Raman scattering. *J. Am. Chem. Soc.* **2009,** *131* (13), 4616-4618.

24. Feuz, L.; Jonsson, M. P.; Höök, F., Material-selective surface chemistry for nanoplasmonic sensors: optimizing sensitivity and controlling binding to local hot spots. *Nano Lett.* **2012,** *12* (2), 873-879.

25. Nah, S.; Li, L.; Liu, R.; Hao, J.; Lee, S. B.; Fourkas, J. T., Metal-enhanced multiphoton absorption polymerization with gold nanowires. *J. Phys. Chem. C* **2010,** *114* (17), 7774-7779.

26. Diebold, E. D.; Mack, N. H.; Doorn, S. K.; Mazur, E., Femtosecond laser-nanostructured substrates for surface-enhanced Raman scattering. *Langmuir* **2009,** *25* (3), 1790-1794.

27. Diebold, E. D.; Peng, P.; Mazur, E., Isolating surface-enhanced Raman scattering hot spots using multiphoton lithography. *J. Am. Chem. Soc.* **2009,** *131* (45), 16356-16357.

28. Maruo, S.; Fourkas, J. T., Recent progress in multiphoton microfabrication. *Laser Photonics Rev.* **2008,** *2* (1-2), 100-111.

29. Ueno, K.; Juodkazis, S.; Shibuya, T.; Yokota, Y.; Mizeikis, V.; Sasaki, K.; Misawa, H., Nanoparticle plasmon-assisted two-photon polymerization induced by incoherent excitation source. *J. Am. Chem. Soc.* **2008,** *130* (22), 6928-6929.

30. Ueno, K.; Takabatake, S.; Nishijima, Y.; Mizeikis, V.; Yokota, Y.; Misawa, H., Nanogap-assisted surface plasmon nanolithography. *J. Phys. Chem. Lett.* **2010,** *1* (3), 657-662.

31. Geldhauser, T.; Ikegaya, S.; Kolloch, A.; Murazawa, N.; Ueno, K.; Boneberg, J.; Leiderer, P.; Scheer, E.; Misawa, H., Visualization of near-field enhancements of gold triangles by nonlinear photopolymerization. *Plasmonics* **2011,** *6* (2), 207-212.

32. Gruber, C.; Hirzer, A.; Schmidt, V.; Trügler, A.; Hohenester, U.; Ditlbacher, H.; Hohenau, A.; Krenn, J. R., Imaging nanowire plasmon modes with two-photon polymerization. *Appl. Phys. Lett.* **2015,** *106* (8), 081101.

33. Murazawa, N.; Ueno, K.; Mizeikis, V.; Juodkazis, S.; Misawa, H., Spatially selective nonlinear photopolymerization induced by the near-field of surface plasmons localized on rectangular gold nanorods. *J. Phys. Chem. C* **2009,** *113* (4), 1147-1149.

34. Hsiao, V. K.; Zheng, Y. B.; Juluri, B. K.; Huang, T. J., Light-driven plasmonic switches based on au nanodisk arrays and photoresponsive liquid crystals. *Adv. Mater.* **2008,** *20* (18), 3528-3532.

35. Zheng, Y. B.; Juluri, B. K.; Lin Jensen, L.; Ahmed, D.; Lu, M.; Jensen, L.; Huang, T. J., Dynamic Tuning of Plasmon–Exciton Coupling in Arrays of Nanodisk–J-aggregate Complexes. *Adv. Mater.* **2010,** *22* (32), 3603-3607.

36. Zheng, Y. B.; Payton, J. L.; Chung, C. H.; Liu, R.; Cheunkar, S.; Pathem, B. K.; Yang, Y.; Jensen, L.; Weiss, P. S., Surface-Enhanced Raman Spectroscopy to Probe Reversibly Photoswitchable Azobenzene in Controlled Nanoscale Environments. *Nano Lett.* **2011,** *11* (8), 3447-3452.

37. Liu, G. L.; Yin, Y.; Kunchakarra, S.; Mukherjee, B.; Gerion, D.; Jett, S. D.; Bear, D. G.; Gray, J. W.; Alivisatos, A. P.; Lee, L. P., A nanoplasmonic molecular ruler

for measuring nuclease activity and DNA footprinting. *Nat. Nanotechnol.* **2006,** *1* (1), 47-52.

38. Sönnichsen, C., Detecting Intruders on the Nanoscale. *Science* **2011,** *332* (6036), 1389-1390.

39. Xing, J.-F.; Zheng, M.-L.; Duan, X.-M., Two-photon polymerization microfabrication of hydrogels: an advanced 3D printing technology for tissue engineering and drug delivery. *Chem. Soc. Rev.* **2015,** *44* (15), 5031-5039.

40. Kaehr, B.; Shear, J. B., Mask-directed multiphoton lithography. *J. Am. Chem. Soc.* **2007,** *129* (7), 1904-1905.

41. Kaehr, B.; Shear, J. B., Multiphoton fabrication of chemically responsive protein hydrogels for microactuation. *Proc. Natl. Acad. Sci. U.S.A.* **2008,** *105* (26), 8850-8854.

42. Chen, X. Y.; Brewer, M. A.; Zou, C. P.; Campagnola, P. J., Adhesion and migration of ovarian cancer cells on crosslinked laminin fibers nanofabricated by multiphoton excited photochemistry. *Integr. Biol.* **2009,** *1* (7), 469-476.

43. Ritschdorff, E. T.; Nielson, R.; Shear, J. B., Multi-focal multiphoton lithography. *Lab Chip* **2012,** *12* (5), 867-871.

44. Galloway, C. M.; Kreuzer, M. P.; Aćimović, S. S.; Volpe, G.; Correia, M.; Petersen, S. B.; Neves-Petersen, M. T.; Quidant, R., Plasmon-assisted delivery of single nano-objects in an optical hot spot. *Nano Lett.* **2013,** *13* (9), 4299-4304.

45. Wiesbauer, M.; Wollhofen, R.; Vasic, B.; Schilcher, K.; Jacak, J.; Klar, T. A., Nano-anchors with single protein capacity produced with STED lithography. *Nano Lett.* **2013,** *13* (11), 5672-5678.

46. Scarabelli, L.; Coronado-Puchau, M.; Giner-Casares, J. J.; Langer, J.; Liz-Marzán, L. M., Monodisperse Gold Nanotriangles: Size Control, Large-Scale Self-Assembly, and Performance in Surface-Enhanced Raman Scattering. *ACS Nano* **2014,** *8* (6), 5833-5842.

47. Pitts, J. D.; Campagnola, P. J.; Epling, G. A.; Goodman, S. L., Submicron multiphoton free-form fabrication of proteins and polymers: studies of reaction efficiencies and applications in sustained release. *Macromolecules* **2000,** *33* (5), 1514-1523.

48. Liu, N.; Tang, M. L.; Hentschel, M.; Giessen, H.; Alivisatos, A. P., Nanoantenna-enhanced gas sensing in a single tailored nanofocus. *Nat. Mater.* **2011,** *10* (8), 631-636.

49. Olson, J.; Dominguez-Medina, S.; Hoggard, A.; Wang, L.-Y.; Chang, W.-S.; Link, S., Optical characterization of single plasmonic nanoparticles. *Chem. Soc. Rev.* **2015,** *44* (1), 40-57.

50. Wang, W.; Tao, N., Detection, counting, and imaging of single nanoparticles. *Anal. Chem.* **2013,** *86* (1), 2-14.

51. Fang, A.; White, S.; Jain, P. K.; Zamborini, F. P., Regio-selective Plasmonic Coupling in Metamolecular Analogs of Benzene Derivatives. *Nano Lett.* **2015,** *15* (1), 542–548.

52. Anker, J. N.; Hall, W. P.; Lyandres, O.; Shah, N. C.; Zhao, J.; Van Duyne, R. P., Biosensing with plasmonic nanosensors. *Nat. Mater.* **2008,** *7* (6), 442-453.

53. Gratton, E.; Breusegem, S.; Sutin, J.; Ruan, Q.; Barry, N., Fluorescence lifetime imaging for the two-photon microscope: time-domain and frequency-domain methods. *J. Biomed. Opt.* **2003,** *8* (3), 381-390.

54. Gabudean, A.-M.; Groza, R.; Maniu, D.; Astilean, S., Steady-state and time-resolved fluorescence studies on the conjugation of Rose Bengal to gold nanorods. *J. Mol. Struct.* **2014,** *1073*, 97-101.

55. Xu, D.; Neckers, D., Aggregation of rose bengal molecules in solution. *J. Photochem. Photobiol., A* **1987,** *40* (2), 361-370.

56. Acuna, G. P.; Bucher, M.; Stein, I. H.; Steinhauer, C.; Kuzyk, A.; Holzmeister, P.; Schreiber, R.; Moroz, A.; Stefani, F. D.; Liedl, T., Distance dependence of single-fluorophore quenching by gold nanoparticles studied on DNA origami. *ACS Nano* **2012,** *6* (4), 3189-3195.

Chapter 3: Large-Area Bubble Printing of Quantum Dots*

3.1 INTRODUCTION

The multi-photon plasmonic lithography approach demonstrated in chapter 2 is can achieve ultra-high resolution, but is confined to a single nanoparticle regime. In this chapter, we further extend the scope of plasmonics to realize large-area immobilization of quantum dots (QDs)/ With strong quantum confinement effect, high crystal quality and precisely controllable size, chemically synthesized semiconductor QDs show their advantages over organic luminescence materials, i.e., tunable absorption and emission wavelength, narrow emission bandwidth, high quantum efficiency, and excellent stability.[1-4] Typical QD applications include light-emitting devices,[5] information displays,[6] photovoltaics,[7] biosensing,[8] nanolasers,[9] and photodetectors.[10-11] The optical performance of QDs can be further enhanced by placing the QDs at plasmonic substrates,[12] which can significantly improve the spontaneous emission rate by the Purcell effect and modify the emission direction by coupling the emitted photon into directional scattering light.[13-14] The plasmon-QDs hybrid systems can enhance many of the applications, including full-color displays and nanolaser.[15]

However, the translation of QDs into real-life applications mentioned above relies on the capability to pattern or print QDs from solutions onto the predetermined locations of solid-state substrate.[16-17] In particular, the realization of applications in photonics and biotechnology are highly depended on the structured patterning of QDs. To this end, the major approaches explored include Langmuir-Blodgett (LB) printing,[18-19] micro-transfer

* Rajeeva, B. B., Lin, L., Perillo, E.P., Peng, X., Yu, W. W., Dunn, A. K., Shear, J. B., Zheng, Y. B. High-Resolution Bubble Printing of Quantum Dots. ACS Applied Mater. Interfaces, 2017, 9, 16725.
Lin, L., Peng, X., Mao, Z., Li, W., Yogeesh, M. N., Rajeeva, B. B., Perillo, E. P., Dunn, A. K., Akinwande, D., Zheng, Y. B. Bubble-Pen Lithography. Nano Lett., 2016, 16, 701.
Rajeeva, B. B. carried out the experimental work and participated in the preparation of manuscript.

printing,[6] intaglio printing,[20] gravure printing,[21] inkjet printing,[22] and electrohydrodynamic jet (E-Jet) printing.[23] The mask-based approaches (i.e., LB printing, transfer and intaglio printing) have shown promise of achieving extremely high-resolution patterning down to single-QD level.[18] In contrast, ink/nozzle-based printing techniques (i.e., Inkjet and E-Jet) are direct-writing approaches, which circumvent the reliance on a mask and thus reduce the overhead cost considerably. However, they have remained challenging to manufacture complex structures at sub-micrometer resolution due to inherent technological barriers such as the spreading of the ink upon exposure to the substrate and long post-processing time for the inks to dry.[22] Therefore, developing a broadly applicable, high-resolution, and precise printing technique is critical for the widespread applications of the semiconductor QDs.

In this chapter, we introduce the concept of bubble printing (BP) wherein we exploit a light-directed microbubble to capture and print QDs in their native liquid environments. By generating and translating opto-thermally generated mesobubbles (bubble with a diameter of < 1μm) on a plasmonic substrate, we are able to rapidly deliver the suspended QDs towards the air-liquid interface by Marangoni convection and to immobilize the QDs on the plasmonic substrates with precise site control over a large area. Our BP technique addresses a major technical challenge regarding the development of a versatile printing technique with resolution of <1 μm.[22] It offers versatility of achieving complex morphologies with extremely low material wastage, high throughput (maximum scanning rate of ~10^{-2} m/s), high resolution (~650 nm) and real-time configurable patterning. To further demonstrate the versatility, we achieve BP patterning of QDs on flexible substrates, which enables multiple applications such as flexible displays,[24] opto-electronic circuits,[25] and sensors.[26]

3.2 BUBBLE-MEDIATED IMMOBILIZATION

Figure 3.1a shows the schematic of the optical setup for BP. The aqueous QD solution is confined between a plasmonic substrate consisting of gold nanoparticles (AuNPs) (see Section 3.2.1 for details) and a glass coverslip with a spacer of 500 μm thickness. Upon irradiation of a continuous wave laser beam (532nm) through a high magnification objective, the AuNPs excited on resonance reemit the energy via nonradiative Landau damping, which results in an elevated temperature over the AuNP surfaces (Figure 3.1b).[27-29] This plasmon-enhanced photothermal heating causes the overheating and leads to the formation of the mesobubble,[30] whose diameter can be controlled from sub-micron to micron regimes by tuning the optical power. The temperature gradient along the bubble surface causes the Marangoni convection and therefore the delivery of QDs towards the bubble surface by convective drag force. The QDs are trapped at the bubble/liquid interface with a force balance of the gas/liquid pressure difference, the drag force and the surface tension.[31-34] The QDs are eventually immobilized on the substrate by the van der Waals interaction between QDs and the plasmonic substrate and the thermal heating. When the bubble is translated over the substrate via deflection (movement of laser beam controlled by spatial light modulator) or displacement (stage movement) techniques, the QDs are patterned along the path traversed by the laser beam (Figure 3.1c). In the present case, we achieve large-area versatile patterning of QDs via stage translation.

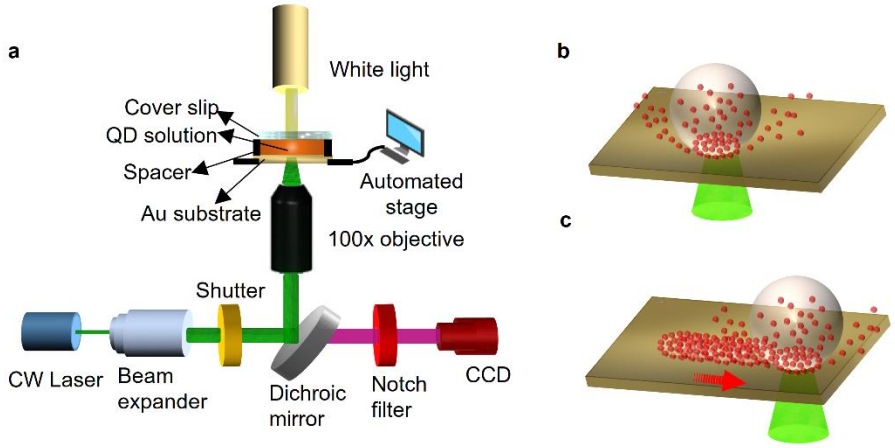

Figure 3.1. Working principle of BP of QDs on plasmonic substrates. (a) Schematic of the optical setup for BP. (b) Schematic showing the QDs being trapped towards the bubble generated on the substrate, and the eventual immobilization of QDs on the substrate. (c) Illustration of the QDs immobilized along the path traversed by the laser beam to create patterns of QDs on the substrate.

3.2.1 Gold Nanoisland Substrate

Since the bubble is created based on the plasmon-enhanced optothermal heating of the plasmonic substrate, the uniformity of the AuNPs and their constituent "hot spots" on the substrate (Figure 3.2) is crucial to ensure the light-directed bubble generation at any arbitrary location. To prepare the plasmonic substrates, 4 nm Au film was deposited on a glass substrate using thermal deposition (Denton Thermal evaporator) at a base pressure of 9×10^{-6} Torr. The sample was subsequently annealed at 550℃ for 2 hours to realize the AuNI substrate.

From the SEM image, we estimate the average AuNP radius and inter-particle distance to be 30 nm and 15 nm, respectively. Assuming a value of 500 nm for FWHM, the ratio is found to be 3×10^{-3}. This implies that the temperature rise is in the delocalized regime, and is a cumulative effect of particles exposed to the laser. A random area selection over the plasmonic substrate establishes the uniformity of AuNP distribution in terms of

area coverage with a standard deviation of 0.54%. The highly uniform AuNP density along with the delocalized photothermal conversion ensures that a constant temperature is generated throughout the substrate, enabling the generation of bubbles with a uniform size.

a

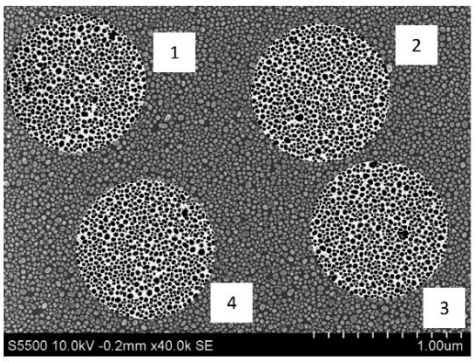

b

Location	% Area
1	52.5
2	51.84
3	52.25
4	51.4

Figure 3.2: (a) SEM image of the plasmonic substrate for bubble printing. Spots of 940 nm in diameter were randomly chosen on the image, and the %area coverage of the AuNPs was calculated as shown in the table. (b) All spots show uniform AuNP coverage with a standard deviation of 0.54%.

3.2.2 Particle-Immobilization Mechanism

The plasmonic substrate is optimized to lower the optical power intensity with the Au nanoislands (AuNIs). The simulated electromagnetic field distributions (excited with a laser wavelength of 532 nm) are displayed in the figure 3.3a, with strong near-field coupling between the neighboring Au nanoparticles observed. Both the simulated and experimental absorption spectra (Figure 3.3.b) reveal the wavelength of the absorption band of the AuNIs is close to the laser wavelength, which can enhance the absorption efficiency and improve the thermal effect.

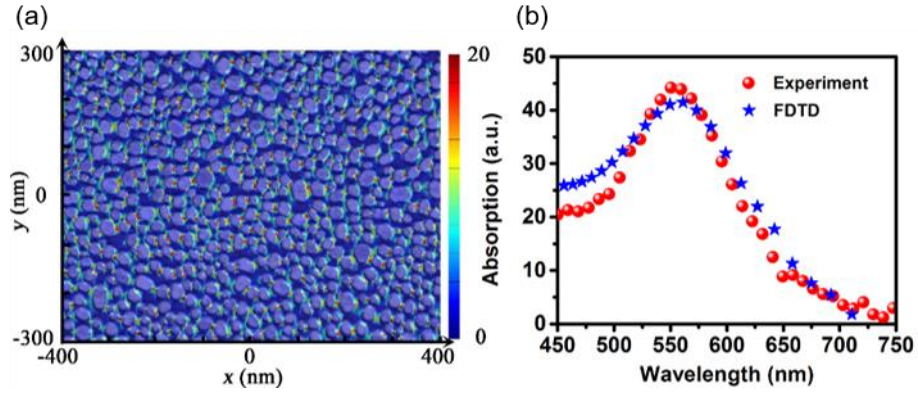

Figure 3.3: Overlay of SEM image and the simulated "hot spots" distributions on the semi-continuous AuNIs substrate. **d,** Simulated and experimental absorption spectra of the AuNIs substrate.

Post-bubble generation, both natural convection and Marangoni convection are responsible for the particle collection process. The former is caused by the temperature gradient on the Au plasmonic substrate and is irrelevant to the microbubble, while the latter is introduced by the surface tension gradient along the microbubble surface, which is observed as soon as the microbubble is generated. The convective flow brings the particles towards the microbubble (Figure 3.4a). The trapping commences when a particle touches the microbubble, as shown in the inset of Figure 3.4a. The surface tension F_S at the gas/liquid interface introduces a force F_D which drags the particle towards the microbubble. The pressure inside the microbubble, which reaches 3.4 bar for the 1 μm bubble[35], is much higher than the pressure in water, which can be treated as atmospheric pressure. The balance is achieved when the two ratio between F_D and F_P becomes 1:

$$\frac{F_D}{F_P} = \frac{R_B}{R}\frac{\sin(|\theta_c - \beta|)}{sin\beta} = 1 \qquad (1)$$

where R_B is the radius of the microbubble, R_B is the radius of the microbubble, F_P is the force induced by the gas/liquid pressure difference, R is the radius of the colloidal particles, θ_C is the contact angle between the particle and the bubble, and β is the half-central angle.

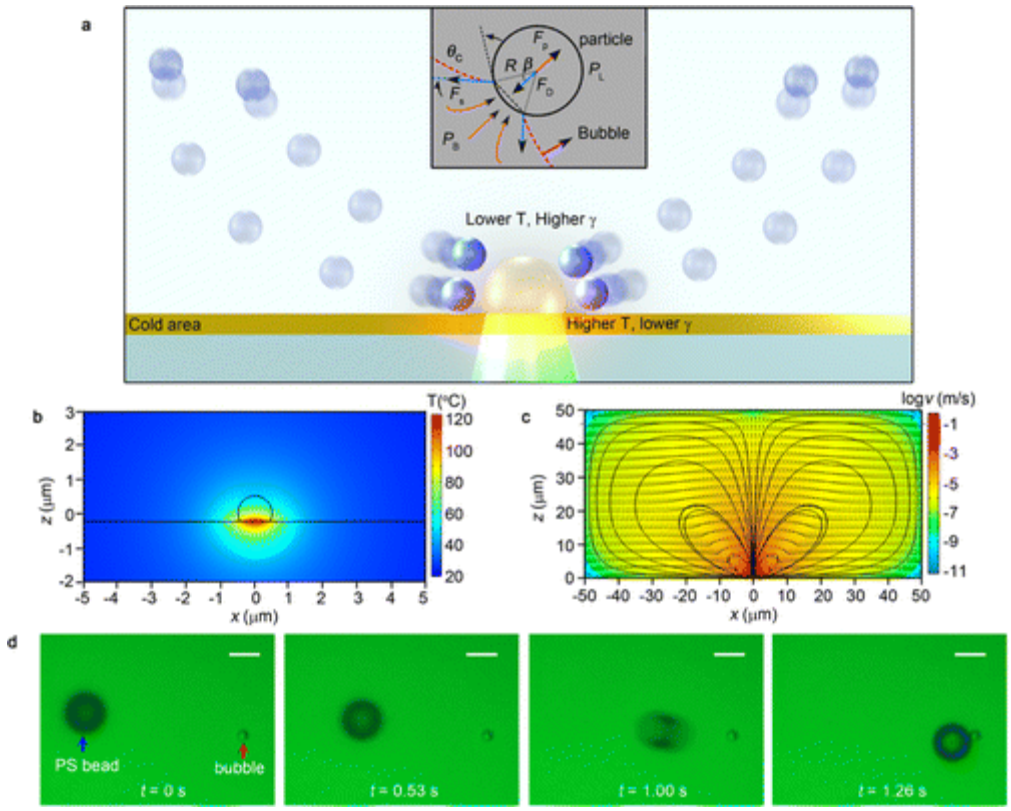

Figure 3.4: Particle trapping at a microbubble that is generated through the plasmon-enhanced photothermal effects. (a) Schematic illustration (in a cross-sectional view) of the particle-trapping mechanism by a single microbubble. The blue spheres indicate the suspended particles in the DI water. The particles follow the convective flow due to the frictional force. The inset shows the force distribution when a particle is trapped by the microbubble (indicated as the red dash line). PB and PL indicate the pressure in the bubble and liquid, respectively, which introduce a net force of FP pushing the particle outward. The surface tension FS introduce a drag force FD. (b) Simulated temperature distribution around a 1 μm bubble in a cross-sectional view. (c) Simulated flow velocity distribution around a 1 μm bubble with logarithmic scale in a cross-sectional view. The black lines indicate streamlines of the convective flow. (d) Time-resolved trapping process of a single 5.31 μm PS bead by a 1 μm bubble. Scale bar: 5 μm

We used computational fluid dynamics (CFD) simulations to obtain the temperature distribution around a 1 μm bubble (Figure 3.4b) when the substrate is illuminated by a focused laser beam with a diameter of 2 μm and power density of 0.56

mW/μm^2 (measured at the focus point of the objective). The resultant bottom-to-top temperature difference of ~60 °C creates the surface tension gradient along the bubble surface. The flow velocity distribution around this microbubble is displayed in Figure 3.4c, with a maximum flow velocity of ~0.3 m/s at the gas/liquid interface. The flow velocity decreases when the distance from the microbubble is increased. It ranges from 1 to 100 μm/s at the distances of 15–5 μm. Due to the convective flow, the particles are dragged toward the microbubble according to Stokes' law:

$$F_d = 6\pi\mu R\nu(R) \quad (2)$$

where μ is the dynamic viscosity of the solution, and ν(R) is the flow velocity of solvent relative to the particles, which is also dependent on R. As shown in Figure 3.4c, the larger particles have the mass center farther away from the substrate surfaces, experiencing a different flow velocity from the smaller particles. At a constant mass density, the acceleration of the particles is estimated as

$$\alpha \propto \mu R^{-2}\nu \quad (3)$$

We measured the particle-trapping speed by recording the time-resolved trapping processes of single PS beads with diameters of 5.31 μm (Figure 3.4d). A traveling distance of ~20 μm is used to estimate the average trapping speed. The 5.31 μm PS bead exhibits a speed of 18.1 μm/s. The drag force and trapping speed depend on the distance between the particle and the microbubble. There is a dramatic increase in the trapping speed when the particle approaches the microbubble (Figure 3.4d), indicating that the relative velocity ν dominates the trapping process.

3.2.3 Large-Area Printing

The precise control of QD patterns in BP requires a stable translation of the photothermally generated bubble along a pre-set trajectory. The translation is governed by

a steady-state process where the photothermal heat on the AuNPs is balanced by the thermal loss from the bubble to the surrounding liquid at room temperature. The thermal analysis of plasmonic substrates has been analyzed in prior works, which revealed the photothermal energy radially propagating outwards from the laser beam spot.[36-37] Treating the bubble as a sphere, we can estimate the outward heat flux from the bubble using Fourier's law:

$$\frac{dQ}{dT} = 4\pi k R^2 \partial_r T \tag{4}$$

wherein Q is the heat power of the incident laser (J), k is the thermal conductivity of water (Js-1m-1K-1), R is the radius of the bubble (m), T is the temperature (K), and $\partial_r T$ is the temperature gradient at the edge of the bubble (K/m). By assuming $\partial_r T \approx \frac{\Delta T}{R}$, where ΔT is the temperature difference across the bubble surface (Figure 1d), we get

$$\frac{dQ}{dT} = 4\pi k R \Delta T \tag{5}$$

With the assumption that temperature difference ΔT remains the same under similar illumination conditions, the steady-state thermal loss is proportional to R.[38] In other words, the smaller bubble can retain the steady state for a longer period due to lower thermal loss. In addition to the lower heat loss, the minimal air concentration within the bubble helps maintain the stability of the mesobubble (bubble diameter < 1 μm). It is noted that the highly focused laser beam and the plasmonic substrate with uniform high-density AuNPs effectively reduce the size of the light-generated bubble for the stable BP of QDs.

3.3 QUANTUM DOT PRINTING

We apply BP to pattern colloidal CdSe/CdS QDs encapsulated with an amphiphilic coating and dispersed in an aqueous medium. Various QDs with emission colors of red, yellow, and green) were used by adding ~50 μl droplets of the solutions over the plasmonic

substrates. Based on the analysis of the video frames, we found the mesobubble dissolution (upon laser switch-off) time is in the range of 250-300ms. For the sub-micron bubble, the concentration of air molecules within the bubble is limited, and the bubble is mostly composed of water vapor. The water vapor ensures extremely fast disappearance of the bubble upon the laser switch-off in contrast to air bubbles, which can last from several seconds to hours.[39] The quick transition between on and off states of the bubble is necessary for high-speed patterning. Further reduction in the dissolution time can be potentially achieved by generating smaller bubbles via utilization of highly-confined hot-spots to realize stronger thermal gradient (e.g. bow-tie antenna array).[29, 40] An alternate strategy could be the utilization of degassed water to reduce the two-way mass transfer between the vapor bubble and dissolved gas in the solvent, thereby leading to the faster bubble dissolution.[41]

A precise control over the line-width of the QD pattern is critical for advanced applications. The lowest line-width of <700 nm (Figure 3.5a) is observed via BP at an incident power intensity of 0.28 mW/μm^2. Increasing power also changes the QD pattern morphology from scalloped lines to lines with uneven line-width, eventually leading to individual bubble geometry. Further increase in the optical power causes the coalescence of adjacent bubbles into the larger bubbles, which are not suitable for BP due to long bubble lifetime.

Figure 3.5b shows a bright-field image of three types of large-area rectangular patterns of QDs fabricated via raster scanning of the laser beam, which demonstrates the tunability of the QD pattern density by line spacing (i.e., 1 μm, 1.5 μm, and 2 μm). Further, by using a stage wait time of 500ms and 1 μm stage steps, crowding of the QDs at the edge of each bubble can be achieved. This creates a pattern resembling arrays of QD clusters as

individual pixels. We observed an average FWHM of 400 nm for the pixels with a high-resolution two-photon fluorescence microscope (Figure 3.5c-d).

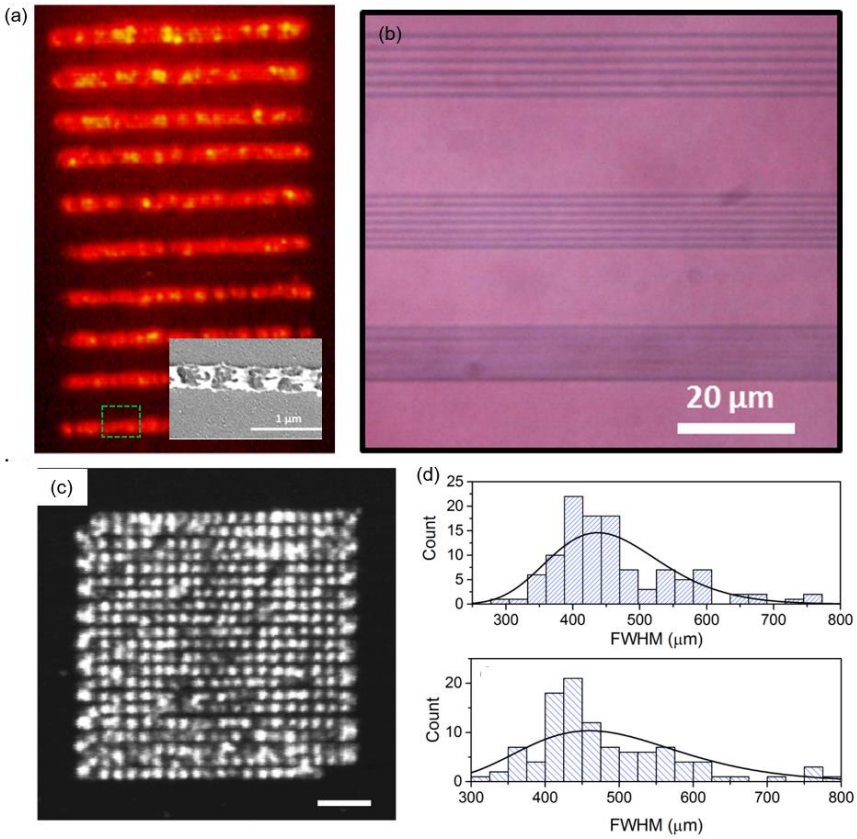

Figure 3.5: (a) Merged fluorescence image of the patterned lines of QDs demonstrating the line-width variation in response to change in the incident laser power. The inset shows the SEM of the patterned line of QDs with a line-width of 680 nm. (b) Large area patterning of QDs rectangles created using BP with various line spacing. The line spacing is 1 µm, 1.5 µm, and 2 µm (bottom to top). (c) (a) High-resolution two-photon fluorescence image which resembles individual pixels. (d) The width of each pixel is obtained by calculation of the FWHM of the spots based on the intensity.

For continuous patterning, the relationship between the incident laser intensity and the pattern line-width was examined (Figure 3.6a). With an increase in the optical power, the bubble size increases due to the higher amount of vapor generation. A linear regression line was obtained from the plot of pattern line-width and the incident laser power,

demonstrating the ease of modulating the patterns by the laser power. Following process parameter optimization, we have demonstrated the versatility of BP in Figure 3.6.

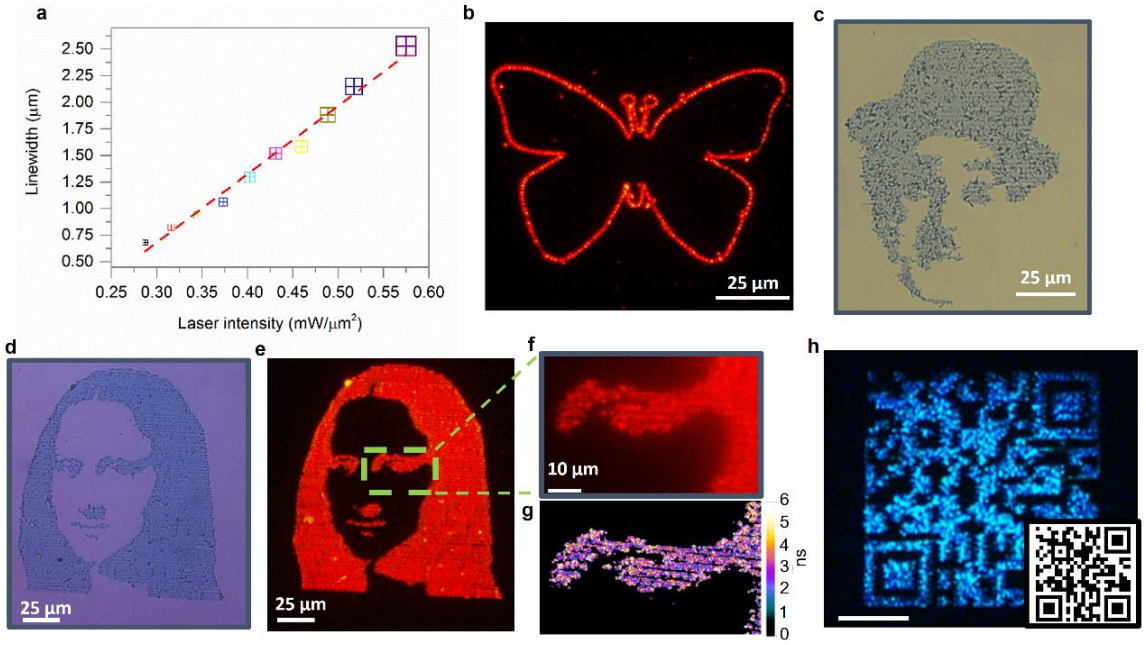

Figure 3.6: Versatile bubble printing capabilities: (a) Plot of pattern line-width vs. incident laser intensity. The linear fitting shows the on-demand capability of tuning the patterning dimensions by the laser power. (b) Bubble printing of red QDs into a contour of a butterfly as shown by fluorescence image. The line-width is 1μm. (c) Bright-field image of a Charlie Chaplin pattern of QDs via raster scanning in BP. The overall size is 120 μm×90 μm with 1μm line-space. (d, e) Bright-field and fluorescence images [tetramethylrhodamine isothiocyanate (TRITC) filter set] of Mona Lisa printed with red QDs using a raster scanning approach. The size of the complete image is 150 μm×90 μm. (f) Magnified fluorescence image depicting the high-resolution patterning capability of BP. (g) Fluorescence lifetime imaging of the QDs showing high-density uniform patterning capability of BP. (h) Fabrication of a microscale (80 μm×80 μm) QR code with blue QDs printed via raster scanning. The scale bar is 25 μm.

Initially, the QDs were bubble printed along a contour by programmed translation of the sample stage. Figure 3.6b shows the microscale patterning of red QDs in the shape of a butterfly. It is worth noting that the head of the butterfly that involves closely spaced

circles of ~8 μm in diameter is precisely patterned without any spreading, bubble coalescence or distortion. With rapid dissolution and generation time of the mesobubble, it is also possible to create more complicated patterns at high resolution and speed. Figure 3.6c and 3.6d show the high-resolution intricate patterns of red QDs resembling famous personalities such as Charlie Chaplin and Mona Lisa with a dimension of 120 μm×90 μm and 150 μm×90 μm, respectively. A magnified image in figure 2f demonstrates the defining strength of bubble printing wherein 1 μm gap between adjacent structures (eyebrow and eye) can be realized. To alleviate concerns of fluorescence image saturation, a fluorescence lifetime image of the same region was taken with fluorescence-lifetime imaging microscopy (FLIM), which demonstrates uniform deposition of QDs within the pattern.

Further, we have demonstrated the capability of BP in fabricating functional luminescent devices in the area of anti-counterfeiting technology.[22] Specifically, high-resolution microscale QR codes are desirable for preventing the forging of IC chips[42]. Using BP, a microscale QR code of 80 μm×80 μm was fabricated. The complicated QR code was achieved by performing a raster scan of green QDs using the laser beam in conjunction with a shutter to determine an on/off state of the printing. In this work, patterns with blue emission were obtained by controlled oxidation of either green or yellow QDs. The average and root-mean-square (rms) surface roughness over 40 μm × 80 μm region are 12.6 nm and 16.5 nm, respectively (Figure 3.7a-b). The printed red QDs show similar emission characteristics as those of pristine QDs (Figure 3.7c). A 3.9 nm increase in FWHM can be attributed to the aggregation of QDs.[43]

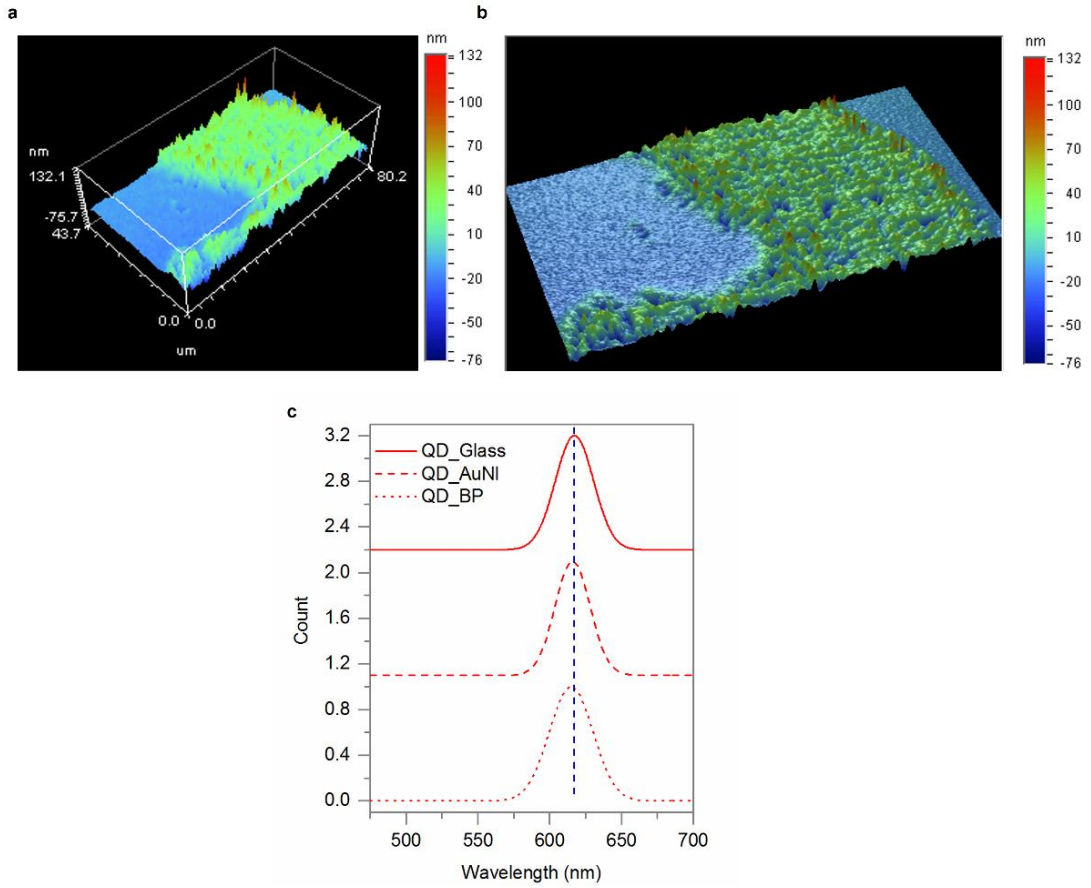

Figure 3.7: (a, b) Optical profilometry images of a 40 µm × 80 µm region around the right eye of the Monalisa pattern (Figure 3.6d). The average and rms roughness of the printed QDs are 12.6 nm and 16.5 nm, respectively. (c) The emission spectrum of control QDs on drop-casted on glass and AuNI (FWHM=30.2 nm), along with printed QDs (FWHM=34.1 nm). The printed QDs showed a blue-shift of ~1 nm and FWHM increase of 3.9 nm.

3.4 Multi-Color Quantum Dot Printing

Since the patterning process is primarily mediated by Marangoni convection and subsequent van der Waals interaction, the BP technique is applicable to QDs of variable sizes (sub 10 nm Pt nanoparticles to micron-sized polystyrene beads), shapes and compositions, which is critical to the fabrication of various devices. We have demonstrated the BP of QDs with different emission colors onto the plasmonic substrates. The same

mechanisms for bubble generation, QD entrapment and QD immobilization on the substrates apply to all types of the QDs. The pattern of Mona Lisa with 1 µm line spacing was replicated with yellow QDs at a high stage-translation speed of 10^{-2} m/s.

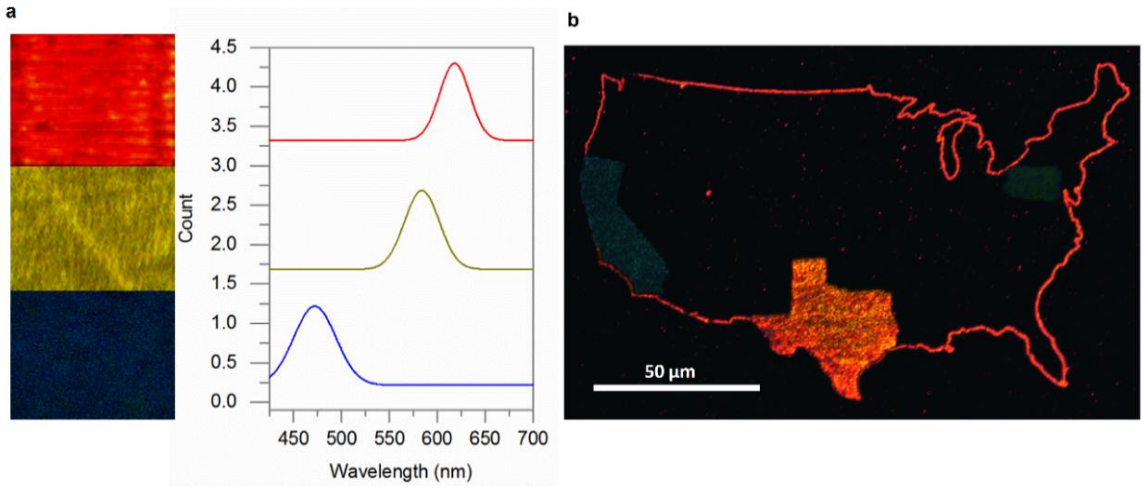

Figure 3.8: Towards multi-color QD printing: (a) (Left) Fluorescence images of bubble-printed red, yellow and blue QDs into three patterns. (Right) Corresponding fluorescence spectra of the three patterns depicting emission peaks from blue to red. (b) Integration of multiple QDs on a single substrate using multi-step bubble printing. The example is a USA map with the states of Texas, California, and Pennsylvania printed with different QDs. The size of the map is 120 µm×200 µm and each state is fabricated via raster scanning with 1 µm line space.

The left panel in figure 3.8a shows high-density bubble printing of three types of QDs that emit red, yellow and blue lights, revealing the potential for printing full-color QD displays[44]. Similar to the QR code scenario, the blue emission was obtained via controlled oxidation of green QDs. The right panel in figure 3.8a shows the corresponding fluorescence spectra of the patterns. For an initial demonstration of multi-color printing, we have demonstrated the regioselective printing of individual red/green/blue emission patterns onto a single substrate. Figure 3.8b shows the fluorescence image (405 nm excitation) of a bubble-printed contour of USA map along with the states of Texas,

California, and Pennsylvania. This map was achieved by a multi-step printing process where cross-markers were created (also by BP) for alignment and a rigorous washing step with isopropyl alcohol and water between each step was applied to remove loosely adsorbed QDs on the substrate. There is strong adhesion of the printed QDs on the plasmonic substrates. For instance, the printed QDs could not be transferred from the substrates to the very sticky polydimethylsiloxane (PDMS, 30:1; pre-polymer: curing agent), which in turn corresponds to an adhesion strength greater than 6 J m^{-2}.[45] The strong adhesion can be attributed to the convection and the thermal heating effects which reduces the ligand length, and thereby the QD-substrate separation to yield stronger van der Waals forces.

3.5 PRINTING ON FLEXIBLE SUBSTRATE

We have further applied BP to pattern QDs on flexible and bendable plastic substrates. A flexible PET substrate with 4 nm Au thin film on the surface was utilized for the demonstration. Figure 3.9a shows the fluorescence image of a longhorn symbol created via BP of red QDs on the PET film. Figure 3.9b shows a magnified bright-field image of part of the longhorn with the PET film mechanically bent, which exhibits the structural integrity of the printed QD pattern under the bent state. Repeating the mechanical bending and recovery of the film 20 times, as shown in Figure 3.9c and d, yielded no significant changes in the structural and optical properties of the pattern. The high adhesion of the QDs to the flexible substrate ensures that the fabricated sample remains stable under various conditions.

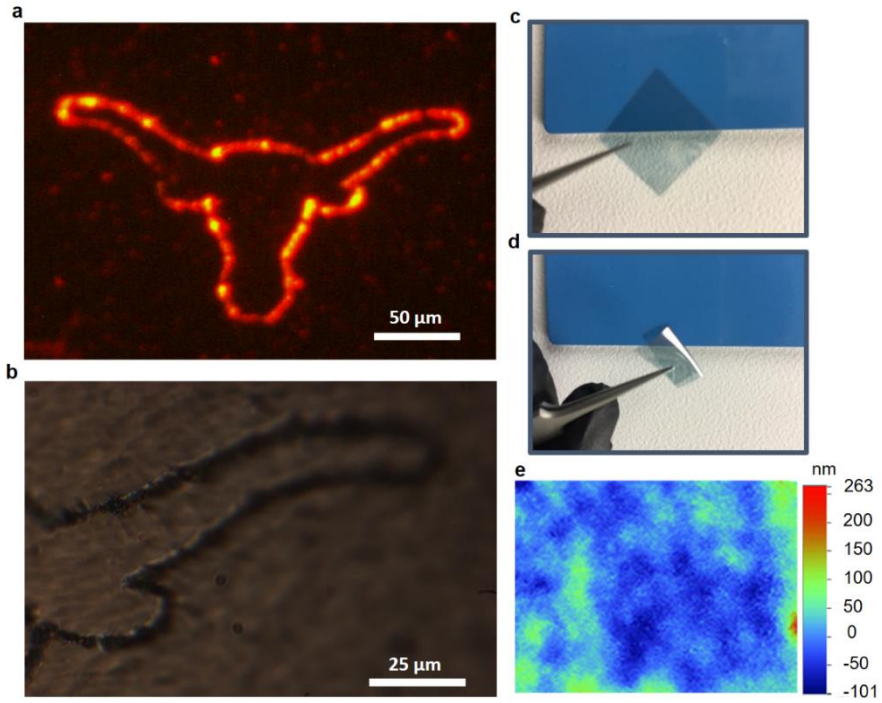

Figure 3.9: Bubble printing of QDs on a flexible substrate: (a) Fluorescence image of the longhorn pattern printed with red QDs over a PET film obtained using TRITC filter set. (b) Bright-field image of the printed QDs with the PET film in the bent state. The strong adhesion of QDs to the substrate ensures that the high integrity of the pattern is maintained after the mechanical bending. (c, d) Optical images of the PET film under the original and bent states, respectively. (e) Optical profilometer image (Wyco 9100) of the PET film showing an RMS roughness of 35 nm.

The printed QDs were able to withstand both uniform and non-uniform bending of the substrate due to their strong adhesion to the substrate surface. Therefore, an increase in root mean square (RMS) roughness to 35 nm for the PET film (Figure 3.9e) isn't a major barrier towards bubble generation and BP process. In fact, numerous reports on bubble generation consider RMS values of > 1 µm as rough surfaces.[46] In addition, BP on flexible substrates can achieve a similar sub-micron resolution as that of the rigid substrates (Figure 3.10 a and b). The bump on the flexible substrate is also visible in the bright-field image.

Further, optical profilometry measurement of the sample reveals non-significant deformation of the underlying PET substrate. This further confirms the compatibility of BP strategy with flexible substrates.

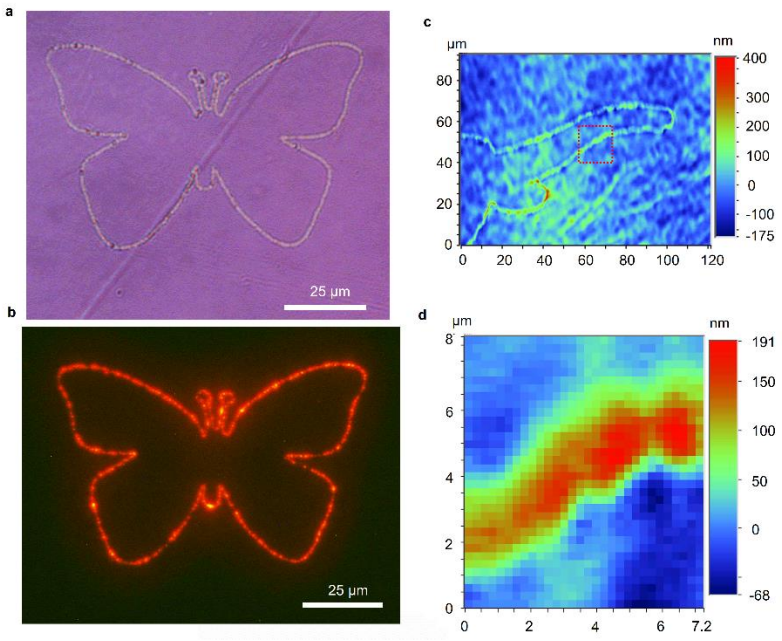

Figure 3.10: (a) Printing of QDs with sub-micron resolution on a PET film. (b) Corresponding fluorescence image. (c) Optical profilometer image of the patterned longhorn, along with zoomed-in portion (d) of the image.

3.6 SUMMARY

In this chapter, we have demonstrated BP of QDs for the fabrication of patterned plasmon-QD hybrid structures. The strong bubble stability is attributed to the delocalized temperature increase over uniform Au nanoparticles on the plasmonic substrates. Furthermore, the vapor bubbles with fast dissolution times improve BP throughput. BP can simultaneously achieve high resolution (<1µm line-width), high throughput (>10^5 µm/s) and low material usage. The versatile printing capabilities of BP are demonstrated for

multi-color QDs on both rigid and flexible substrates. With high resolution and throughput, BP will find applications in high-resolution QD display, high-density information storage, and biomedical assays.

3.7 REFERENCES

1. Pietryga, J. M.; Park, Y. S.; Lim, J. H.; Fidler, A. F.; Bae, W. K.; Brovelli, S.; Klimov, V. I., Spectroscopic and Device Aspects of Nanocrystal Quantum Dots. *Chem. Rev.* **2016,** *116* (18), 10513-10622.
2. Yin, Y. D.; Talapin, D., The chemistry of functional nanomaterials. *Chem. Soc. Rev.* **2013,** *42* (7), 2484-2487.
3. Yu, W. W.; Peng, X. G., Formation of high-quality CdS and other II-VI semiconductor nanocrystals in noncoordinating solvents: Tunable reactivity of monomers. *Angew. Chem., Int. Ed.* **2002,** *41* (13), 2368-2371.
4. Cassette, E.; Helle, M.; Bezdetnaya, L.; Marchal, F.; Dubertret, B.; Pons, T., Design of new quantum dot materials for deep tissue infrared imaging. *Adv. Drug Deliver. Rev.* **2013,** *65* (5), 719-731.
5. Mashford, B. S.; Stevenson, M.; Popovic, Z.; Hamilton, C.; Zhou, Z. Q.; Breen, C.; Steckel, J.; Bulovic, V.; Bawendi, M.; Coe-Sullivan, S.; Kazlas, P. T., High-efficiency quantum-dot light-emitting devices with enhanced charge injection. *Nat. Photon.* **2013,** *7* (5), 407-412.
6. Kim, T. H.; Cho, K. S.; Lee, E. K.; Lee, S. J.; Chae, J.; Kim, J. W.; Kim, D. H.; Kwon, J. Y.; Amaratunga, G.; Lee, S. Y.; Choi, B. L.; Kuk, Y.; Kim, J. M.; Kim, K., Full-colour quantum dot displays fabricated by transfer printing. *Nat. Photon.* **2011,** *5* (3), 176-182.
7. Lan, X. Z.; Masala, S.; Sargent, E. H., Charge-extraction strategies for colloidal quantum dot photovoltaics. *Nat. Mater.* **2014,** *13* (3), 233-240.
8. Medintz, I. L.; Clapp, A. R.; Mattoussi, H.; Goldman, E. R.; Fisher, B.; Mauro, J. M., Self-assembled nanoscale biosensors based on quantum dot FRET donors. *Nat. Mater.* **2003,** *2* (9), 630-638.
9. Lee, A. D.; Jiang, Q.; Tang, M. C.; Zhang, Y. Y.; Seeds, A. J.; Liu, H. Y., InAs/GaAs Quantum-Dot Lasers Monolithically Grown on Si, Ge, and Ge-on-Si Substrates. *IEEE J. Sel. Top. Quantum Electon.* **2013,** *19* (4), 1901107.
10. Konstantatos, G.; Howard, I.; Fischer, A.; Hoogland, S.; Clifford, J.; Klem, E.; Levina, L.; Sargent, E. H., Ultrasensitive solution-cast quantum dot photodetectors. *Nature* **2006,** *442* (7099), 180-183.

11. Kagan, C. R.; Lifshitz, E.; Sargent, E. H.; Talapin, D. V., Building devices from colloidal quantum dots. *Science* **2016,** *353* (6302), 885.

12. Gu, H. W.; Zheng, R. K.; Zhang, X. X.; Xu, B., Facile one-pot synthesis of bifunctional heterodimers of nanoparticles: A conjugate of quantum dot and magnetic nanoparticles. *J. Am. Chem. Soc.* **2004,** *126* (18), 5664-5665.

13. Curto, A. G.; Volpe, G.; Taminiau, T. H.; Kreuzer, M. P.; Quidant, R.; van Hulst, N. F., Unidirectional Emission of a Quantum Dot Coupled to a Nanoantenna. *Science* **2010,** *329* (5994), 930-933.

14. Hoang, T. B.; Akselrod, G. M.; Mikkelsen, M. H., Ultrafast Room-Temperature Single Photon Emission from Quantum Dots Coupled to Plasmonic Nanocavities. *Nano Lett.* **2016,** *16* (1), 270-275.

15. Yang, A. K.; Odom, T. W., Breakthroughs in Photonics 2014: Advances in Plasmonic Nanolasers. *IEEE Photonics J.* **2015,** *7* (3), 1-6.

16. Galatsis, K.; Wang, K. L.; Ozkan, M.; Ozkan, C. S.; Huang, Y.; Chang, J. P.; Monbouquette, H. G.; Chen, Y.; Nealey, P.; Botros, Y., Patterning and Templating for Nanoelectronics. *Adv. Mater.* **2010,** *22* (6), 769-778.

17. Lan, H. B.; Ding, Y. C., Ordering, positioning and uniformity of quantum dot arrays. *Nano Today* **2012,** *7* (2), 94-123.

18. Xie, W. Q.; Gomes, R.; Aubert, T.; Bisschop, S.; Zhu, Y. P.; Hens, Z.; Brainis, E.; Van Thourhout, D., Nanoscale and Single-Dot Patterning of Colloidal Quantum Dots. *Nano Lett.* **2015,** *15* (11), 7481-7487.

19. Park, J. S.; Kyhm, J.; Kim, H. H.; Jeong, S.; Kang, J.; Lee, S. E.; Lee, K. T.; Park, K.; Barange, N.; Han, J.; Song, J. D.; Choi, W. K.; Han, I. K., Alternative Patterning Process for Realization of Large-Area, Full-Color, Active Quantum Dot Display. *Nano Lett.* **2016,** *16* (11), 6946-6953.

20. Choi, M. K.; Yang, J.; Kang, K.; Kim, D. C.; Choi, C.; Park, C.; Kim, S. J.; Chae, S. I.; Kim, T. H.; Kim, J. H.; Hyeon, T.; Kim, D. H., Wearable red-green-blue quantum dot light-emitting diode array using high-resolution intaglio transfer printing. *Nat. Commun.* **2015,** *6*, 7149.

21. Sun, L.-W.; Shi, H.-Q.; Li, W.-N.; Xiao, H.-M.; Fu, S.-Y.; Cao, X.-Z.; Li, Z.-X., Lanthanum-doped ZnO quantum dots with greatly enhanced fluorescent quantum yield. *J. Mater. Chem.* **2012,** *22* (17), 8221-8227.

22. Bao, B.; Li, M. Z.; Li, Y.; Jiang, J. K.; Gu, Z. K.; Zhang, X. Y.; Jiang, L.; Song, Y. L., Patterning Fluorescent Quantum Dot Nanocomposites by Reactive Inkjet Printing. *Small* **2015,** *11* (14), 1649-1654.

23. Kim, B. H.; Onses, M. S.; Lim, J. B.; Nam, S.; Oh, N.; Kim, H.; Yu, K. J.; Lee, J. W.; Kim, J. H.; Kang, S. K.; Lee, C. H.; Lee, J.; Shin, J. H.; Kim, N. H.; Leal, C.; Shim, M.; Rogers, J. A., High-Resolution Patterns of Quantum Dots Formed by

Electrohydrodynamic Jet Printing for Light-Emitting Diodes. *Nano Lett.* **2015,** *15* (2), 969-973.

24. Shirasaki, Y.; Supran, G. J.; Bawendi, M. G.; Bulović, V., Emergence of colloidal quantum-dot light-emitting technologies. *Nat. Photon.* **2013,** *7* (1), 13-23.

25. Koh, W.-k.; Saudari, S. R.; Fafarman, A. T.; Kagan, C. R.; Murray, C. B., Thiocyanate-capped PbS nanocubes: ambipolar transport enables quantum dot based circuits on a flexible substrate. *Nano Lett.* **2011,** *11* (11), 4764-4767.

26. Meng, C.; Xiao, Y.; Wang, P.; Zhang, L.; Liu, Y.; Tong, L., Quantum-Dot-Doped Polymer Nanofibers for Optical Sensing. *Adv. Mater.* **2011,** *23* (33), 3770-3774.

27. Neumann, O.; Urban, A. S.; Day, J.; Lal, S.; Nordlander, P.; Halas, N. J., Solar Vapor Generation Enabled by Nanoparticles. *ACS Nano* **2013,** *7* (1), 42-49.

28. Fang, Z. Y.; Zhen, Y. R.; Neumann, O.; Polman, A.; de Abajo, F. J. G.; Nordlander, P.; Halas, N. J., Evolution of Light-Induced Vapor Generation at a Liquid-Immersed Metallic Nanoparticle. *Nano Lett.* **2013,** *13* (4), 1736-1742.

29. Roxworthy, B. J.; Ko, K. D.; Kumar, A.; Fung, K. H.; Chow, E. K. C.; Liu, G. L.; Fang, N. X.; Toussaint, K. C., Application of Plasmonic Bowtie Nanoantenna Arrays for Optical Trapping, Stacking, and Sorting. *Nano Lett.* **2012,** *12* (2), 796-801.

30. Lin, L. H.; Peng, X. L.; Mao, Z. M.; Li, W.; Yogeesh, M. N.; Rajeeva, B. B.; Perillo, E. P.; Dunn, A. K.; Akinwande, D.; Zheng, Y. B., Bubble-Pen Lithography. *Nano Lett.* **2016,** *16* (1), 701-708.

31. Zhao, C. L.; Xie, Y. L.; Mao, Z. M.; Zhao, Y. H.; Rufo, J.; Yang, S. K.; Guo, F.; Mai, J. D.; Huang, T. J., Theory and experiment on particle trapping and manipulation via optothermally generated bubbles. *Lab Chip* **2014,** *14* (2), 384-391.

32. Zheng, Y. J.; Liu, H.; Wang, Y.; Zhu, C.; Wang, S. M.; Cao, J. X.; Zhu, S. N., Accumulating microparticles and direct-writing micropatterns using a continuous-wave laser-induced vapor bubble. *Lab Chip* **2011,** *11* (22), 3816-3820.

33. Fujii, S.; Kanaizuka, K.; Toyabe, S.; Kobayashi, K.; Muneyuki, E.; Haga, M., Fabrication and Placement of a Ring Structure of Nanoparticles by a Laser-Induced Micronanobubble on a Gold Surface. *Langmuir* **2011,** *27* (14), 8605-8610.

34. Xie, Y.; Zhao, C. L., Optothermally generated surface bubble and its applications. *Nanoscale* **2017,** *9* (20), 6622-6631.

35. Baffou, G.; Polleux, J.; Rigneault, H.; Monneret, S., Super-Heating and Micro-Bubble Generation around Plasmonic Nanoparticles under cw Illumination. *J. Phys. Chem. C* **2014,** *118* (9), 4890-4898.

36. Baffou, G.; Quidant, R.; de Abajo, F. J. G., Nanoscale Control of Optical Heating in Complex Plasmonic Systems. *ACS Nano* **2010,** *4* (2), 709-716.

37. Liu, X. M.; Bao, L.; Dipalo, M.; De Angelis, F.; Zhang, X. H., Formation and dissolution of microbubbles on highly-ordered plasmonic nanopillar arrays. *Sci. Rep.* **2015,** *5*, 18515.

38. Lohse, D.; Zhang, X. H., Surface nanobubbles and nanodroplets. *Rev. Mod. Phys.* **2015,** *87* (3), 981-1035.

39. Baffou, G.; Polleux, J.; Rigneault, H.; Monneret, S., Super-Heating and Micro-Bubble Generation around Plasmonic Nanoparticles under cw Illumination. *J. Phys. Chem. C.* **2014,** *118* (9), 4890-4898.

40. Baffou, G.; Berto, P.; Urena, E. B.; Quidant, R.; Monneret, S.; Polleux, J.; Rigneault, H., Photoinduced Heating of Nanoparticle Arrays. *ACS Nano* **2013,** *7* (8), 6478-6488.

41. Dalvi, S. V.; Joshi, J. R., Modeling of microbubble dissolution in aqueous medium. *J. Colloid Interface Sci.* **2015,** *437*, 259-269.

42. Markman, A.; Javidi, B.; Tehranipoor, M., Photon-Counting Security Tagging and Verification Using Optically Encoded QR Codes. *IEEE Photonics J.* **2014,** *6* (1), 1-9.

43. Eisfeld, A.; Briggs, J. S., Absorption spectra of quantum aggregates interacting via long-range forces. *Phys. Rev. Lett.* **2006,** *96* (11), 113003.

44. Kim, B. H.; Nam, S.; Oh, N.; Cho, S. Y.; Yu, K. J.; Lee, C. H.; Zhang, J. Q.; Deshpande, K.; Trefonas, P.; Kim, J. H.; Lee, J.; Shin, J. H.; Yu, Y.; Lim, J. B.; Won, S. M.; Cho, Y. K.; Kim, N. H.; Seo, K. J.; Lee, H.; Kim, T. I.; Shim, M.; Rogers, J. A., Multilayer Transfer Printing for Pixelated, Multicolor Quantum Dot Light-Emitting Diodes. *ACS Nano* **2016,** *10* (5), 4920-4925.

45. Meitl, M. A.; Zhu, Z. T.; Kumar, V.; Lee, K. J.; Feng, X.; Huang, Y. Y.; Adesida, I.; Nuzzo, R. G.; Rogers, J. A., Transfer printing by kinetic control of adhesion to an elastomeric stamp. *Nat. Mater.* **2006,** *5* (1), 33-38.

46. McHale, J. P.; Garimella, S. V., Bubble nucleation characteristics in pool boiling of a wetting liquid on smooth and rough surfaces. *Int. J. Multiphase Flow* **2010,** *36* (4), 249-260.

Chapter 4: Haptic-Interfaced Printing and Fluorescence Tuning*

4.1 INTRODUCTION

Colloidal semiconductor quantum dots (QDs) have shown tremendous scientific and technological impacts. For example, QDs exhibit exceptional optoelectronic properties due to their size-dependent quantum confinement effect, which enables tunable light emission with narrow bandwidth and high brightness.[1-3] One can further enhance the optical performances of QDs by positioning them in the proximity of plasmonic substrates, leading to improved emission rate and directionality.[4] In addition, the development of bulk solution-phase synthesis of QDs in both aqueous and non-aqueous solvents has significantly enhanced their applicability.[5-7] So far, QDs have been explored for various applications such as light-emitting devices,[8] displays,[9] photovoltaics,[10] biosensing,[11] lasers,[12] and photodetectors.[13]

The applications can be greatly improved by the capability of fabricating spatially addressable patterns of QDs with precisely tuned properties.[14-15] Chen *et al.* achieved laser-induced tunability of optical properties of self-assembled films of QDs.[16] However, with the self-assembly process, it is challenging to achieve site-specific deposition of QDs on the substrates. Due to their simplicity, additive nature, and real-time configurability via digital control,[17] direct-write techniques such as inkjet printing, electrohydrodynamic jet printing, and gravure printing have been explored to realize the site-specific deposition of QDs with high throughput and material saving. However, these traditional printing techniques have their resolution limited at the micrometer scale due to technical issues such

*Rajeeva, B. B., Alabandi, M., Lin, L., Perillo, E.P., Dunn, A. K., Shear, J. B., Zheng, Y. B. Patterning and Fluorescence Tuning of Quantum Dots with Haptic-Interfaced Bubble Printing. Journal of Materials Chemistry C, 2017,5, 5693.
Rajeeva, B. B., Lin, L., Perillo, E.P., Peng, X., Yu, W. W., Dunn, A. K., Shear, J. B., Zheng, Y. B. High-Resolution Bubble Printing of Quantum Dots. ACS Applied Mater. Interfaces, 2017, 9, 16725.
Rajeeva, B. B. carried out the experimental work and participated in the preparation of manuscript.

as ink coalescence and oversizing.[18] In addition, the tedious multi-step synthesis and deposition are needed to pattern QDs of variable optical properties on the same substrates, as required for some of the applications.[19] Hence, the development of a widely accessible printing technique with sub-micrometer resolution and fluorescence-tuning capability is highly desired to expand the applications of QDs.

In this chapter, we detail the development and application of a haptic-interfaced bubble printing (HIBP) technique for free-form patterning. The fluorescence tuning of QDs on plasmonic substrates using conventional and haptic-interfaced bubble printing is also shown. Bubble printing exploits the photothermal heating of the substrates to generate the bubble, which captures and immobilize the QDs at the substrate-solution interfaces via coordinated actions of Marangoni convection, surface tension, van der Waals interaction, and thermal adhesion.[20] The integration of haptic interface to printing techniques caters to the engineering demands for precise and interactive processes at the micro and nanoscale.[21] In our case, we integrate the printing process with a smartphone to achieve the haptic operation. Specifically, we have applied BP and HIBP to achieve site-specific patterning of QDs on the plasmonic substrates consisted of Au nanoislands (AuNI). The effects of printing conditions on the emission characteristics of the patterned QDs in terms of emission wavelength and lifetime are studied based on both programmed stage control and haptic operation. By optimizing the printing parameters, we demonstrate simultaneous high resolution (510 nm line-width) and high throughput ($>10^4$ μm/s) HIBP with the QD emission wavelengths tuned across the visible spectrum. The haptic integration provides a single-step macroscale platform to manipulate properties at the nanoscale.

4.2 HAPTIC-INTEGRATION AND PRINTING

The printing was performed by programmed translation of a plasmonic substrate located on an automated optical stage. Similar to the substrates in Chapter 3, 4 nm Au thin film was deposited on a glass substrate using thermal deposition (Denton Thermal evaporator), and the sample was subsequently annealed at 550℃ for 2 hours. The printing process was achieved using a prior proscan scientific stage (x-y resolution = 14 nm) in conjunction with a motorized flipper (ThorLabs MFF102, 500 ms response time) that performed the function of a shutter. A custom-written LabView code guided the stage along the predetermined coordinates and an on/off shutter status. To achieve haptic operation, an android app registered the coordinates and shutter status, which were subsequently imported into the LabView code.

4.2.1 Coordinates Registration

The haptic integration is enabled by using a smartphone and transferring the hand-written features written on the screen to the printing platform. To enable the registration of the haptic movements on the screen, and its eventual translation into the coordinate space, a mobile app was built on the Android Studio platform using Java, and it is compatible with all Android OS phones and tablets.

Figure 4.1a shows the screenshot of the application interface wherein the movements within the white space are registered and converted to coordinates. Figure 4.1b shows a flow chart of the algorithm for registering and populating the coordinate and shutter matrix based on the hand-drawn pattern and touch event, respectively. In order to provide vector coordinates that are compatible with our bubble printing, the app initializes, updates, and keeps track of three arraylist variables: x_coordinates, y_coordinates, and IO. We utilize Android's built-in coordinate system as well as built-in event.getX() and event.getY() methods to populate the x and y arraylists with Float coordinates as the user

is drawing. The IO arraylist is populated simultaneously with 0 and 1. 1 indicates that the laser beam should be turned on, and 0 to indicate that it should be turned off. Before the arraylists are saved, the first coordinates entered (X_i,Y_i) - the first coordinates touched in the drawing - are subtracted from each x and y coordinate respectively to make (X_i,Y_i) the origin of our pattern. Upon saving a finished pattern, the three arraylists are saved into an XLS Excel file and uploaded to the computer. The excel file is constructed of three columns: x_coordinates, y_coordinates, and IO. These are input into the custom written LabView code to perform the printing.

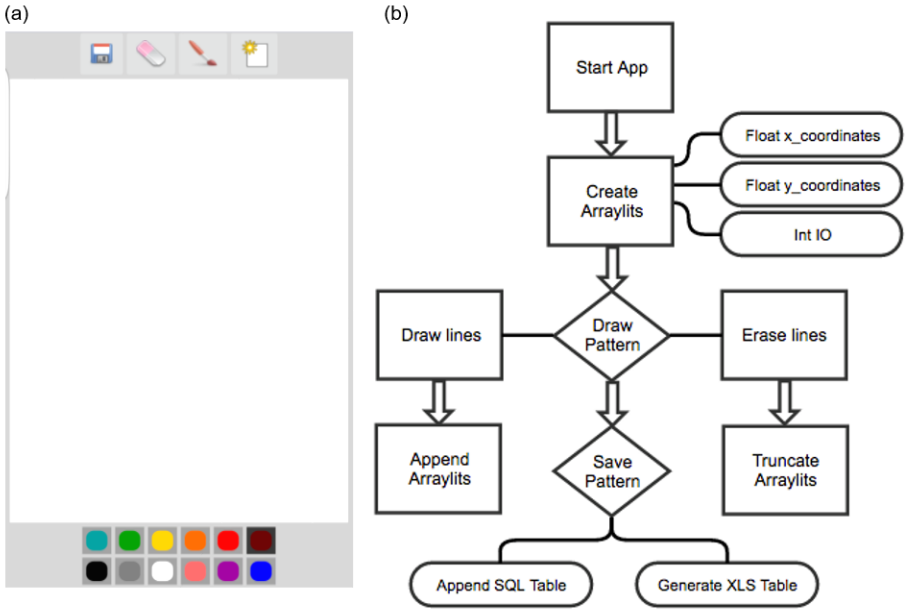

Figure 4.1: (a) A schematic of the draw-view of the app showing the various buttons such as save, undo, and the new file. (b) A flow chart of the algorithm for registering and populating the coordinate and shutter matrix.

4.2.2 Haptic-Interfaced Printing

Figure 4.2a illustrates that HIBP process to pattern QDs from an aqueous solution, onto the plasmonic substrate. A laser beam focused with a 100× oil objective is used to print the QDs over a plasmonic substrate, which is positioned on an automated stage

(Figure 4.2b). To enable the haptic operation of the bubble printing, we utilize a smartphone app and define the desired hand-drawn patterns over the display. The app-registered data are transferred to the custom-written LabView code to direct the printing process.

The capture and immobilization of the QDs benefit from the plasmon-enhanced photothermal response of the AuNI substrate.[20, 22] Briefly, upon incidence of a continuous wave laser beam (532 nm) on the AuNI substrate, the reemitted energy from the resonant AuNI via non-radiative Landau damping leads to the overheating of the water molecules to generate mesobubbles over the substrate surface. The Marangoni convection arising from the temperature gradient creates a convective drag force towards the bubble surface. The QDs are subsequently trapped via the multi-force balance of vapor-liquid pressure difference, drag force, and surface tension, and eventually immobilized on the substrate due to Van der Waals interaction and thermal adhesion.

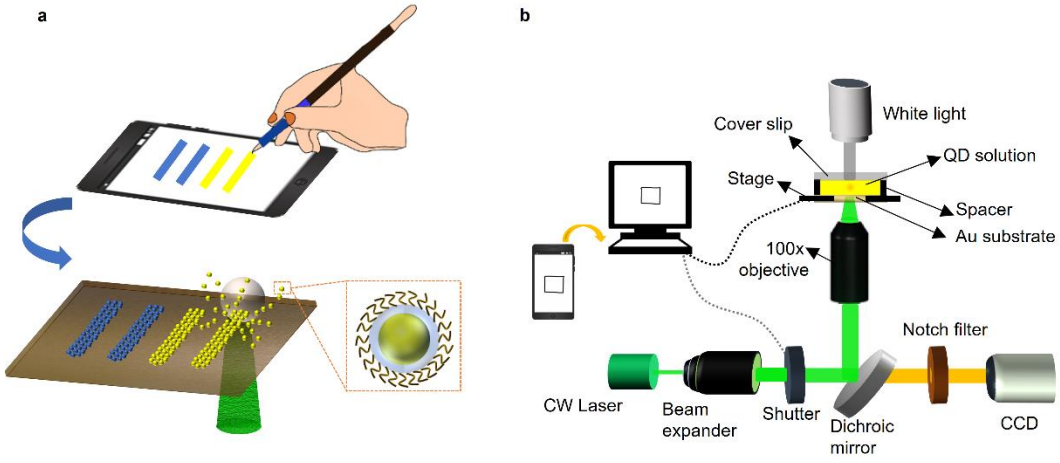

Figure 4.2: Haptic-interfaced bubble printing: (a) Illustration of haptic-interfaced bubble printing (HIBP). QDs in a single aqueous suspension can be immobilized on the substrate to exhibit variable emission wavelengths based on the hand movement over the smartphone screen, which in turn is replicated in the printing process. The bottom inset shows a magnified view of the CdSe/CdS QD along with an amphiphilic coating of PMAO-PEG. (b) Schematic of the experimental setup for the haptic-interfaced bubble printing.

4.3 COORDINATE SCALING

Figure 4.3a shows an inward spiral pattern of red QDs fabricated by the HIBP strategy. The coordinates registered on the screen were scaled down× to realize the printed spiral which has an overall dimension of ~30 μm and sub-micron line-width. We can further optimize the scaling when translating the pattern from the smartphone coordinate system based on its resolution (2560 × 1440) to the actual print coordinates (in μm).

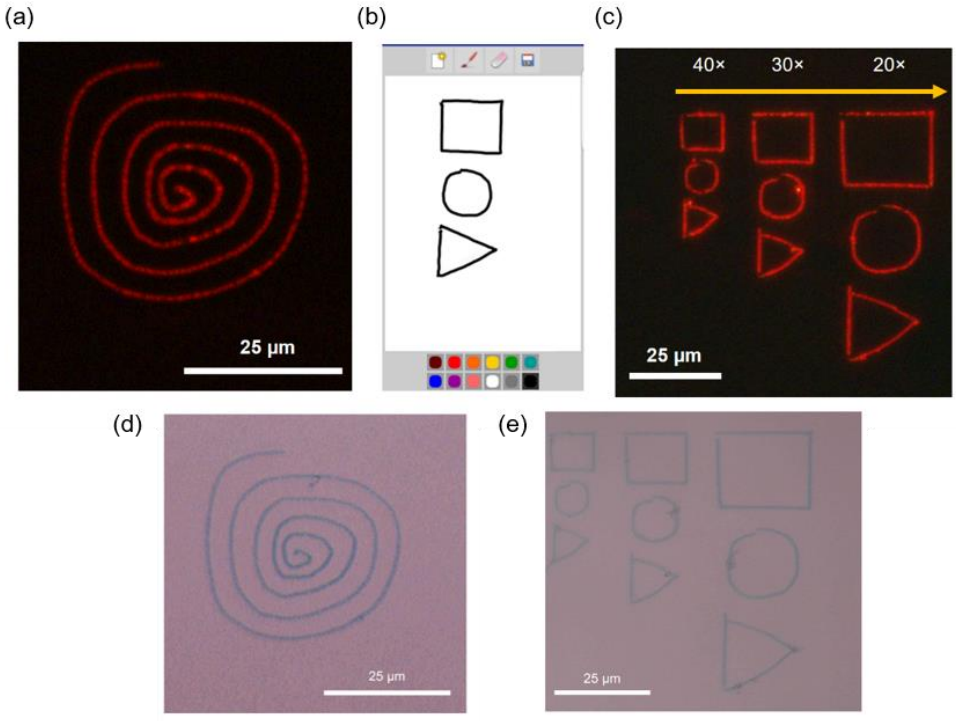

Figure 4.3: Haptic printing and pattern scalability: (a) A hand-drawn spiral pattern over the smartphone is printed using red QDs on a plasmonic substrate. The fluorescence image of the spiral under the Tetramethylrhodamine (TRITC) channel is shown. (b) A snapshot of the basic shapes drawn on the smartphone screen. (c) HIBP of the pattern in (b) using red QDs at the different downscaling factors. (d-e) Bright-field optical images of the patterns of QDs on plasmonic substrates by HIBP.

The sub-micron resolution of HIBP enables us to control the dimensions of the printed QDs over a large range from a few micrometers to tens of micrometers. Based on the shapes hand-drawn over the smartphone (Figure 4.3b) and the scaling factors ranging

from 20× to 40×, we replicate the patterns of red QDs with different dimensions from 35 µm × 12 µm to 68 µm × 25 µm. The higher downscaling factors lead to smaller dimensions. The scalability of the pattern dimensions is useful for many applications such as multi-sensor integration with each sensor fabricated at a different dimension for enhanced performance.[23] The bright-field images of the QD patterns are shown in Figure 4.3d-e.

4.4 Quantum Dot Fluorescence Tuning

Based on the interaction of the QDs with the bubble, we further exploited the BP process to modify the fluorescence characteristics of the patterned QDs on the plasmonic substrates. A Zeiss LSM 710 microscope was used for wide-field fluorescence imaging. The imaging was performed with a 405 nm excitation source and without any emission filters. The composite images were generated via wavelength-dependent coloring feature in the Zeiss ZEN software.

As shown in Figure 4.4a, the originally yellow QDs that were bubble-printed into square structures (20 µm×20 µm) via raster scanning exhibited the variable fluorescence from different BP parameters. From square 1 to square 4, the laser exposure time over QDs increases and the fluorescence wavelength makes a continuous blue shift. The higher incident laser power in conjunction with longer exposure time results in the photon-induced oxidation of the patterned QDs, which causes a spectral shift to shorter wavelengths.[24-25] The formation of the oxide layer reduces the effective diameter of the QDs, thereby increasing the quantum confinement and the bandgap energy. The oxidation effect is evident in the spectrum of square 2 wherein a small shoulder starts appearing at ~525 nm. In this work, the peak wavelength of the patterned QDs can be modified from 591 nm to 475 nm. The continued oxidation also caused the spectrum to broaden (square 4) (Figure 4.4b).[25] A relative decrease in the intensity of the QDs is observed with a progressive blue-

shift. However, it is worth noting that the relative PL intensities do not provide a true metric since the absorbance of the blue *vs.* yellow QDs vastly differs, with the blue QDs expected to have much lower absorbance.[26] In addition, the concentration of QDs among the various squares isn't the same.

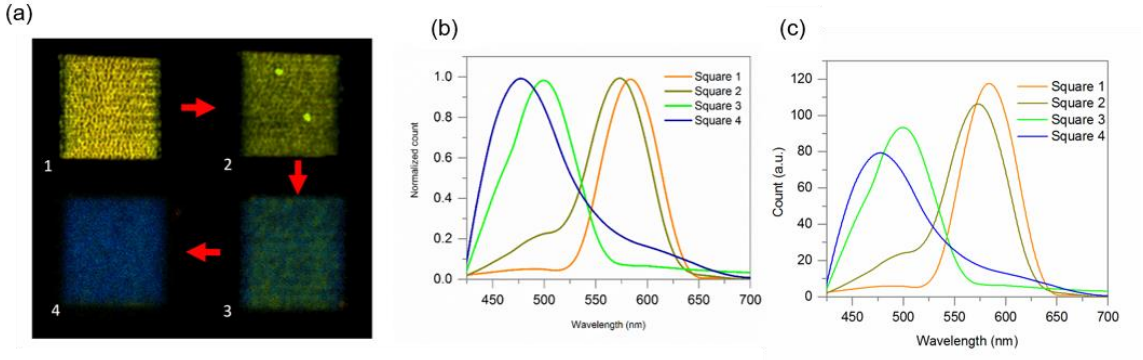

Figure 4.4: Modification of fluorescence wavelengths and dynamics of patterned QDs: (a) Merged fluorescence image of yellow QDs patterned in four squares by variable BP parameters. The optical power, stage-translation speed, waiting time between the neighbouring lines, and line-spacing for the squares 1-4: (i) 0.52 mW/μm^2, 1000 μm/s, 500 ms, and 1 μm, (ii) 0.54 mW/μm^2, 500 μm/s, 600 ms, and 1 μm, (iii) 0.56 mW/μm^2, 100 μm/s, 800 ms, and 1 μm (iv) 0.58 mW/μm^2, 100 μm/s, 1 s, and 0.5 μm. Scale bar: 10 μm. (b) Fluorescence spectra from the four squares in a. (c) The relative intensity plots of the patterns fabricated in (a).

To provide guidance on fluorescence tuning of QDs in case of HIBP, we perform systematic investigation and have shown that the bubble-printing process and the properties of the resulted QD patterns primarily depend on the interplay of three parameters: (i) stage translation speed, (ii) stage hold time, and (iii) line spacing in the patterns. We have systematically studied the influences of stage translation speed and line spacing on the fluorescence properties of yellow QDs patterned on the plasmonic substrate. As shown in Figure 4.5a, three patterns consisting of parallel lines with gradually decreased line space from 4 μm to 0.5 μm were fabricated at stage speeds of 1 μm/s, 6 μm/s and 10^4 μm/s (the highest speed), respectively. The printed QDs can achieve sub-micron line-widths, as low

as 510nm (Figure 4.5b). From the fluorescence images in Figure 4.5a, we can see that the emission of QDs makes a shift from originally yellow to a blue color with the decreased stage speed and line spacing. The QDs printed with the lowest stage speed (1 μm/s) exhibit blue emission irrespective of the line space. At an intermediate stage speed of 6 μm/s, the effect of line spacing on the fluorescence wavelength is evident, with the blue emission occurring at the lowest space of 0.5 μm.

We attribute the spectral shifts to the oxidation of QDs during the bubble printing. Due to the resonant heating upon the laser irradiation, the temperature at the plasmonic nanoparticle surfaces can reach >100℃.[20] Such elevated temperatures can lead to the photo-oxidation of the printed QDs, which reduces the effective size of the QDs and thus causes a spectral blue-shift.[27] The rapid photo-oxidation process can limit the introduction of multiple non-radiative states on the QD surfaces, minimizing the influence on the quantum yield and brightness of the QDs.[27] The bubble printing at the lowest stage speed (1μm/s) has the maximum laser-heating effect and the photo-oxidation is sufficient to have the QDs emit blue light irrespective of the line space. For the bubble printing at an intermediate stage speed of 6 μm/s, the blue emission occurs at the lowest space of 0.5 μm because the elongated laser exposure resulting from double scanning increases the photo-oxidation of the QDs. With the higher stage speeds, the exposure time of the printed QDs to the laser heating isn't long enough to cause significant photo-oxidation. Figure 4.5c shows a contour plot of the ratio of the peak intensities for the blue (450-495 nm) and yellow (560-595 nm) light as a function of stage speed and line spacing. We can see that fine tuning of the emission color of the printed QDs is possible by controlling the stage speed and line spacing.

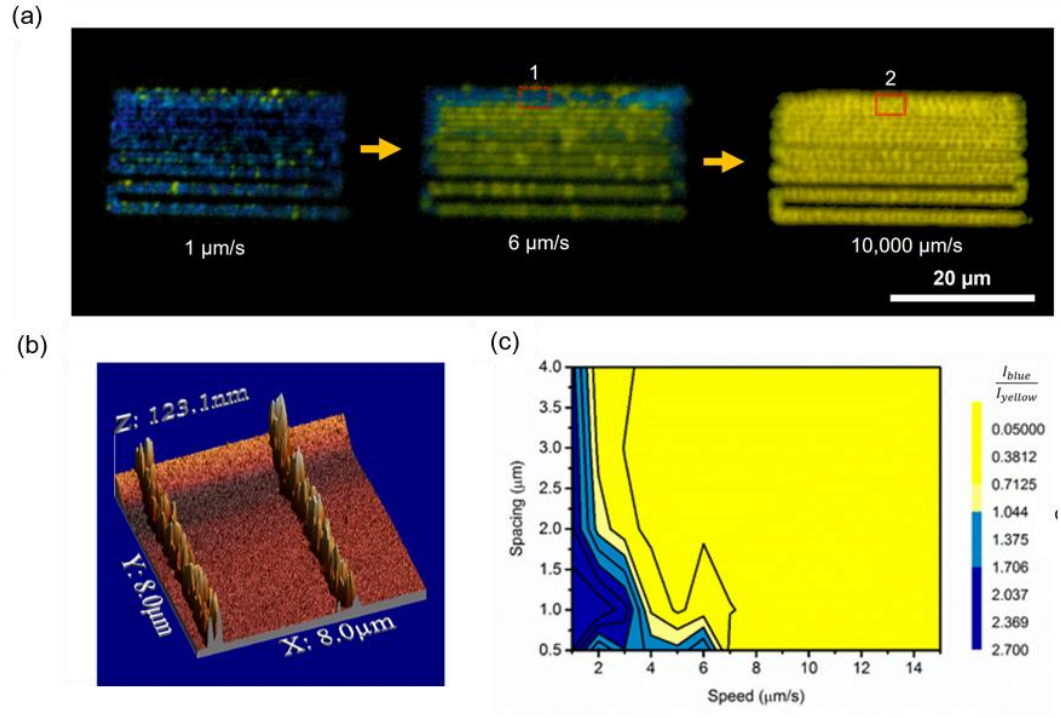

Figure 4.5: (a) Merged fluorescence images of patterns of yellow QDs printed with the various stage speeds and line spacing. For each pattern, the line spacing decreases from 4 µm to 0.5 µm (from bottom to top). The blue shifts occur at the lower stage speeds and the smaller line spacing. (b) Atomic force micrograph of the QDs printed at 10,000 µm/s. The image depicts a line-width of ~510 nm. (c) A contour plot of the ratio of the peak intensities for the blue (450-495 nm) and yellow (560-595 nm) light as a function of stage speed and line spacing.

4.5 PLASMON-QUANTUM DOT INTERACTIONS

The use of plasmonic substrates in BP provides another opportunity to modify the optical properties of patterned QDs. To investigate the dynamics of the interactions between the QD excitons and the plasmons at the substrates, we applied time-resolved fluorescence measurements to characterize spontaneous emission rates of QDs at the variable conditions.

The fluorescence lifetime imaging microscopy (FLIM) of the QDs was done via time-correlated single photon counting (TCSPC) technique. Figure 4.6 shows the optical

setup comprising a femtosecond Titanium:Sapphire laser modified to 800 nm (~200 fs) (Mira 900, Coherent), galvo scanning mirrors (6215H, Cambridge Tech.), and a GaAsP photomultiplier tube (PMT) (H7422PA-40, Hamamatsu) in non-descanned detection scheme. The output current of the PMT was amplified using a preamplifier with 2 GHz cutoff (HFAC- 26, Becker and Hickl GmbH). The amplified pulses from the PMTs were sent to the TCSPC module (SPC-150, Becker and Hickl GmbH). The objective was a silicone oil-immersion lens with NA of 1.3 (UPLSAPO60X, Olympus).

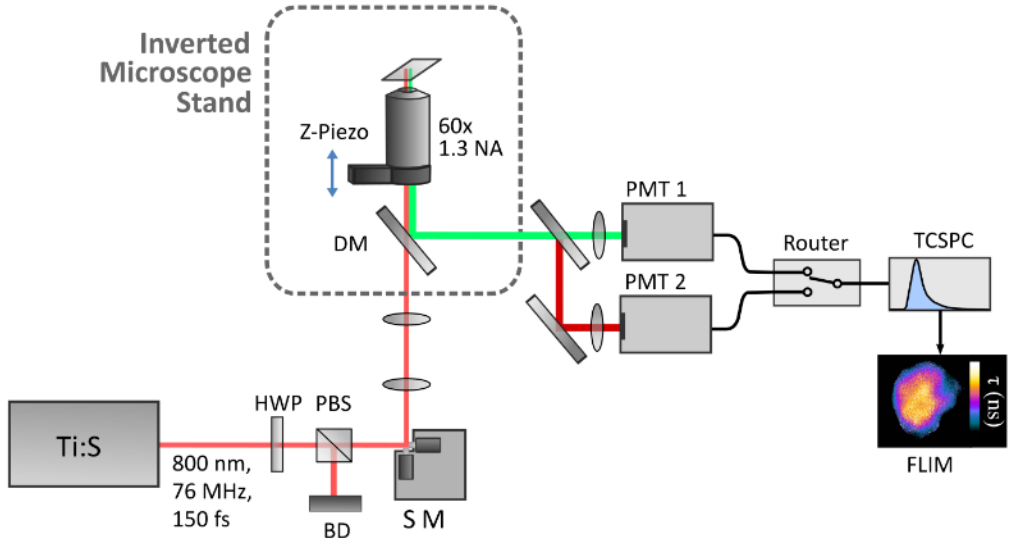

Figure 4.6: Schematic of the optical setup for fluorescence-lifetime imaging microscopy (FLIM). PBS: Polarizing beam splitter, BD: Beam dump, SM: Scanning mirrors, DM: Dichroic mirror, PMT: Photomultiplier tube, and TCPSC: Time-correlated single-photon counting.

Using an average laser power of 1 mW, fluorescence lifetimes were recorded with a 20 ps time resolution and a pixel integration time of 5 ms. The lifetime fitting was done with the least-squares method using a model of a single exponential decay convolved with a Gaussian impulse function. The resultant lifetime image was threshold-based on intensity to remove the background signals from the plasmonic substrate. In order to ensure a high

fitting quality, data points with less than 500 photons were removed from the fitting and the fittings with a χ^2 value less than 2 were discarded.

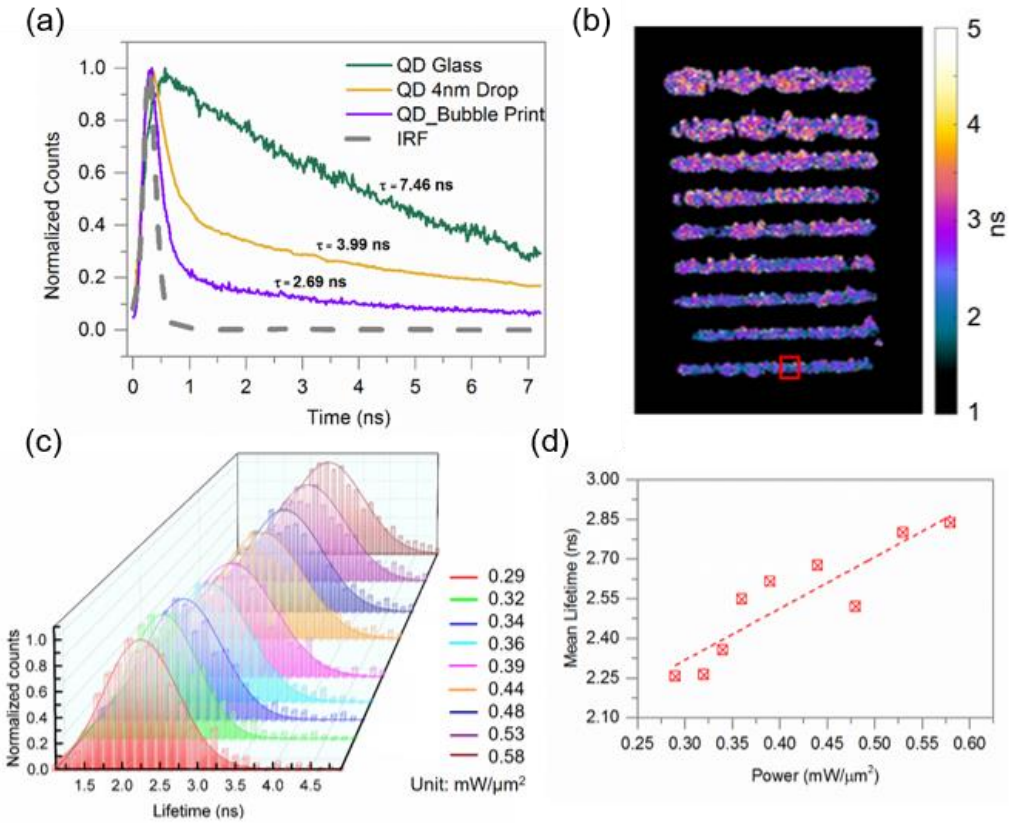

Figure 4.7: (a) Time-correlated fluorescence of red QDs (i) drop-casted on the glass, (ii) drop-casted on the plasmonic substrate, and (iii) bubble-printed on the plasmonic substrate. The lifetime decreases from 7.46 ns (QDs on glass) to 2.69 ns (QDs printed on the plasmonic substrate). (b) FLIM image of the patterned QDs with increasing power. (c) Fluorescence-lifetime modification by tuning the optical power in BP. (d) The plot of the mean lifetime vs optical power in BP. The mean lifetime increases from 2.26 ns to 2.84 ns with an increase of optical power in BP.

To study the interactions between the QD excitons and the plasmons at the substrates, we fabricated QDs at various printing conditions and characterized them using FLIM, as shown in Figure 4.7a. A femtosecond Titanium:Sapphire laser (800 nm) was used for two-photon excitation of the QDs[28]. The average laser power was 1 mW corresponding

to a relatively low fluence of 7×10^{10} W/cm^2 at the focal point. The shortening of the lifetime of QDs drop-casted on the plasmonic substrates (compared to QDs on glass substrates) can be ascribed to the Purcell effect arising from the plasmonic effects.[29] A further reduction in the average lifetime to $\tau_{BP\text{-}Au}$=2.69±0.29 ns is observed upon BP of QDs over the plasmonic substrates, which is attributed to the reduced QD-substrate separation due to flow-induced bombardment effect and laser-induced ligand shortening along with QD oxidation.[4, 30]

We further studied the influence of the printing conditions on the emission rate of the patterned QDs. Straight lines of QDs were printed with increased incident laser intensity from 0.29 mW/μm^2 to 0.58 mW/μm^2. The FLIM images were collected by scanning the probing laser beam over the sample area (Figure 4.7b). Figure 4.7c shows a histogram of the lifetimes obtained from each line fabricated at various optical power intensities along with the Gaussian fitting of the lifetime distribution. The lifetime distribution for each power is statistically significant with ~1000 pixels analyzed for each dataset (Figure 4.7c). The mean lifetime of the printed patterns increases from 2.26 ns at 0.29 mW/μm^2 to 2.84 ns at the maximum power intensity of 0.58 mW/ μm^2 (Figure 4.7d). The lifetime increase is due to the larger average-separation between QDs and the substrate when the optical power increases the over-stacking of the QDs. Further, the lifetime distribution broadens at the higher power due to the higher thickness variations in the lines of QDs. The mean-lifetime modification capability will find applications as an encoding scheme to produce distinguishable optical codes and to study biological processes.[31]

4.6 HAPTIC-INTERFACED TUNING OF PLASMON-QD INTERACTION

Following the establishment of the processing-structure-property relationship for the patterned QDs by bubble printing, we move on to demonstrate the fluorescence tuning

of the printed QDs with the haptic operation. The number of coordinates in the matrix is populated based on the speed of the hand movement over the smartphone display.

Figure 4.8a shows that the coordinate density is increased from 0.2 coordinate/μm to 10 coordinates/μm when the speed of the hand movement is decreased. The increase in the coordinate density is manifested as a decrease in the printing speed since the stage has an inherent hold time at each coordinate. Therefore, blue emission is observed from the QDs patterned at a coordinate density > 7 coordinates/μm, which leads to an effective stage speed of < 3 μm/s (Figure 4.8b). This observation is consistent with the contour plot in Figure 4.5c. Figure 4.8c shows the corresponding fluorescence spectra for the lines of QDs in Figure 4.8b. There is initially a minimal blue shift in the peak wavelength, followed by prominent blue shift for the three slowest hand-written lines. In addition, the spectrum broadens at the slower hand movement due to the continued photo-oxidation.[25]

We further combine hand movement speed with line spacing in the hand-drawn patterns to tune the QD fluorescence. Figure 4.8d shows the coordinates with a simultaneous decrease in the hand movement speed and line spacing upon moving away from the origin along the y-axis. From the fluorescence image in Figure 4.8e, we can see that blue emission starts to appear at the slower movement speed. With a reduced line spacing that leads to a double exposure of the QDs to the laser beam, the blue emission is observed at a relatively lower coordinate density of 4 coordinates/μm (compared to > 7 coordinates/μm in Figure 4.8b). The blue shift is also evidenced by the fluorescence spectra (Figure 4.8f) taken at the various locations in the QD pattern. Thus, we can pattern the QDs and tune their site-specific emission properties at the sub-microscale level by simply controlling hand movement over the smartphone display.

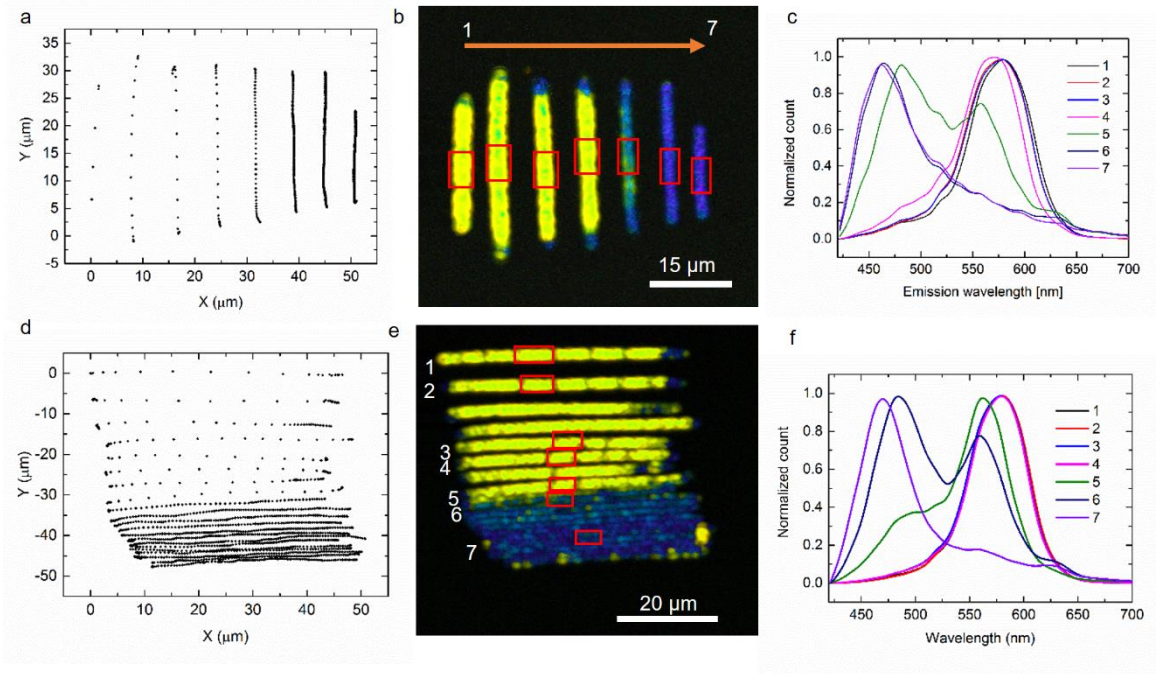

Figure 4.8. (a) The registered coordinates from the smartphone based on hand-drawn lines with the decreased hand movement speed (from left to right). (b) Fluorescence image of the corresponding patterns of yellow QDs by HIBP based on the hand-drawn lines in (a). Blue emission occurs to the printed QDs at the slower hand movement. (c) Fluorescence spectra of the corresponding marked regions on the lines of QDs in (b). (d) The registered coordinates from the smartphone based on hand-drawn patterns combining the variations of hand movement speed and line spacing. (e) Fluorescence image of the corresponding patterns of yellow QDs by HIBP based on the hand-drawn lines in (d). (f) Fluorescence spectra recorded from the marked regions in (e). The rectangles in (b) and (e) indicate the regions from which the fluorescence spectra are recorded. The numbers in (b) and (e) correspond to those in (c) and (f), respectively.

4.7 SUMMARY

We have developed and applied HIBP to achieve the versatile patterning of QDs on the plasmonic substrates. An Android app was utilized as a platform to register haptic movements as coordinates and to direct the printing process in a free form. HIBP has achieved the high printing speed (>10^4 μm/s), high resolution (~510 nm) and high pattern scalability, as well as the ability to simultaneously tune the fluorescence properties of the

printed QDs. The tuning of fluorescence wavelength and lifetime of the QDs is through controlling the plasmonic and photothermal effects in the case of conventional bubble printing as well as via HIBP. HIBP was readily applied to pattern other types of colloidal particles. By providing a highly accessible tool to manipulate matter at the nanoscale, HIBP can significantly advance research and education in nanoscience and nanotechnology.

4.8 REFERENCES

1. Li, X. Q.; Wu, Y. W.; Steel, D.; Gammon, D.; Stievater, T. H.; Katzer, D. S.; Park, D.; Piermarocchi, C.; Sham, L. J., An all-optical quantum gate in a semiconductor quantum dot. *Science* **2003,** *301* (5634), 809-811.
2. Vanmaekelbergh, D.; Liljeroth, P., Electron-conducting quantum dot solids: novel materials based on colloidal semiconductor nanocrystals. *Chem. Soc. Rev.* **2005,** *34* (4), 299-312.
3. Kim, J. Y.; Voznyy, O.; Zhitomirsky, D.; Sargent, E. H., 25th Anniversary Article: Colloidal Quantum Dot Materials and Devices: A Quarter-Century of Advances. *Adv. Mater.* **2013,** *25* (36), 4986-5010.
4. Pietryga, J. M.; Park, Y. S.; Lim, J. H.; Fidler, A. F.; Bae, W. K.; Brovelli, S.; Klimov, V. I., Spectroscopic and Device Aspects of Nanocrystal Quantum Dots. *Chem. Rev.* **2016,** *116* (18), 10513-10622.
5. Yin, Y. D.; Talapin, D., The chemistry of functional nanomaterials. *Chem. Soc. Rev.* **2013,** *42* (7), 2484-2487.
6. Yu, W. W.; Peng, X. G., Formation of high-quality CdS and other II-VI semiconductor nanocrystals in noncoordinating solvents: Tunable reactivity of monomers. *Angew. Chem. Int. Edit.* **2002,** *41* (13), 2368-2371.
7. Cassette, E.; Helle, M.; Bezdetnaya, L.; Marchal, F.; Dubertret, B.; Pons, T., Design of new quantum dot materials for deep tissue infrared imaging. *Adv. Drug Deliver. Rev.* **2013,** *65* (5), 719-731.
8. Mashford, B. S.; Stevenson, M.; Popovic, Z.; Hamilton, C.; Zhou, Z. Q.; Breen, C.; Steckel, J.; Bulovic, V.; Bawendi, M.; Coe-Sullivan, S.; Kazlas, P. T., High-efficiency quantum-dot light-emitting devices with enhanced charge injection. *Nat. Photon.* **2013,** *7* (5), 407-412.
9. Kim, T. H.; Cho, K. S.; Lee, E. K.; Lee, S. J.; Chae, J.; Kim, J. W.; Kim, D. H.; Kwon, J. Y.; Amaratunga, G.; Lee, S. Y.; Choi, B. L.; Kuk, Y.; Kim, J. M.; Kim, K., Full-colour quantum dot displays fabricated by transfer printing. *Nat. Photon.* **2011,** *5* (3), 176-182.

10. Lan, X. Z.; Masala, S.; Sargent, E. H., Charge-extraction strategies for colloidal quantum dot photovoltaics. *Nat. Mater.* **2014,** *13* (3), 233-240.

11. Medintz, I. L.; Clapp, A. R.; Mattoussi, H.; Goldman, E. R.; Fisher, B.; Mauro, J. M., Self-assembled nanoscale biosensors based on quantum dot FRET donors. *Nat. Mater.* **2003,** *2* (9), 630-638.

12. Lee, A. D.; Jiang, Q.; Tang, M. C.; Zhang, Y. Y.; Seeds, A. J.; Liu, H. Y., InAs/GaAs Quantum-Dot Lasers Monolithically Grown on Si, Ge, and Ge-on-Si Substrates. *IEEE J. Sel. Topics Quantum Electon.* **2013,** *19* (4), 19001107.

13. Konstantatos, G.; Howard, I.; Fischer, A.; Hoogland, S.; Clifford, J.; Klem, E.; Levina, L.; Sargent, E. H., Ultrasensitive solution-cast quantum dot photodetectors. *Nature* **2006,** *442* (7099), 180-183.

14. Sapsford, K. E.; Pons, T.; Medintz, I. L.; Mattoussi, H., Biosensing with luminescent semiconductor quantum dots. *Sensors-Basel* **2006,** *6* (8), 925-953.

15. Zhang, L.; Chen, C.; Li, W. J.; Gao, G. H.; Gong, P.; Cai, L. T., Living Cell Multilifetime Encoding Based on Lifetime-Tunable Lattice Strained Quantum Dots. *ACS Appl. Mater. Inter.* **2016,** *8* (21), 13187-13191.

16. Chen, J. X.; Chan, Y. H.; Yang, T. L.; Wark, S. E.; Son, D. H.; Batteas, J. D., Spatially Selective Optical Tuning of Quantum Dot Thin Film Luminescence. *J. Am. Chem. Soc.* **2009,** *131* (51), 18204-18205.

17. Singh, M.; Haverinen, H. M.; Dhagat, P.; Jabbour, G. E., Inkjet Printing-Process and Its Applications. *Adv. Mater.* **2010,** *22* (6), 673-685.

18. Castrejon-Pita, J. R.; Baxter, W. R. S.; Morgan, J.; Temple, S.; Martin, G. D.; Hutchings, I. M., Future, Opportunities and Challenges of Inkjet Technologies. *At. Spray* **2013,** *23* (6), 541-565.

19. Medintz, I. L.; Uyeda, H. T.; Goldman, E. R.; Mattoussi, H., Quantum dot bioconjugates for imaging, labelling and sensing. *Nat. Mater.* **2005,** *4* (6), 435-446.

20. Lin, L. H.; Peng, X. L.; Mao, Z. M.; Li, W.; Yogeesh, M. N.; Rajeeva, B. B.; Perillo, E. P.; Dunn, A. K.; Akinwande, D.; Zheng, Y. B., Bubble-Pen Lithography. *Nano Lett.* **2016,** *16* (1), 701-708.

21. Sun, J.; Liu, Y.; Ritchie, J. M.; Luo, X., A haptic digital tool to assist the design, planning and manufacture of micro- and nanostructures. *Proc. Inst. Mech. Eng. E J. Process Mech. Eng.* **2015,** *229* (4), 290-298.

22. Baffou, G.; Polleux, J.; Rigneault, H.; Monneret, S., Super-Heating and Micro-Bubble Generation around Plasmonic Nanoparticles under cw Illumination. *J. Phys. Chem. C.* **2014,** *118* (9), 4890-4898.

23. Pang, C.; Zhao, Z.; Zhang, J. G.; Shi, L.; Du, L. D.; Fang, Z.; Liu, Y. H., An Advantageous Fabrication Technology to Integrate Pressure Sensor into Multi-

sensor for Micro Weather Station. *2009 4th IEEE International Conference on Nano/Micro Engineered and Molecular Systems, Vols 1 and 2* **2009**, 270-273.

24. Kimura, J.; Uematsu, T.; Maenosono, S.; Yamaguchi, Y., Photoinduced fluorescence enhancement in CdSe/ZnS quantum dot submonolayers sandwiched between insulating layers: Influence of dot proximity. *J. Phys. Chem. B.* **2004,** *108* (35), 13258-13264.

25. Shcherbatyuk, G. V.; Inman, R. H.; Ghosh, S., Anomalous photo-induced spectral changes in CdSe/ZnS quantum dots. *J. Appl. Phys.* **2011,** *110* (5), 053518.

26. Dabbousi, B. O.; RodriguezViejo, J.; Mikulec, F. V.; Heine, J. R.; Mattoussi, H.; Ober, R.; Jensen, K. F.; Bawendi, M. G., (CdSe)ZnS core-shell quantum dots: Synthesis and characterization of a size series of highly luminescent nanocrystallites. *J. Phys. Chem. B.* **1997,** *101* (46), 9463-9475.

27. Wang, X. Y.; Zhang, J. Y.; Nazzal, A.; Xiao, M., Photo-oxidation-enhanced coupling in densely packed CdSe quantum-dot films. *Appl. Phys. Lett.* **2003,** *83* (1), 162-164.

28. Rajeeva, B. B.; Hernandez, D. S.; Wang, M. S.; Perillo, E.; Lin, L. H.; Scarabelli, L.; Pingali, B.; Liz-Marzan, L. M.; Dunn, A. K.; Shear, J. B.; Zheng, Y. B., Regioselective Localization and Tracking of Biomolecules on Single Gold Nanoparticles. *Adv. Sci.* **2015,** *2* (11), 1500232.

29. Hoang, T. B.; Akselrod, G. M.; Argyropoulos, C.; Huang, J. N.; Smith, D. R.; Mikkelsen, M. H., Ultrafast spontaneous emission source using plasmonic nanoantennas. *Nat. Commun.* **2015,** *6*, 7788.

30. Chen, J. X.; Chan, Y. H.; Yang, T. L.; Wark, S. E.; Son, D. H.; Batteas, J. D., Spatially Selective Optical Tuning of Quantum Dot Thin Film Luminescence. *J. Am. Chem. Soc.* **2009,** *131* (51), 18204-18205.

31. Zhang, L.; Chen, C.; Li, W.; Gao, G.; Gong, P.; Cai, L., Living Cell Multilifetime Encoding Based on Lifetime-Tunable Lattice-Strained Quantum Dots. *ACS Appl. Mater. Inter.* **2016,** *8* (21), 13187-13191.

Chapter 5: "Point-and-Shoot" Synthesis and Applications of Metallic Ring Arrays*

5.1 INTRODUCTION

Advancements in the fields of plasmonics and metamaterials have enabled exploration of variable materials, architectures and fabrication protocols to achieve multifunctional substrates for surface-enhanced optical spectroscopies.[1] Metallic rings are actively explored due to their unique optical, electrical and magnetic properties.[2-4] The metallic ring morphology presents high symmetry and surface area. At the excitation of surface plasmons, the uniformly enhanced electric field exists inside the circular cavity, which benefits biosensors,[5-9] metamaterials,[10-11] surface-enhanced optical spectroscopies,[12-13] and other optical applications.[14-15] Further integration of the plasmonic structures with microfluidics can enable multiple applications such as microreactors and point-of-care devices.[16-17]

Several approaches such as colloidal templating and self-assembly have been applied to fabricate metallic ring-shaped architectures.[18-20] Colloidal templating usually consists of multiple steps, including colloidal particle assembly, polishing, metal deposition, and selective etching.[21] Scherer and co-workers reported self-organized nanorings arrays based on colloidal silica spheres.[20] In contrast to the template-based techniques, the direct-write process could enable real-time structural configurability, minimal material wastage, and multi-component integration.[22] However, the dominant direct-writing-based approaches such as electron beam lithography[23-24] and femtosecond laser writing technique[25] still require multi-step processes, which involve resist patterning,

*Rajeeva, B. B., Wu, Z., Briggs, A., Acharya, P. V., Walker, B. S., Peng, X., Bahadur, V., Bank, S., Zheng, Y. B. "Point-and-Shoot" Synthesis of Metallic Ring Arrays and Surface-Enhanced Optical Spectroscopy. Advanced Optical Materials, 2018,6, 1701213.
Rajeeva, B. B. carried out the experimental work and participated in the preparation of manuscript.

metal deposition and selective etching, to achieve the metallic rings. The multi-step processes hinder the *in-situ* ring fabrication within the microfluidic channels. Laser-writing with a precursor ink is a viable strategy to exploit the full advantages of a direct-writing process for *in-situ* fabrication under various spatial constraints.[26] However, existing strategies for *in-situ* synthesis in microfluidic channels have limited control over the structural integrity and morphology of the fabricated micro/nanostructures.

In this chapter, we report a simple "point-and-shoot" technique for single-step site-specific fabrication of Ag rings to realize multi-responsive plasmonic substrates for surface-enhanced optical spectroscopies. The technique involves direct synthesis and immobilization of Ag rings over an Au nanoisland (AuNI) substrate from an Ag precursor ink using a laser-generated microbubble. By using the low-temperature reducible Ag ink and controlling the laser-induced microbubble growth via highly-localized optothermal effects, we realize optically active Ag rings with tunable diameters between 1 and 2 μm. The ring morphology is defined by the immobilization of thermally reduced Ag from the precursor along the bubble/water interface. Analytical modeling of the immobilization process demonstrates the dynamics of Ag post-nucleation, eventually leading to the formation of the ring structures. We show that the tunable mid-IR and visible responses arise from the Ag rings and the underlying AuNIs. We employ the multi-responsive ring-AuNI substrate to sequentially perform surface-enhanced infrared spectroscopy (SEIRS) of 2, 4, 6 – trinitrotoluene (TNT) and surface-enhanced Raman spectroscopy (SERS) of rhodamine 6G (R6G) and crystal violet (CV). The above analytes are used as model molecules to establish the multi-mode response of the substrate. Furthermore, we demonstrate the *in-situ* fabrication of Ag rings with a versatile structural and optical control for "point-and-shoot" surface-enhanced optical spectroscopy within a single microfluidic channel.

5.2 PRINTING SETUP

Figure 5.1 depicts the working mechanism and the optical setup for the bubble-mediated Ag ring fabrication. The Ag precursor ink is positioned on the AuNI substrate consisting of a network of Au nanoparticles (NPs) with an average size of ~30 nm and an inter-particle distance of ~15 nm. Direct synthesis and immobilization of Ag structures on the substrate are achieved via photothermal effects of AuNIs upon the excitation of surface plasmons by a continuous-wave laser (532 nm).

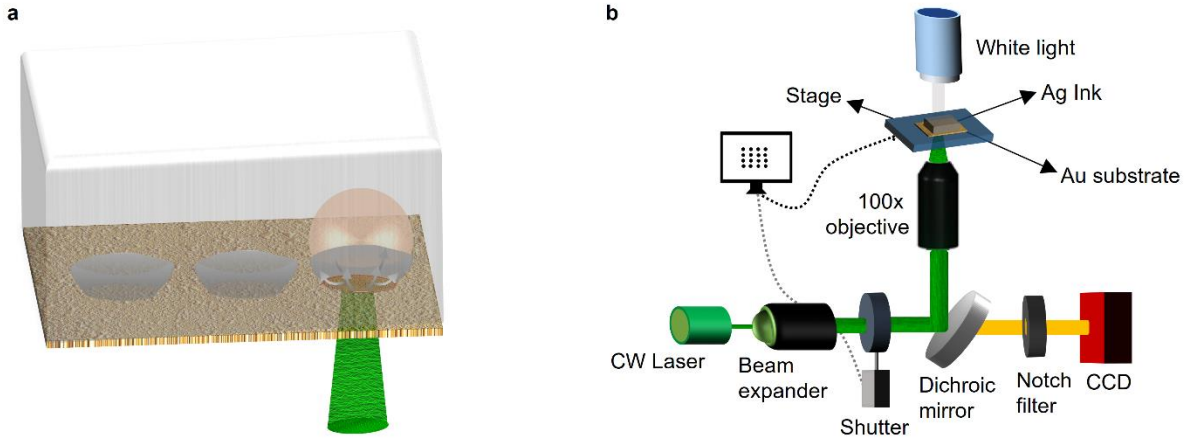

Figure 5.1: (a) Illustration of the bubble-mediated fabrication of Ag rings over the AuNI substrate. (b) Schematic of the optical setup comprising of the synchronized automated stage and optical shutter.

The laser beam focused on the AuNI substrate results in a highly localized temperature increase due to the non-radiative Landau damping of surface plasmons,[27] which generates a size-controllable microbubble.[28-30] The thermal gradient around the microbubble induces Marangoni convection, which concentrates the Ag^+ ions at the bubble surface and thermally reduces the ions into Ag NPs forming a ring-like structure.[31] Thus, the process can be divided into two regimes: (i) reduction and nucleation of Ag^+ ions into Ag NPs, and (ii) bubble growth dynamics leading to an Ag ring. The AuNI substrate is

placed on an automated stage synchronized with an optical shutter to achieve site-specific fabrication of the Ag rings.

5.3 Silver Ring Printing

The Ag precursor ink from Electroninks was prepared as per the previously reported procedure and procured directly from the company.[32] The solution contains diamminesilver (I) cations, acetate anions, and formate anions. At elevated temperatures, the ammonia ligands and the low-boiling-point reactants evaporate. Ag precursor ink has a very low precipitation temperature of ~85℃, which facilitates the simultaneous reduction and patterning of Ag structures on the AuNI substrate. At relatively lower laser power (<0.5 $mW/\mu m^2$), conventional photothermal heating at the AuNI substrate leads to continuous Ag lines with a power-dependent line-width (Figure 5.2a). The uniform hot-spot distribution at the AuNI substrate sustains a stable temperature increase over a large area, which leads to the consistent line-width of individual Ag lines.

Complex patterns such as gammadion arrays and inverted U-structure arrays with sub-micron line-width (~0.8 μm) were also fabricated with the direct-printing technique at the lower laser power (Figures 5.2b). With an increased power (>0.5 $mW/\mu m^2$), the laser beam generates microbubbles. The Ag precursor is thermally reduced and deposited along the bubble interfaces to form an Ag ring in a single step. By repeatedly generating isolated individual bubbles at pre-determined locations, we create an array of Ag rings on the substrate. To limit the growth of the bubble to create small rings of 1-2 μm in diameter, a short stage-waiting time of 350 ms is used at each location. It is worth noting that the high-density uniform particles and hot spots at the AuNI substrate enable the consistent fabrication of the uniform Ag rings. An Ag ring array (60 μm × 50 μm) with a 3 μm inter-

ring spacing along x and y directions was fabricated. As shown in Figures 5.2 (c-f), we can control ring sizes by the laser power.

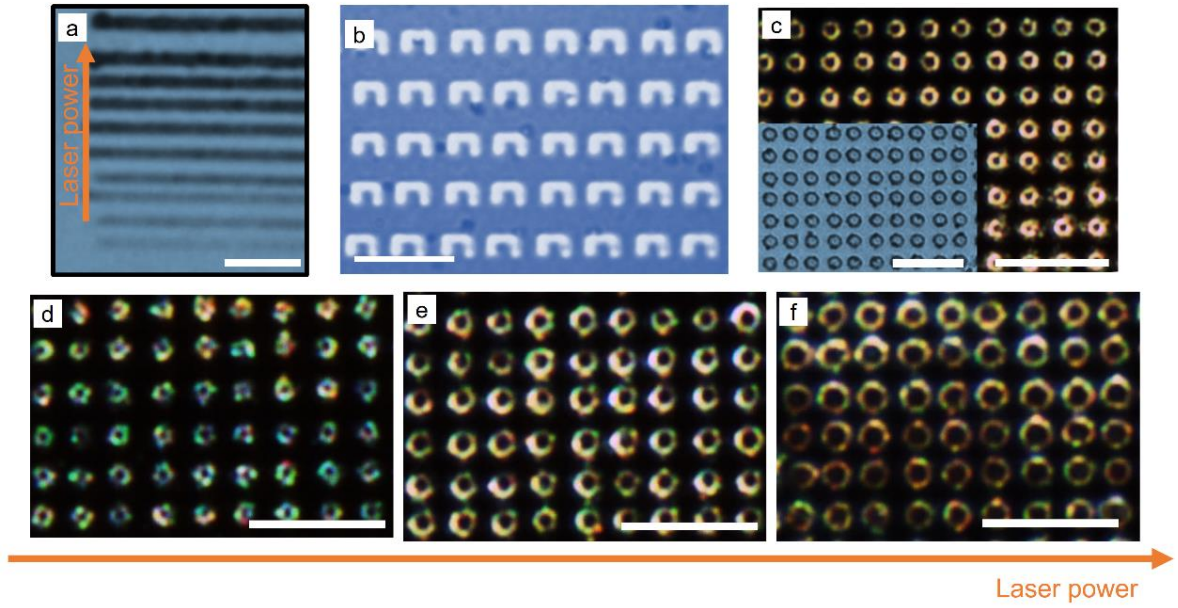

Figure 5.2: (a) Fabrication of Ag lines by a laser beam below the bubble-generation threshold power. The line-width increases when the laser power is increased from 0.2 mW/μm^2 to 0.5 mW/μm^2. The bubble is observable when the laser beam is at the end of the line. (b) Arrays of Ag inverted-U structures fabricated by a laser beam below the bubble-generation threshold power. (c) Dark-field optical image of an Ag ring array fabricated at a laser power of 0.75 mW/μm^2. The inset shows the bright-field optical image. (d-e) Dark-field optical images of arrays of Ag rings of variable sizes. The incident laser power is (d) 0.55 mW/μm^2, (e) 0.81 mW/μm^2, and (f) 0.95 mW/μm^2. The scale bar is 10 μm for all the panels.

5.3.1 Silver Ink Reduction

Precise control of Ag ring structures and optical responses relies on the ability to instantaneously nucleate and immobilize Ag NPs at high spatial resolution. However, a low viscosity (2 mPa·s) of the precursor Ag ink usually limits the printing resolution to several micrometers.[32] In our bubble-mediated printing, the plasmon-enhanced localized thermal field over the AuNI substrate confines the active reaction area at the sub-micron

scale to improve the resolution.[33] The bubble also concentrates the Ag^+ ions at the three-phase contact line via Marangoni convection. The ions are subsequently reduced to Ag according to equation (1).

$$[Ag(NH_3)_2]^+[C_2H_3O_2]^- \rightarrow Ag \qquad (1)$$

High temperature (>100 ℃) arises from the photothermal effects associated with the dense and uniform plasmonic hot spots at the AuNI substrate.[28] The high temperature and ion concentration lead to instantaneous (< 100 ms) nucleation of Ag. According to classical nucleation theory, the nucleation rate R is given by

$$R = N_s Z j e^{\frac{-\Delta G}{k_B T}} \qquad (2)$$

where N_s is the density of Ag^+ ions, Z is the Zeldovich factor, j is the rate at which molecules attach for the nucleus to grow, ΔG is the critical free energy of nucleation, k_B is the Boltzmann constant and T is the absolute temperature. With the reaction primarily confined to the three-phase contact line, the free energy change for the heterogeneous nucleation is given by[34]

$$\Delta G_{hetero} = \Delta G f(\theta) \qquad (3)$$

$$f(\theta) = \frac{1}{2} - \frac{3}{4}cos\theta + \frac{1}{4}cos^3\theta \qquad (4)$$

where θ is the contact angle. The reduced free energy barrier at the heterogeneous bubble/substrate interface leads to the faster nucleation. The higher ion concentration at the interface reduces the critical nucleus radius, leading to the higher-resolution Ag structures.[34]

5.3.2 Mechanism for Ring Morphology

To explain the physics behind the Ag ring formation, we consider the force balance on a single Ag particle following the nucleation event. The particle dynamics is governed by an interplay among the surface tension (F_s), pressure (F_p) and drag force (F_d).[28, 35] The

particle accumulation at the bubble interface is also intertwined with the bubble growth dynamics.

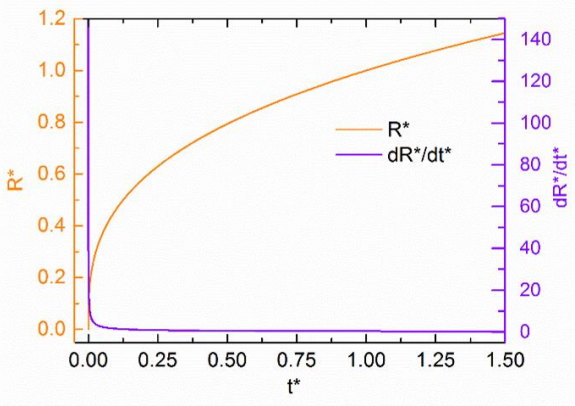

Figure 5.3: Calculated temporal evolution of the bubble radius and the growth rate in the nondimensionalized form.

We explore the bubble growth dynamics using an analytical model. Briefly, the laser-induced heat at the AuNI substrate generates and grows the bubble. In the model, we assume that: (i) the surrounding liquid is at the saturation temperature (T_{sat}), (ii) the bubble assumes a hemispherical geometry throughout its growth, and (iii) the laser-generated heat is partly dissipated in the medium. When the liquid is at the saturation temperature, we can assume that the laser-generated heat is used for liquid-to-vapor phase change as per:

$$\dot{q}_{vap} = \dot{m} h_{fg} \qquad (5)$$

where $\dot{q}_{vap}$ is the heat associated with bubble formation, $\dot{m}$ is the mass conversion rate of liquid to vapor, and h_{fg} is the latent heat of vaporization.

By incorporating the heat dissipation through an efficiency term (η) in our model., we apply the following scaling variables to non-dimensionalize the radius of the bubble (R_b) and the time (t):

$$R^* = \left(\frac{1}{r}\right) R_b \text{ and } t^* = \left(\frac{3\eta P}{2\rho r h_{fg}}\right) t \qquad (6)$$

where r is the radius of the laser beam (m) and ρ is the density. As plotted in Figure 3a, the evolution of the bubble radius and the growth rate in the non-dimensionalized form can be described as:

$$R^* = t^{*^{1/3}} \text{ and } \frac{dR^*}{dt^*} = \frac{1}{3t^{*^{2/3}}} \qquad (7)$$

From Figure 5.3a, we can see that the bubble has a high initial growth rate, which decreases drastically. The Ag NPs are pushed towards the bubble surface due to the high inertial thrust imparted at the instant when the bubble is formed. This explains the absence of Ag NPs around the point of laser incidence and the formation of the Ag rings, as shown in Figure 5.2. The near-instantaneous formation of Ag ring in the silver ink solution without exposure to the ambient atmosphere limits the plausibility of silver oxidation, thereby improving the sample's shelf life.

5.3.3 Structural Characterization

The ability to tune the properties of the Ag rings is crucial for their applications.[36] We have experimentally established a correlation between the incident laser power and the resultant ring diameter. The Ag ring diameter can be modulated between 1.08 ± 0.07 μm and 2.02 ± 0.08 μm (Figure 5.4a). The increased ring diameter at the elevated laser power is attributed to the increased bubble size due to the larger amount of vapor generated. A further increase of the laser power causes unstable bubble growth, resulting in a large variation (σ >15%) in the Ag ring diameter. In addition, scanning electron microscopy (SEM) and atomic force microscopy (AFM) images of the ring arrays are shown in Figure 5.4b-c. The Ag rings demonstrate increasing size, with near constant ring width. The ring composition is further analyzed by EDS mapping. As shown in Figures 5.4d-f, Ag is concentrated along the ring and Au is spread out all over the substrate. The AFM images reveal a diameter of 1.7 μm and a height of ~145 nm for the Ag ring.

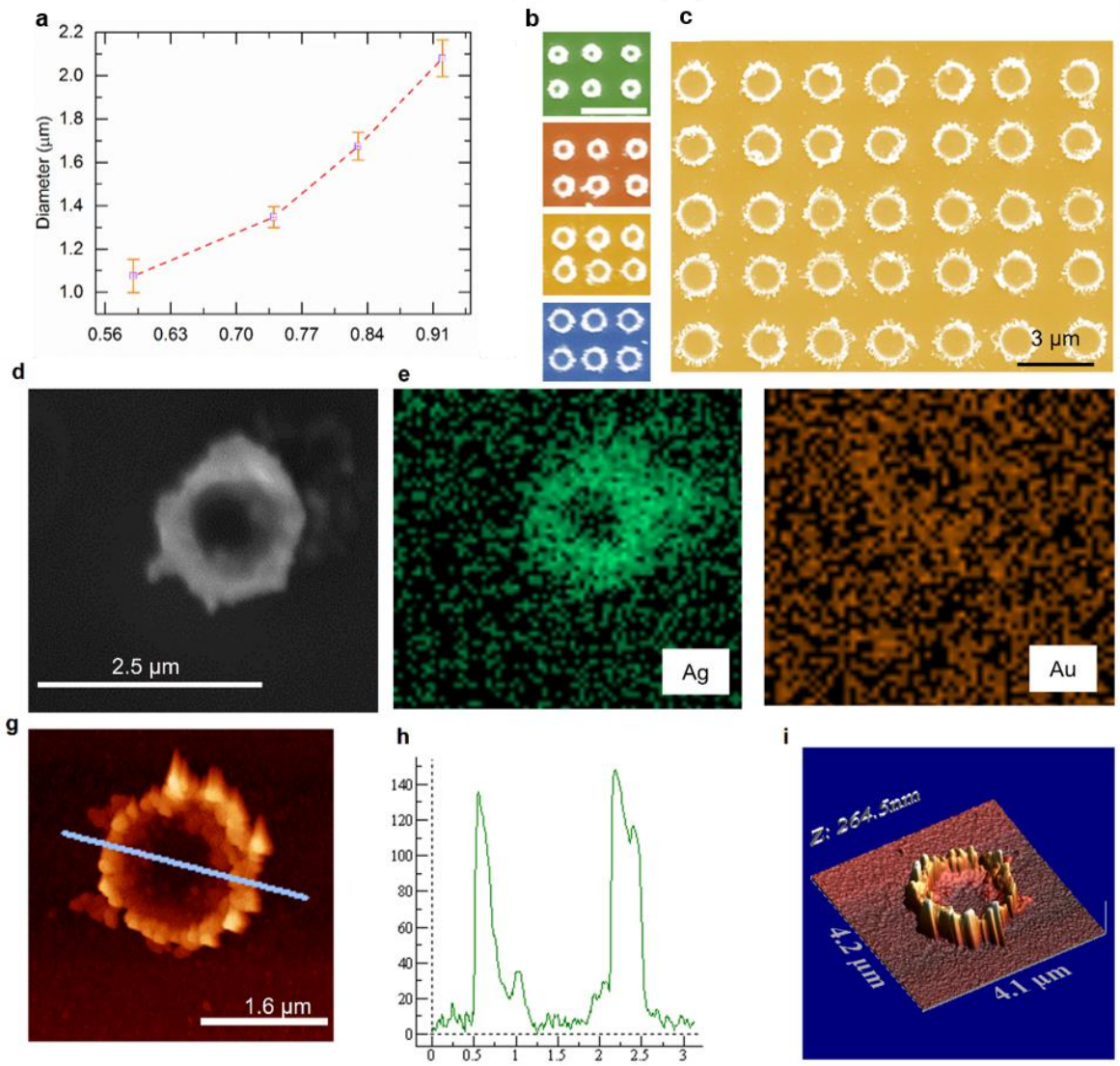

Figure 5.4: (a) Measured Ag ring diameter as a function of the incident laser power (b-c) SEM images of different Ag ring arrays fabricated with varied incident laser power. Scale bar in (b): 4 μm. (d-f) SEM image, EDS Ag mapping, and EDS Au mapping of an Ag ring on the AuNI substrate, which shows that the ring is composed of Ag while the Au nanoparticles are spread out everywhere. (g-i) AFM images and sectional analysis of a typical Ag ring.

5.3.4 Optical Characterization

We perform the optical characterization of the variable arrays of Ag rings (60 µm × 50 µm) on the AuNI substrates in the infrared and visible regime. Our printing strategy's capability of fabricating structures with sub-micron line-width enables the creation of optically active structures.

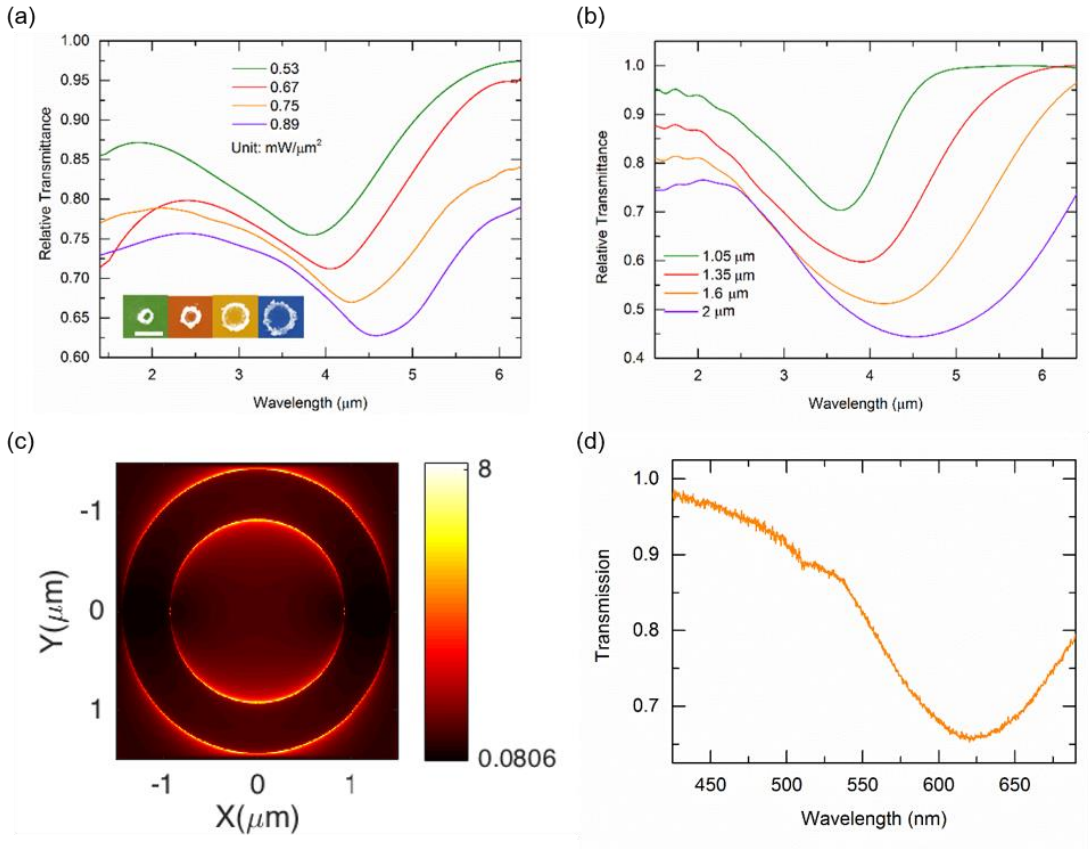

Figure 5.5: (a) The relative transmittance spectra of the arrays of Ag rings fabricated at the variable laser power. The spectra were normalized with respect to that of the AuNI substrate as background. The inset show representative SEM images of four individual rings that increase their diameters (1.08 µm, 1.35 µm, 1,67 µm, and 2.02 µm) when the incident laser power changes from 0.53 mW/µm^2 to 0.89 mW/µm^2. (b) The FDTD-simulated relative transmittance spectra for the Ag rings in (a). (c) Simulated electric-field distribution at a 2 µm Ag ring upon the excitation of dipolar surface plasmon resonance mode. (d) The transmission spectra in the visible region.

To measure the optical spectra in the infrared regime, we utilized a Bruker Vertex v80 FTIR operating in a step-scan mode. The unpolarized broadband infrared light from a thermal Globar source of the FTIR was modulated by an optical chopper at a frequency of 500 Hz and focused onto the sample surface using an objective. The transmitted signal, which was collimated by two ZnSe lenses, was collected and averaged by a mid-infrared HgCdTe detector and a lock-in amplifier, respectively. The transmittance of the Ag ring arrays was normalized to that of the AuNI substrate as background. Due to the symmetric nature of the Ag ring, there is no dependence on the polarization of the incident infrared beam.

As shown in Figure 5.5a, all the arrays exhibit transmission dips in the mid-infrared regime, which arises from the surface plasmon resonances at the rings. The resonant wavelength varies from 3.8 μm to 4.6 μm when the Ag ring diameter is increased, as shown in the SEM images in the inset of Figure 5.5a. A further analysis of the SEM images shows that the ring diameter increases from 1.08 μm to 2.02 μm and the ring width is between 130 nm and 200 nm.

We performed electromagnetic simulations using finite-difference time-domain (FDTD) method to better understand the experimental optical spectra of the Ag rings. As shown in Figure 5.5b, the resonant peak wavelength, bandwidth, and symmetry of the simulated spectra are comparable to the experimental data (Figure 5.5a). A further study of the electric-field distribution at a single Ag ring indicates that the resonance arises from the dipolar plasmon mode (Figure5.5c). The resonance tunability of the Ag rings is expected to benefit SEIRA and other sensing applications where a good match between the resonant wavelength and the wavelength of the vibrational mode of the molecular analytes is preferred. Further, the AuNI substrate underneath results in the plasmonic activity within the visible region and shows a broad plasmonic resonance feature (Figure 5.5d).

5.4 DUAL-MODE OPTICAL SPECTROSCOPY

With the visible and infrared surface plasmon resonances that arise from the AuNIs and Ag rings, the Ag ring-AuNI substrate presents an opportunity to achieve dual-mode surface-enhanced optical spectroscopies. We demonstrate SEIRS and SERS of TNT, R6G, and CV, respectively. As shown in Figure 5.6a, the aromatic (3.43 μm) and aliphatic (3.51 μm) C-H stretch bands of TNT on the Ag ring-AuNI substrate are enhanced via SEIRS.[25] The signal enhancements highly depend on the match between vibrational (ω_{vib}) and plasmonic frequencies (ω_p). No vibrational signal is observed when there is a large frequency mismatch. The detuning variation results in the different signal enhancements and line-shapes. To further elucidate the plasmon-molecular vibration coupling, we obtain the baseline-corrected SEIRS spectra. As shown in the lower panel of Figure 5.6a, a clear Fano-line sharp features appear in the spectra due to the coupling between the vibrational and plasmonic excitations, confirming the SEIRS effect.

We measured the SERS spectra of R6G molecules drop-casted on the Ag ring-AuNI substrate. The incident laser power for the measurement was 0.7 mW and the laser beam had a diameter of 2 μm. The Raman acquisition time was 1s. Figure 5.6b shows the concentration-dependent SERS spectra with 532nm incident laser, where distinguishable Raman modes are observed even at the lowest concentration of 10^{-7} M. Many standard modes such as C-C-C ring in-plane bending (610 cm^{-1}), C-C stretching (1360 cm^{-1} and 1506 cm^{-1}) and C-H bending (769 cm^{-1} and 1648 cm^{-1}) appear in the spectra.[37] Further, we evaluated the Raman enhancement stability across the substrate by measuring multiple spectra at random locations all over the substrate (Figure 5.6c). The R6G concentration, in this case, was 1 μM.

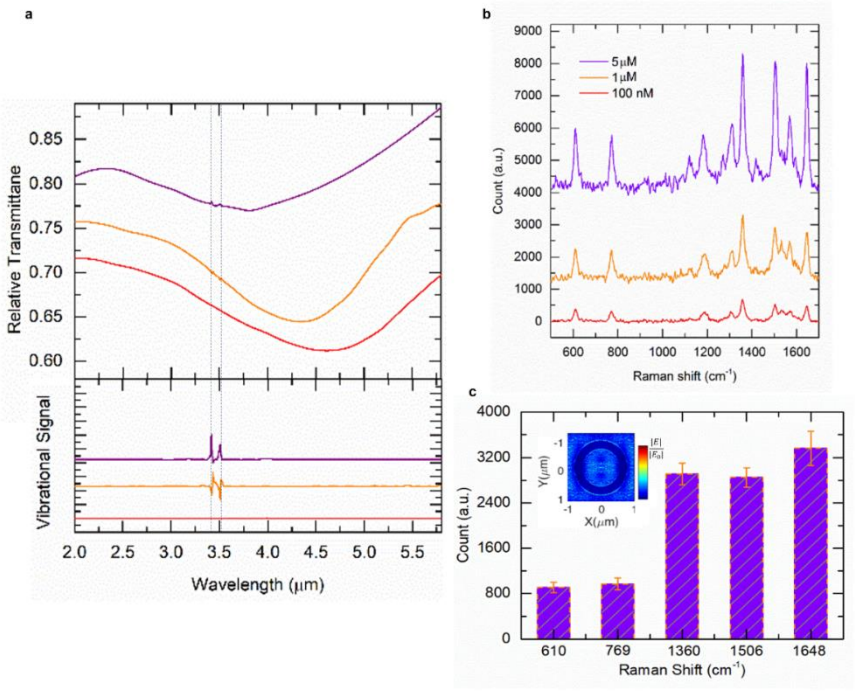

Figure 5.6: (a) SEIRS of TNT on the three types of the Ag ring-AuNI substrates, which exhibit the different detuning between the plasmonic and molecular excitations. The spectra correspond to ring sizes of 1.08 μm, 1.67 μm and 2.02 μm from top to bottom, respectively. The lower panel shows the baseline-corrected spectra, which clearly reveal the molecular resonances. The baseline was obtained via a second-derivative method. (b) SERS spectra of R6G of variable concentrations on the Ag ring-AuNI substrate. (c) SERS signal counts of the different R6G modes based on multiple spectra taken at various random locations on the sample. The inset shows the simulated field distributions at the Ag ring-AuNI substrate.

In general, randomly distributed AuNIs on the substrates do not possess high E-field enhancement. Additional steps such as bubble-mediated molecule concentration are often applied to improve the SERS performances on such substrates.[38] However, for our hybrid Ag ring- AuNI substrate, we observed a high E-field enhancement at the Ag-ring/AuNI interface, as shown in the inset of Figure 5.6c. The field enhancement arises from the intense hot spots at the multiple Ag-Au junctions with the sub-20 nm gaps. In

comparison to the bare AuNI substrate, a 10-fold increase in the SERS count is observed for the Ag ring-AuNI substrate (Figure 5.7a).

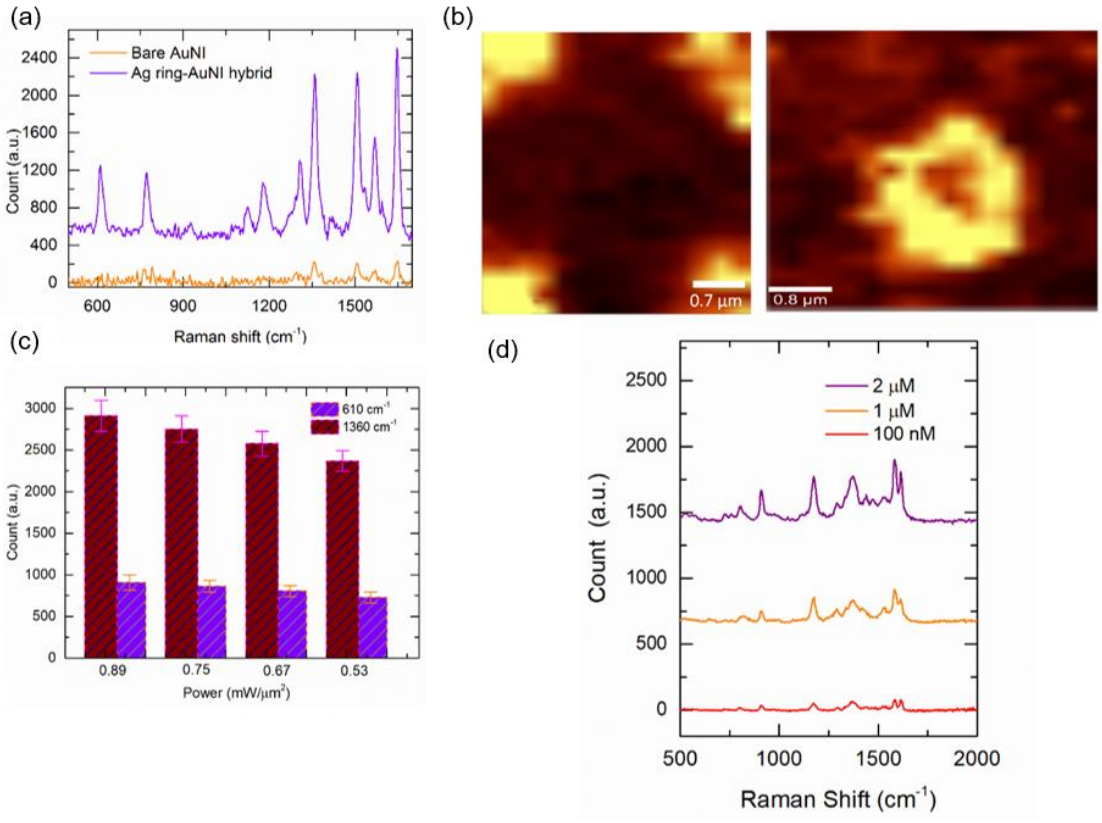

Figure 5.7: (a) SERS spectra for 1µM R6G on the hybrid Ag ring-AuNI substrate *vs.* the bare AuNI substrate. (b) High-resolution Raman mapping of R6G over the Ag ring/AuNI hybrid substrate. (c) Raman counts of 1 µM R6G at 610 cm^{-1} and 1360 cm^{-1} as a function of the Ag ring size. The ring size decreases from 2.02 ± 0.08 µm to 1.08 ± 0.07 µm as the power reduces. (d) Concentration-dependent SERS spectra of crystal violet (CV) molecules on the 2.02 µm Ag ring substrate.

The high-resolution Raman mapping with the 610 cm^{-1} peak signal also confirms the enhancement at the interfaces (Figure 5.7b). The left panel shows the inter-ring region, with the rings present at the edges. The right panel in figure 5.7b shows the high-resolution image of a single Ag-ring, clearly demonstrating the signal enhancement at Ag ring/AuNI interface. The compatibility with a 532nm laser for both fabrication and Raman sensing

can be beneficial for device miniaturization via reduced cost and improved throughput. We have also studied the influence of the ring size on the Raman counts (Figure 5.7c). The laser was centered on the Ag ring to obtain the spectra. An increase in the counts is observed with increasing radius since the overlap area between Ag ring/AuNI increases from ~95 μm^2 to ~360 μm^2 as the radius increase from 1.08 to 2.02 μm. In addition, we have also demonstrated the sensing of CV at various concentrations, as detailed in Figure 5.7d. The standard modes such as the ring breathing mode (914 cm^{-1}), C-H stretch mode (1177 cm^{-1}), C-N stretch mode (1370 cm^{-1}) are clearly seen.

5.5 MICROFLUIDIC DEVICE INTEGRATION

The applicability of plasmonic sensors is greatly enhanced by their integration with microfluidic systems.[17, 26] We demonstrate the "point-and-shoot" *in-situ* fabrication of Ag rings within a microfluidic channel. Due to the non-invasive remote control of light, the light-based synthesis allows us to fabricate Ag rings without any constraints to the channel design and hence is compatible with various on-chip applications.[39]

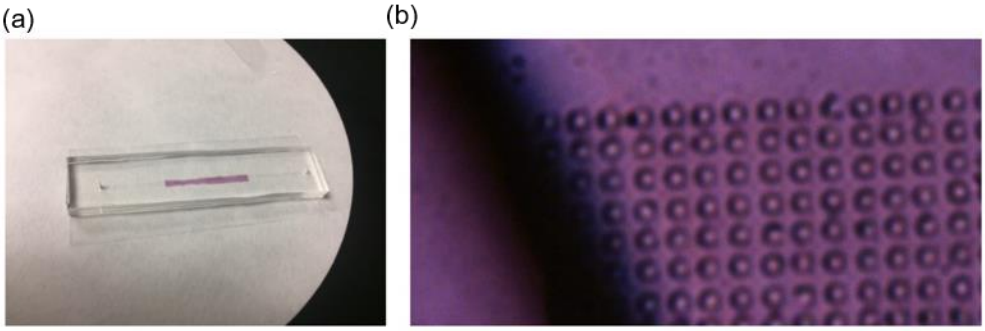

Figure 5.8: (a) A photo of a microfluidic chip consisted of a network of AuNIs confined within a microfluidic channel. (b) A bright-field optical image showing the fluid flow over the Ag ring array.

Figure 5.8 shows a photo of our microfluidic chip where the AuNIs are confined within the PDMS channel to directly contact the PDMS on the glass substrate for the strong

adhesion. The Ag precursor ink was introduced to the microfluidic channel via the inlet (Figure 5.9a). The fabrication of Ag rings was performed at a laser power of 0.75 mW/μm^2 to yield Ag rings with 1.84±0.11 μm rings. Despite the channel constraint, the laser-generated microbubble induces sufficient flows to concentrate the Ag^+ ions at the bubble interfaces to form the Ag rings.[40]

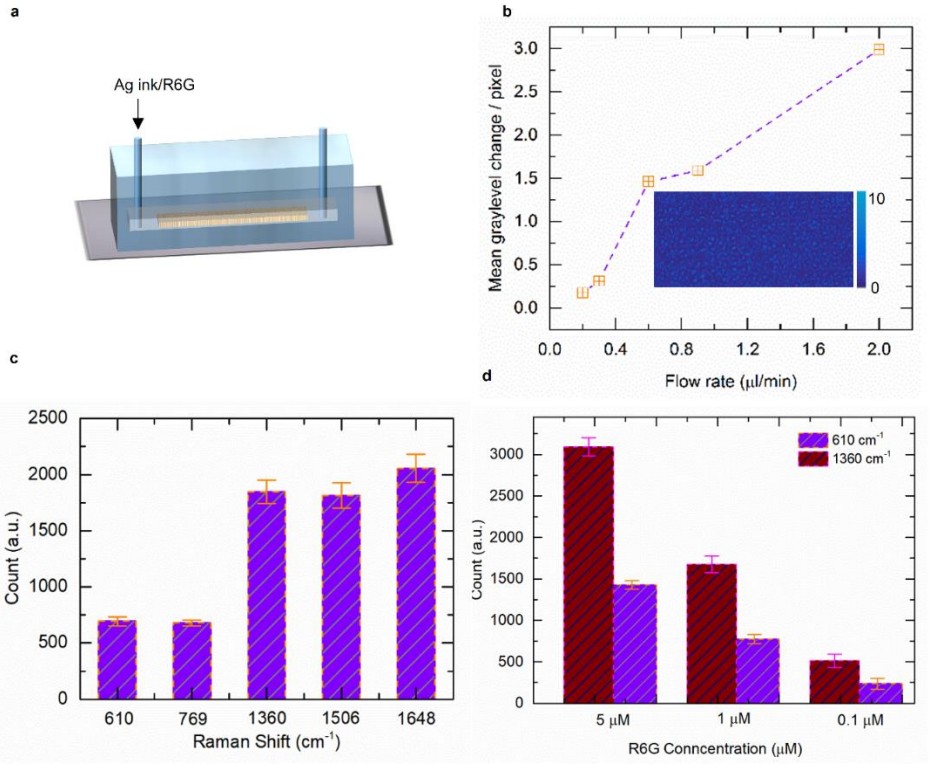

Figure 5.9: (a) Schematic of the one-inlet, one-outlet microfluidic setup wherein the silver precursor ink and R6G are introduced sequentially. The microfluidic channel width and height are 500 μm and 80 μm, respectively. (b) The plot of the mean pixel change of the optical images taken at various flow rates to demonstrate the stability of the fabricated Ag rings. The inset shows a typical difference image. (c) SERS signal counts of the different R6G modes based on many spectra taken at various random locations on the sample with 1.8 μm Ag ring. (d) SERS signal counts in the microfluidic chamber as a function of R6G concentration on the sample with 1.8 μm Ag ring.

We employ image processing to analyze the stability of *in-situ* fabricated Ag rings in a microfluidic channel. We record a series of optical images of the Ag ring arrays at the

various flow rates. For a pair of the images (m×n pixels) taken at the same location before flow (0^{th} image) and after flow with a rate of *x μl/min*, we convert the images to the grayscale. The conversion provides two sets of images corresponding to pre-flow and post-flow, comprised of grayscale pixels. We then analyze the differences in the gray level using a pixel-by-pixel approach. The mean pixel-to-pixel change is obtained by averaging all the values in the difference-image matrix as per the equation:

$$\Delta GL_{avg} = \frac{1}{m+n}\sum_{i=0}^{m}\sum_{j=0}^{n} GL_{x,i.j} - GL_{0,i,j} \qquad (8)$$

where the images have m × n pixels. The typical mean difference is ≤3 at the various flow rates, demonstrating the high stability of the Ag rings (Inset of Figure 5.9b).

Finally, we demonstrate *in-situ* SERS of R6G molecules based on the Ag ring-AuNI substrate in the microfluidic channel. The channel was thoroughly cleaned with DI water prior to the introduction of the R6G solution. Figure 5.9c shows the SERS signal counts of the different R6G (1 μM) modes based on many spectra taken at various random locations of the substrate within the channel, revealing the spatially uniform and repeatable measurements. Further, the SERS spectra at various concentrations of R6G from 5 μM to 100 nM were obtained (Figure 5.9d). A similar decreasing trend with reducing concentration was observed. However, the standard deviation of the counts was reduced by ~35% owing to the even distribution of the analyte molecule.

5.6 SUMMARY

In summary, the laser-induced bubble printing enables "point-and-shoot" one-step synthesis of Ag rings for surface-enhanced optical spectroscopies. Though e-beam based metal deposition for mask repair is a mature technique with high accuracy and resolution, it is limited in terms of versatility and configurability.[41] Our technique is applicable to microfluidic systems with spatial constraints. The ring fabrication benefits from the low-

temperature reducible Ag precursor ink, the AuNI substrate that provides highly localized temperature increase upon the laser irradiation, and the high inertial thrust imparted at the instant when the bubble is formed. The high temperature and convection-mediated Ag^+ ion concentration at the three-phase line enable ultra-fast Ag particle synthesis and immobilization at high spatial resolution. With their tunable plasmon resonances in the visible and infrared regimes, the hybrid Ag ring-AuNI substrates have been applied for SERS and SEIRS of R6G, CV, and TNT, respectively. With its simplicity, high efficiency and integrability in the fabrication of micro/nanostructures, our "point-and-shoot" approach paves the way towards device miniaturization, portability, and multi-functionality.

5.7 REFERENCES

1. Meinzer, N.; Barnes, W. L.; Hooper, I. R., Plasmonic meta-atoms and metasurfaces. *Nat. Photon.* **2014,** *8* (12), 889-898.
2. Nordlander, P., The Ring: A Leitmotif in Plasmonics. *ACS Nano* **2009,** *3* (3), 488-492.
3. Aizpurua, J.; Hanarp, P.; Sutherland, D. S.; Kall, M.; Bryant, G. W.; de Abajo, F. J. G., Optical properties of gold nanorings. *Phys. Rev. Lett.* **2003,** *90* (5), 057401.
4. Ye, J.; Van Dorpe, P.; Lagae, L.; Maes, G.; Borghs, G., Observation of plasmonic dipolar anti-bonding mode in silver nanoring structures. *Nanotechnology* **2009,** *20* (46), 465203.
5. Larsson, E. M.; Alegret, J.; Kall, M.; Sutherland, D. S., Sensing characteristics of NIR localized surface plasmon resonances in gold nanorings for application as ultrasensitive biosensors. *Nano Lett.* **2007,** *7* (5), 1256-1263.
6. Cetin, A. E.; Altug, H., Fano Resonant Ring/Disk Plasmonic Nanocavities on Conducting Substrates for Advanced Biosensing. *ACS Nano* **2012,** *6* (11), 9989-9995.
7. Banaee, M. G.; Crozier, K. B., Gold nanorings as substrates for surface-enhanced Raman scattering. *Opt. Lett.* **2010,** *35* (5), 760-762.
8. Hao, F.; Sonnefraud, Y.; Van Dorpe, P.; Maier, S. A.; Halas, N. J.; Nordlander, P., Symmetry Breaking in Plasmonic Nanocavities: Subradiant LSPR Sensing and a Tunable Fano Resonance. *Nano Lett.* **2008,** *8* (11), 3983-3988.

9. Huang, C. J.; Ye, J.; Wang, S.; Stakenborg, T.; Lagae, L., Gold nanoring as a sensitive plasmonic biosensor for on-chip DNA detection. *Appl. Phys. Lett.* **2012,** *100* (17), 173114.

10. Lewicka, Z. A.; Li, Y.; Bohloul, A.; Yu, W. W.; Colvin, V. L., Nanorings and nanocrescents formed via shaped nanosphere lithography: a route toward large areas of infrared metamaterials. *Nanotechnology* **2013,** *24* (11), 115303.

11. Zhao, J.; Frank, B.; Neubrech, F.; Zhang, C. J.; Braun, P. V.; Giessen, H., Hole-mask colloidal nanolithography combined with tilted-angle-rotation evaporation: A versatile method for fabrication of low-cost and large-area complex plasmonic nanostructures and metamaterials. *Beilstein J. Nanotechnol.* **2014,** *5*, 577-586.

12. Rajeeva, B. B.; Zheng, Y. B., Molecular Plasmonics: From Molecular-Scale Measurements and Control to Applications. *Nanotechnology: Delivering on the Promise, Vol 2* **2016,** *1224*, 23-52.

13. Neubrech, F.; Huck, C.; Weber, K.; Pucci, A.; Giessen, H., Surface-Enhanced Infrared Spectroscopy Using Resonant Nanoantennas. *Chem. Rev.* **2017,** *117* (7), 5110-5145.

14. Babayan, Y.; McMahon, J. M.; Li, S. Z.; Gray, S. K.; Schatz, G. C.; Odom, T. W., Confining Standing Waves in Optical Corrals. *ACS Nano* **2009,** *3* (3), 615-620.

15. Sounas, D. L.; Alu, A., Angular-Momentum-Biased Nanorings To Realize Magnetic-Free Integrated Optical Isolation. *ACS Photonics* **2014,** *1* (3), 198-204.

16. Xu, B.-B.; Zhang, R.; Liu, X.-Q.; Wang, H.; Zhang, Y.-L.; Jiang, H.-B.; Wang, L.; Ma, Z.-C.; Ku, J.-F.; Xiao, F.-S., On-chip fabrication of silver microflower arrays as a catalytic microreactor for allowing in situ SERS monitoring. *Chem. Commun.* **2012,** *48* (11), 1680-1682.

17. Tokel, O.; Inci, F.; Demirci, U., Advances in plasmonic technologies for point of care applications. *Chem. Rev.* **2014,** *114* (11), 5728-5752.

18. Chen, J.; Liao, W.-S.; Chen, X.; Yang, T.; Wark, S. E.; Son, D. H.; Batteas, J. D.; Cremer, P. S., Evaporation-induced assembly of quantum dots into nanorings. *ACS Nano* **2008,** *3* (1), 173-180.

19. Halpern, A. R.; Corn, R. M., Lithographically patterned electrodeposition of gold, silver, and nickel nanoring arrays with widely tunable near-infrared plasmonic resonances. *ACS Nano* **2013,** *7* (2), 1755-1762.

20. Bao, Y.; Witten, T. A.; Scherer, N. F., Self-Organizing Arrays of Size Scalable Nanoparticle Rings. *ACS Nano* **2016,** *10* (9), 8947-8955.

21. Zheng, Y.; Wang, S.; Huan, A.; Wang, Y., Fabrication of large area ordered metal nanoring arrays for nanoscale optical sensors. *J. Non-Cryst. Solids* **2006,** *352* (23), 2532-2535.

22. Winkler, R.; Schmidt, F.-P.; Haselmann, U.; Fowlkes, J. D.; Lewis, B. B.; Kothleitner, G.; Rack, P. D.; Plank, H., Direct-Write 3D Nanoprinting of Plasmonic Structures. *ACS Appl. Mater. Inter.* **2016,** *9* (9), 8233–8240.

23. Taylor, A. B.; Michaux, P.; Mohsin, A. S.; Chon, J. W., Electron-beam lithography of plasmonic nanorod arrays for multilayered optical storage. *Opt. Express* **2014,** *22* (11), 13234-13243.

24. Wolf, O.; Campione, S.; Benz, A.; Ravikumar, A. P.; Liu, S.; Luk, T. S.; Kadlec, E. A.; Shaner, E. A.; Klem, J. F.; Sinclair, M. B., Phased-array sources based on nonlinear metamaterial nanocavities. *Nat. Commun.* **2015,** *6*, 7667.

25. Bagheri, S.; Weber, K.; Gissibl, T.; Weiss, T.; Neubrech, F.; Giessen, H., Fabrication of square-centimeter plasmonic nanoantenna arrays by femtosecond direct laser writing lithography: effects of collective excitations on SEIRA enhancement. *ACS Photonics* **2015,** *2* (6), 779-786.

26. Xie, Y.; Yang, S.; Mao, Z.; Li, P.; Zhao, C.; Cohick, Z.; Huang, P.-H.; Huang, T. J., In situ fabrication of 3D Ag@ ZnO nanostructures for microfluidic surface-enhanced Raman scattering systems. *ACS Nano* **2014,** *8* (12), 12175-12184.

27. Roxworthy, B. J.; Ko, K. D.; Kumar, A.; Fung, K. H.; Chow, E. K. C.; Liu, G. L.; Fang, N. X.; Toussaint, K. C., Application of Plasmonic Bowtie Nanoantenna Arrays for Optical Trapping, Stacking, and Sorting. *Nano Lett.* **2012,** *12* (2), 796-801.

28. Lin, L. H.; Peng, X. L.; Mao, Z. M.; Li, W.; Yogeesh, M. N.; Rajeeva, B. B.; Perillo, E. P.; Dunn, A. K.; Akinwande, D.; Zheng, Y. B., Bubble-Pen Lithography. *Nano Lett.* **2016,** *16* (1), 701-708.

29. Bangalore Rajeeva, B.; Lin, L.; Perillo, E. P.; Peng, X.; Yu, W. W.; Dunn, A.; Zheng, Y., High-Resolution Bubble Printing of Quantum Dots. *ACS Appl. Mater. Inter.* **2017,** *9* (19), 16725–16733.

30. Rajeeva, B. B.; Alabandi, M. A.; Lin, L.; Perillo, E. P.; Dunn, A. K.; Zheng, Y., Patterning and fluorescence tuning of quantum dots with haptic-interfaced bubble printing. *J. Mater. Chem. C* **2017,** *5*, 5693-5699.

31. Fujii, S.; Fukano, R.; Hayami, Y.; Ozawa, H.; Muneyuki, E.; Kitamura, N.; Hag, M., Simultaneous Formation and Spatial Patterning of ZnO on ITO Surfaces by Local Laser-Induced Generation of Microbubbles in Aqueous Solutions of [Zn(NH3)(4)](2+). *ACS Appl. Mater. Inter.* **2017,** *9* (9), 8413-8419.

32. Walker, S. B.; Lewis, J. A., Reactive silver inks for patterning high-conductivity features at mild temperatures. *J. Am. Chem. Soc.* **2012,** *134* (3), 1419-1421.

33. Enders, M.; Mukai, S.; Uwada, T.; Hashimoto, S., Plasmonic Nanofabrication through Optical Heating. *J. Phys. Chem. C.* **2016,** *120* (12), 6723-6732.

34. Sear, R. P., Nucleation: theory and applications to protein solutions and colloidal suspensions. *J. Phys. Condens. Matter* **2007,** *19* (3), 033101.

35. Zhao, C. L.; Xie, Y. L.; Mao, Z. M.; Zhao, Y. H.; Rufo, J.; Yang, S. K.; Guo, F.; Mai, J. D.; Huang, T. J., Theory and experiment on particle trapping and manipulation via optothermally generated bubbles. *Lab Chip* **2014,** *14* (2), 384-391.

36. Aksu, S.; Cetin, A. E.; Adato, R.; Altug, H., Plasmonically Enhanced Vibrational Biospectroscopy Using Low-Cost Infrared Antenna Arrays by Nanostencil Lithography. *Adv. Opt. Mater.* **2013,** *1* (11), 798-803.

37. Jensen, L.; Schatz, G. C., Resonance Raman scattering of rhodamine 6G as calculated using time-dependent density functional theory. *J. Phys. Chem. A* **2006,** *110* (18), 5973-5977.

38. Kang, Z. W.; Chen, J. J.; Ho, H. P., Surface-enhanced Raman scattering via entrapment of colloidal plasmonic nanocrystals by laser generated microbubbles on random gold nano-islands. *Nanoscale* **2016,** *8* (19), 10266-10272.

39. Chiou, P. Y.; Ohta, A. T.; Wu, M. C., Massively parallel manipulation of single cells and microparticles using optical images. *Nature* **2005,** *436* (7049), 370-372.

40. Xie, Y. L.; Zhao, C. L.; Zhao, Y. H.; Li, S. X.; Rufo, J.; Yang, S. K.; Guo, F.; Huang, T. J., Optoacoustic tweezers: a programmable, localized cell concentrator based on opto-thermally generated, acoustically activated, surface bubbles. *Lab Chip* **2013,** *13* (9), 1772-1779.

41. Noh, J.H.; Stanford, M. G.; Lewis, B. B.; Fowlkes, J. D.; Plank, H.; Rack, P. D.,. Nanoscale electron beam-induced deposition and purification of ruthenium for extreme ultraviolet lithography mask repair. *Appl. Phys. A* **2014,** *117 (4)*, 1705-1713.

Chapter 6: Unified Synthesis and Structuring of Immiscible Metallic Nanoalloys*

6.1 INTRODUCTION

Accumulation-mediated concentration has been a ubiquitous phenomenon in nature to facilitate complex reactions, starting with the vital building blocks such as DNA and RNA essential for the emergence of early life. [1] The accumulation phenomenon has also been demonstrated to support the formation of cell-like lipid vesicles,[2] induce proton gradients,[3] and enhance chemical reaction rates.[4] Multiple moieties such as ions and molecules can be triggered to move in response to an electrical or thermal gradient generated in scenarios ranging from nanoneedles to macroscale hydrothermal vents or cooling volcanic sites in geothermally heated porous rocks.[1, 4] In particular, the accumulation via thermal gradients can significantly increase molecule concentration by a factor of 10^6.[1] In addition, ultra-fast nucleation and growth process reaching up to 10 μm/s can be realized upon accumulation of ions and molecules in confined spaces.[5]

Similar to the creation of complex multicomponent biological building blocks, the blending of multiple elements is an attractive strategy to tune the properties of inorganic materials via atomic ordering, size, and composition.[6-7] For instance, in a multi-metallic nanoparticle (NP) system, d-band intermixing amongst the hetero-atoms leads to a broader tuning of the chemical reactivity on the NP surface.[8] Bimetallic NP alloys have been found to exhibit unique and significantly enhanced optical, electrical and catalytic characteristics, which are distinct from the pure metals.[9] Synthesis and fabrication of alloy metallic

*Rajeeva, B. B., Kunal, P., Kollipara, P. S., Acharya, P. V., Joe, M., Jarvis, L., Liu, Y., Bahadur, V., Humphrey, S., Zheng, Y. B. In-Situ Unified Synthesis and Structuring of Immiscible Metallic Nanoalloys. (under preparation)
Rajeeva, B. B. carried out the experimental work and participated in the preparation of manuscript.

composites, specifically composed of immiscible counterparts are highly desirable as they manifest synergistic properties not seen in phase segregated systems. [10-11]

Both traditional and unconventional protocols for immiscible nanoalloys require complex synthetic techniques, templates, and chemical precursors.[12] They typically involve encapsulation of precursor reagents with appropriate surfactants in confined spaces such as micelles,[13] dendrimers,[14] and femto-droplets,[15] as well as long thermal annealing at high temperatures. The resultant alloys possess excessive surfactants or coatings, which hinder their catalytic performance.[16] Light-induced nucleation provides an attractive approach to nucleating and crystallizing multi-element materials in solutions with a high spatiotemporal control.[17] Liquid-phase laser synthesis requires no surfactants, leading to ligand-free NPs.[16, 18] Herein, we exploit the integration of accumulation-mediated concentration and laser-induced nucleation to enable the simultaneous synthesis and structuring of metallic alloys. An ultra-high precursor supersaturation along with light-controlled temperature gradient and microbubble trap (MBT) leads to nucleation and growth of immiscible nanoalloys.

In this chapter, we extend the simultaneous synthesis and immobilization strategy to a multi-elemental system. As a case-in-point, we demonstrate the *in-situ* unified synthesis and structuring (US^3) of classically immiscible rhodium-gold nanoalloys (RGNs). RGNs are challenging systems to synthesize, with the phase diagrams of these alloys predicting no stable regions below 2139 K and 1.0 atm.[19] By harnessing the confinement effect, high fluid flow, and site-specific heating at a laser-induced MBT, we achieve one-shot RhAu alloying and structuring. Random walk simulations reveal the highly enhanced concentration of ions in the vicinity of the MBT within milliseconds timeframe. The ion supersaturation leads to ~3 orders of reduction in the critical radius and synthesis time. The ultra-fast nucleation and growth process occurs on the millisecond

regime and enables time-synced low-power synthesis and structuring of surfactant-free RGNs. We are able to modulate the density of the alloys over the substrate via control of substrate stage by computer programming. Furthermore, we explore the catalytic activity of the fabricated RhAu structures using reduction of *p*-nitrophenol to *p*-aminophenol by $NaBH_4$ as a model and demonstrate structure-property relationship based on the modulated density of alloys. The fabricated structures of alloys possess superior catalytic performance compared to individual counterparts. With advantages such as simplified manufacturing process, ultra-fast nucleation time with micro/nanoscale reaction confinement, and structuring of thermodynamically-challenging immiscible nanoalloys, US^3 provides a way to fabricate and screen a variety of new materials for superior functionalities.

6.2 PRINTING SETUP

The unification of synthesis and printing steps depends on the occurrence of site-specific ultra-fast nucleation and growth, high thermal gradient and precursor supersaturation. The US^3 strategy instantaneously achieves all these criteria within milliseconds using a thermoplasmonic Au nanoisland (AuNI) substrate capable of attaining laser-induced highly-confined thermal gradient in the vicinity of a MBT. Figure 6.1 shows the fabrication setup and concept of US^3, wherein the precursor solution consisting of an equimolar mixture of $RhCl_3$ and $HAuCl_4$ solutions is present over an AuNI substrate. Upon the incidence of a low-power (≈ 0.6 mW/μm^2) continuous wave (CW) laser beam (532 nm) through a high-magnification objective, the AuNIs excited on resonance reemit the energy via nonradiative Landau damping, which results in intense localized thermal gradients and eventually leads to the formation of MBT.[20] The Marangoni-convection-mediated ultra-fast accumulation (refer to section 6.4 for more details) at the MBT-substrate interface leads to the synthesis and eventual structuring of the RGNs.

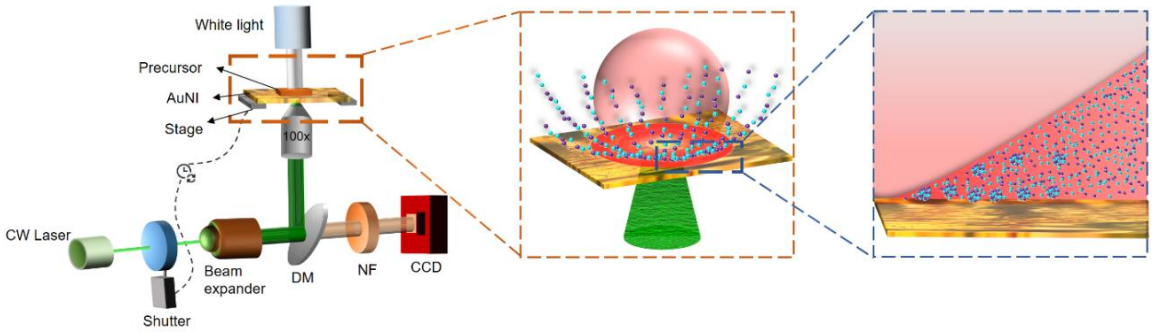

Figure 6.1: Schematic demonstrating the optical setup and ion accumulation aspect of the US^3 strategy. The laser-induced MBT can lead to highly localized supersaturation of precursor ions near the substrate, enabling the synthesis and structuring of immiscible alloys.

6.3 NANOALLOY STRUCTURING

For catalytic applications of structured alloys, it is desired to achieve modular patterning independence and versatility along with a high resolution to attain the maximum surface areas. To achieve structuring of the RGNs, a combination of the stage translation and shutter activation/deactivation was employed.

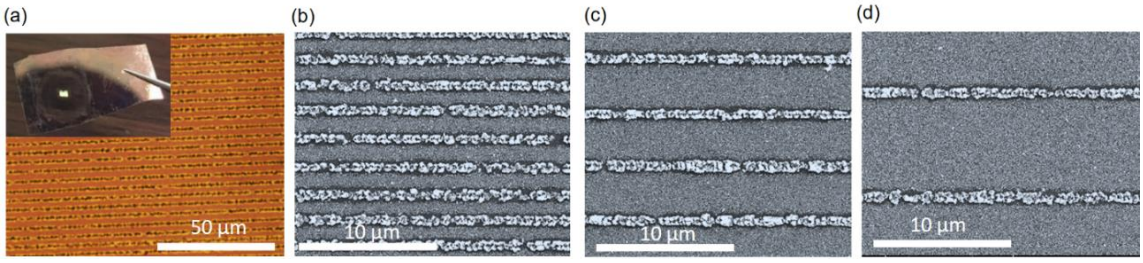

Figure 6.2: (a) Bright-field optical image of the RGNs fabricated using US^3 strategy. The inset shows a completed sample of 2.25 mm^2 area. The bright reflection observed is due to the diffraction effect from the closely printed RGN lines. (b-d) Scanning electron microscopy (SEM) images of the printed RGNs with (b) 2 µm, (c) 4 µm, and (d) 8 µm line-widths.

Figure 6.2a shows the low-magnification image of RGNs structured on the substrate with an inter-line spacing of 4 µm at a stage speed of 30 µm/s, while the inset shows a complete fabricated sample of 2.25 mm^2 in area. To achieve the modulation of the structured RGN density, pre-programmed patterns with line-spacings from 2 µm to 8 µm were fabricated (Figures 6.2b-d). As the stage traverses, the synthesized RGNs get instantaneously deposited along the contact-line of the MBT due to a combination of van der Waals attraction and force balance on the bubble interface.[21-22]

6.3.1 Structural Characterizations

To study the uniformity and features of the immobilized RGNs, we perform both low and high-resolution imaging. Large-area optical profilometry performed using Wyko NY9100 optical profilometer reveals the structuring confinement and uniform deposition of the RGNs with an average height of 44.9 ± 5.1 nm (Figure 6.3a-c). The sample has an interline spacing of 4 µm, which is consistent with the height profile observed in Figure 6.3c.

The height profile is further confirmed by high-resolution atomic force microscopy (AFM) imaging (Park Scientific AFM), along with a characteristic half-ring morphology supporting the immobilization of reaction product at the MBT-substrate contact line (Figure 6.3d). In addition, the realization of sub-micron line-widths can provide advantages in terms of surface area, which can be harnessed for enhanced applications through nanoscale design.[23] Further, the MBT-mediated immobilization leads to tunable sub-micron line-widths based on the stage speed, with lower line-widths observed as the printing speed increases (Figure 6.3e). This is a consequence of lower MBT time at a given instant of time at higher stage speeds.

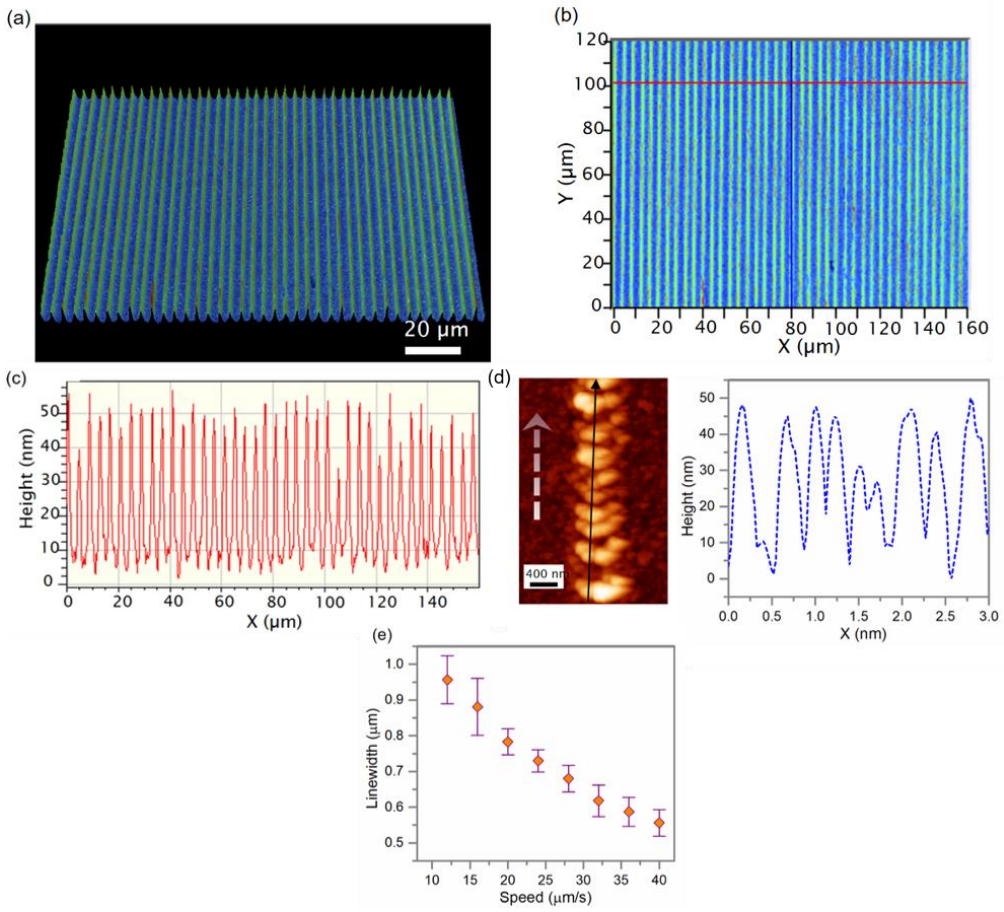

Figure 6.3: (a) Optical profilometry data of printing rhodium gold (RhAu) nanoalloys (RGNs) with 4 µm line-spacing. (b,c) The height profile of the printed RGNs (along the red line). (d) High-resolution AFM imaging which corroborates the immobilization morphology, and the height profile of the printed RGNs. (e) Tunable sub-micron line-width of the structured RGNs as a function of the stage translation speed.

6.3.2 High-Resolution Transmission Electron Microscopy

To further validate the RGN synthesis process, high-resolution transmission electron microscopy (HRTEM) imaging was performed by transferring the particles onto a 200 mesh copper Formvar grid (Ted Pella Inc.). Low-resolution TEM images were obtained using a FEI Tecnai TEM, while the high-resolution TEM images, high-angle annular dark field scanning transmission electron microscopy (HAADF-STEM) images,

and EDS spectra were acquired using a JEOL 2010F TEM equipped with an Oxford EDS detector. The instrument was operated at 200 keV with a 0.19 nm point to point resolution. Further, the lattice spacing values were calculated using FFT.

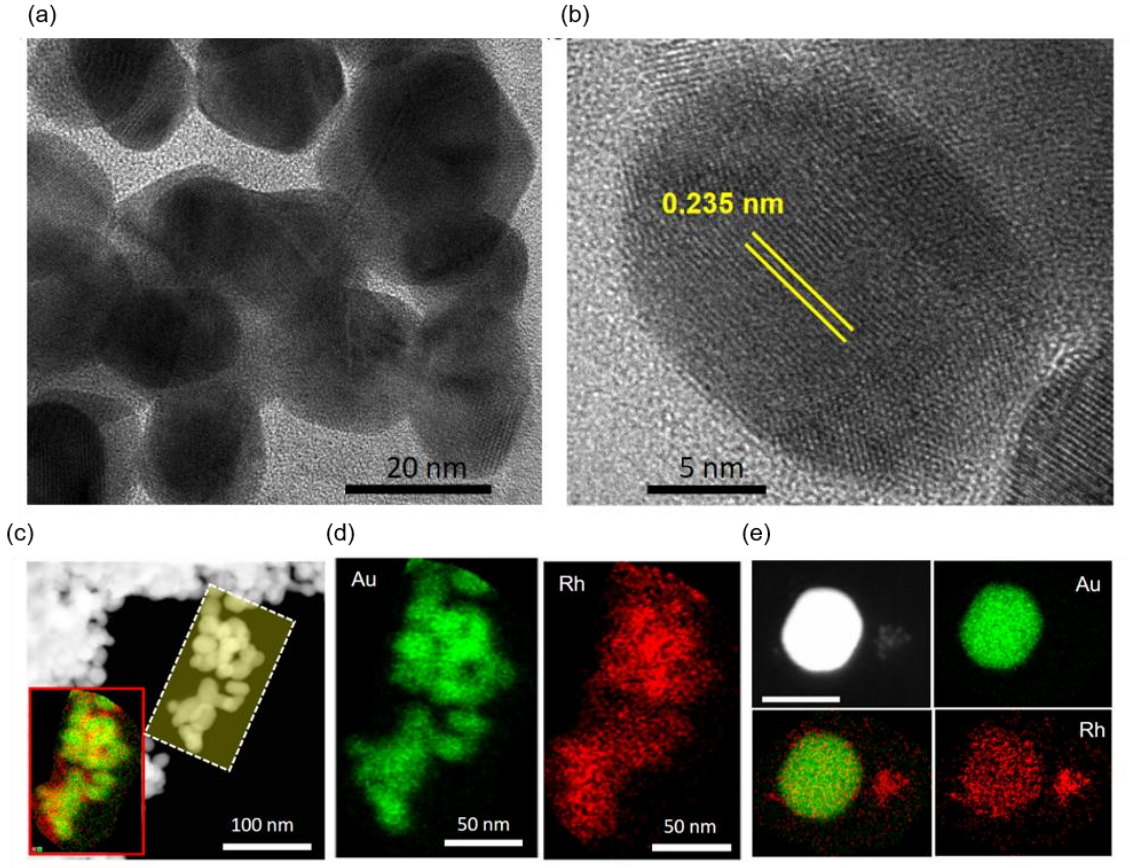

Figure 6.4: (a-b) HRTEM images of the transferred RGNs showing the crystallinity and the d lattice spacing of RGN. (c) HAADF-STEM image of the transferred RGNs, along with the inset of a two-dimensional (2D) overlapped energy-dispersive X-ray spectroscopy (EDS) mapping of Rh and Au. (d) Segregated Rh and Au 2D EDS mapping results showing the distribution of both the elements. (e) High-resolution transmission electron microscopy (HRTEM) image and 2D EDS mapping of a single RGN. Scale bar is 25 nm.

The presence of the AuNI substrate can provide heterogeneous nucleation sites, with initial nucleation likely occurring over the substrate.[24] These RGNs were highly crystalline in nature as confirmed by HRTEM analysis where a mixture of well-defined

lattice planes was seen. The images show that the particles are predominantly cuboctahedral with various degrees of truncation (Figure 6.4a-b). Measured $d_{<111>}$ from various regions of interest showing increased d spacing between 0.23-0.235 nm (Figure 6.4b). In comparison, Figures 6.5a-b shows the non-alloyed Rh clusters exhibiting a d spacing of 0.217 nm (theoretical Rh $d_{<111>}$= 0.219 nm). High-angle annular dark field scanning transmission electron microscopy (HAADF-STEM) imaging and energy dispersive X-ray (EDS) analysis of RGNs shows that Rh and Au are homogeneously alloyed with Rh:Au molar ratio of 0.03 (Figure 6.4d-e).

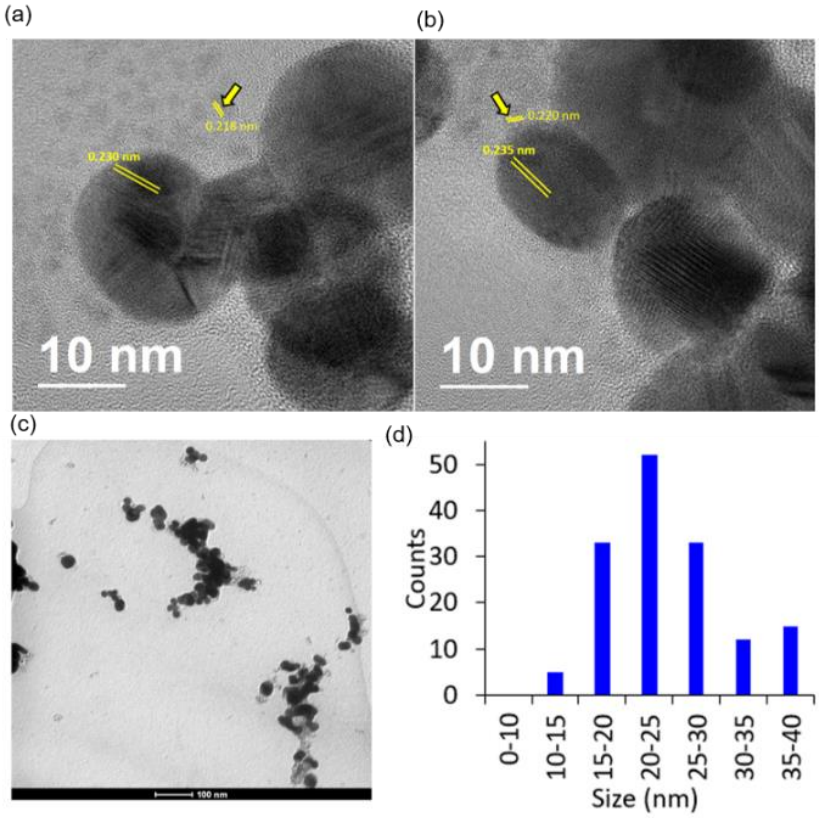

Figure 6.5: (a-b) Additional HRTEM images of the RGNs showing the increased d spacing of the particles in comparison with the pure Rh particles ($d_{<111>}$=0.219 nm). (a) Low-resolution TEM images of the RGNs transferred onto a TEM grid. (b) The particle size distribution of the RGNs showing a quasi-Gaussian distribution.

Since multiple nuclei are created via ultra-high supersaturation, there exists a small number of non-alloyed Rh particles (Figure 6.5a-b) besides relatively large-size RGNs.[8, 25] These observations are in agreement with what has been reported previously, wherein surface segregation of Rh was also observed for RGNs synthesized using microwave heating.[8] Low-resolution TEM imaging of RGNs reveals a pseudo-Gaussian distribution of particle sizes with an average size of 24.62 ± 6.38 nm (Figure 6.5c-d).

6.3.2 Chemical Characterizations

In addition to analyzing the structural integrity of the RGNs, we perform additional characterization to determine the chemical composition. SEM and EDS imaging of the structured RGNs shows the confinement of the reaction to the lines traversed by the incident laser (Figure 6.6a). The confinement of the reaction is confirmed by the Rh map showing lines along the trajectory of the laser. The Au maps are even due to the sputtered Au layer over the substrate to prevent charging. Further, X-ray photon spectroscopy (XPS) analysis of RGNs performed using a Kratos X-Ray Photoelectron Spectrometer-Axis Ultra DLD machine over a 300 × 500 μm^2 area showed that successful reduction of both Rh^{3+} and Au^{3+} has indeed occurred using the US^3 strategy discussed herein. For Rh, peaks corresponding to only Rh(0) are observed whereas a small fraction of Au(I) (a side product of Au^{3+} reduction) is also detected (Figure 6.6b). To validate the uniformity of the US^3 process, we obtained the transmission spectrum of the sample at random locations with 200 μm spacing. The localized transmission spectra of the sample are sensitive to the substrate's composition. The consistent spectra of the various sites on the sample with a narrow transmission dip of 561.46 ± 1.52 nm confirm the large-area structuring uniformity (Figure 6.6c).

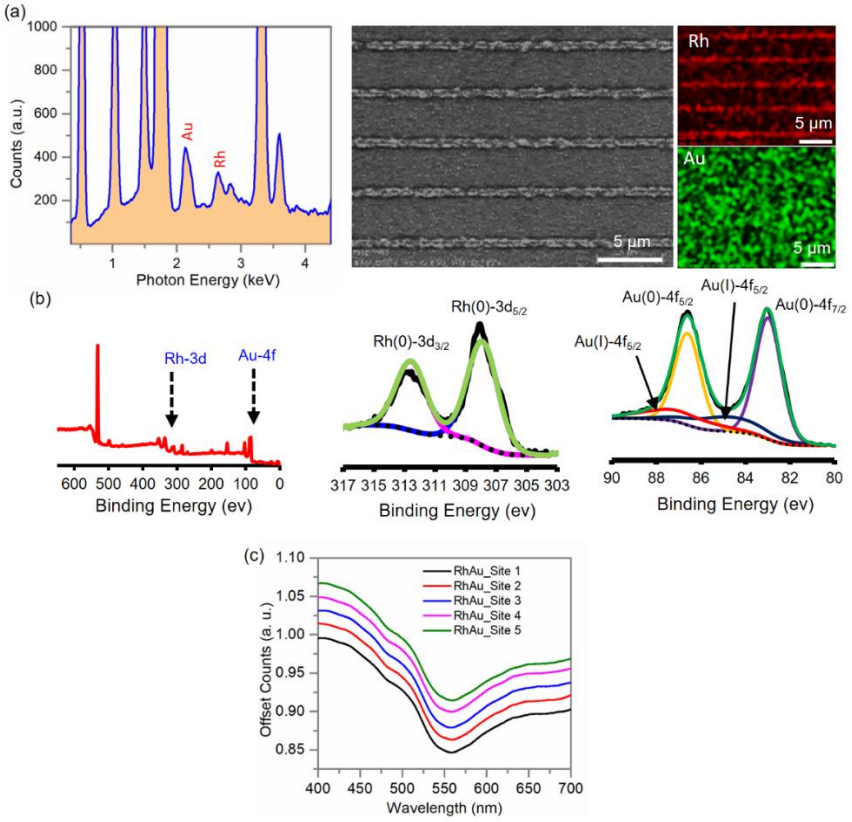

Figure 6.6: (a) EDS Spectra and 2D EDS mapping of the structured RGNs. (b) XPS of the RhAu sample with 2 µm line-spacing showing the surface characteristics of the sample. The molar ratio of Rh:Au obtained using XPS was 31:69 and 67% of the total detected Au was in the form of Au(0). Since maximum penetration depth of X-ray photoelectrons during analyses is only 8 nm, the entire structure of the resulting ≈25 nm RGNs cannot be probed using XPS and hence values obtained here are distinct from EDS analyses discussed above. (c) Transmission spectra of the sample at random locations spaced 200 µm away from each other.

6.4 US^3 MECHANISM

The prerequisite of the US^3 strategy is to attain ultra-fast supersaturation at the MBT. The ion accumulation phenomenon is simulated using random walk (RW) simulation, while the nucleation is modeled using classical nucleation theory and modified embedded atom method (MEAM).

6.4.1 Computational Fluid Dynamics and Random Walk Simulations

RW processes are one of the fundamental types of stochastic processes, with applications in neuron studies, operations theory, and so on.[26] RW has been used to study processes under thermal gradients, such as to determine the concentration increment of protobio-molecules toward high molecular aggregation,[1] and to determine pH cycling statistics.[3] Our temperature and flow profile around the MBT were simulated using existing modules in COMSOL.

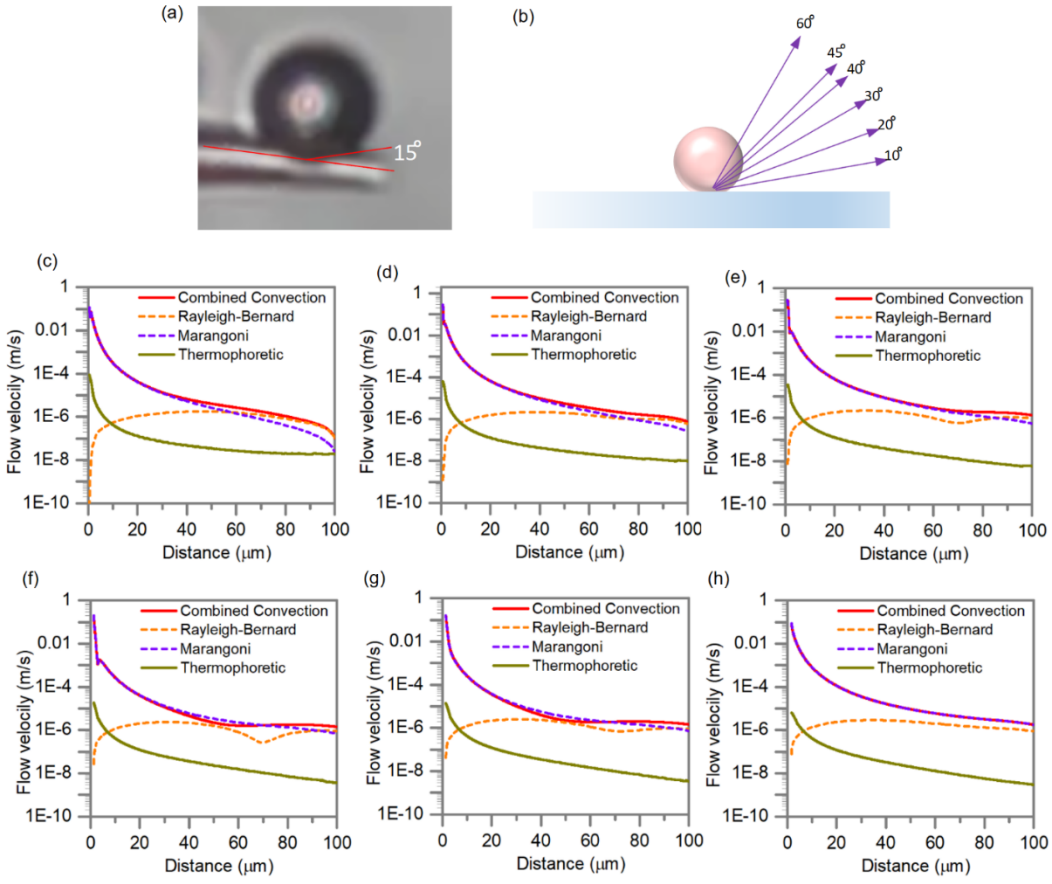

Figure 6.7: (a) A side view bright field image of the microbubble showing a contact angle of 15. (b) The angle-dependent comparative analysis of the three major flow velocity components evaluated at angles of (c) 10°, (d) 20°, (e) 30°, (f) 40°, (g) 45°, (g) 60°. The thermophoretic flow velocity is observed to be two-orders lower than convection velocities, and thus neglected in the random walk simulations.

The simulations were performed using finite-element solver (COMSOL Multiphysics). A 2D axis-symmetric model comprising of a glass substrate and water was established. The physics of the model includes pre-loaded modules of heat transfer in solids, liquids and non-isothermal laminar flow coupled with conjugate heat transfer physics. Marangoni flow within the laminar flow module is included in Multiphysics as the surface tension gradient on the bubble surface. Laser power absorbed by the gold substrate is modeled as Gaussian heat influx and is coupled with heat transfer in water using temperature continuity at the surface (Figure 6.8a-b). Other surfaces are maintained at room temperature of 293 K.

The surface tension on the bubble surface is modeled as a linear dependence with temperature and is given by Equation 1

$$\nabla\gamma = \frac{d\gamma}{dT} * \nabla T \tag{1}$$

Since $\frac{d\gamma}{dT}$ is approximately a constant for water over the range 0-100 ^{0}C, Equation 1 can be re-arranged as,

$$\gamma = \frac{d\gamma}{dT} * \Delta T + \gamma_0 \tag{2}$$

γ_0 is the reference surface tension at room temperature.

Upon the MBT generation, three primary phenomena influence the flow of ions in the solution: (i) Rayleigh Bernard (RB) convection velocity due to solution density gradient, (ii) Marangoni convection velocity due to bubble surface tension gradient, and (iii) thermophoretic drift velocity from inherent thermal gradient, an effect known as the Ludwig-Soret effect. An angular-dependent comparison reveals that Marangoni convection dominates in the vicinity of the MBT, while the thermophoretic drift velocity is at least two orders of magnitude less than the other individual components of the flow velocity (Figures 6.7a-h).

The flow profile is then imposed onto the ions and their trajectory is noted using RW simulation. To determine the concentration of ions near the bubble, the flow profile that is obtained from COMSOL simulations is incremented with Brownian motion and incremental displacement is evaluated using Equation 3.

$$\Delta s(r,z) = \sqrt{4D\Delta t}\eta(t) + \{v(x,y) + D * S_T * \nabla T(x,y)\}\Delta t \qquad (3)$$

where, $\Delta s(r,z)$ is the displacement of ion in a unit time step Δt, D is the diffusion coefficient, $\eta(t)$ is the viscosity, S_T is the Soret coefficient, $v\ (x,y)$ is the convective velocity at a given position and ∇T is the gradient of temperature.

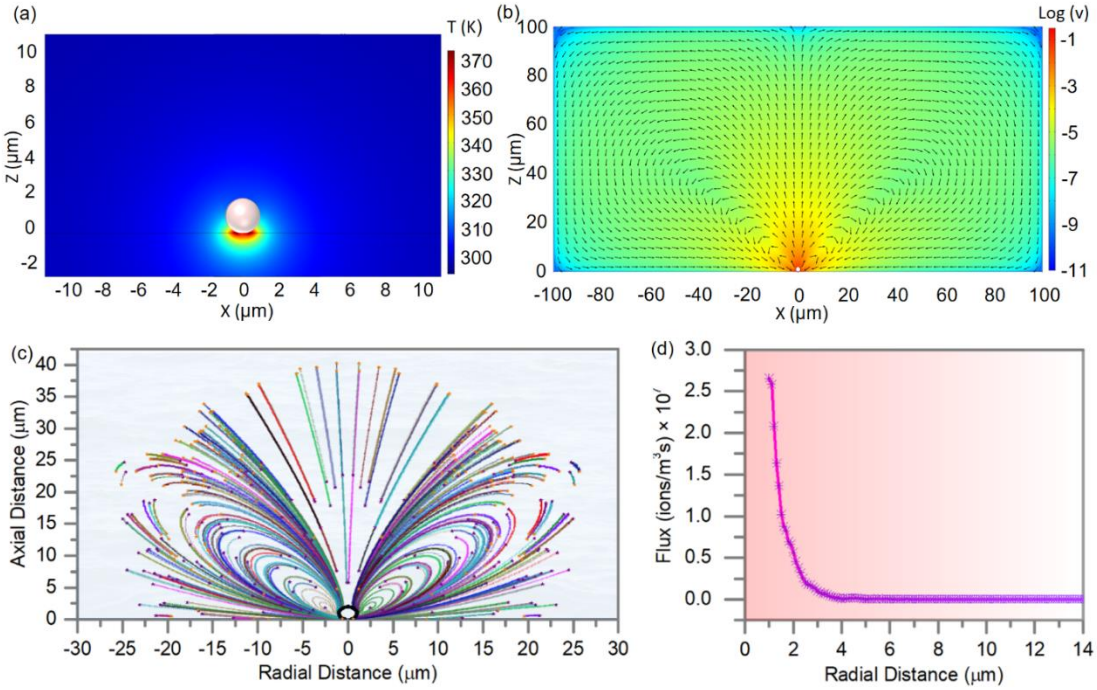

Figure 6.8: (a) Simulated temperature distribution in the vicinity of an MBT. The radius of the bubble is 1 μm. (b) Simulated flow velocity distribution around MBT with logarithmic scale in a cross-sectional view. (c) The trajectory of 200 ions simulated using the random walk simulations for a total time duration of 300 ms, showing the concentration of ions at the MBT/substrate interface. (d) The calculated incident ion flux, showing an exponential increase in the close vicinity of the MBT required to supplement the reduced ions.

Since the Marangoni velocity spans over several orders of magnitude (0.1 μm/s to 0.8 m/s), a dynamic time step is chosen to be inversely proportional to the velocity that the ion experiences at given spatial coordinates. The ion accumulation statistics in 300 ms timeframe are inferred from 5000 particles randomly distributed in 25 × 25 μm^2 area. Figure 6.8c shows a random selection of 200 ions and their simulated trajectories, while the ion trajectory shows the crucial role of Marangoni convection toward ultrafast accumulation. As the ions come closer to the three-phase contact (TPC) line (air/substrate/water), surface and capillary forces dominate within ~ 200 nm of the bubble, attracting the particles towards the TPC line.[27-28] In addition, near the MBT, counteracting Marangoni and capillary forces eventually lead to a stagnation point on the bubble surface, where the velocity of the flow is zero under the bubble and the particles reaching beyond this point head towards the TPC line.[29-30] By incorporating the stagnation phenomenon and the flow profile in RW simulation, an ultra-high supersaturation ratio of 27.2 ± 1.48 is observed. Further, the ion flux toward the MBT plays an important role in supersaturation, which increases linearly with the supply rate of ions. [31]

An exponential increase in the flux is observed in the vicinity of the MBT, helping maintain a high supersaturation value (Figure 6.8d). Ion flux plays an important role in supersaturation as supersaturation increases linearly with supply rate of ions/particles [2]. The following algorithm was employed to determine the ion in-flux near the bubble:

1. Distribute 1000 particles in the lower half region of 45^0 and run the simulation for $10\mu s$ with a timestep of 1 μs.
2. An imaginary cylindrical surface at a radial distance (r) is assumed with a height = radius.
3. Number of particles beyond this surface are counted as n_{start} at the start of the simulation and as n_{end} at the end of the simulation.

4. Number of ions crossing the surface (n) = $n_{start} - n_{end}$.

5. Flux can be calculated as the number of ions crossing the imaginary surface as:

$$Flux(r) = \frac{\frac{n_{start} - n_{end}}{1000} * NA * c_0}{2\pi r^2}$$

6.4.2 Thermodynamic Analysis

The MBT generation process is fast (< 10 ms) and, post MBT generation, the ions from within 10 µm vicinity reach the MBT in less than 1 ms (Figure 6.9). Instantaneous high ion saturation and multiple looping capabilities in conjunction with the elevated temperature at the MBT provide an ideal environment for the synthesis of RGNs.

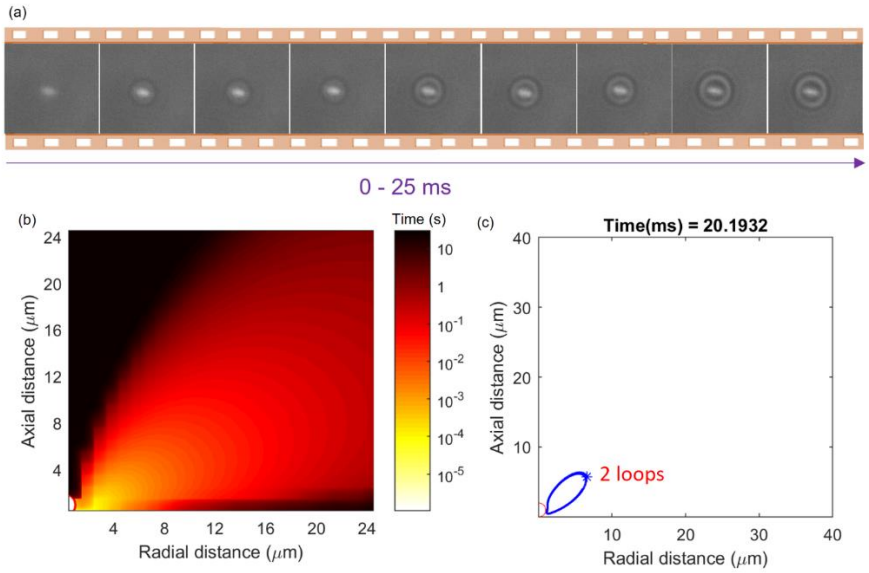

Figure 6.9: (a) Ultra-fast camera image revealing the ultra-fast generation of the MBT. (b) Contour plot showing the average time required for an ion to reach from a specific location to the MBT. A majority of the ions within 10 µm vicinity reach the MBT in less than 1 ms. (c) A typical trajectory of an ion which can perform multiple loops in millisecond timeframe.

The overall net free energy change accompanying the nucleation process can be expressed as the sum of a surface free energy term (ΔG_s) and a volumetric free energy term (Go),[24] according to Equation 4:

$$\Delta G(r) = \Delta G_s + \Delta G_v = 4\pi r^2\gamma - \frac{4}{3}\pi r^3 \frac{RTln(S)}{V_m} \qquad (4)$$

Where γ is the surface free energy per unit area, R is the universal gas constant, r is the NP radius, T is the temperature in Kelvin, S is the supersaturation ratio which is defined as the ratio of the number densities of the nucleating phase in the bulk and at coexistence, and V_m is the molar volume of the nucleating phase.[24] Since the volumetric and surface free energy terms are negative and positive in nature, respectively, there exists a critical radius (r_c) which is defined as a metastable state wherein any infinitesimal positive/negative variation from the critical radius will lead to a continuous growth/dissolution of the nucleating phase. The critical radius can be expressed as:

$$r^* = \frac{2\gamma V_m}{RT\ln(S)} \qquad (5)$$

Herein we plot the normalized critical radius for RGNs as a function of supersaturation (S). As seen in Figure 6.10a, the critical radius shows an exponential decrease with increasing S. A supersaturation of S ≈ 27 present in the asymptotic region results in the most favorable thermodynamic conditions for nucleation.

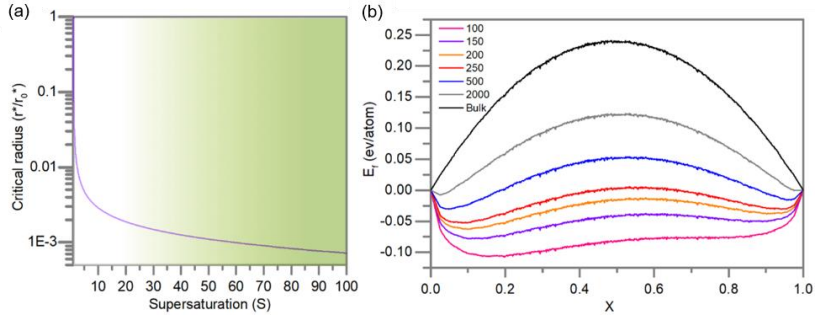

Figure 6.10: (a) The normalized critical nuclear radius as a function of supersaturation S, demonstrating a 3 order reduction in the radius. (b) The heat of formation E_f for RGNs at different Rh atomic concentration *x* and a total number of atoms of the NPs.

Further, we evaluate the alloying ability by calculating the heat of formation (E_f) for RGNs of different sizes from their monometallic constituents using a thermodynamic model and the modified embedded atom method (MEAM).[32] The heat of formation (E_f) for the RGNs under the assumption of homogeneously disordered NPs can be expressed as a function of the cohesive energies of its constituent elemental bulk and bulk alloy as:

$$E_f^{p\ A-B} = E_f^{b\ A-B}\left(1-\sqrt[3]{\frac{1}{N}}\right) - (1-x)E_c^{bA}\left(1-\sqrt[3]{\frac{1}{N(1-x)}}\right) - xE_c^{bB}\left(1-\sqrt[3]{\frac{1}{Nx}}\right) \quad (6)$$

Here, E_f represents the formation energy for an alloy particle containing N number of atoms (Au & Rh represented as A & B, respectively) with x being the chemical concentration of Rh in the RGN. The subscript p and b represent the cohesive energy (E_c) of NP and bulk alloy, respectively. The cohesive energies of the bulk alloy at x were calculated using MEAM interatomic potential for RhAu system.[33] The heat of formation shows a clear enhancement of alloying ability for all the range of Rh atomic concentration x with decreasing total number of atoms (Figure 6.10b). At the very initial growth stage, a negative heat of formation is obtained in full range of x, implying the favorability of RGN synthesis. In particular, the Au-rich region has more capability to accommodate RGN synthesis since the heat of formation is the lowest in this regime, which corroborates with the Au rich RGNs observed in the experimental results (Figure 6.4c). Since the MBT provides a micro-sized reaction region close to the TPC and convection-driven currents promote instantaneous supersaturation of the ions, spontaneous alloying of the NPs at lower temperatures is enabled. Post-synthesis, the RGNs are structured on the substrate as per the mechanism. These results reveal that the RGN synthesis shifts from a temperature-driven phenomenon at the bulk scale to a coalescence-driven phenomenon at the nanoscale.

6.5 CATALYSIS

The catalytic applications of metal nanoalloys have attracted significant interest.[15, 34-36] Specifically, RGNs have been established to exhibit enhanced activity as compared to individual Rh and Au components in reduction reactions.[8, 37] To evaluate the activity of the fabricated RGNs via US^3, we prepared millimeter-scale arrays of RGNs (Figure 6.11a inset) along with pristine Rh and Au substrates and used them to catalyze the well-studied reduction of *p*-nitrophenol with $NaBH_4$ into *p*-aminophenol. The pristine Rh substrate was fabricated by employing only $RhCl_3$ in the precursor solution.

The catalytic activity of RGNs and control substrates are measured by drop casting 15 μL of an aqueous p-nitrophenol solution (1.5 mmol/L) and 15 μL of a freshly prepared aqueous $NaBH_4$ solution (750 mmol/L) onto the millimeter-scale substrate. The drop was confined within a spacer to minimize water evaporation and the reaction was allowed to proceed for 1 h at room temperature. After completion, the droplet is collected and an additional 470 μL of deionized water was added to rinse the substrate and dilute the droplet. The final solution was transferred to a quartz cuvette to collect UV−visible absorption spectra (ThermoFisher, Genesis). The product and reactant peaks are at 296 nm and 400 nm, respectively. The change in the absorption at 400 nm was used to quantify reaction conversion.

All the nanoparticle substrates showed reduction in activity, with the conversion using the RGNs being the highest (Figures 6.11 a,b). During the fabrication, the RGNs are adhered strongly to the substrates and virtually no RGN-leaching is observed. Further, we explore the structure-property relationship by using US^3 to fabricate millimeter-scale RGNs with varied line-spacing of 2 μm, 4 μm and 8 μm. The EDS spectra normalized with the Au peak shows the reduction in the quantity of RGNs with increasing line-spacing (Figure 6.11c). The modulation is manifested into the catalytic performance, with the

RGNs with a spacing of 2 µm showing the highest activity (Figure 6.11d). The above results confirm the US^3 to be a feasible strategy to unify the synthesis and structuring of nanoalloys for catalytic applications.

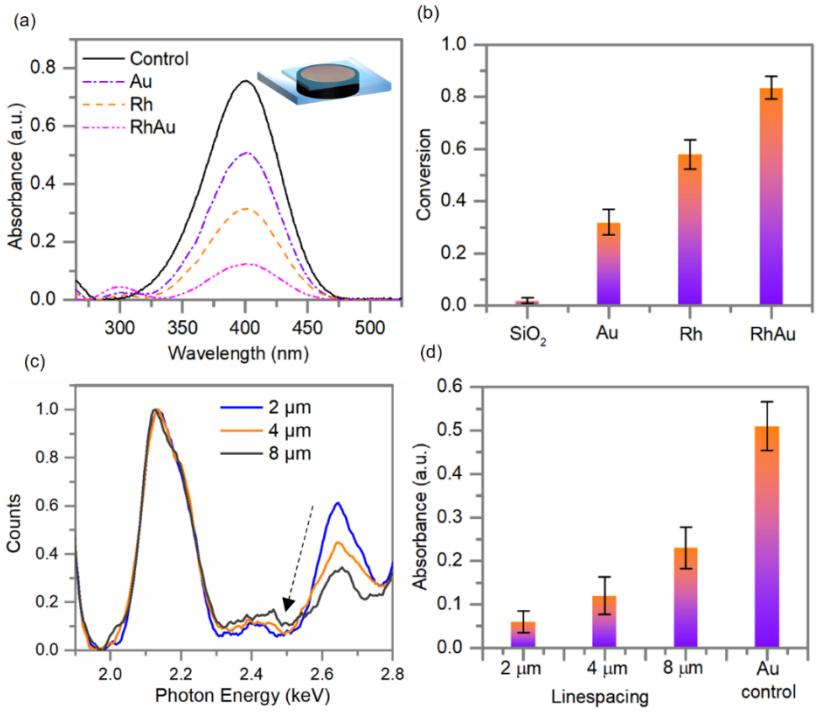

Figure 6.11: (a) UV-Visible absorption spectra showing the reduction of p-nitrophenol (pNP) catalyzed by the structured RGNs, Rh and Au substrates as well as control pNP solution. The inset shows the measurement configuration. (b) Conversation percentage of the reactants catalyzed by control samples (SiO_2, Rh and Au) and the RGNs. (c) EDS spectra of RGNs fabricated via US^3 with 2 µm, 4 µm and 8 µm line-spacing. The spectra are normalized with respect to Au peak. (d) Catalytic dependence of the RGNs on the line-spacing as characterized using the 400 nm reactant peak.

6.6 SUMMARY

In summary, we have successfully demonstrated the US^3 strategy wherein the in-situ synthesis and structuring of catalytically active RGNs are realized. In order to unify these discrete aspects, we synergize the ion accumulation effect, high fluid flow velocity

and site-selective temperature increment of a laser-induced MBT. HRTEM imaging reveals the complete mixing of the elements as well as their crystalline nature. RW and modified MEAM simulations justify the ion accumulation effect, and the subsequent multiple-order-of-magnitude reduction in the synthesis time. The structured RGNs are utilized for the reduction of pNP with the enhanced catalytic activity. With its unique advantages in in-situ synthesis and structuring and avoidance of surfactants, our US^3 strategy is promising for high-throughput development and screening of various multi-element nanomaterials with desired catalytic, optical, electronic and magnetic functions.

6.7 REFERENCES

1. Keil, L.; Hartmann, M.; Lanzmich, S.; Braun, D., Probing of molecular replication and accumulation in shallow heat gradients through numerical simulations. *Phys. Chem. Chem. Phys.* **2016,** *18* (30), 20153-20159.
2. Budin, I.; Bruckner, R. J.; Szostak, J. W., Formation of Protocell-like Vesicles in a Thermal Diffusion Column. *J. Am. Chem. Soc.* **2009,** *131* (28), 9628-9629.
3. Keil, L. M. R.; Moller, F. M.; Kiess, M.; Kudella, P. W.; Mast, C. B., Proton gradients and pH oscillations emerge from heat flow at the microscale. *Nat. Commun.* **2017,** *8*, 1897.
4. Liu, M.; Pang, Y. J.; Zhang, B.; De Luna, P.; Voznyy, O.; Xu, J. X.; Zheng, X. L.; Dinh, C. T.; Fan, F. J.; Cao, C. H.; de Arquer, F. P. G.; Safaei, T. S.; Mepham, A.; Klinkova, A.; Kumacheva, E.; Filleter, T.; Sinton, D.; Kelley, S. O.; Sargent, E. H., Enhanced electrocatalytic CO2 reduction via field-induced reagent concentration. *Nature* **2016,** *537* (7620), 382-386.
5. Grossier, R.; Magnaldo, A.; Veesler, S., Ultra-fast crystallization due to confinement. *J. Cryst. Growth* **2010,** *312* (4), 487-489.
6. He, R.; Wang, Y. C.; Wang, X. Y.; Wang, Z. T.; Liu, G.; Zhou, W.; Wen, L. P.; Li, Q. X.; Wang, X. P.; Chen, X. Y.; Zeng, J.; Hou, J. G., Facile synthesis of pentacle gold-copper alloy nanocrystals and their plasmonic and catalytic properties. *Nat. Commun.* **2014,** *5*, 4327.
7. Ferrando, R.; Jellinek, J.; Johnston, R. L., Nanoalloys: From theory to applications of alloy clusters and nanoparticles. *Chem. Rev.* **2008,** *108* (3), 845-910.
8. Garcia, S.; Zhang, L.; Piburn, G. W.; Henkelman, G.; Humphrey, S. M., Microwave Synthesis of Classically Immiscible Rhodium-Silver and Rhodium-Gold Alloy

Nanoparticles: Highly Active Hydrogenation Catalysts. *ACS Nano* **2014,** *8* (11), 11512-11521.

9. Swiatkowska-Warkocka, Z.; Pyatenko, A.; Krok, F.; Jany, B. R.; Marszalek, M., Synthesis of new metastable nanoalloys of immiscible metals with a pulse laser technique. *Sci. Rep.* **2015,** *5*, 9849.

10. Wang, D.; Villa, A.; Porta, F.; Prati, L.; Su, D. S., Bimetallic gold/palladium catalysts: Correlation between nanostructure and synergistic effects. *J. Phys. Chem. C* **2008,** *112* (23), 8617-8622.

11. Kunal, P.; Roberts, E. J.; Riche, C. T.; Jarvis, K.; Malrnstadt, N.; Brutchey, R. L.; Humphrey, S. M., Continuous Flow Synthesis of Rh and RhAg Alloy Nanoparticle Catalysts Enables Scalable Production and Improved Morphological Control. *Chem. Mater.* **2017,** *29* (10), 4341-4350.

12. Essinger-Hileman, E. R.; DeCicco, D.; Bondi, J. F.; Schaak, R. E., Aqueous room-temperature synthesis of Au-Rh, Au-Pt, Pt-Rh, and Pd-Rh alloy nanoparticles: fully tunable compositions within the miscibility gaps. *J. Mater. Chem.* **2011,** *21* (31), 11599-11604.

13. Yonezawa, T.; Toshima, N., Polymer-Protected and Micelle-Protected Gold Platinum Bimetallic Systems - Preparation, Application to Catalysis for Visible-Light-Induced Hydrogen Evolution, and Analysis of Formation Process with Optical Methods. *J. Mol. Catal.* **1993,** *83* (1-2), 167-181.

14. Endo, T.; Fukunaga, T.; Yoshimura, T.; Esumi, K., Scavenging DPPH radicals catalyzed by binary noble metal-dendrimer nanocomposites. *J. Colloid Interf. Sci.* **2006,** *302* (2), 516-521.

15. Chen, P. C.; Liu, G. L.; Zhou, Y.; Brown, K. A.; Chernyak, N.; Hedrick, J. L.; He, S.; Xie, Z.; Lin, Q. Y.; Dravid, V. P.; O'Neill-Slawecki, S. A.; Mirkin, C. A., Tip-Directed Synthesis of Multimetallic Nanoparticles. *J. Am. Chem. Soc.* **2015,** *137* (28), 9167-9173.

16. Zhang, D. S.; Goekce, B.; Barcikowski, S., Laser Synthesis and Processing of Colloids: Fundamentals and Applications. *Chem. Rev.* **2017,** *117* (5), 3990-4103.

17. Tominaga, Y.; Maruyama, M.; Yoshimura, M.; Koizumi, H.; Tachibana, M.; Sugiyama, S.; Adachi, H.; Tsukamoto, K.; Matsumura, H.; Takano, K.; Murakami, S.; Inoue, T.; Yoshikawa, H. Y.; Mori, Y., Promotion of protein crystal growth by actively switching crystal growth mode via femtosecond laser ablation. *Nat. Photon.* **2016,** *10* (11), 723-726.

18. Rajeeva, B. B.; Wu, Z. L.; Briggs, A.; Acharya, P. V.; Walker, S. B.; Peng, X. L.; Bahadur, V.; Bank, S. R.; Zheng, Y. B., "Point-and-Shoot" Synthesis of Metallic Ring Arrays and Surface-Enhanced Optical Spectroscopy. *Adv. Opt. Mat.* **2018,** *6* (10), 1701213.

19. Davies, R.; Dinsdale, A.; Gisby, J.; Robinson, J.; Martin, a. M., MTDATA-thermodynamic and phase equilibrium software from the national physical laboratory. *Calphad* **2002,** *26* (2), 229-271.

20. Fang, Z. Y.; Zhen, Y. R.; Neumann, O.; Polman, A.; de Abajo, F. J. G.; Nordlander, P.; Halas, N. J., Evolution of Light-Induced Vapor Generation at a Liquid-Immersed Metallic Nanoparticle. *Nano Lett.* **2013,** *13* (4), 1736-1742.

21. Lin, L. H.; Peng, X. L.; Mao, Z. M.; Li, W.; Yogeesh, M. N.; Rajeeva, B. B.; Perillo, E. P.; Dunn, A. K.; Akinwande, D.; Zheng, Y. B., Bubble-Pen Lithography. *Nano Lett.* **2016,** *16* (1), 701-708.

22. Rajeeva, B. B.; Lin, L. H.; Perillo, E. P.; Peng, X. L.; Yu, W. W.; Dunn, A. K.; Zheng, Y. B., High-Resolution Bubble Printing of Quantum Dots. *ACS Appl. Mater. Interfaces* **2017,** *9* (19), 16725-16733.

23. Zhakeyev, A.; Wang, P. F.; Zhang, L.; Shu, W. M.; Wang, H. Z.; Xuan, J., Additive Manufacturing: Unlocking the Evolution of Energy Materials. *Adv. Sci.* **2017,** *4* (10), 1700187.

24. Thanh, N. T. K.; Maclean, N.; Mahiddine, S., Mechanisms of Nucleation and Growth of Nanoparticles in Solution. *Chem. Rev.* **2014,** *114* (15), 7610-7630.

25. De Yoreo, J. J.; Vekilov, P. G., Principles of crystal nucleation and growth. *Biomineralization* **2003,** *54*, 57-93.

26. Weiss, G. H.; Rubin, R. J., Random-Walks - Theory and Selected Applications. *Adv. Chem. Phys.* **1983,** *52*, 363-505.

27. Preuss, M.; Butt, H. J., Direct measurement of forces between particles and bubbles. *Int. J. Miner. Process* **1999,** *56* (1-4), 99-115.

28. Fielden, M. L.; Hayes, R. A.; Ralston, J., Surface and capillary forces affecting air bubble-particle interactions in aqueous electrolyte. *Langmuir* **1996,** *12* (15), 3721-3727.

29. Wang, L. H.; Harris, M. T., Stagnation Point of Surface Flow during Drop Evaporation. *Langmuir* **2018,** *34* (20), 5918-5925.

30. Xu, X. F.; Luo, J. B., Marangoni flow in an evaporating water droplet. *Appl. Phys. Lett.* **2007,** *91* (12), 124102.

31. Shiba, F.; Okawa, Y., Relationship between supersaturation ratio and supply rate of solute in the growth process of monodisperse colloidal particles and application to AgHr systems. *J. Phys. Chem. B.* **2005,** *109* (46), 21664-21668.

32. Xiao, S.; Hu, W.; Luo, W.; Wu, Y.; Li, X.; Deng, H., Size effect on alloying ability and phase stability of immiscible bimetallic nanoparticles. *Eur. Phys. J. B* **2006,** *54* (4), 479-484.

33. Yang, J., Computationally assisted STEM and EXAFS characterization of tunable Rh/Au and Rh/Ag bimetallic nanoparticle catalysts. *Abstr. Pap. Am. Chem. Soc.* **2017,** *254*.

34. Chen, P. C.; Liu, X. L.; Hedrick, J. L.; Xie, Z.; Wang, S. Z.; Lin, Q. Y.; Hersam, M. C.; Dravid, V. P.; Mirkin, C. A., Polyelemental nanoparticle libraries. *Science* **2016,** *352* (6293), 1565-1569.

35. Holewinski, A.; Idrobo, J. C.; Linic, S., High-performance Ag-Co alloy catalysts for electrochemical oxygen reduction. *Nat. Chem.* **2014,** *6* (9), 828-834.

36. Zugic, B.; Wang, L. C.; Heine, C.; Zakharov, D. N.; Lechner, B. A. J.; Stach, E. A.; Biener, J.; Salmeron, M.; Madix, R. J.; Friend, C. M., Dynamic restructuring drives catalytic activity on nanoporous gold-silver alloy catalysts. *Nat. Mater.* **2017,** *16* (5), 558-564.

37. Li, H.; Luo, L.; Kunal, P.; Bonifacio, C. S.; Duan, Z. Y.; Yang, J. C.; Humphrey, S. M.; Crooks, R. M.; Henkelman, G., Oxygen Reduction Reaction on Classically Immiscible Bimetallics: A Case Study of RhAu. *J. Phys. Chem. C* **2018,** *122* (5), 2712-2716.

Chapter 7: Conclusion

7.1 SUMMARY

In conclusion, the immobilization of a variety of nanoparticles (NPs) and biomolecules was achieved by exploiting the nanoscale plasmonic effects. The fabrication was realized over a wide regime, ranging from single NP to large-area surfaces. The enhanced optical fields were utilized to enhance non-linear absorption phenomenon to achieve regioselective immobilization of BSA hydrogels on single Au nanotriangles with sub-25nm resolution. To extend the scope toward large-area immobilization, bubble printing over gold nanoisland (AuNI) substrate was developed and quantum dots (QDs) with multiple emission peaks were immobilized on both rigid and flexible substrates. The plasmon-QD coupling along with its influence on printing parameters was also investigated. Further, the photothermal effects of NP were used to induce chemical reduction of Ag from its precursor and simultaneously immobilize them on the substrate. Finally, the technique was demonstrated on a microfluidic device to achieve surface-enhanced optical spectroscopies. These preliminary studies establish the potential of plasmon-mediated NP/biomolecule immobilization. In my future work, I wish to extend the scope of my research to ultra-small sub-10nm NPs and into the fabrication of bimetallic NPs.

After systematic study and research over the last few years, I have achieved several milestones. My research work has resulted in 3 book chapters, and 18 peer-reviewed articles, including 7 first-authored articles, on high-profile journals such as *Nano Letters*, *ACS Nano, Advanced Science, Advanced Optical Materials, ACS Applied Materials & Interfaces,* and *Nano Research.* [1-20] My research work has also led to 2 filed patents and 10 conference presentations. Due to its significance, my work has been highlighted by >10 media outlets and published on the cover pages of 9 journals.

Figure 7.1: (a) Our work “"Point-and-Shoot" Synthesis of Metallic Ring Arrays and Surface-Enhanced Optical Spectroscopy” featured as Cover Picture by Advanced Optical Materials;[18] (b) Our work “Patterning and fluorescence tuning of quantum dots with haptic-interfaced bubble printing” featured as Back Cover by Journal of Materials Chemistry C;[11] (c) Our work “Regioselective Localization and Tracking of Biomolecules on Single Gold Nanoparticles” featured as Frontispiece by Advanced Science;[4] (d) Our work “Design and Applications of Lattice Plasmon Resonances” featured as Front Cover by Nano Research.[17]

Following is a description of my major research achievements during the doctoral study:

7.1.1 Immobilization at Single Nanoparticle Resolution

Conventionally, the realization of ultra-high sub 50nm resolution is highly challenging. In chapter 2, I have demonstrated regioselective positioning along with control over the amount of protein deposited on single gold nanotriangles (AuNTs) with ~10 nm positioning accuracy.[4] I have also shown the capability to track the changes occurring on a single AuNT using dark-field scattering spectroscopy and compared the experimental results with finite-difference time domain (FDTD) simulations. In addition, fluorescence lifetime imaging microscopy (FLIM) imaging was performed for additional confirmation of the immobilization. Our rapid and single-step protein immobilization technique along with single-nanoparticle dark-field monitoring can act as a framework to better understand

light-molecule interactions at the sub-nanoparticle level. These precisely controllable nanoparticle-biomolecule complexes have potential applications in nanophotonics, nanomedicine and life sciences.

7.1.2 Large-area Immobilization via Bubble Printing

In order to extend from a single nanoparticle immobilization regime to large-area patterning, I have developed a microbubble-mediated patterning strategy termed as bubble printing (BP). As detailed in chapter 3, we have demonstrated immobilization of QDs for the fabrication of patterned plasmon-QD hybrid structures.[12] To enable large-area printing capability, I have established high bubble stability as well as millisecond scale bubble generation and dissolution time. Bubble printing (BP) can simultaneously achieve high resolution (<1μm line-width), high throughput (>10^5 μm/s) and low material usage. I have extended the capability of BP by demonstrating immobilization of multi-color QDs on both rigid and flexible substrates. In chapter 4, I have shown the compatibility of BP with a haptic interface wherein designs drawn on a smartphone screen was replicated on the nanoscale.[11] In addition, the tunability of plasmon-QD coupling was demonstrated by modulating the printing parameters. The coupling resulted in enhanced emission rate of the QDs. With high resolution, multi-elemental compatibility and high throughput, BP will find applications in high-resolution QD display, high-density information storage, and biomedical assays.

7.1.3 One-step synthesis and patterning of metal nanoparticles and nanoalloys

The realms of nanoparticle synthesis and patterning have been predominantly explored as discrete aspects due to the complexity of each individual process. I have demonstrated the unification of synthesis and structuring steps, wherein millisecond-scale accumulation of the precursor ions in a highly confined laser-mediated microbubble trap

(MBT) drives ultra-fast alloy reactions in sync with the structuring process.[18] Initially, a one-step synthesis of Ag rings was demonstrated for surface-enhanced optical spectroscopies. I have also shown the technique's compatibility within spatially-constrained microfluidic systems. The technique's capability toward the bimetallic system was also shown using in-situ synthesis and structuring of catalytically active rhodium-gold nanoalloys (RGNs). The structured RGNs showed enhanced catalytic activity compared to pure Au and Rh. With its unique advantages in the *in-situ* synthesis and structuring and avoidance of surfactants, the integrated strategy is promising for high-throughput development and screening of various multi-element nanomaterials with desired catalytic, optical, electronic and magnetic functions.

7.2 FUTURE WORK

The wide array of applications outlined in this work highlight the flexibility of the plasmon-mediated immobilization platform. Despite our recent achievements in large-area bubble printing, the printing prototype's throughput can be significantly improved. To reach this goal, parallelized printing using a multi-beam setup will be further studied. The multiple laser beams can be generated using a spatial light modulator or a digital micromirror device.

The unified spatiotemporal synthesis and structuring (US^3) have unique advantages of acting as a nanoscale process intensifier as well as immobilizer. This capability can be utilized to extend toward multi-metallic element synthesis. By integration of multiple precursor solutions, trinary and quaternary metallic alloys can be synthesized. In addition, fabrication and characterization of high-entropy alloys (HEAs) can also be performed, which can result in material systems comprising unique physical and chemical properties.

Finally, the plasmon-mediated immobilization strategy can be integrated into a compact microfluidic device to fabricate a massively paralleled system capable of simultaneously studying and screening multi-elements. A multi-input and multi-channel microfluidic reactor can enable the spatiotemporal fabrication of new materials based on the initial precursor concentration. Such control also enables a design-driven approach wherein the concentrations of precursors can be pre-determined by employing dynamics (MD) simulations. Multi-elemental libraries containing a combination of elements such as Au, Pd, Rh, Ag, Pt, Cu, and Ni are of great interest towards optical, magnetic, sensing and catalytic applications. The spatiotemporal segregation within a microfluidic reactor further enables massively parallelized characterization based on optical spectroscopy techniques using a charged coupled device (CCD) spectrometer. These features will aid in the advancement of research for design-driven screening platforms with high throughput, limited material usage, and wider compatibility.

7.3 REFERENCES

1. Rajeeva, B. B.; Menz, R.; Zheng, Y. B., Towards rational design of multifunctional theranostic nanoparticles: what barriers do we need to overcome? *Nanomedicine* **2014,** *9* (12), 1767-1770.
2. Chen, K.; Rajeeva, B. B.; Wu, Z. L.; Rukavina, M.; Dao, T. D.; Ishii, S.; Aono, M.; Nagao, T.; Zheng, Y. B., Moire Nanosphere Lithography. *ACS Nano* **2015,** *9* (6), 6031-6040.
3. Gan, J. Y.; Lu, X. H.; Rajeeva, B. B.; Menz, R.; Tong, Y. X.; Zheng, Y. B., Efficient Photoelectrochemical Water Oxidation over Hydrogen-Reduced Nanoporous BiVO4 with Ni-B-i Electrocatalyst. *Chemelectrochem* **2015,** *2* (9), 1385-1395.
4. Rajeeva, B. B.; Hernandez, D. S.; Wang, M. S.; Perillo, E.; Lin, L. H.; Scarabelli, L.; Pingali, B.; Liz-Marzan, L. M.; Dunn, A. K.; Shear, J. B.; Zheng, Y. B., Regioselective Localization and Tracking of Biomolecules on Single Gold Nanoparticles. *Adv. Sci.* **2015,** *2* (11), 1500232.
5. Gan, J. Y.; Rajeeva, B. B.; Wu, Z. L.; Penley, D.; Liang, C. L.; Tong, Y. X.; Zheng, Y. B., Plasmon-enhanced nanoporous BiVO4 photoanodes for efficient photoelectrochemical water oxidation. *Nanotechnology* **2016,** *27* (23), 235401.

6. Gan, J. Y.; Rajeeva, B. B.; Wu, Z. L.; Penley, D.; Zheng, Y. B., Hydrogen-reduced bismuth oxyiodide nanoflake arrays with plasmonic enhancements for efficient photoelectrochemical water reduction. *Electrochim. Acta* **2016,** *219*, 20-27.

7. Lee, J.; Rajeeva, B. B.; Yuan, T. Y.; Guo, Z. H.; Lin, Y. H.; Al-Hashimi, M.; Zheng, Y. B.; Fang, L., Thermodynamic synthesis of solution processable ladder polymers. *Chem. Sci.* **2016,** *7* (2), 881-889.

8. Lin, L. H.; Peng, X. L.; Mao, Z. M.; Li, W.; Yogeesh, M. N.; Rajeeva, B. B.; Perillo, E. P.; Dunn, A. K.; Akinwande, D.; Zheng, Y. B., Bubble-Pen Lithography. *Nano Lett.* **2016,** *16* (1), 701-708.

9. Wang, M. S.; Rajeeva, B. B.; Scarabelli, L.; Perillo, E. P.; Dunn, A. K.; Liz-Marzan, L. M.; Zheng, Y. B., Molecular-Fluorescence Enhancement via Blue-Shifted Plasmon-Induced Resonance Energy Transfer. *J. Phys. Chem. C.* **2016,** *120* (27), 14820-14827.

10. Wu, Z. L.; Kelp, G.; Yogeesh, M. N.; Li, W.; McNicholas, K. M.; Briggs, A.; Rajeeva, B. B.; Akinwande, D.; Bank, S. R.; Shvets, G.; Zheng, Y. B., Dual-band moire metasurface patches for multifunctional biomedical applications. *Nanoscale* **2016,** *8* (43), 18461-18468.

11. Rajeeva, B. B.; Alabandi, M. A.; Lin, L. H.; Perillo, E. P.; Dunn, A. K.; Zheng, Y. B., Patterning and fluorescence tuning of quantum dots with haptic-interfaced bubble printing. *J. Mater. Chem. C.* **2017,** *5* (23), 5693-5699.

12. Rajeeva, B. B.*; Lin, L. H.*; Perillo, E. P.; Peng, X. L.; Yu, W. W.; Dunn, A. K.; Zheng, Y. B., High-Resolution Bubble Printing of Quantum Dots. *ACS Appl. Mater. Inter.* **2017,** *9* (19), 16725-16733.

13. Wang, M. S.; Hartmann, G.; Wu, Z. L.; Scarabelli, L.; Rajeeva, B. B.; Jarrett, J. W.; Perillo, E. P.; Dunn, A. K.; Liz-Marzan, L. M.; Hwang, G. S.; Zheng, Y. B., Controlling Plasmon-Enhanced Fluorescence via Intersystem Crossing in Photoswitchable Molecules. *Small* **2017,** *13* (38), 1701763.

14. Wang, M. S.; Li, W.; Scarabelli, L.; Rajeeva, B. B.; Terrones, M.; Liz-Marzan, L. M.; Akinwande, D.; Zheng, Y. B., Plasmon-trion and plasmon-exciton resonance energy transfer from a single plasmonic nanoparticle to monolayer MoS2. *Nanoscale* **2017,** *9* (37), 13947-13955.

15. Lin, L.; Li, J.; Li, W.; Yogeesh, M. N.; Shi, J.; Peng, X.; Liu, Y.; Rajeeva, B. B.; Becker, M. F.; Liu, Y.; Zheng, Y., Optothermoplasmonic Nanolithography for On-Demand Patterning of 2D Materials. *Adv. Funct. Mater.* **2018,** *28* (41), 1803990.

16. Liu, Y.*; Lin, L.*; Bangalore Rajeeva, B.*; Jarrett, J. W.; Li, X.; Peng, X.; Kollipara, P.; Yao, K.; Akinwande, D.; Dunn, A. K.; Zheng, Y., Nanoradiator-Mediated Deterministic Opto-Thermoelectric Manipulation. *ACS Nano* **2018,** *12* (10), 10383-10392.

17. Rajeeva, B. B.; Lin, L.; Zheng, Y., Design and Applications of Lattice Plasmon Resonances. *Nano Res.* **2018,** *11* (9), 4423-4440.

18. Rajeeva, B. B.; Wu, Z. L.; Briggs, A.; Acharya, P. V.; Walker, S. B.; Peng, X. L.; Bahadur, V.; Bank, S. R.; Zheng, Y., "Point-and-Shoot" Synthesis of Metallic Ring Arrays and Surface-Enhanced Optical Spectroscopy. Adv. Opt. Mater. **2018**, *6* (10), 1701213.

19. Rajeeva, B. B.; Zheng, Y. B. "Molecular plasmonics: From molecular-scale measurements and control to applications." Nanotechnology: Delivering on the Promise Volume 2. American Chemical Society, **2016**, *2*, 23-52.

20. Peng, X.; Rajeeva, B. B.; Teal, D.; Zheng, Y. "Plasmofluidics for Biosensing and Medical Diagnostics." Nanotechnology Characterization Tools for Biosensing and Medical Diagnosis. Springer, Berlin, Heidelberg, **2018**, 213-247.

Bibliography

Chapter 1

1. Lohse, S. E.; Murphy, C. J., Applications of Colloidal Inorganic Nanoparticles: From Medicine to Energy. *J Am Chem Soc* **2012,** *134* (38), 15607-15620.
2. Howes, P. D.; Chandrawati, R.; Stevens, M. M., Colloidal nanoparticles as advanced biological sensors. *Science* **2014,** *346* (6205), 53.
3. Pellegrino, T.; Kudera, S.; Liedl, T.; Javier, A. M.; Manna, L.; Parak, W. J., On the development of colloidal nanoparticles towards multifunctional structures and their possible use for biological applications. *Small* **2005,** *1* (1), 48-63.
4. De Jong, W. H.; Borm, P. J. A., Drug delivery and nanoparticles: Applications and hazards. *Int. J. Nanomed.* **2008,** *3* (2), 133-149.
5. Murray, C. B.; Norris, D. J.; Bawendi, M. G., Synthesis and Characterization of Nearly Monodisperse Cde (E = S, Se, Te) Semiconductor Nanocrystallites. *J. Am. Chem. Soc.* **1993,** *115* (19), 8706-8715.
6. Brust, M.; Walker, M.; Bethell, D.; Schiffrin, D. J.; Whyman, R., Synthesis of thiol-derivatised gold nanoparticles in a two-phase liquid–liquid system. *Chem. Commun.* **1994,** (7), 801-802.
7. Xiu, Z. M.; Zhang, Q. B.; Puppala, H. L.; Colvin, V. L.; Alvarez, P. J. J., Negligible Particle-Specific Antibacterial Activity of Silver Nanoparticles. *Nano Lett.* **2012,** *12* (8), 4271-4275.
8. Goesmann, H.; Feldmann, C., Nanoparticulate Functional Materials. *Angew. Chem. Int. Edit.* **2010,** *49* (8), 1362-1395.
9. Rajeeva, B. B.; Menz, R.; Zheng, Y. B., Towards rational design of multifunctional theranostic nanoparticles: what barriers do we need to overcome? *Nanomedicine* **2014,** *9* (12), 1767-1770.
10. Wolfbeis, O. S., An overview of nanoparticles commonly used in fluorescent bioimaging. *Chem. Soc. Rev.* **2015,** *44* (14), 4743-4768.
11. Michalet, X.; Pinaud, F. F.; Bentolila, L. A.; Tsay, J. M.; Doose, S.; Li, J. J.; Sundaresan, G.; Wu, A. M.; Gambhir, S. S.; Weiss, S., Quantum dots for live cells, in vivo imaging, and diagnostics. *Science* **2005,** *307* (5709), 538-544.
12. Winnik, F. M.; Maysinger, D., Quantum Dot Cytotoxicity and Ways To Reduce It. *Acc. Chem. Res.* **2013,** *46* (3), 672-680.
13. Dreaden, E. C.; Alkilany, A. M.; Huang, X. H.; Murphy, C. J.; El-Sayed, M. A., The golden age: gold nanoparticles for biomedicine. *Chem. Soc. Rev.* **2012,** *41* (7), 2740-2779.

14. You, J. B.; Meng, L.; Song, T. B.; Guo, T. F.; Yang, Y.; Chang, W. H.; Hong, Z. R.; Chen, H. J.; Zhou, H. P.; Chen, Q.; Liu, Y. S.; De Marco, N.; Yang, Y., Improved air stability of perovskite solar cells via solution-processed metal oxide transport layers. *Nat. Nanotechnol.* **2016,** *11* (1), 75-81.

15. Chakraborty, I.; Pradeep, T., Atomically Precise Clusters of Noble Metals: Emerging Link between Atoms and Nanoparticles. *Chem. Rev.* **2017,** *117* (12), 8208-8271.

16. Saldanha, P. L.; Lesnyak, V.; Manna, L., Large scale syntheses of colloidal nanomaterials. *Nano Today* **2017,** *12*, 46-63.

17. Shen, C. Q.; Lan, X.; Zhu, C. G.; Zhang, W.; Wang, L. Y.; Wang, Q. B., Spiral Patterning of Au Nanoparticles on Au Nanorod Surface to Form Chiral AuNR@AuNP Helical Superstructures Templated by DNA Origami. *Adv. Mat.* **2017,** *29* (16), 1606533.

18. Kagan, C. R.; Lifshitz, E.; Sargent, E. H.; Talapin, D. V., Building devices from colloidal quantum dots. *Science* **2016,** *353* (6302), 885.

19. Zhu, J.; Hersam, M. C., Assembly and Electronic Applications of Colloidal Nanomaterials. *Adv. Mat.* **2017,** *29* (4), 1603895.

20. Kershaw, S. V.; Jing, L. H.; Huang, X. D.; Gao, M. Y.; Rogach, A. L., Materials aspects of semiconductor nanocrystals for optoelectronic applications. *Mater. Horiz.* **2017,** *4* (2), 155-205.

21. Wang, Y. Y.; Fedin, I.; Zhang, H.; Talapin, D. V., Direct optical lithography of functional inorganic nanomaterials. *Science* **2017,** *357* (6349), 385-388.

22. Hou, J.; Li, M. Z.; Song, Y. L., Patterned Colloidal Photonic Crystals. *Angew. Chem. Int. Edit.* **2018,** *57* (10), 2544-2553.

23. Zhang, N.; Sun, W. Z.; Rodrigues, S. P.; Wang, K. Y.; Gu, Z. Y.; Wang, S.; Cai, W. S.; Xiao, S. M.; Song, Q. H., Highly Reproducible Organometallic Halide Perovskite Microdevices based on Top-Down Lithography. *Adv. Mat.* **2017,** *29* (15), 1606205.

24. Rajoua, K.; Baklouti, L.; Favier, F., Electronic and Mechanical Antagonist Effects in Resistive Hydrogen Sensors Based on Pd@Au Core-Shell Nanoparticle Assemblies Prepared by Langmuir-Blodgett. *J. Phys. Chem. C* **2015,** *119* (18), 10130-10139.

25. Kim, B. H.; Nam, S.; Oh, N.; Cho, S. Y.; Yu, K. J.; Lee, C. H.; Zhang, J. Q.; Deshpande, K.; Trefonas, P.; Kim, J. H.; Lee, J.; Shin, J. H.; Yu, Y.; Lim, J. B.; Won, S. M.; Cho, Y. K.; Kim, N. H.; Seo, K. J.; Lee, H.; Kim, T. I.; Shim, M.; Rogers, J. A., Multilayer Transfer Printing for Pixelated, Multicolor Quantum Dot Light-Emitting Diodes. *ACS Nano* **2016,** *10* (5), 4920-4925.

26. Homenick, C. M.; James, R.; Lopinski, G. P.; Dunford, J.; Sun, J.; Park, H.; Jung, Y.; Cho, G.; Malenfant, P. R. L., Fully Printed and Encapsulated SWCNT-Based

Thin Film Transistors via a Combination of R2R Gravure and Inkjet Printing. *ACS Appl. Mater. Interfaces* **2016,** *8* (41), 27900-27910.

27. You, M. L.; Zhong, J. J.; Hong, Y.; Duan, Z. F.; Lin, M.; Xu, F., Inkjet printing of upconversion nanoparticles for anti-counterfeit applications. *Nanoscale* **2015,** *7* (10), 4423-4431.

28. Kim, B. H.; Onses, M. S.; Lim, J. B.; Nam, S.; Oh, N.; Kim, H.; Yu, K. J.; Lee, J. W.; Kim, J. H.; Kang, S. K.; Lee, C. H.; Lee, J.; Shin, J. H.; Kim, N. H.; Leal, C.; Shim, M.; Rogers, J. A., High-Resolution Patterns of Quantum Dots Formed by Electrohydrodynamic Jet Printing for Light-Emitting Diodes. *Nano Lett.* **2015,** *15* (2), 969-973.

29. Homola, J., Surface plasmon resonance sensors for detection of chemical and biological species. *Chem. Rev.* **2008,** *108* (2), 462-493.

30. Homola, J., Present and future of surface plasmon resonance biosensors. *Anal. Bioanal. Chem.* **2003,** *377* (3), 528-539.

31. Wang, M. S.; Li, W.; Scarabelli, L.; Rajeeva, B. B.; Terrones, M.; Liz-Marzan, L. M.; Akinwande, D.; Zheng, Y. B., Plasmon-trion and plasmon-exciton resonance energy transfer from a single plasmonic nanoparticle to monolayer MoS2. *Nanoscale* **2017,** *9* (37), 13947-13955.

32. Zayats, A. V.; Smolyaninov, I. I.; Maradudin, A. A., Nano-optics of surface plasmon polaritons. *Phys. Rep.* **2005,** *408* (3-4), 131-314.

33. Zhang, Z. L.; Fang, Y. R.; Wang, W. H.; Chen, L.; Sun, M. T., Propagating Surface Plasmon Polaritons: Towards Applications for Remote-Excitation Surface Catalytic Reactions. *Adv. Sci.* **2016,** *3* (1), 1500215.

34. Echtermeyer, T. J.; Milana, S.; Sassi, U.; Eiden, A.; Wu, M.; Lidorikis, E.; Ferrari, A. C., Surface Plasmon Polariton Graphene Photodetectors. *Nano Lett.* **2016,** *16* (1), 8-20.

35. Ee, H. S.; No, Y. S.; Kim, J.; Park, H. G.; Seo, M. K., Long-range surface plasmon polariton detection with a graphene photodetector. *Opt. Lett.* **2018,** *43* (12), 2889-2892.

36. Baffou, G.; Quidant, R., Thermo-plasmonics: using metallic nanostructures as nano-sources of heat. *Laser Photonics Rev.* **2013,** *7* (2), 171-187.

37. Fan, X.; Zheng, W.; Singh, D. J., Light scattering and surface plasmons on small spherical particles. *Light Sci. Appl.* **2014,** *3*, e179.

38. Luther, J. M.; Jain, P. K.; Ewers, T.; Alivisatos, A. P., Localized surface plasmon resonances arising from free carriers in doped quantum dots. *Nat. Mater.* **2011,** *10*, 361.

39. Schuller, J. A.; Barnard, E. S.; Cai, W. S.; Jun, Y. C.; White, J. S.; Brongersma, M. L., Plasmonics for extreme light concentration and manipulation. *Nat. Mater.* **2010,** *9* (3), 193-204.

40. Lakowicz, J. R., Plasmonics in biology and plasmon-controlled fluorescence. *Plasmonics* **2006,** *1* (1), 5-33.

41. Eggleston, M. S.; Messer, K.; Zhang, L. M.; Yablonovitch, E.; Wu, M. C., Optical antenna enhanced spontaneous emission. *Proc. Natl. Acad. Sci. USA.* **2015,** *112* (6), 1704-1709.

42. Cai, Y. Y.; Liu, J. G.; Tauzin, L. J.; Huang, D.; Sung, E.; Zhang, H.; Joplin, A.; Chang, W. S.; Nordlander, P.; Link, S., Photoluminescence of Gold Nanorods: Purcell Effect Enhanced Emission from Hot Carriers. *ACS Nano* **2018,** *12* (2), 976-985.

43. Hoang, T. B.; Akselrod, G. M.; Argyropoulos, C.; Huang, J. N.; Smith, D. R.; Mikkelsen, M. H., Ultrafast spontaneous emission source using plasmonic nanoantennas. *Nat. Commun.* **2015,** *6*, 7788.

44. Kinkhabwala, A.; Yu, Z.; Fan, S.; Avlasevich, Y.; Müllen, K.; Moerner, W. E., Large single-molecule fluorescence enhancements produced by a bowtie nanoantenna. *Nat. Photon.* **2009,** *3*, 654.

Chapter 2:

1. Deng, W.; Xie, F.; Baltar, H. T.; Goldys, E. M., Metal-enhanced fluorescence in the life sciences: here, now and beyond. *Phys. Chem. Chem. Phys.* **2013,** *15* (38), 15695-15708.

2. Darvill, D.; Centeno, A.; Xie, F., Plasmonic fluorescence enhancement by metal nanostructures: shaping the future of bionanotechnology. *Phys. Chem. Chem. Phys.* **2013,** *15* (38), 15709-15726.

3. Tam, F.; Goodrich, G. P.; Johnson, B. R.; Halas, N. J., Plasmonic enhancement of molecular fluorescence. *Nano Lett.* **2007,** *7* (2), 496-501.

4. Shiohara, A.; Wang, Y.; Liz-Marzán, L. M., Recent approaches toward creation of hot spots for SERS detection. *J. Photochem. Photobiol. C: Photochem. Rev.* **2014,** *21*, 2-25.

5. Li, W.; Camargo, P. H.; Lu, X.; Xia, Y., Dimers of silver nanospheres: facile synthesis and their use as hot spots for surface-enhanced Raman scattering. *Nano Lett.* **2008,** *9* (1), 485-490.

6. Hsu, K. H.; Back, J. H.; Fung, K. H.; Ferreira, P. M.; Shim, M.; Fang, N. X., SERS EM field enhancement study through fast Raman mapping of Sierpinski carpet arrays. *J. Raman Spectrosc.* **2010,** *41* (10), 1124-1130.

7. Rodríguez-Fernández, J.; Funston, A. M.; Pérez-Juste, J.; Álvarez-Puebla, R. A.; Liz-Marzán, L. M.; Mulvaney, P., The effect of surface roughness on the plasmonic response of individual sub-micron gold spheres. *Phys. Chem. Chem. Phys.* **2009,** *11* (28), 5909-5914.

8. Tsoutsi, D.; Guerrini, L.; Hermida-Ramon, J. M.; Giannini, V.; Liz-Marzán, L. M.; Wei, A.; Alvarez-Puebla, R. A., Simultaneous SERS detection of copper and cobalt at ultratrace levels. *Nanoscale* **2013,** *5* (13), 5841-5846.

9. Lal, S.; Grady, N. K.; Kundu, J.; Levin, C. S.; Lassiter, J. B.; Halas, N. J., Tailoring plasmonic substrates for surface enhanced spectroscopies. *Chem. Soc. Rev.* **2008,** *37* (5), 898-911.

10. Le, F.; Brandl, D. W.; Urzhumov, Y. A.; Wang, H.; Kundu, J.; Halas, N. J.; Aizpurua, J.; Nordlander, P., Metallic nanoparticle arrays: a common substrate for both surface-enhanced Raman scattering and surface-enhanced infrared absorption. *ACS Nano* **2008,** *2* (4), 707-718.

11. Brown, L. V.; Zhao, K.; King, N.; Sobhani, H.; Nordlander, P.; Halas, N. J., Surface-Enhanced Infrared Absorption Using Individual Cross Antennas Tailored to Chemical Moieties. *J. Am. Chem. Soc.* **2013,** *135* (9), 3688-3695.

12. Camden, J. P.; Dieringer, J. A.; Wang, Y.; Masiello, D. J.; Marks, L. D.; Schatz, G. C.; Van Duyne, R. P., Probing the structure of single-molecule surface-enhanced Raman scattering hot spots. *J. Am. Chem. Soc.* **2008,** *130* (38), 12616-12617.

13. Cang, H.; Labno, A.; Lu, C.; Yin, X.; Liu, M.; Gladden, C.; Liu, Y.; Zhang, X., Probing the electromagnetic field of a 15-nanometre hotspot by single molecule imaging. *Nature* **2011,** *469* (7330), 385-388.

14. Guan, Z.; Polavarapu, L.; Xu, Q.-H., Enhanced two-photon emission in coupled metal nanoparticles induced by conjugated polymers. *Langmuir* **2010,** *26* (23), 18020-18023.

15. Ward, D. R.; Hüser, F.; Pauly, F.; Cuevas, J. C.; Natelson, D., Optical rectification and field enhancement in a plasmonic nanogap. *Nat. Nanotechnol.* **2010,** *5* (10), 732-736.

16. Ko, K. D.; Kumar, A.; Fung, K. H.; Ambekar, R.; Liu, G. L.; Fang, N. X.; Toussaint Jr, K. C., Nonlinear optical response from arrays of Au bowtie nanoantennas. *Nano Lett.* **2011,** *11* (1), 61-65.

17. Sundaramurthy, A.; Schuck, P. J.; Conley, N. R.; Fromm, D. P.; Kino, G. S.; Moerner, W., Toward nanometer-scale optical photolithography: utilizing the near-field of bowtie optical nanoantennas. *Nano Lett.* **2006,** *6* (3), 355-360.

18. Nah, S.; Li, L.; Fourkas, J. T., Field-Enhanced Phenomena of Gold Nanoparticles. *J. Phys. Chem. A* **2009,** *113* (16), 4416-4422.

19. Saboktakin, M.; Ye, X.; Chettiar, U. K.; Engheta, N.; Murray, C. B.; Kagan, C. R., Plasmonic enhancement of nanophosphor upconversion luminescence in Au nanohole arrays. *ACS Nano* **2013,** *7* (8), 7186-7192.

20. Metzger, B.; Hentschel, M.; Schumacher, T.; Lippitz, M.; Ye, X.; Murray, C. B.; Knabe, B.; Buse, K.; Giessen, H., Doubling the efficiency of third harmonic generation by positioning ITO nanocrystals into the hot-spot of plasmonic gap-antennas. *Nano Lett.* **2014,** *14* (5), 2867-2872.

21. Ropp, C.; Cummins, Z.; Nah, S.; Fourkas, J. T.; Shapiro, B.; Waks, E., Nanoscale imaging and spontaneous emission control with a single nano-positioned quantum dot. *Nat. Commun.* **2013,** *4*, 1447.

22. Bek, A.; Jansen, R.; Ringler, M.; Mayilo, S.; Klar, T. A.; Feldmann, J., Fluorescence enhancement in hot spots of AFM-designed gold nanoparticle sandwiches. *Nano Lett.* **2008,** *8* (2), 485-490.

23. Rodríguez-Lorenzo, L.; Alvarez-Puebla, R. A.; Pastoriza-Santos, I.; Mazzucco, S.; Stéphan, O.; Kociak, M.; Liz-Marzán, L. M.; García de Abajo, F. J., Zeptomol detection through controlled ultrasensitive surface-enhanced Raman scattering. *J. Am. Chem. Soc.* **2009,** *131* (13), 4616-4618.

24. Feuz, L.; Jonsson, M. P.; Höök, F., Material-selective surface chemistry for nanoplasmonic sensors: optimizing sensitivity and controlling binding to local hot spots. *Nano Lett.* **2012,** *12* (2), 873-879.

25. Nah, S.; Li, L.; Liu, R.; Hao, J.; Lee, S. B.; Fourkas, J. T., Metal-enhanced multiphoton absorption polymerization with gold nanowires. *J. Phys. Chem. C* **2010,** *114* (17), 7774-7779.

26. Diebold, E. D.; Mack, N. H.; Doorn, S. K.; Mazur, E., Femtosecond laser-nanostructured substrates for surface-enhanced Raman scattering. *Langmuir* **2009,** *25* (3), 1790-1794.

27. Diebold, E. D.; Peng, P.; Mazur, E., Isolating surface-enhanced Raman scattering hot spots using multiphoton lithography. *J. Am. Chem. Soc.* **2009,** *131* (45), 16356-16357.

28. Maruo, S.; Fourkas, J. T., Recent progress in multiphoton microfabrication. *Laser Photonics Rev.* **2008,** *2* (1-2), 100-111.

29. Ueno, K.; Juodkazis, S.; Shibuya, T.; Yokota, Y.; Mizeikis, V.; Sasaki, K.; Misawa, H., Nanoparticle plasmon-assisted two-photon polymerization induced by incoherent excitation source. *J. Am. Chem. Soc.* **2008,** *130* (22), 6928-6929.

30. Ueno, K.; Takabatake, S.; Nishijima, Y.; Mizeikis, V.; Yokota, Y.; Misawa, H., Nanogap-assisted surface plasmon nanolithography. *J. Phys. Chem. Lett.* **2010,** *1* (3), 657-662.

31. Geldhauser, T.; Ikegaya, S.; Kolloch, A.; Murazawa, N.; Ueno, K.; Boneberg, J.; Leiderer, P.; Scheer, E.; Misawa, H., Visualization of near-field enhancements of gold triangles by nonlinear photopolymerization. *Plasmonics* **2011,** *6* (2), 207-212.

32. Gruber, C.; Hirzer, A.; Schmidt, V.; Trügler, A.; Hohenester, U.; Ditlbacher, H.; Hohenau, A.; Krenn, J. R., Imaging nanowire plasmon modes with two-photon polymerization. *Appl. Phys. Lett.* **2015,** *106* (8), 081101.

33. Murazawa, N.; Ueno, K.; Mizeikis, V.; Juodkazis, S.; Misawa, H., Spatially selective nonlinear photopolymerization induced by the near-field of surface plasmons localized on rectangular gold nanorods. *J. Phys. Chem. C* **2009,** *113* (4), 1147-1149.

34. Hsiao, V. K.; Zheng, Y. B.; Juluri, B. K.; Huang, T. J., Light-driven plasmonic switches based on au nanodisk arrays and photoresponsive liquid crystals. *Adv. Mater.* **2008,** *20* (18), 3528-3532.

35. Zheng, Y. B.; Juluri, B. K.; Lin Jensen, L.; Ahmed, D.; Lu, M.; Jensen, L.; Huang, T. J., Dynamic Tuning of Plasmon–Exciton Coupling in Arrays of Nanodisk–J-aggregate Complexes. *Adv. Mater.* **2010,** *22* (32), 3603-3607.

36. Zheng, Y. B.; Payton, J. L.; Chung, C. H.; Liu, R.; Cheunkar, S.; Pathem, B. K.; Yang, Y.; Jensen, L.; Weiss, P. S., Surface-Enhanced Raman Spectroscopy to Probe Reversibly Photoswitchable Azobenzene in Controlled Nanoscale Environments. *Nano Lett.* **2011,** *11* (8), 3447-3452.

37. Liu, G. L.; Yin, Y.; Kunchakarra, S.; Mukherjee, B.; Gerion, D.; Jett, S. D.; Bear, D. G.; Gray, J. W.; Alivisatos, A. P.; Lee, L. P., A nanoplasmonic molecular ruler for measuring nuclease activity and DNA footprinting. *Nat. Nanotechnol.* **2006,** *1* (1), 47-52.

38. Sönnichsen, C., Detecting Intruders on the Nanoscale. *Science* **2011,** *332* (6036), 1389-1390.

39. Xing, J.-F.; Zheng, M.-L.; Duan, X.-M., Two-photon polymerization microfabrication of hydrogels: an advanced 3D printing technology for tissue engineering and drug delivery. *Chem. Soc. Rev.* **2015,** *44* (15), 5031-5039.

40. Kaehr, B.; Shear, J. B., Mask-directed multiphoton lithography. *J. Am. Chem. Soc.* **2007,** *129* (7), 1904-1905.

41. Kaehr, B.; Shear, J. B., Multiphoton fabrication of chemically responsive protein hydrogels for microactuation. *Proc. Natl. Acad. Sci. U.S.A.* **2008,** *105* (26), 8850-8854.

42. Chen, X. Y.; Brewer, M. A.; Zou, C. P.; Campagnola, P. J., Adhesion and migration of ovarian cancer cells on crosslinked laminin fibers nanofabricated by multiphoton excited photochemistry. *Integr. Biol.* **2009,** *1* (7), 469-476.

43. Ritschdorff, E. T.; Nielson, R.; Shear, J. B., Multi-focal multiphoton lithography. *Lab Chip* **2012,** *12* (5), 867-871.

44. Galloway, C. M.; Kreuzer, M. P.; Aćimović, S. S.; Volpe, G.; Correia, M.; Petersen, S. B.; Neves-Petersen, M. T.; Quidant, R., Plasmon-assisted delivery of single nano-objects in an optical hot spot. *Nano Lett.* **2013,** *13* (9), 4299-4304.

45. Wiesbauer, M.; Wollhofen, R.; Vasic, B.; Schilcher, K.; Jacak, J.; Klar, T. A., Nano-anchors with single protein capacity produced with STED lithography. *Nano Lett.* **2013,** *13* (11), 5672-5678.

46. Scarabelli, L.; Coronado-Puchau, M.; Giner-Casares, J. J.; Langer, J.; Liz-Marzán, L. M., Monodisperse Gold Nanotriangles: Size Control, Large-Scale Self-Assembly, and Performance in Surface-Enhanced Raman Scattering. *ACS Nano* **2014,** *8* (6), 5833-5842.

47. Pitts, J. D.; Campagnola, P. J.; Epling, G. A.; Goodman, S. L., Submicron multiphoton free-form fabrication of proteins and polymers: studies of reaction efficiencies and applications in sustained release. *Macromolecules* **2000,** *33* (5), 1514-1523.

48. Liu, N.; Tang, M. L.; Hentschel, M.; Giessen, H.; Alivisatos, A. P., Nanoantenna-enhanced gas sensing in a single tailored nanofocus. *Nat. Mater.* **2011,** *10* (8), 631-636.

49. Olson, J.; Dominguez-Medina, S.; Hoggard, A.; Wang, L.-Y.; Chang, W.-S.; Link, S., Optical characterization of single plasmonic nanoparticles. *Chem. Soc. Rev.* **2015,** *44* (1), 40-57.

50. Wang, W.; Tao, N., Detection, counting, and imaging of single nanoparticles. *Anal. Chem.* **2013,** *86* (1), 2-14.

51. Fang, A.; White, S.; Jain, P. K.; Zamborini, F. P., Regio-selective Plasmonic Coupling in Metamolecular Analogs of Benzene Derivatives. *Nano Lett.* **2015,** *15* (1), 542–548.

52. Anker, J. N.; Hall, W. P.; Lyandres, O.; Shah, N. C.; Zhao, J.; Van Duyne, R. P., Biosensing with plasmonic nanosensors. *Nat. Mater.* **2008,** *7* (6), 442-453.

53. Gratton, E.; Breusegem, S.; Sutin, J.; Ruan, Q.; Barry, N., Fluorescence lifetime imaging for the two-photon microscope: time-domain and frequency-domain methods. *J. Biomed. Opt.* **2003,** *8* (3), 381-390.

54. Gabudean, A.-M.; Groza, R.; Maniu, D.; Astilean, S., Steady-state and time-resolved fluorescence studies on the conjugation of Rose Bengal to gold nanorods. *J. Mol. Struct.* **2014,** *1073*, 97-101.

55. Xu, D.; Neckers, D., Aggregation of rose bengal molecules in solution. *J. Photochem. Photobiol., A* **1987,** *40* (2), 361-370.

56. Acuna, G. P.; Bucher, M.; Stein, I. H.; Steinhauer, C.; Kuzyk, A.; Holzmeister, P.; Schreiber, R.; Moroz, A.; Stefani, F. D.; Liedl, T., Distance dependence of single-fluorophore quenching by gold nanoparticles studied on DNA origami. *ACS Nano* **2012,** *6* (4), 3189-3195.

Chapter 3:

1. Pietryga, J. M.; Park, Y. S.; Lim, J. H.; Fidler, A. F.; Bae, W. K.; Brovelli, S.; Klimov, V. I., Spectroscopic and Device Aspects of Nanocrystal Quantum Dots. *Chem. Rev.* **2016,** *116* (18), 10513-10622.
2. Yin, Y. D.; Talapin, D., The chemistry of functional nanomaterials. *Chem. Soc. Rev.* **2013,** *42* (7), 2484-2487.
3. Yu, W. W.; Peng, X. G., Formation of high-quality CdS and other II-VI semiconductor nanocrystals in noncoordinating solvents: Tunable reactivity of monomers. *Angew. Chem., Int. Ed.* **2002,** *41* (13), 2368-2371.
4. Cassette, E.; Helle, M.; Bezdetnaya, L.; Marchal, F.; Dubertret, B.; Pons, T., Design of new quantum dot materials for deep tissue infrared imaging. *Adv. Drug Deliver. Rev.* **2013,** *65* (5), 719-731.
5. Mashford, B. S.; Stevenson, M.; Popovic, Z.; Hamilton, C.; Zhou, Z. Q.; Breen, C.; Steckel, J.; Bulovic, V.; Bawendi, M.; Coe-Sullivan, S.; Kazlas, P. T., High-efficiency quantum-dot light-emitting devices with enhanced charge injection. *Nat. Photon.* **2013,** *7* (5), 407-412.
6. Kim, T. H.; Cho, K. S.; Lee, E. K.; Lee, S. J.; Chae, J.; Kim, J. W.; Kim, D. H.; Kwon, J. Y.; Amaratunga, G.; Lee, S. Y.; Choi, B. L.; Kuk, Y.; Kim, J. M.; Kim, K., Full-colour quantum dot displays fabricated by transfer printing. *Nat. Photon.* **2011,** *5* (3), 176-182.
7. Lan, X. Z.; Masala, S.; Sargent, E. H., Charge-extraction strategies for colloidal quantum dot photovoltaics. *Nat. Mater.* **2014,** *13* (3), 233-240.
8. Medintz, I. L.; Clapp, A. R.; Mattoussi, H.; Goldman, E. R.; Fisher, B.; Mauro, J. M., Self-assembled nanoscale biosensors based on quantum dot FRET donors. *Nat. Mater.* **2003,** *2* (9), 630-638.
9. Lee, A. D.; Jiang, Q.; Tang, M. C.; Zhang, Y. Y.; Seeds, A. J.; Liu, H. Y., InAs/GaAs Quantum-Dot Lasers Monolithically Grown on Si, Ge, and Ge-on-Si Substrates. *IEEE J. Sel. Top. Quantum Electon.* **2013,** *19* (4), 1901107.
10. Konstantatos, G.; Howard, I.; Fischer, A.; Hoogland, S.; Clifford, J.; Klem, E.; Levina, L.; Sargent, E. H., Ultrasensitive solution-cast quantum dot photodetectors. *Nature* **2006,** *442* (7099), 180-183.
11. Kagan, C. R.; Lifshitz, E.; Sargent, E. H.; Talapin, D. V., Building devices from colloidal quantum dots. *Science* **2016,** *353* (6302), 885.
12. Gu, H. W.; Zheng, R. K.; Zhang, X. X.; Xu, B., Facile one-pot synthesis of bifunctional heterodimers of nanoparticles: A conjugate of quantum dot and magnetic nanoparticles. *J. Am. Chem. Soc.* **2004,** *126* (18), 5664-5665.

13. Curto, A. G.; Volpe, G.; Taminiau, T. H.; Kreuzer, M. P.; Quidant, R.; van Hulst, N. F., Unidirectional Emission of a Quantum Dot Coupled to a Nanoantenna. *Science* **2010,** *329* (5994), 930-933.

14. Hoang, T. B.; Akselrod, G. M.; Mikkelsen, M. H., Ultrafast Room-Temperature Single Photon Emission from Quantum Dots Coupled to Plasmonic Nanocavities. *Nano Lett.* **2016,** *16* (1), 270-275.

15. Yang, A. K.; Odom, T. W., Breakthroughs in Photonics 2014: Advances in Plasmonic Nanolasers. *IEEE Photonics J.* **2015,** *7* (3), 1-6.

16. Galatsis, K.; Wang, K. L.; Ozkan, M.; Ozkan, C. S.; Huang, Y.; Chang, J. P.; Monbouquette, H. G.; Chen, Y.; Nealey, P.; Botros, Y., Patterning and Templating for Nanoelectronics. *Adv. Mater.* **2010,** *22* (6), 769-778.

17. Lan, H. B.; Ding, Y. C., Ordering, positioning and uniformity of quantum dot arrays. *Nano Today* **2012,** *7* (2), 94-123.

18. Xie, W. Q.; Gomes, R.; Aubert, T.; Bisschop, S.; Zhu, Y. P.; Hens, Z.; Brainis, E.; Van Thourhout, D., Nanoscale and Single-Dot Patterning of Colloidal Quantum Dots. *Nano Lett.* **2015,** *15* (11), 7481-7487.

19. Park, J. S.; Kyhm, J.; Kim, H. H.; Jeong, S.; Kang, J.; Lee, S. E.; Lee, K. T.; Park, K.; Barange, N.; Han, J.; Song, J. D.; Choi, W. K.; Han, I. K., Alternative Patterning Process for Realization of Large-Area, Full-Color, Active Quantum Dot Display. *Nano Lett.* **2016,** *16* (11), 6946-6953.

20. Choi, M. K.; Yang, J.; Kang, K.; Kim, D. C.; Choi, C.; Park, C.; Kim, S. J.; Chae, S. I.; Kim, T. H.; Kim, J. H.; Hyeon, T.; Kim, D. H., Wearable red-green-blue quantum dot light-emitting diode array using high-resolution intaglio transfer printing. *Nat. Commun.* **2015,** *6*, 7149.

21. Sun, L.-W.; Shi, H.-Q.; Li, W.-N.; Xiao, H.-M.; Fu, S.-Y.; Cao, X.-Z.; Li, Z.-X., Lanthanum-doped ZnO quantum dots with greatly enhanced fluorescent quantum yield. *J. Mater. Chem.* **2012,** *22* (17), 8221-8227.

22. Bao, B.; Li, M. Z.; Li, Y.; Jiang, J. K.; Gu, Z. K.; Zhang, X. Y.; Jiang, L.; Song, Y. L., Patterning Fluorescent Quantum Dot Nanocomposites by Reactive Inkjet Printing. *Small* **2015,** *11* (14), 1649-1654.

23. Kim, B. H.; Onses, M. S.; Lim, J. B.; Nam, S.; Oh, N.; Kim, H.; Yu, K. J.; Lee, J. W.; Kim, J. H.; Kang, S. K.; Lee, C. H.; Lee, J.; Shin, J. H.; Kim, N. H.; Leal, C.; Shim, M.; Rogers, J. A., High-Resolution Patterns of Quantum Dots Formed by Electrohydrodynamic Jet Printing for Light-Emitting Diodes. *Nano Lett.* **2015,** *15* (2), 969-973.

24. Shirasaki, Y.; Supran, G. J.; Bawendi, M. G.; Bulović, V., Emergence of colloidal quantum-dot light-emitting technologies. *Nat. Photon.* **2013,** *7* (1), 13-23.

25. Koh, W.-k.; Saudari, S. R.; Fafarman, A. T.; Kagan, C. R.; Murray, C. B., Thiocyanate-capped PbS nanocubes: ambipolar transport enables quantum dot based circuits on a flexible substrate. *Nano Lett.* **2011,** *11* (11), 4764-4767.

26. Meng, C.; Xiao, Y.; Wang, P.; Zhang, L.; Liu, Y.; Tong, L., Quantum-Dot-Doped Polymer Nanofibers for Optical Sensing. *Adv. Mater.* **2011,** *23* (33), 3770-3774.

27. Neumann, O.; Urban, A. S.; Day, J.; Lal, S.; Nordlander, P.; Halas, N. J., Solar Vapor Generation Enabled by Nanoparticles. *ACS Nano* **2013,** *7* (1), 42-49.

28. Fang, Z. Y.; Zhen, Y. R.; Neumann, O.; Polman, A.; de Abajo, F. J. G.; Nordlander, P.; Halas, N. J., Evolution of Light-Induced Vapor Generation at a Liquid-Immersed Metallic Nanoparticle. *Nano Lett.* **2013,** *13* (4), 1736-1742.

29. Roxworthy, B. J.; Ko, K. D.; Kumar, A.; Fung, K. H.; Chow, E. K. C.; Liu, G. L.; Fang, N. X.; Toussaint, K. C., Application of Plasmonic Bowtie Nanoantenna Arrays for Optical Trapping, Stacking, and Sorting. *Nano Lett.* **2012,** *12* (2), 796-801.

30. Lin, L. H.; Peng, X. L.; Mao, Z. M.; Li, W.; Yogeesh, M. N.; Rajeeva, B. B.; Perillo, E. P.; Dunn, A. K.; Akinwande, D.; Zheng, Y. B., Bubble-Pen Lithography. *Nano Lett.* **2016,** *16* (1), 701-708.

31. Zhao, C. L.; Xie, Y. L.; Mao, Z. M.; Zhao, Y. H.; Rufo, J.; Yang, S. K.; Guo, F.; Mai, J. D.; Huang, T. J., Theory and experiment on particle trapping and manipulation via optothermally generated bubbles. *Lab Chip* **2014,** *14* (2), 384-391.

32. Zheng, Y. J.; Liu, H.; Wang, Y.; Zhu, C.; Wang, S. M.; Cao, J. X.; Zhu, S. N., Accumulating microparticles and direct-writing micropatterns using a continuous-wave laser-induced vapor bubble. *Lab Chip* **2011,** *11* (22), 3816-3820.

33. Fujii, S.; Kanaizuka, K.; Toyabe, S.; Kobayashi, K.; Muneyuki, E.; Haga, M., Fabrication and Placement of a Ring Structure of Nanoparticles by a Laser-Induced Micronanobubble on a Gold Surface. *Langmuir* **2011,** *27* (14), 8605-8610.

34. Xie, Y.; Zhao, C. L., Optothermally generated surface bubble and its applications. *Nanoscale* **2017,** *9* (20), 6622-6631.

35. Baffou, G.; Polleux, J.; Rigneault, H.; Monneret, S., Super-Heating and Micro-Bubble Generation around Plasmonic Nanoparticles under cw Illumination. *J. Phys. Chem. C* **2014,** *118* (9), 4890-4898.

36. Baffou, G.; Quidant, R.; de Abajo, F. J. G., Nanoscale Control of Optical Heating in Complex Plasmonic Systems. *ACS Nano* **2010,** *4* (2), 709-716.

37. Liu, X. M.; Bao, L.; Dipalo, M.; De Angelis, F.; Zhang, X. H., Formation and dissolution of microbubbles on highly-ordered plasmonic nanopillar arrays. *Sci. Rep.* **2015,** *5,* 18515.

38. Lohse, D.; Zhang, X. H., Surface nanobubbles and nanodroplets. *Rev. Mod. Phys.* **2015,** *87* (3), 981-1035.

39. Baffou, G.; Polleux, J.; Rigneault, H.; Monneret, S., Super-Heating and Micro-Bubble Generation around Plasmonic Nanoparticles under cw Illumination. *J. Phys. Chem. C.* **2014,** *118* (9), 4890-4898.

40. Baffou, G.; Berto, P.; Urena, E. B.; Quidant, R.; Monneret, S.; Polleux, J.; Rigneault, H., Photoinduced Heating of Nanoparticle Arrays. *ACS Nano* **2013,** *7* (8), 6478-6488.

41. Dalvi, S. V.; Joshi, J. R., Modeling of microbubble dissolution in aqueous medium. *J. Colloid Interface Sci.* **2015,** *437*, 259-269.

42. Markman, A.; Javidi, B.; Tehranipoor, M., Photon-Counting Security Tagging and Verification Using Optically Encoded QR Codes. *IEEE Photonics J.* **2014,** *6* (1), 1-9.

43. Eisfeld, A.; Briggs, J. S., Absorption spectra of quantum aggregates interacting via long-range forces. *Phys. Rev. Lett.* **2006,** *96* (11), 113003.

44. Kim, B. H.; Nam, S.; Oh, N.; Cho, S. Y.; Yu, K. J.; Lee, C. H.; Zhang, J. Q.; Deshpande, K.; Trefonas, P.; Kim, J. H.; Lee, J.; Shin, J. H.; Yu, Y.; Lim, J. B.; Won, S. M.; Cho, Y. K.; Kim, N. H.; Seo, K. J.; Lee, H.; Kim, T. I.; Shim, M.; Rogers, J. A., Multilayer Transfer Printing for Pixelated, Multicolor Quantum Dot Light-Emitting Diodes. *ACS Nano* **2016,** *10* (5), 4920-4925.

45. Meitl, M. A.; Zhu, Z. T.; Kumar, V.; Lee, K. J.; Feng, X.; Huang, Y. Y.; Adesida, I.; Nuzzo, R. G.; Rogers, J. A., Transfer printing by kinetic control of adhesion to an elastomeric stamp. *Nat. Mater.* **2006,** *5* (1), 33-38.

46. McHale, J. P.; Garimella, S. V., Bubble nucleation characteristics in pool boiling of a wetting liquid on smooth and rough surfaces. *Int. J. Multiphase Flow* **2010,** *36* (4), 249-260.

Chapter 4:

1. Li, X. Q.; Wu, Y. W.; Steel, D.; Gammon, D.; Stievater, T. H.; Katzer, D. S.; Park, D.; Piermarocchi, C.; Sham, L. J., An all-optical quantum gate in a semiconductor quantum dot. *Science* **2003,** *301* (5634), 809-811.

2. Vanmaekelbergh, D.; Liljeroth, P., Electron-conducting quantum dot solids: novel materials based on colloidal semiconductor nanocrystals. *Chem. Soc. Rev.* **2005,** *34* (4), 299-312.

3. Kim, J. Y.; Voznyy, O.; Zhitomirsky, D.; Sargent, E. H., 25th Anniversary Article: Colloidal Quantum Dot Materials and Devices: A Quarter-Century of Advances. *Adv. Mater.* **2013,** *25* (36), 4986-5010.

4. Pietryga, J. M.; Park, Y. S.; Lim, J. H.; Fidler, A. F.; Bae, W. K.; Brovelli, S.; Klimov, V. I., Spectroscopic and Device Aspects of Nanocrystal Quantum Dots. *Chem. Rev.* **2016,** *116* (18), 10513-10622.

5. Yin, Y. D.; Talapin, D., The chemistry of functional nanomaterials. *Chem. Soc. Rev.* **2013,** *42* (7), 2484-2487.

6. Yu, W. W.; Peng, X. G., Formation of high-quality CdS and other II-VI semiconductor nanocrystals in noncoordinating solvents: Tunable reactivity of monomers. *Angew. Chem. Int. Edit.* **2002,** *41* (13), 2368-2371.

7. Cassette, E.; Helle, M.; Bezdetnaya, L.; Marchal, F.; Dubertret, B.; Pons, T., Design of new quantum dot materials for deep tissue infrared imaging. *Adv. Drug Deliver. Rev.* **2013,** *65* (5), 719-731.

8. Mashford, B. S.; Stevenson, M.; Popovic, Z.; Hamilton, C.; Zhou, Z. Q.; Breen, C.; Steckel, J.; Bulovic, V.; Bawendi, M.; Coe-Sullivan, S.; Kazlas, P. T., High-efficiency quantum-dot light-emitting devices with enhanced charge injection. *Nat. Photon.* **2013,** *7* (5), 407-412.

9. Kim, T. H.; Cho, K. S.; Lee, E. K.; Lee, S. J.; Chae, J.; Kim, J. W.; Kim, D. H.; Kwon, J. Y.; Amaratunga, G.; Lee, S. Y.; Choi, B. L.; Kuk, Y.; Kim, J. M.; Kim, K., Full-colour quantum dot displays fabricated by transfer printing. *Nat. Photon.* **2011,** *5* (3), 176-182.

10. Lan, X. Z.; Masala, S.; Sargent, E. H., Charge-extraction strategies for colloidal quantum dot photovoltaics. *Nat. Mater.* **2014,** *13* (3), 233-240.

11. Medintz, I. L.; Clapp, A. R.; Mattoussi, H.; Goldman, E. R.; Fisher, B.; Mauro, J. M., Self-assembled nanoscale biosensors based on quantum dot FRET donors. *Nat. Mater.* **2003,** *2* (9), 630-638.

12. Lee, A. D.; Jiang, Q.; Tang, M. C.; Zhang, Y. Y.; Seeds, A. J.; Liu, H. Y., InAs/GaAs Quantum-Dot Lasers Monolithically Grown on Si, Ge, and Ge-on-Si Substrates. *IEEE J. Sel. Topics Quantum Electon.* **2013,** *19* (4), 19001107.

13. Konstantatos, G.; Howard, I.; Fischer, A.; Hoogland, S.; Clifford, J.; Klem, E.; Levina, L.; Sargent, E. H., Ultrasensitive solution-cast quantum dot photodetectors. *Nature* **2006,** *442* (7099), 180-183.

14. Sapsford, K. E.; Pons, T.; Medintz, I. L.; Mattoussi, H., Biosensing with luminescent semiconductor quantum dots. *Sensors-Basel* **2006,** *6* (8), 925-953.

15. Zhang, L.; Chen, C.; Li, W. J.; Gao, G. H.; Gong, P.; Cai, L. T., Living Cell Multilifetime Encoding Based on Lifetime-Tunable Lattice Strained Quantum Dots. *ACS Appl. Mater. Inter.* **2016,** *8* (21), 13187-13191.

16. Chen, J. X.; Chan, Y. H.; Yang, T. L.; Wark, S. E.; Son, D. H.; Batteas, J. D., Spatially Selective Optical Tuning of Quantum Dot Thin Film Luminescence. *J. Am. Chem. Soc.* **2009,** *131* (51), 18204-18205.

17. Singh, M.; Haverinen, H. M.; Dhagat, P.; Jabbour, G. E., Inkjet Printing-Process and Its Applications. *Adv. Mater.* **2010,** *22* (6), 673-685.

18. Castrejon-Pita, J. R.; Baxter, W. R. S.; Morgan, J.; Temple, S.; Martin, G. D.; Hutchings, I. M., Future, Opportunities and Challenges of Inkjet Technologies. *At. Spray* **2013,** *23* (6), 541-565.

19. Medintz, I. L.; Uyeda, H. T.; Goldman, E. R.; Mattoussi, H., Quantum dot bioconjugates for imaging, labelling and sensing. *Nat. Mater.* **2005,** *4* (6), 435-446.

20. Lin, L. H.; Peng, X. L.; Mao, Z. M.; Li, W.; Yogeesh, M. N.; Rajeeva, B. B.; Perillo, E. P.; Dunn, A. K.; Akinwande, D.; Zheng, Y. B., Bubble-Pen Lithography. *Nano Lett.* **2016,** *16* (1), 701-708.

21. Sun, J.; Liu, Y.; Ritchie, J. M.; Luo, X., A haptic digital tool to assist the design, planning and manufacture of micro- and nanostructures. *Proc. Inst. Mech. Eng. E J. Process Mech. Eng.* **2015,** *229* (4), 290-298.

22. Baffou, G.; Polleux, J.; Rigneault, H.; Monneret, S., Super-Heating and Micro-Bubble Generation around Plasmonic Nanoparticles under cw Illumination. *J. Phys. Chem. C.* **2014,** *118* (9), 4890-4898.

23. Pang, C.; Zhao, Z.; Zhang, J. G.; Shi, L.; Du, L. D.; Fang, Z.; Liu, Y. H., An Advantageous Fabrication Technology to Integrate Pressure Sensor into Multi-sensor for Micro Weather Station. *2009 4th IEEE International Conference on Nano/Micro Engineered and Molecular Systems, Vols 1 and 2* **2009**, 270-273.

24. Kimura, J.; Uematsu, T.; Maenosono, S.; Yamaguchi, Y., Photoinduced fluorescence enhancement in CdSe/ZnS quantum dot submonolayers sandwiched between insulating layers: Influence of dot proximity. *J. Phys. Chem. B.* **2004,** *108* (35), 13258-13264.

25. Shcherbatyuk, G. V.; Inman, R. H.; Ghosh, S., Anomalous photo-induced spectral changes in CdSe/ZnS quantum dots. *J. Appl. Phys.* **2011,** *110* (5), 053518.

26. Dabbousi, B. O.; RodriguezViejo, J.; Mikulec, F. V.; Heine, J. R.; Mattoussi, H.; Ober, R.; Jensen, K. F.; Bawendi, M. G., (CdSe)ZnS core-shell quantum dots: Synthesis and characterization of a size series of highly luminescent nanocrystallites. *J. Phys. Chem. B.* **1997,** *101* (46), 9463-9475.

27. Wang, X. Y.; Zhang, J. Y.; Nazzal, A.; Xiao, M., Photo-oxidation-enhanced coupling in densely packed CdSe quantum-dot films. *Appl. Phys. Lett.* **2003,** *83* (1), 162-164.

28. Rajeeva, B. B.; Hernandez, D. S.; Wang, M. S.; Perillo, E.; Lin, L. H.; Scarabelli, L.; Pingali, B.; Liz-Marzan, L. M.; Dunn, A. K.; Shear, J. B.; Zheng, Y. B., Regioselective Localization and Tracking of Biomolecules on Single Gold Nanoparticles. *Adv. Sci.* **2015,** *2* (11), 1500232.

29. Hoang, T. B.; Akselrod, G. M.; Argyropoulos, C.; Huang, J. N.; Smith, D. R.; Mikkelsen, M. H., Ultrafast spontaneous emission source using plasmonic nanoantennas. *Nat. Commun.* **2015,** *6*, 7788.

30. Chen, J. X.; Chan, Y. H.; Yang, T. L.; Wark, S. E.; Son, D. H.; Batteas, J. D., Spatially Selective Optical Tuning of Quantum Dot Thin Film Luminescence. *J. Am. Chem. Soc.* **2009,** *131* (51), 18204-18205.

31. Zhang, L.; Chen, C.; Li, W.; Gao, G.; Gong, P.; Cai, L., Living Cell Multilifetime Encoding Based on Lifetime-Tunable Lattice-Strained Quantum Dots. *ACS Appl. Mater. Inter.* **2016,** *8* (21), 13187-13191.

Chapter 5:

1. Meinzer, N.; Barnes, W. L.; Hooper, I. R., Plasmonic meta-atoms and metasurfaces. *Nat. Photon.* **2014,** *8* (12), 889-898.

2. Nordlander, P., The Ring: A Leitmotif in Plasmonics. *ACS Nano* **2009,** *3* (3), 488-492.

3. Aizpurua, J.; Hanarp, P.; Sutherland, D. S.; Kall, M.; Bryant, G. W.; de Abajo, F. J. G., Optical properties of gold nanorings. *Phys. Rev. Lett.* **2003,** *90* (5), 057401.

4. Ye, J.; Van Dorpe, P.; Lagae, L.; Maes, G.; Borghs, G., Observation of plasmonic dipolar anti-bonding mode in silver nanoring structures. *Nanotechnology* **2009,** *20* (46), 465203.

5. Larsson, E. M.; Alegret, J.; Kall, M.; Sutherland, D. S., Sensing characteristics of NIR localized surface plasmon resonances in gold nanorings for application as ultrasensitive biosensors. *Nano Lett.* **2007,** *7* (5), 1256-1263.

6. Cetin, A. E.; Altug, H., Fano Resonant Ring/Disk Plasmonic Nanocavities on Conducting Substrates for Advanced Biosensing. *ACS Nano* **2012,** *6* (11), 9989-9995.

7. Banaee, M. G.; Crozier, K. B., Gold nanorings as substrates for surface-enhanced Raman scattering. *Opt. Lett.* **2010,** *35* (5), 760-762.

8. Hao, F.; Sonnefraud, Y.; Van Dorpe, P.; Maier, S. A.; Halas, N. J.; Nordlander, P., Symmetry Breaking in Plasmonic Nanocavities: Subradiant LSPR Sensing and a Tunable Fano Resonance. *Nano Lett.* **2008,** *8* (11), 3983-3988.

9. Huang, C. J.; Ye, J.; Wang, S.; Stakenborg, T.; Lagae, L., Gold nanoring as a sensitive plasmonic biosensor for on-chip DNA detection. *Appl. Phys. Lett.* **2012,** *100* (17), 173114.

10. Lewicka, Z. A.; Li, Y.; Bohloul, A.; Yu, W. W.; Colvin, V. L., Nanorings and nanocrescents formed via shaped nanosphere lithography: a route toward large areas of infrared metamaterials. *Nanotechnology* **2013,** *24* (11), 115303.

11. Zhao, J.; Frank, B.; Neubrech, F.; Zhang, C. J.; Braun, P. V.; Giessen, H., Hole-mask colloidal nanolithography combined with tilted-angle-rotation evaporation: A versatile method for fabrication of low-cost and large-area complex plasmonic nanostructures and metamaterials. *Beilstein J. Nanotechnol.* **2014,** *5*, 577-586.

12. Rajeeva, B. B.; Zheng, Y. B., Molecular Plasmonics: From Molecular-Scale Measurements and Control to Applications. *Nanotechnology: Delivering on the Promise, Vol 2* **2016,** *1224*, 23-52.

13. Neubrech, F.; Huck, C.; Weber, K.; Pucci, A.; Giessen, H., Surface-Enhanced Infrared Spectroscopy Using Resonant Nanoantennas. *Chem. Rev.* **2017,** *117* (7), 5110-5145.

14. Babayan, Y.; McMahon, J. M.; Li, S. Z.; Gray, S. K.; Schatz, G. C.; Odom, T. W., Confining Standing Waves in Optical Corrals. *ACS Nano* **2009,** *3* (3), 615-620.

15. Sounas, D. L.; Alu, A., Angular-Momentum-Biased Nanorings To Realize Magnetic-Free Integrated Optical Isolation. *ACS Photonics* **2014,** *1* (3), 198-204.

16. Xu, B.-B.; Zhang, R.; Liu, X.-Q.; Wang, H.; Zhang, Y.-L.; Jiang, H.-B.; Wang, L.; Ma, Z.-C.; Ku, J.-F.; Xiao, F.-S., On-chip fabrication of silver microflower arrays as a catalytic microreactor for allowing in situ SERS monitoring. *Chem. Commun.* **2012,** *48* (11), 1680-1682.

17. Tokel, O.; Inci, F.; Demirci, U., Advances in plasmonic technologies for point of care applications. *Chem. Rev.* **2014,** *114* (11), 5728-5752.

18. Chen, J.; Liao, W.-S.; Chen, X.; Yang, T.; Wark, S. E.; Son, D. H.; Batteas, J. D.; Cremer, P. S., Evaporation-induced assembly of quantum dots into nanorings. *ACS Nano* **2008,** *3* (1), 173-180.

19. Halpern, A. R.; Corn, R. M., Lithographically patterned electrodeposition of gold, silver, and nickel nanoring arrays with widely tunable near-infrared plasmonic resonances. *ACS Nano* **2013,** *7* (2), 1755-1762.

20. Bao, Y.; Witten, T. A.; Scherer, N. F., Self-Organizing Arrays of Size Scalable Nanoparticle Rings. *ACS Nano* **2016,** *10* (9), 8947-8955.

21. Zheng, Y.; Wang, S.; Huan, A.; Wang, Y., Fabrication of large area ordered metal nanoring arrays for nanoscale optical sensors. *J. Non-Cryst. Solids* **2006,** *352* (23), 2532-2535.

22. Winkler, R.; Schmidt, F.-P.; Haselmann, U.; Fowlkes, J. D.; Lewis, B. B.; Kothleitner, G.; Rack, P. D.; Plank, H., Direct-Write 3D Nanoprinting of Plasmonic Structures. *ACS Appl. Mater. Inter.* **2016,** *9* (9), 8233–8240.

23. Taylor, A. B.; Michaux, P.; Mohsin, A. S.; Chon, J. W., Electron-beam lithography of plasmonic nanorod arrays for multilayered optical storage. *Opt. Express* **2014,** *22* (11), 13234-13243.

24. Wolf, O.; Campione, S.; Benz, A.; Ravikumar, A. P.; Liu, S.; Luk, T. S.; Kadlec, E. A.; Shaner, E. A.; Klem, J. F.; Sinclair, M. B., Phased-array sources based on nonlinear metamaterial nanocavities. *Nat. Commun.* **2015,** *6*, 7667.

25. Bagheri, S.; Weber, K.; Gissibl, T.; Weiss, T.; Neubrech, F.; Giessen, H., Fabrication of square-centimeter plasmonic nanoantenna arrays by femtosecond

direct laser writing lithography: effects of collective excitations on SEIRA enhancement. *ACS Photonics* **2015,** *2* (6), 779-786.

26. Xie, Y.; Yang, S.; Mao, Z.; Li, P.; Zhao, C.; Cohick, Z.; Huang, P.-H.; Huang, T. J., In situ fabrication of 3D Ag@ ZnO nanostructures for microfluidic surface-enhanced Raman scattering systems. *ACS Nano* **2014,** *8* (12), 12175-12184.

27. Roxworthy, B. J.; Ko, K. D.; Kumar, A.; Fung, K. H.; Chow, E. K. C.; Liu, G. L.; Fang, N. X.; Toussaint, K. C., Application of Plasmonic Bowtie Nanoantenna Arrays for Optical Trapping, Stacking, and Sorting. *Nano Lett.* **2012,** *12* (2), 796-801.

28. Lin, L. H.; Peng, X. L.; Mao, Z. M.; Li, W.; Yogeesh, M. N.; Rajeeva, B. B.; Perillo, E. P.; Dunn, A. K.; Akinwande, D.; Zheng, Y. B., Bubble-Pen Lithography. *Nano Lett.* **2016,** *16* (1), 701-708.

29. Bangalore Rajeeva, B.; Lin, L.; Perillo, E. P.; Peng, X.; Yu, W. W.; Dunn, A.; Zheng, Y., High-Resolution Bubble Printing of Quantum Dots. *ACS Appl. Mater. Inter.* **2017,** *9* (19), 16725–16733.

30. Rajeeva, B. B.; Alabandi, M. A.; Lin, L.; Perillo, E. P.; Dunn, A. K.; Zheng, Y., Patterning and fluorescence tuning of quantum dots with haptic-interfaced bubble printing. *J. Mater. Chem. C* **2017,** *5*, 5693-5699.

31. Fujii, S.; Fukano, R.; Hayami, Y.; Ozawa, H.; Muneyuki, E.; Kitamura, N.; Hag, M., Simultaneous Formation and Spatial Patterning of ZnO on ITO Surfaces by Local Laser-Induced Generation of Microbubbles in Aqueous Solutions of [Zn(NH3)(4)](2+). *ACS Appl. Mater. Inter.* **2017,** *9* (9), 8413-8419.

32. Walker, S. B.; Lewis, J. A., Reactive silver inks for patterning high-conductivity features at mild temperatures. *J. Am. Chem. Soc.* **2012,** *134* (3), 1419-1421.

33. Enders, M.; Mukai, S.; Uwada, T.; Hashimoto, S., Plasmonic Nanofabrication through Optical Heating. *J. Phys. Chem. C.* **2016,** *120* (12), 6723-6732.

34. Sear, R. P., Nucleation: theory and applications to protein solutions and colloidal suspensions. *J. Phys. Condens. Matter* **2007,** *19* (3), 033101.

35. Zhao, C. L.; Xie, Y. L.; Mao, Z. M.; Zhao, Y. H.; Rufo, J.; Yang, S. K.; Guo, F.; Mai, J. D.; Huang, T. J., Theory and experiment on particle trapping and manipulation via optothermally generated bubbles. *Lab Chip* **2014,** *14* (2), 384-391.

36. Aksu, S.; Cetin, A. E.; Adato, R.; Altug, H., Plasmonically Enhanced Vibrational Biospectroscopy Using Low-Cost Infrared Antenna Arrays by Nanostencil Lithography. *Adv. Opt. Mater.* **2013,** *1* (11), 798-803.

37. Jensen, L.; Schatz, G. C., Resonance Raman scattering of rhodamine 6G as calculated using time-dependent density functional theory. *J. Phys. Chem. A* **2006,** *110* (18), 5973-5977.

38. Kang, Z. W.; Chen, J. J.; Ho, H. P., Surface-enhanced Raman scattering via entrapment of colloidal plasmonic nanocrystals by laser generated microbubbles on random gold nano-islands. *Nanoscale* **2016,** *8* (19), 10266-10272.

39. Chiou, P. Y.; Ohta, A. T.; Wu, M. C., Massively parallel manipulation of single cells and microparticles using optical images. *Nature* **2005,** *436* (7049), 370-372.

40. Xie, Y. L.; Zhao, C. L.; Zhao, Y. H.; Li, S. X.; Rufo, J.; Yang, S. K.; Guo, F.; Huang, T. J., Optoacoustic tweezers: a programmable, localized cell concentrator based on opto-thermally generated, acoustically activated, surface bubbles. *Lab Chip* **2013,** *13* (9), 1772-1779.

41. Noh, J.H.; Stanford, M. G.; Lewis, B. B.; Fowlkes, J. D.; Plank, H.; Rack, P. D.,. Nanoscale electron beam-induced deposition and purification of ruthenium for extreme ultraviolet lithography mask repair. *Appl. Phys. A* **2014,** *117 (4)*, 1705-1713.

Chapter 6:

1. Keil, L.; Hartmann, M.; Lanzmich, S.; Braun, D., Probing of molecular replication and accumulation in shallow heat gradients through numerical simulations. *Phys. Chem. Chem. Phys.* **2016,** *18* (30), 20153-20159.

2. Budin, I.; Bruckner, R. J.; Szostak, J. W., Formation of Protocell-like Vesicles in a Thermal Diffusion Column. *J. Am. Chem. Soc.* **2009,** *131* (28), 9628-9629.

3. Keil, L. M. R.; Moller, F. M.; Kiess, M.; Kudella, P. W.; Mast, C. B., Proton gradients and pH oscillations emerge from heat flow at the microscale. *Nat. Commun.* **2017,** *8*, 1897.

4. Liu, M.; Pang, Y. J.; Zhang, B.; De Luna, P.; Voznyy, O.; Xu, J. X.; Zheng, X. L.; Dinh, C. T.; Fan, F. J.; Cao, C. H.; de Arquer, F. P. G.; Safaei, T. S.; Mepham, A.; Klinkova, A.; Kumacheva, E.; Filleter, T.; Sinton, D.; Kelley, S. O.; Sargent, E. H., Enhanced electrocatalytic CO2 reduction via field-induced reagent concentration. *Nature* **2016,** *537* (7620), 382-386.

5. Grossier, R.; Magnaldo, A.; Veesler, S., Ultra-fast crystallization due to confinement. *J. Cryst. Growth* **2010,** *312* (4), 487-489.

6. He, R.; Wang, Y. C.; Wang, X. Y.; Wang, Z. T.; Liu, G.; Zhou, W.; Wen, L. P.; Li, Q. X.; Wang, X. P.; Chen, X. Y.; Zeng, J.; Hou, J. G., Facile synthesis of pentacle gold-copper alloy nanocrystals and their plasmonic and catalytic properties. *Nat. Commun.* **2014,** *5*, 4327.

7. Ferrando, R.; Jellinek, J.; Johnston, R. L., Nanoalloys: From theory to applications of alloy clusters and nanoparticles. *Chem. Rev.* **2008,** *108* (3), 845-910.

8. Garcia, S.; Zhang, L.; Piburn, G. W.; Henkelman, G.; Humphrey, S. M., Microwave Synthesis of Classically Immiscible Rhodium-Silver and Rhodium-Gold Alloy

Nanoparticles: Highly Active Hydrogenation Catalysts. *ACS Nano* **2014,** *8* (11), 11512-11521.

9. Swiatkowska-Warkocka, Z.; Pyatenko, A.; Krok, F.; Jany, B. R.; Marszalek, M., Synthesis of new metastable nanoalloys of immiscible metals with a pulse laser technique. *Sci. Rep.* **2015,** *5*, 9849.

10. Wang, D.; Villa, A.; Porta, F.; Prati, L.; Su, D. S., Bimetallic gold/palladium catalysts: Correlation between nanostructure and synergistic effects. *J. Phys. Chem. C* **2008,** *112* (23), 8617-8622.

11. Kunal, P.; Roberts, E. J.; Riche, C. T.; Jarvis, K.; Malrnstadt, N.; Brutchey, R. L.; Humphrey, S. M., Continuous Flow Synthesis of Rh and RhAg Alloy Nanoparticle Catalysts Enables Scalable Production and Improved Morphological Control. *Chem. Mater.* **2017,** *29* (10), 4341-4350.

12. Essinger-Hileman, E. R.; DeCicco, D.; Bondi, J. F.; Schaak, R. E., Aqueous room-temperature synthesis of Au-Rh, Au-Pt, Pt-Rh, and Pd-Rh alloy nanoparticles: fully tunable compositions within the miscibility gaps. *J. Mater. Chem.* **2011,** *21* (31), 11599-11604.

13. Yonezawa, T.; Toshima, N., Polymer-Protected and Micelle-Protected Gold Platinum Bimetallic Systems - Preparation, Application to Catalysis for Visible-Light-Induced Hydrogen Evolution, and Analysis of Formation Process with Optical Methods. *J. Mol. Catal.* **1993,** *83* (1-2), 167-181.

14. Endo, T.; Fukunaga, T.; Yoshimura, T.; Esumi, K., Scavenging DPPH radicals catalyzed by binary noble metal-dendrimer nanocomposites. *J. Colloid Interf. Sci.* **2006,** *302* (2), 516-521.

15. Chen, P. C.; Liu, G. L.; Zhou, Y.; Brown, K. A.; Chernyak, N.; Hedrick, J. L.; He, S.; Xie, Z.; Lin, Q. Y.; Dravid, V. P.; O'Neill-Slawecki, S. A.; Mirkin, C. A., Tip-Directed Synthesis of Multimetallic Nanoparticles. *J. Am. Chem. Soc.* **2015,** *137* (28), 9167-9173.

16. Zhang, D. S.; Goekce, B.; Barcikowski, S., Laser Synthesis and Processing of Colloids: Fundamentals and Applications. *Chem. Rev.* **2017,** *117* (5), 3990-4103.

17. Tominaga, Y.; Maruyama, M.; Yoshimura, M.; Koizumi, H.; Tachibana, M.; Sugiyama, S.; Adachi, H.; Tsukamoto, K.; Matsumura, H.; Takano, K.; Murakami, S.; Inoue, T.; Yoshikawa, H. Y.; Mori, Y., Promotion of protein crystal growth by actively switching crystal growth mode via femtosecond laser ablation. *Nat. Photon.* **2016,** *10* (11), 723-726.

18. Rajeeva, B. B.; Wu, Z. L.; Briggs, A.; Acharya, P. V.; Walker, S. B.; Peng, X. L.; Bahadur, V.; Bank, S. R.; Zheng, Y. B., "Point-and-Shoot" Synthesis of Metallic Ring Arrays and Surface-Enhanced Optical Spectroscopy. *Adv. Opt. Mat.* **2018,** *6* (10), 1701213.

19. Davies, R.; Dinsdale, A.; Gisby, J.; Robinson, J.; Martin, a. M., MTDATA-thermodynamic and phase equilibrium software from the national physical laboratory. *Calphad* **2002,** *26* (2), 229-271.

20. Fang, Z. Y.; Zhen, Y. R.; Neumann, O.; Polman, A.; de Abajo, F. J. G.; Nordlander, P.; Halas, N. J., Evolution of Light-Induced Vapor Generation at a Liquid-Immersed Metallic Nanoparticle. *Nano Lett.* **2013,** *13* (4), 1736-1742.

21. Lin, L. H.; Peng, X. L.; Mao, Z. M.; Li, W.; Yogeesh, M. N.; Rajeeva, B. B.; Perillo, E. P.; Dunn, A. K.; Akinwande, D.; Zheng, Y. B., Bubble-Pen Lithography. *Nano Lett.* **2016,** *16* (1), 701-708.

22. Rajeeva, B. B.; Lin, L. H.; Perillo, E. P.; Peng, X. L.; Yu, W. W.; Dunn, A. K.; Zheng, Y. B., High-Resolution Bubble Printing of Quantum Dots. *ACS Appl. Mater. Interfaces* **2017,** *9* (19), 16725-16733.

23. Zhakeyev, A.; Wang, P. F.; Zhang, L.; Shu, W. M.; Wang, H. Z.; Xuan, J., Additive Manufacturing: Unlocking the Evolution of Energy Materials. *Adv. Sci.* **2017,** *4* (10), 1700187.

24. Thanh, N. T. K.; Maclean, N.; Mahiddine, S., Mechanisms of Nucleation and Growth of Nanoparticles in Solution. *Chem. Rev.* **2014,** *114* (15), 7610-7630.

25. De Yoreo, J. J.; Vekilov, P. G., Principles of crystal nucleation and growth. *Biomineralization* **2003,** *54*, 57-93.

26. Weiss, G. H.; Rubin, R. J., Random-Walks - Theory and Selected Applications. *Adv. Chem. Phys.* **1983,** *52*, 363-505.

27. Preuss, M.; Butt, H. J., Direct measurement of forces between particles and bubbles. *Int. J. Miner. Process* **1999,** *56* (1-4), 99-115.

28. Fielden, M. L.; Hayes, R. A.; Ralston, J., Surface and capillary forces affecting air bubble-particle interactions in aqueous electrolyte. *Langmuir* **1996,** *12* (15), 3721-3727.

29. Wang, L. H.; Harris, M. T., Stagnation Point of Surface Flow during Drop Evaporation. *Langmuir* **2018,** *34* (20), 5918-5925.

30. Xu, X. F.; Luo, J. B., Marangoni flow in an evaporating water droplet. *Appl. Phys. Lett.* **2007,** *91* (12), 124102.

31. Shiba, F.; Okawa, Y., Relationship between supersaturation ratio and supply rate of solute in the growth process of monodisperse colloidal particles and application to AgHr systems. *J. Phys. Chem. B.* **2005,** *109* (46), 21664-21668.

32. Xiao, S.; Hu, W.; Luo, W.; Wu, Y.; Li, X.; Deng, H., Size effect on alloying ability and phase stability of immiscible bimetallic nanoparticles. *Eur. Phys. J. B* **2006,** *54* (4), 479-484.

33. Yang, J., Computationally assisted STEM and EXAFS characterization of tunable Rh/Au and Rh/Ag bimetallic nanoparticle catalysts. *Abstr. Pap. Am. Chem. Soc.* **2017,** *254*.

34. Chen, P. C.; Liu, X. L.; Hedrick, J. L.; Xie, Z.; Wang, S. Z.; Lin, Q. Y.; Hersam, M. C.; Dravid, V. P.; Mirkin, C. A., Polyelemental nanoparticle libraries. *Science* **2016,** *352* (6293), 1565-1569.

35. Holewinski, A.; Idrobo, J. C.; Linic, S., High-performance Ag-Co alloy catalysts for electrochemical oxygen reduction. *Nat. Chem.* **2014,** *6* (9), 828-834.

36. Zugic, B.; Wang, L. C.; Heine, C.; Zakharov, D. N.; Lechner, B. A. J.; Stach, E. A.; Biener, J.; Salmeron, M.; Madix, R. J.; Friend, C. M., Dynamic restructuring drives catalytic activity on nanoporous gold-silver alloy catalysts. *Nat. Mater.* **2017,** *16* (5), 558-564.

37. Li, H.; Luo, L.; Kunal, P.; Bonifacio, C. S.; Duan, Z. Y.; Yang, J. C.; Humphrey, S. M.; Crooks, R. M.; Henkelman, G., Oxygen Reduction Reaction on Classically Immiscible Bimetallics: A Case Study of RhAu. *J. Phys. Chem. C* **2018,** *122* (5), 2712-2716.

Chapter 7:

1. Rajeeva, B. B.; Menz, R.; Zheng, Y. B., Towards rational design of multifunctional theranostic nanoparticles: what barriers do we need to overcome? *Nanomedicine* **2014,** *9* (12), 1767-1770.

2. Chen, K.; Rajeeva, B. B.; Wu, Z. L.; Rukavina, M.; Dao, T. D.; Ishii, S.; Aono, M.; Nagao, T.; Zheng, Y. B., Moire Nanosphere Lithography. *ACS Nano* **2015,** *9* (6), 6031-6040.

3. Gan, J. Y.; Lu, X. H.; Rajeeva, B. B.; Menz, R.; Tong, Y. X.; Zheng, Y. B., Efficient Photoelectrochemical Water Oxidation over Hydrogen-Reduced Nanoporous BiVO4 with Ni-B-i Electrocatalyst. *Chemelectrochem* **2015,** *2* (9), 1385-1395.

4. Rajeeva, B. B.; Hernandez, D. S.; Wang, M. S.; Perillo, E.; Lin, L. H.; Scarabelli, L.; Pingali, B.; Liz-Marzan, L. M.; Dunn, A. K.; Shear, J. B.; Zheng, Y. B., Regioselective Localization and Tracking of Biomolecules on Single Gold Nanoparticles. *Adv. Sci.* **2015,** *2* (11), 1500232.

5. Gan, J. Y.; Rajeeva, B. B.; Wu, Z. L.; Penley, D.; Liang, C. L.; Tong, Y. X.; Zheng, Y. B., Plasmon-enhanced nanoporous BiVO4 photoanodes for efficient photoelectrochemical water oxidation. *Nanotechnology* **2016,** *27* (23), 235401.

6. Gan, J. Y.; Rajeeva, B. B.; Wu, Z. L.; Penley, D.; Zheng, Y. B., Hydrogen-reduced bismuth oxyiodide nanoflake arrays with plasmonic enhancements for efficient photoelectrochemical water reduction. *Electrochim. Acta* **2016,** *219*, 20-27.

7. Lee, J.; Rajeeva, B. B.; Yuan, T. Y.; Guo, Z. H.; Lin, Y. H.; Al-Hashimi, M.; Zheng, Y. B.; Fang, L., Thermodynamic synthesis of solution processable ladder polymers. *Chem. Sci.* **2016,** *7* (2), 881-889.

8. Lin, L. H.; Peng, X. L.; Mao, Z. M.; Li, W.; Yogeesh, M. N.; Rajeeva, B. B.; Perillo, E. P.; Dunn, A. K.; Akinwande, D.; Zheng, Y. B., Bubble-Pen Lithography. *Nano Lett.* **2016,** *16* (1), 701-708.

9. Wang, M. S.; Rajeeva, B. B.; Scarabelli, L.; Perillo, E. P.; Dunn, A. K.; Liz-Marzan, L. M.; Zheng, Y. B., Molecular-Fluorescence Enhancement via Blue-Shifted Plasmon-Induced Resonance Energy Transfer. *J. Phys. Chem. C.* **2016,** *120* (27), 14820-14827.

10. Wu, Z. L.; Kelp, G.; Yogeesh, M. N.; Li, W.; McNicholas, K. M.; Briggs, A.; Rajeeva, B. B.; Akinwande, D.; Bank, S. R.; Shvets, G.; Zheng, Y. B., Dual-band moire metasurface patches for multifunctional biomedical applications. *Nanoscale* **2016,** *8* (43), 18461-18468.

11. Rajeeva, B. B.; Alabandi, M. A.; Lin, L. H.; Perillo, E. P.; Dunn, A. K.; Zheng, Y. B., Patterning and fluorescence tuning of quantum dots with haptic-interfaced bubble printing. *J. Mater. Chem. C.* **2017,** *5* (23), 5693-5699.

12. Rajeeva, B. B.*; Lin, L. H.*; Perillo, E. P.; Peng, X. L.; Yu, W. W.; Dunn, A. K.; Zheng, Y. B., High-Resolution Bubble Printing of Quantum Dots. *ACS Appl. Mater. Inter.* **2017,** *9* (19), 16725-16733.

13. Wang, M. S.; Hartmann, G.; Wu, Z. L.; Scarabelli, L.; Rajeeva, B. B.; Jarrett, J. W.; Perillo, E. P.; Dunn, A. K.; Liz-Marzan, L. M.; Hwang, G. S.; Zheng, Y. B., Controlling Plasmon-Enhanced Fluorescence via Intersystem Crossing in Photoswitchable Molecules. *Small* **2017,** *13* (38), 1701763.

14. Wang, M. S.; Li, W.; Scarabelli, L.; Rajeeva, B. B.; Terrones, M.; Liz-Marzan, L. M.; Akinwande, D.; Zheng, Y. B., Plasmon-trion and plasmon-exciton resonance energy transfer from a single plasmonic nanoparticle to monolayer MoS2. *Nanoscale* **2017,** *9* (37), 13947-13955.

15. Lin, L.; Li, J.; Li, W.; Yogeesh, M. N.; Shi, J.; Peng, X.; Liu, Y.; Rajeeva, B. B.; Becker, M. F.; Liu, Y., Optothermoplasmonic Nanolithography for On-Demand Patterning of 2D Materials. *Adv. Funct. Mater.* **2018,** *28* (41), 1803990.

16. Liu, Y.*; Lin, L.*; Bangalore Rajeeva, B.*; Jarrett, J. W.; Li, X.; Peng, X.; Kollipara, P.; Yao, K.; Akinwande, D.; Dunn, A. K.; Zheng, Y., Nanoradiator-Mediated Deterministic Opto-Thermoelectric Manipulation. *ACS Nano* **2018,** *12* (10), 10383-10392.

17. Rajeeva, B. B.; Lin, L.; Zheng, Y., Design and Applications of Lattice Plasmon Resonances. *Nano Res.* **2018,** *11* (9), 4423-4440.

18. Rajeeva, B. B.; Wu, Z. L.; Briggs, A.; Acharya, P. V.; Walker, S. B.; Peng, X. L.; Bahadur, V.; Bank, S. R.; Zheng, Y. B., "Point-and-Shoot" Synthesis of Metallic

Ring Arrays and Surface-Enhanced Optical Spectroscopy. *Adv. Opt. Mater.* **2018,** *6* (10), 1701213.

19. Rajeeva, B. B.; Zheng, Y. B. "Molecular plasmonics: From molecular-scale measurements and control to applications." Nanotechnology: Delivering on the Promise Volume 2. American Chemical Society, **2016**, *2*, 23-52.

20. Peng, X.; Rajeeva, B. B.; Teal, D.; Zheng, Y. "Plasmofluidics for Biosensing and Medical Diagnostics." Nanotechnology Characterization Tools for Biosensing and Medical Diagnosis. Springer, Berlin, Heidelberg, **2018**, 213-247.